WILEY-VCH

Naminosuke Kubota

Propellants and Explosives

Thermochemical Aspects of Combustion

Propellants and Explosives: Thermochemical Aspects of Combustion. Naminosuke Kubota
Copyright © 2002 Wiley-VCH Verlag GmbH & Co. KGaA
ISBNs: 3-527-30210-7 (Hardback); 3-527-60050-7 (Electronic)

Naminosuke Kubota

Propellants and Explosives

Propellants and Explosives: Thermochemical Aspects of Combustion. Naminosuke Kubota
Copyright © 2002 Wiley-VCH Verlag GmbH & Co. KGaA
ISBNs: 3-527-30210-7 (Hardback); 3-527-60050-7 (Electronic)

Naminosuke Kubota

Propellants and Explosives

Thermochemical Aspects of Combustion

WILEY-VCH

Propellants and Explosives: Thermochemical Aspects of Combustion. Naminosuke Kubota
Copyright © 2002 Wiley-VCH Verlag GmbH & Co. KGaA
ISBNs: 3-527-30210-7 (Hardback); 3-527-60050-7 (Electronic)

Author

Dr. Naminosuke Kubota
Mitsubishi Electric Corporation
Kamimachiya 325
Kamakura 247-0065
Japan

This book was carefully produced. Nevertheless, author and publisher do not warrant the information contained therein to be free of errors. Readers are advised to keep in mind that statements, data, illustrations, procedural details or other items may inadvertently be inaccurate.

Library of Congress Card No.:
Applied for.

British Library Cataloguing-in-Publication Data:
A catalogue record for this book is available from the British Library.

Die Deutsche Bibliothek – CIP Cataloguing-in-Publication Data:
A catalogue record for this publication is available from Die Deutsche Bibliothek.

© WILEY-VCH GmbH, Weinheim, Germany, 2002

Printed on acid-free paper.
All rights reserved (including those of translation in other languages). No part of this book may be reproduced in any form – by photoprinting, microfilm, or any other means – nor transmitted or translated into a machine language without written permission from the publishers. Registered names, trademarks, etc. used in this book, even when not specifically marked as such, are not to be considered unprotected by law.

Printed in the Federal Republic of Germany.

Composition Kühn & Weyh, Freiburg
Printing betzdruck GmbH, Darmstadt
Bookbinding Großbuchbinderei J. Schäffer GmbH & Co. KG, Grünstadt
ISBN 3-527-30210-7

Propellants and Explosives: Thermochemical Aspects of Combustion. Naminosuke Kubota
Copyright © 2002 Wiley-VCH Verlag GmbH & Co. KGaA
ISBNs: 3-527-30210-7 (Hardback); 3-527-60050-7 (Electronic)

Contents

Propellants and Explosives: Thermochemical Aspects of Combustion. Naminosuke Kubota
Copyright © 2002 Wiley-VCH Verlag GmbH & Co. KGaA
ISBNs: 3-527-30210-7 (Hardback); 3-527-60050-7 (Electronic)

Preface

Propellants and explosives are composed of energetic materials that produce high temperature and pressure through combustion phenomena. These phenomena include complex physicochemical changes from solid to liquid and gas, accompanied by exothermic rapid reactions. A number of books related to combustion have been published, such as an excellent theoretical book, Combustion Theory, 2nd edition, by F. A. Williams, Benjamin/Cummings, New York (1985) and an instructive book for graduate students, Combustion, by I. Glassman, Academic Press, New York (1977). However, no instructive books related to the combustion of solid energetic materials have been published. Therefore, this book is intended as an introductory text in the combustion of energetic materials for the reader engaged in rocketry or in explosives technology.

The book is divided into four parts. The first part (Chapters 1–3) includes brief reviews of the fundamentals of the conversion from chemical energy to aerothermal energy. References listed in each chapter are useful to the reader for better understanding of the physical basis of the energy conversion process: energy formation, supersonic flow, shock wave, detonation, and deflagration. The second part (Chapter 4) presents the energetics of chemical compounds used for propellants and explosives, such as heat of formation, heat of explosion, adiabatic flame temperature, and specific impulse.

The third part (Chapters 5–8) deals with the measurement results of burning rate behavior of various types of chemical compounds, propellants, and explosives. The combustion wave structures and the heat feedback processes from the gas phase to the condensed phase are also discussed in the light of the understanding of their combustion mechanisms. The experimental and analytical data described in the chapters are mostly from results previously presented by the author. Descriptions of the detailed thermal decomposition mechanisms from solid phase to liquid phase or to gas phase are not included. The fourth part (Chapter 9) describes the combustion phenomena encountered during rocket motor operation, such as the stability criterion of a rocket motor, temperature sensitivity, ignition transients, erosive burning, and combustion oscillations. The fundamental principle of variable-flow ducted rockets is also presented. The combustion characteristics and energetics of the gas-generating propellants use for ducted rockets are discussed.

Since numerous kinds of energetic materials are used for propellants and explosives, it is not possible to give a comprehensive view of the combustion processes of energetic materials. In this book, the combustion processes of typical energetic crystalline and polymeric materials and various types of propellants are presented in order to give a generalized approach to understanding their combustion mechanisms.

Kamakura, Japan
November, 2001

Naminosuke Kubota

Propellants and Explosives: Thermochemical Aspects of Combustion. Naminosuke Kubota
Copyright © 2002 Wiley-VCH Verlag GmbH & Co. KGaA
ISBNs: 3-527-30210-7 (Hardback); 3-527-60050-7 (Electronic)

1
Thermodynamics of Energy Conversion

1.1
Fundamentals of Thermodynamics

1.1.1
First Law of Thermodynamics

The first law of thermodynamics relates the energy conversion produced by chemical reaction of an energetic material to the work acting on a propulsive or explosive system. The heat produced by chemical reaction (q) is converted to the internal energy of the reaction product (e) and the work done to the system (w) as

$$dq = de + dw \tag{1.1}$$

The work is done by the expansion of the reaction product, as given by

$$dw = pdv \quad \text{or} \quad dw = pd\,(1/\rho) \tag{1.2}$$

where v is the specific volume (volume per unit mass) of the reaction product and ρ is density defined in $v = 1/\rho$. Enthalpy h is defined by

$$dh = de + d\,(pv) \tag{1.3}$$

Substituting Eqs (1.1) and (1.2) into Eq. (1.3), one gets

$$dh = dq + vdp \tag{1.4}$$

The equation of state for one gram of a perfect gas is represented by

$$pv = RT \quad \text{or} \quad p = \rho RT \tag{1.5}$$

where T is temperature and R is the gas constant. The gas constant is given by

$$R = \mathrm{R}/M_g \tag{1.6}$$

where M_g is molecular mass, and R is the universal gas constant, R = 8.315 J/mol K = 847.9 kg m/kmol K = 1.987 kcal/kmol K. In the case of n moles of a perfect gas and volume V, the equation of state is represented by

$$pV = n\mathrm{R}T \tag{1.5a}$$

1.1.2
Specific Heat

The specific heat is defined as

$$c_v = \left(\frac{de}{dT}\right)_v \qquad c_p = \left(\frac{dh}{dT}\right)_p \tag{1.7}$$

where c_v is specific heat at constant volume and c_p is specific heat at constant pressure. Both specific heats represent change of energy content with temperature. Using Eqs. (1.3) and (1.5), one gets the relationship

$$c_p - c_v = R \tag{1.8}$$

Specific heat ratio γ is defined as

$$\gamma = c_p \,/\, c_v \tag{1.9}$$

Using Eq. (1.9), one gets the relationship

$$c_v = \frac{R}{\gamma - 1} \qquad c_p = \frac{\gamma R}{\gamma - 1} \tag{1.10}$$

Specific heat is an important parameter for energy conversion from heat energy to mechanical energy through temperature as defined in Eqs. (1.7) and (1.4). Hence, the specific heat of gases is discussed to understand the fundamental physics of the energy of molecules based on a kinetic theory of molecules.[1–2] The energy of a single molecule ε_m is given by the sum of the internal energies, consisting of translational energy ε_t, rotational energy ε_r, vibrational energy ε_v, electronic energy ε_e, and their interaction energy ε_i:

$$\varepsilon_m = \varepsilon_t + \varepsilon_r + \varepsilon_v + \varepsilon_e + \varepsilon_i$$

A molecule containing n atoms has $3n$ degrees of freedom of motion in space:

Molecular structure	Degree of freedom		Translational		Rotational		Vibrational
Monatomic	3	=	3				
Diatomic	6	=	3	+	2	+	1
Polyatomic linear	$3n$	=	3	+	2	+	$(3n - 5)$
Polyatomic nonlinear	$3n$	=	3	+	3	+	$(3n - 6)$

A statistical theorem on the equipartition of energy shows that $kT/2$ energy is given to each degree of freedom of translational and rotational modes and kT energy is given to each degree of freedom of vibrational modes. Boltzmann constant k is given by $k = 1.38054 \times 10^{-23}$ J/molecule K. The universal gas constant R defined in Eq. (1.6) is given by $\mathrm{R} = k\zeta$, where ζ is Avogadro's number; $\zeta = 6.02252 \times 10^{23}$ molecules/mol.

When the temperature of a molecule is increased, rotational and vibrational modes are excited and the internal energy is increased. The excitation of each degree of freedom is calculated from statistical mechanics as a function of temperature. Though the translational and rotational modes of a molecule are fully excited at low temperatures, the vibrational modes become excited at above room temperatures. The excitation of electrons and interaction modes occurs much higher temperatures than those of combustion. Dissociation and ionization of molecules occur when the combustion temperature is very high.

When the translational, rotational, and vibrational modes of monatomic, diatomic, and polyatomic molecules are fully excited, the energies of the molecules are given by

$$\varepsilon_m = \varepsilon_t + \varepsilon_r + \varepsilon_v$$

$$\varepsilon_m = 3 \times kT/2 = 3\ kT/2 \quad \text{for monatomic molecules}$$

$$\varepsilon_m = 3 \times kT/2 + 2 \times kT/2 + 1 \times kT = 7\ kT/2 \quad \text{for diatomic molecules}$$

$$\varepsilon_m = 3 \times kT/2 + 2 \times kT/2 + (3n - 5) \times kT = (6n - 5)\ kT/2 \quad \text{for linear molecules}$$

$$\varepsilon_m = 3 \times kT/2 + 3 \times kT/2 + (3n - 6) \times kT = 3(n - 1)\ kT \quad \text{for nonlinear molecules}$$

Since the specific heat at constant volume is given by the temperature derivative of the internal energy as defined in Eq. (1.7), the specific heat of a molecule $c_{v,m}$ is represented by

$$c_{v,m} = d\varepsilon_m/dT = d\varepsilon_t/dT + d\varepsilon_r/dT + d\varepsilon_v/dT + d\varepsilon_e/dT + d\varepsilon_i/dT \quad \text{J/molecule K}$$

Thus, one gets the molar specific heats of the gases composed of monatomic, diatomic, and polyatomic molecules as

$$c_v = 3\mathrm{R}/2 = 12.47\ \text{J/mol K} \quad \text{for monatomic molecules}$$

$c_v = 7R/2 = 29.10$ J/mol K for diatomic molecules

$c_v = (6n - 5)R/2$ J/mol K for linear molecules

$c_v = 3(n - 1)R$ J/mol K for nonlinear molecules

The specific heat ratio defined in Eq. (1.9) is 5/3 for monatomic molecules and 9/7 for diatomic molecules. Since the excitations of rotational and vibrational freedoms occur only over restricted temperatures, the specific heats determined by kinetic theory are different from the specific heats determined by experiments. However, the results obtained by the theory are valuable to understand the behavior of molecules and the process of energy conversion in the thermochemistry of combustion. Figure 1-1 shows the specific heats of real gases appearing in combustion.[3] The specific heats of monatomic gases remain constant when temperature is increased as are determined by kinetic theory. The specific heats of diatomic and polyatomic gases are increased as the rotational and vibrational modes are excited by the increases of temperature.

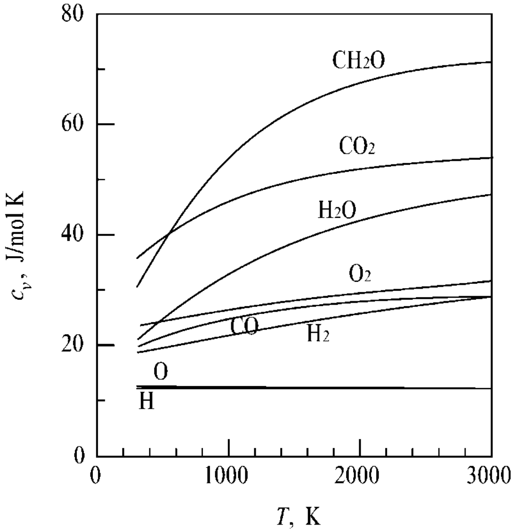

Figure 1-1. Specific heat of gases at constant volume as a function of temperature.

1.1.3
Entropy Change

Entropy s is defined in

$$ds \equiv \frac{dq}{T} \tag{1.11}$$

Substituting Eqs. (1.4), (1.5), and (1.7) into Eq. (1.11). one gets

$$ds = c_p \frac{dT}{T} - R\frac{dp}{p} \tag{1.12}$$

In the case of isentropic change, $ds = 0$. Eq. (1.12) is integrated as

$$\frac{p}{p_1} = \left(\frac{T}{T_1}\right)^{\frac{cp}{R}} \tag{1.13}$$

where the subscript 1 indicates the initial state 1. Using Eqs. (1.10), (1.5), and (1.13), one gets

$$\frac{p}{p_1} = \left(\frac{T}{T_1}\right)^{\frac{\gamma}{\gamma-1}} \quad \text{and} \quad p\left(\frac{1}{\rho}\right)^{\gamma} = p_1\left(\frac{1}{\rho_1}\right)^{\gamma} \tag{1.14}$$

When a system involves dissipative effects such as friction caused by molecular collisions and turbulence caused by a non-uniform molecular distribution even under adiabatic conditions, *ds* becomes positive, and then Eqs. (1.13) and (1.14) are no longer valid. However, when these physical effects are very small and heat loss from the system or heat gain to the system are also small, the system is considered to show isentropic change.

1.2
Thermodynamics in Flow Field

1.2.1
One-Dimensional Steady-State Flow

1.2.1.1 Sonic Velocity and Mach Number

The sonic velocity propagating in a perfect gas a is given by

$$a = \sqrt{(\partial p/\partial \rho)_s} \tag{1.15}$$

Using the equation of state Eq. (1.8) and the adiabatic change Eq. (1.14), one gets

$$a = \sqrt{\gamma R T} \tag{1.16}$$

Mach number M is defined as

$$M = \frac{u}{a} \tag{1.17}$$

where u is a local flow velocity in a flow field. Mach number is an important parameter to characterize the flow field.

1.2.1.2 Conservation Equations in a Flow Field

Let us consider a simplified flow, i.e. a one-dimensional steady state flow without viscous stress or gravitational force. The conservation equations of mass, momentum, and energy are represented by

Rate of mass in – Rate of mass out = 0

$$d(\rho u) = 0 \tag{1.18}$$

Rate of momentum gain by convection + pressure difference acting on flow = 0

$$\rho u du + dp = 0 \tag{1.19}$$

Rate of energy input by conduction + Rate of energy input by convection = 0

$$d\left(h + \frac{u^2}{2}\right) = 0 \tag{1.20}$$

Combining Eqs. (1.19) and Eq. (1.4), one gets the relationship of the enthalpy change by the change of flow velocity as

$$dh = dq - u\,du \tag{1.21}$$

1.2.1.3 Stagnation Point

If one can assume that the process in the flow field is adiabatic and dissipative effects are negligibly small, the flow in the system is isentropic ($ds = 0$), and then Eq. (1.21) becomes

$$dh = -\,u\,du \tag{1.22}$$

Integration of Eq. (1.22) gives

$$h_0 = h + \frac{u^2}{2} \tag{1.23}$$

where h_0 is the stagnation enthalpy at $u = 0$ of a stagnation flow point. Substituting Eq. (1.7) into Eq. (1.23), one gets

$$c_p T_0 = c_p T + \frac{u^2}{2} \tag{1.24}$$

where T_0 is the stagnation temperature at $u = 0$.

The changes of temperature, pressure, and density in the flow field are expressed as a function of Mach number as

$$\frac{T_0}{T} = 1 + \frac{\gamma - 1}{2} M^2 \tag{1.25}$$

$$\frac{p_0}{p} = \left(1 + \frac{\gamma - 1}{2} M^2\right)^{\frac{\gamma}{\gamma - 1}} \tag{1.26}$$

$$\frac{\rho_0}{\rho} = \left(1 + \frac{\gamma - 1}{2} M^2\right)^{\frac{1}{\gamma - 1}} \tag{1.27}$$

1.2.2
Formation of Shock Wave

One assumes that a discontinuous flow occurs between 1 and 2 as shown in Fig. 1-2. The flow is also assumed to be one-dimensional at steady state without viscous force, external force, and chemical reaction.

The mass continuity equation is given by

$$\rho_1 u_1 = \rho_2 u_2 = m \tag{1.28}$$

The momentum equation is represented by

$$p_1 + m u_1 = p_2 + m u_2 \tag{1.29}$$

The energy equation is represented by the use of Eq. (1.20) as

$$c_p T_1 + \frac{u_1^2}{2} = c_p T_2 + \frac{u_2^2}{2} \tag{1.30}$$

where the subscripts 1 and 2 indicate the upstream and the downstream of the discontinuity, respectively. Substituting Eq. (1.28) into Eq. (1.29), one gets

$$p_1 + \rho_1 u_1^2 = p_2 + \rho_2 u_2^2 \tag{1.31}$$

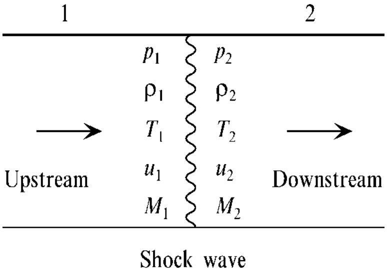

Figure 1-2. Shock wave propagation.

Using Eq. (1.25), the temperature ratio at 2 and 1 is represented by the Mach number at 2 and 1 as

$$\frac{T_2}{T_1}=\frac{1+\frac{\gamma-1}{2}M_1^2}{1+\frac{\gamma-1}{2}M_2^2} \tag{1.32}$$

Using Eqs. (1.5) and (1.28), one gets

$$\frac{T_2}{T_1}=\left(\frac{M_2}{M_1}\right)^2\left(\frac{p_2}{p_1}\right)^2 \tag{1.33}$$

Combining Eqs. (1.33) and (1.32), the pressure ratio is obtained as a function of M_1 and M_2,

$$\frac{p_2}{p_1}=\frac{M_1}{M_2}\,\frac{\sqrt{1+\frac{\gamma-1}{2}M_1^2}}{\sqrt{1+\frac{\gamma-1}{2}M_2^2}} \tag{1.34}$$

Combining Eqs. (1.16), (1.17), (1.31) and (1.34), the Mach number relation at the upstream 1 and the downstream 2 is obtained as

$$\frac{M_1\sqrt{1M_1\frac{\gamma-1}{2}M_1^2}}{1+\gamma M_1^2}=\frac{M_2\sqrt{1M_2\frac{\gamma-1}{2}M_2^2}}{1+\gamma M_2^2} \tag{1.35}$$

One gets two solutions from Eq. (1.35):

$$M_2=M_1 \tag{1.36}$$

$$M_2=\left[\frac{\frac{2}{\gamma-1}+M_1^2}{\frac{2\gamma}{\gamma-1}M_1^2-1}\right]^{\frac{1}{2}} \tag{1.37}$$

From the solution Eq. (1.36), it is evident that no discontinuous flow occurs between the upstream 1 and the downstream 2. However, the solution Eq. (1.37) indicates the existence of discontinuity of pressure, density, and temperature between 1 and 2. This discontinuity is called a "normal shock wave", which is present in a flow field perpendicular to the flow direction. Discussions on the structures of the normal shock waves and supersonic flow fields are in [4] and [5].

Substituting Eq. (1.37) into Eq. (1.34), one gets the pressure ratio as

$$\frac{p_2}{p_1}=\frac{2\gamma}{\gamma+1}M_1^2-\frac{\gamma-1}{\gamma+1} \tag{1.38}$$

Substituting Eq. (1.37) into Eq. (1.33), one also gets the temperature ratio as

$$\frac{T_2}{T_1} = \frac{1}{M_1^2}\frac{2(\gamma-1)}{(\gamma+1)^2}\left(1+\frac{\gamma-1}{2}M_1^2\right)\left(\frac{2\gamma}{\gamma-1}M_1^2-1\right) \tag{1.39}$$

The density ratio is obtained by the use of Eqs. (1.38), (1.39) and (1.8) as

$$\frac{\rho_2}{\rho_1} = \frac{p_2}{p_1}\frac{T_1}{T_2} \tag{1.40}$$

Using Eq. (1.24) for the upstream and the downstream and Eq. (1.38), one gets the ratio of stagnation pressure as

$$\frac{p_{02}}{p_{01}} = \left(\frac{\gamma+1}{2}M_1^2\right)^{\frac{\gamma}{\gamma-1}}\left(1+\frac{\gamma-1}{2}M_1^2\right)^{\frac{\gamma}{1-\gamma}}\left(\frac{2\gamma}{\gamma+1}M_1^2-\frac{\gamma-1}{\gamma+1}\right)^{\frac{1}{1-\gamma}} \tag{1.41}$$

The ratios of the temperature, pressure, and density of downstream and upstream are expressed as the following relationships:

$$\frac{T_2}{T_1} = \frac{p_2}{p_1}\left(1+\frac{1}{\zeta}\frac{p_2}{p_1}\right)\Big/\left(\frac{1}{\zeta}+\frac{p_2}{p_1}\right) \tag{1.42}$$

$$\frac{p_2}{p_1} = \left(\zeta\frac{\rho_2}{\rho_1}-1\right)\Big/\left(\zeta-\frac{\rho_2}{\rho_1}\right) \tag{1.43}$$

$$\frac{\rho_2}{\rho_1} = \left(\zeta\frac{p_2}{p_1}+1\right)\Big/\left(\zeta+\frac{p_2}{p_1}\right) \tag{1.44}$$

where $\zeta = (\gamma + 1)/(\gamma - 1)$. The set of Eqs. (1.42), (1.43), and (1.44) is known as the Rankine-Hugoniot equation for shock wave without any chemical reactions. The relationship of p_2/p_1 and ρ_2/ρ_1 at $\gamma = 1.4$ (for example, in the case of air) shows that the pressure of the downstream increases infinitely when the density of the downstream is increased approximately six times. This is evident from Eq. (1.43) when $\rho_2/\rho_1 \to \zeta$, when $p_2/p_1 \to \infty$.

Though the set of Rankine-Hugoniot equations, Eqs. (1.42) – (1.44), is obtained when a stationary shock wave is created in a moving coordinate system, the same relationship is obtained for a moving shock wave in a stationary coordinate system. In a stationary coordinate system, the velocity of the moving shock wave is u_1 and the particle velocity u_p is given by $u_p = u_1 - u_2$. The ratios of temperature, pressure, and density are the same for both moving and stationary coordinates.

The entropy change across the shock wave characterizes the shock wave. Using the equation of state for a perfect gas shown in Eq. (1.5), the entropy change is represented by

$$s_2 - s_1 = c_p \ln(T_2/T_1) - R\ln(p_2/p_1) \tag{1.45}$$

Substituting Eqs. (1.38) and (1.39) into Eq. (1.45), one gets

$$s_2 - s_1 = c_p \ln\left[\frac{2}{(\gamma+1)M_1^2} + \frac{1}{\zeta}\right] + \frac{c_p}{\gamma} \ln\left[\frac{2\gamma}{\gamma+1} M_1^2 - \frac{1}{\zeta}\right] \tag{1.46}$$

It is obvious that the entropy change is positive in the region of $M_1 > 1$ and negative in the region of $M_1 < 1$ for the gases of $1 < \gamma < 1.67$. Thus, Eq. (1.46) is valid only when M_1 is greater than unity. In other words, a discontinuous flow is formed only when $M_1 > 1$. This discontinuous surface perpendicular to the flow direction is the normal shock wave. The downstream Mach number is always $M_1 < 1$ (subsonic flow), and the stagnation pressure ratio is obtained as a function of M_1 by Eqs. (1.37) and (1.41). The ratios of temperature, pressure, and density between the shock wave are obtained as a function of M_1 by the use of Eqs. (1.38) – (1.40) and Eqs. (1.25) – (1.27). The characteristics of a normal shock wave are summarized as follows:

	Front	←	Shock wave	Behind
Velocity	u_1		>	u_2
Pressure	p_1		<	p_2
Density	ρ_1		<	ρ_2
Temperature	T_1		<	T_2
Mach number	M_1		>	M_2
Stagnation pressure	p_{01}		>	p_{02}
Stagnation density	ρ_{01}		>	ρ_{02}
Stagnation temperature	T_{01}		=	T_{02}
Entropy	s_1		<	s_2

1.2.3
Supersonic Nozzle Flow

When gas flows from a stagnation condition through a nozzle under isentropic change, the enthalpy change is represented by Eq. (1.23). The flow velocity is obtained by the substitution of Eq. (1.14) into Eq. (1.24) as

$$u^2 = 2\, c_p T_0 \left[1 - \left(\frac{p}{p_0}\right)^{\frac{R}{c_p}}\right] \tag{1.47}$$

Substitution of Eqs. (1.6) and (1.47) gives the following relationship:

$$u = \left[\frac{2\gamma}{\gamma-1} R T_0 \left\{1 - \left(\frac{p}{p_0}\right)^{\frac{\gamma-1}{\gamma}}\right\}\right]^{\frac{1}{2}} \tag{1.48a}$$

The flow velocity at the nozzle exit is represented by

$$u_e = \left[\frac{2\gamma}{\gamma-1} R T_0 \left\{1 - \left(\frac{p_e}{p_0}\right)^{\frac{\gamma-1}{\gamma}}\right\}\right]^{\frac{1}{2}} \tag{1.48b}$$

where the subscript e is the exit of the nozzle. The mass flow rate is given by the law of mass conservation at steady-state one-dimensional flow as

$$\dot{m} = \rho\, uA \tag{1.49}$$

where $\dot{m}$ is the mass flow rate in the nozzle, ρ is the gas density, and A is the cross-sectional area of the nozzle. Substituting Eqs. (1.48), (1.5), (1.14) into Eq.(1.49), one gets

$$\dot{m} = p_0\ A\left[\frac{2\gamma}{\gamma-1}\frac{1}{RT_0}\left(\frac{p}{p_0}\right)^{\frac{2}{\gamma}}\left\{1 - \left(\frac{p}{p_0}\right)^{\frac{\gamma-1}{\gamma}}\right\}\right]^{\frac{1}{2}} \tag{1.50}$$

Thus, the mass flux defined in $\dot{m}/A$ is given by

$$\frac{\dot{m}}{A} = p_0\left[\frac{2\gamma}{\gamma-1}\frac{1}{RT_0}\left(\frac{p}{p_0}\right)^{\frac{2}{\gamma}}\left\{1 - \left(\frac{p}{p_0}\right)^{\frac{\gamma-1}{\gamma}}\right\}\right]^{\frac{1}{2}} \tag{1.51a}$$

The mass flux is also expressed as a function of Mach number using Eqs.(1.25) and (1.26) as

$$\begin{aligned}\frac{\dot{m}}{A} &= \rho u = \frac{pu}{RT}\\ &= \sqrt{\frac{\gamma}{RT_0}}\, pM\left(1+\frac{\gamma-1}{2}M^2\right)^{\frac{1}{2}}\\ &= \sqrt{\frac{\gamma}{RT_0}}\, p_0 M\left(1+\frac{\gamma-1}{2}M^2\right)^{-\frac{\xi}{2}}\end{aligned} \tag{1.51b}$$

The differentiation of Eq. (1.51b) is represented by

$$\frac{d}{dM}\left(\frac{\dot{m}}{A}\right) = \sqrt{\frac{\gamma}{RT_0}}\, p_0(1-M^2)\left(1+\frac{\gamma-1}{2}M^2\right)^{\frac{1-3\gamma}{2(\gamma-1)}}$$

It is evident that $\dot{m}$ reaches a maximum at $M = 1$. The maximum mass flux, $(\dot{m}/A)_{max}$, is obtained when the cross-sectional area is A^* as

$$\left(\frac{\dot{m}}{A^*}\right)_{max} = \sqrt{\frac{\gamma}{RT_0}}\, p_0\left(\frac{2}{\gamma+1}\right)^{\frac{\xi}{2}} \tag{1.52}$$

Thus, the area ratio of A/A^* is obtained as

$$\frac{A}{A^*} = \frac{1}{M}\left\{\frac{2}{\gamma+1}\left(1+\frac{\gamma-1}{2}M^2\right)\right\}^{\frac{\zeta}{2}} \tag{1.53}$$

The flow Mach number at A is obtained by using Eq. (1.53) when m, T_0, p_0, R, and γ are given. In addition, T, p, and ρ are obtained by using Eq. (1.25), (1.26), and (1.27). The differentiation of Eq. (1.53) with respect to Mach number is shown in Eq. (1.54) as

$$\frac{d}{dM}\left(\frac{A}{A^*}\right) = \frac{M^2-1}{M^2}\frac{2}{\gamma+1}\left\{\frac{2}{\gamma+1}\left(1+\frac{\gamma-1}{2}M^2\right)\right\}^{\frac{2}{\gamma-1}\;-\;\frac{\zeta}{2}} \tag{1.54}$$

Equation (1.54) indicates that A/A^* reaches a minimum at $M = 1$. The flow Mach number increases as A/A^* decreases when $M < 1$, and also increases as A/A^* increases when $M > 1$. When $M = 1$, the relationship of $A = A^*$ is obtained and is independent of γ. It is evident that A^* is the minimum cross-sectional area of the nozzle flow, the so called "nozzle throat" where the flow velocity becomes the sonic velocity. Furthermore, the velocity increases in the subsonic flow of a convergent part and also increases in the supersonic flow of a divergent part.

The velocity u^*, temperature T^*, pressure p^*, and density ρ^* at the nozzle throat are obtained by using Eqs. (1.16), (1.18), (1.19), and (1.20), respectively:

$$u^* = \sqrt{\gamma R T^*} \tag{1.55}$$

$$\frac{T^*}{T_0} = \frac{2}{\gamma+1} \tag{1.56}$$

$$\frac{p^*}{p_0} = \left(\frac{2}{\gamma+1}\right)^{\frac{\gamma}{\gamma-1}} \tag{1.57}$$

$$\frac{\rho^*}{\rho_0} = \left(\frac{2}{\gamma+1}\right)^{\frac{1}{\gamma-1}} \tag{1.58}$$

For example, $T^*/T_0 = 0.833$, $p^*/p_0 = 0.528$, and $\rho^*/\rho_0 = 0.634$ are obtained when $\gamma = 1.4$. The temperature T_0 at the stagnation condition decreases 17% and the pressure p_0 decreases 50% at the nozzle throat. The pressure decrease is more rapid than the temperature decrease when the flow expands through a convergent nozzle. The maximum flow velocity is obtained at the exit of the divergent part of the nozzle. When the pressure at the nozzle exit is vacuum, the maximum velocity is obtained by the use of Eqs. (1.48) and (1.6) as

$$u_{e,max} = \sqrt{\frac{2\gamma}{\gamma-1}\frac{R}{M_g}T_0} \tag{1.59}$$

This maximum velocity depends on the molecular mass M_g, specific heat γ, and stagnation temperature T_0. The velocity increases as γ and M_g decreases and T_0 increases. Based on Eq. (1.52), a simplified expression of mass flow rate in terms of the nozzle throat area A_t (= A^*) and the chamber pressure p_c (= p_0) is

$$\dot{m} = c_D A_t p_c \tag{1.60}$$

where c_D is the nozzle discharge coefficient given by

$$c_D = \sqrt{\frac{M_g}{T_0}} \sqrt{\frac{\gamma}{R} \left(\frac{2}{\gamma+1}\right)^{\zeta}} \tag{1.61}$$

1.3
Formation of Propulsive Forces

1.3.1
Momentum Change and Thrust

One assumes a propulsion engine operated in the atmosphere to be as shown in Fig. 1-3. Air is coming in at the front end *i* and passing through the combustion chamber *c*, and going out from the exit *e*. The heat generated by the combustion of an energetic material is given to the combustion chamber. The momentum balance to generate thrust *F* is represented by the terms of

$$F + p_a\ (A_e - A_i) = (\dot{m}_e\ u_e + p_e\ A_e) - (\dot{m}_i\ u_i + p_i\ A_i) \tag{1.62}$$

$\dot{m}_i\ u_i$ = momentum coming in at *i*

$\dot{m}_e\ u_e$ = momentum flowing out at *e*

$p_i\ A_i$ = pressure force acting at *i*

$p_e\ A_e$ = pressure force acting at *e*

$F + p_a\ (A_e - A_i)$ = force acting on the outer surface of engine

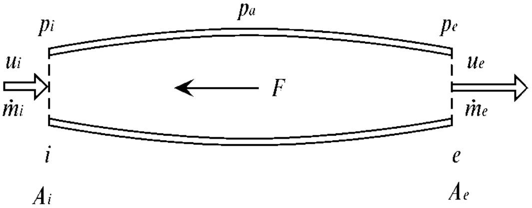

Figure 1-3. Momentum change for propulsion.

where u is flow velocity, $\dot{m}$ is mass flux, A is area, and the subscript i is inlet, e is exit, a is ambient atmosphere. The mass flux of the energetic material given to the combustion chamber m_p is given by the difference of the out-flow mass flux and in-flow mass flux, $\dot{m}_e - \dot{m}_i$. In the case of rocket propulsion, the front end is closed ($A_i = 0$) and there is no in-flow mass flux to the combustion chamber ($\dot{m}_i = 0$). Thus the thrust for rocket propulsion is represented by

$$F = \dot{m}_e\, u_e + A_e\,(p_e - p_a) \tag{1.63}$$

where $\dot{m}_p = \dot{m}_g$. Thus, the thrust is determined by the flow velocity and pressure at the exit when $\dot{m}_e$, A_e, and p_a are given.

The differentiation of Eq. (1.63) with respect to A_e gives

$$\frac{dF}{dA_e} = u_e \frac{d\dot{m}_g}{dA_e} + \dot{m}_g \frac{du_e}{dA_e} + A_e \frac{dp_e}{dA_e} + p_e - p_a \tag{1.64}$$

The momentum equation at the nozzle exit is represented by $\dot{m}_g\, du_e = -A_e\, dp_e$ and $d\dot{m}_g = 0$ at steady-state flow at the nozzle. Thus, one gets the relationship from Eq. (1.64)

$$\frac{dF}{dA_e} = p_e - p_a \tag{1.65}$$

The maximum thrust is obtained at $p_e = p_a$, i.e., the pressure at the nozzle exit is equal to the ambient pressure.

1.3.2
Rocket Propulsion

Figure 1-4 shows a schematic drawing of a rocket motor composed of propellant, combustion chamber, and nozzle. The nozzle is a convergent–divergent nozzle in order to accelerate the combustion gas from subsonic to supersonic flow through the nozzle throat. The thermodynamic process in a rocket motor is shown in Fig. 1-4 as a pressure-volume diagram and an enthalpy-entropy diagram.[6] The propellant contained in the chamber burns, generates combustion product, and increases the temperature from T_i to T_c at a constant pressure p_c. The combustion product expands through the convergent nozzle and becomes pressure p_t and temperature T_t at the nozzle throat. The combustion product continues to expand through a divergent nozzle and becomes pressure p_e and temperature T_e at the nozzle exit.

If one can assume (1) the flow is one-dimensional and steady-state, (2) the flow is isentropic, and (3) the combustion gas is an ideal gas and the specific heat ratio is constant, the diagrams of $p - v$ and $h - s$ are uniquely determined.[6–9] The enthalpy change due to the propellant combustion is given by

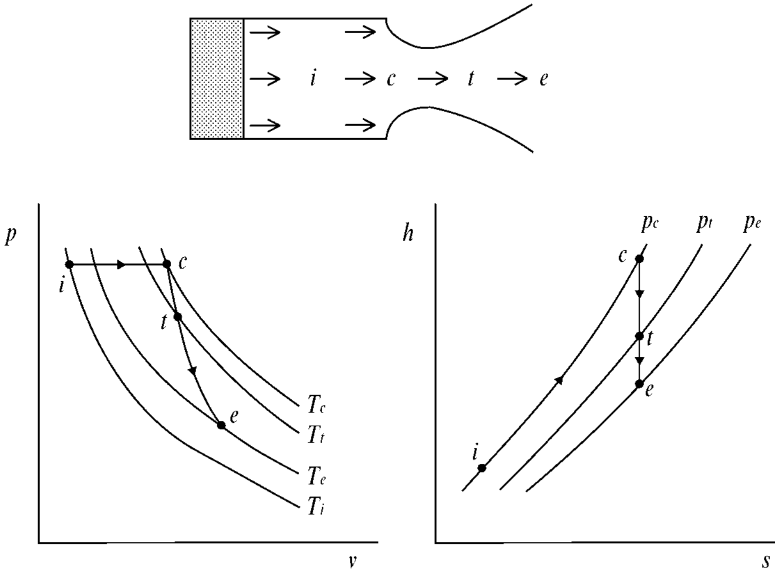

Figure 1-4. Pressure–volume and enthalpy–entropy diagrams of rocket propulsion.

$$\Delta h = c_p\,(T_c - T_i) \tag{1.66}$$

where Δh is the heat of reaction of propellant per unit mass. The expansion process $c \rightarrow t \rightarrow e$ shown in Fig. 1-4 follows the thermodynamic process described in Section 1.2.3 in this Chapter.

1.3.2.1 **Thrust Coefficient**

The thrust generated by a rocket motor is represented by Eq. (1.63). Substituting Eqs. (1.48b) and (1.52) into Eq. (1.63), one gets

$$F = A_t p_c \left[\frac{2\gamma^2}{\gamma-1}\left(\frac{2}{\gamma+1}\right)^{\frac{\gamma+1}{\gamma-1}}\left\{1 - \left(\frac{p_e}{p_c}\right)^{\frac{\gamma-1}{\gamma}}\right\}\right]^{\frac{1}{2}} + (p_e - p_a)\,A_e \tag{1.67}$$

As shown in Eq. (1.65), the maximum thrust F_{max} is obtained when $p_e = p_a$ at a given specific heat ratio of the combustion gas:

$$F_{max} = A_t p_c \left[\frac{2\gamma^2}{\gamma-1}\left(\frac{2}{\gamma+1}\right)^{\frac{\gamma+1}{\gamma-1}}\left\{1 - \left(\frac{p_e}{p_c}\right)^{\frac{\gamma-1}{\gamma}}\right\}\right]^{\frac{1}{2}} \tag{1.68}$$

Equation (1.68) is represented by a simplified expression of thrust in terms of nozzle throat area and chamber pressure:

$$F = c_F A_t p_c \tag{1.69}$$

where c_F is the thrust coefficient and is given by

$$c_F = \left[\frac{2\gamma^2}{\gamma-1}\left(\frac{2}{\gamma+1}\right)^{\frac{\gamma+1}{\gamma-1}}\left\{1 - \left(\frac{p_e}{p_c}\right)^{\frac{\gamma-1}{\gamma}}\right\}\right]^{\frac{1}{2}} + \frac{p_e - p_a}{p_c}\frac{A_e}{A_t} \tag{1.70}$$

The maximum thrust coefficient $c_{F,max}$ becomes

$$c_{F,max} = \left[\frac{2\gamma^2}{\gamma-1}\left(\frac{2}{\gamma+1}\right)^{\frac{\gamma+1}{\gamma-1}}\left\{1 - \left(\frac{p_e}{p_c}\right)^{\frac{\gamma-1}{\gamma}}\right\}\right]^{\frac{1}{2}} \tag{1.71}$$

When the nozzle expansion ratio becomes infinity, the pressure ratio p_c/p_a also becomes infinity. The maximum thrust coefficient $c_{F,max}$ becomes

$$c_{F,max} = \left[\frac{2\gamma^2}{\gamma-1}\left(\frac{2}{\gamma+1}\right)^{\frac{\gamma+1}{\gamma-1}}\right]^{\frac{1}{2}} \tag{1.72}$$

For example, $c_{F,max}$ is 2.246 for $\gamma = 1.20$ and 1.812 for $\gamma = 1.40$.

1.3.2.2 Characteristic Velocity

The characteristic velocity c^* is defined in

$$c^* = \frac{A_t p_c}{\dot{m}_g} \tag{1.73}$$

Substituting Eq. (1.52) into Eq. (1.73), one gets

$$c^* = \sqrt{\frac{RT_c}{\gamma M_g}}\left(\frac{2}{\gamma+1}\right)^{-\frac{\zeta}{2}} \tag{1.74}$$

It is shown that c^* is dependent only on T_g, M_g, and γ and is not dependent on pressure and physical dimensions of combustion chamber and exhaust nozzle. As shown in Eq. (1.74), c^* is a parameter used to identify the energetics of combustion.

1.3.2.3 Specific Impulse

Specific impulse I_{sp} is a parameter to identify the energy efficiency of propellant combustion, which is represented by

$$I_{sp} = \frac{F}{\dot{m}_g g} \tag{1.75}$$

where g is the gravitational acceleration, 9.80665 m/s^2, and the unit of specific impulse is given in seconds. Thermodynamically, specific impulse is the effective time to generate thrust which can sustain the propellant mass against the gravitational force through energy conversion. Since the mass flow rate $\dot{m}_g$ is given by Eq. (1.50) and F is given by Eq. (1.67), I_{sp} is represented by

$$I_{sp} = \frac{1}{g}\left[\frac{2\gamma}{\gamma-1}\frac{\mathrm{R}}{M_g}T_c\left\{1-\left(\frac{p_e}{p_c}\right)^{\frac{\gamma-1}{\gamma}}\right\}\right]^{\frac{1}{2}} + \frac{1}{g}\left(\frac{\gamma+1}{2}\right)^{\frac{\zeta}{2}}\sqrt{\frac{\mathrm{R}T_c}{\gamma M_g}}\left(\frac{p_e-p_a}{p_c}\right)\frac{A_e}{A_t} \tag{1.76}$$

$$\sim\sqrt{\frac{T_g}{M_g}} \tag{1.77}$$

where T_g is combustion temperature and M_g is molecular mass of the combustion product. Though $I_{sp,max}$ is also a function of the specific heat ratio γ of the combustion products, γ is relatively unchanged among propellants. It is evident from Eq. (1.77) that an energetic material that produces high-T_g and high-M_g combustion products is not always a useful propellant. The propellant that generates low-T_g is also useful if the M_g is low enough. Similar to F_{max} and $c_{F,max}$, the maximum specific impulse $I_{sp,max}$ is obtained when $p_e = p_a$ as

$$I_{sp,max} = \frac{1}{g}\left[\frac{2\gamma}{\gamma-1}\frac{\mathrm{R}}{M_g}T_g\left\{1-\left(\frac{p_a}{p_c}\right)^{\frac{\gamma-1}{\gamma}}\right\}\right]^{\frac{1}{2}} \tag{1.78}$$

In addition, the specific impulse is given by the thrust coefficient and the characteristic velocity as

$$I_{sp} = \frac{c_F c^*}{g} \tag{1.79}$$

Since c_F indicates the efficiency of the expansion process in the nozzle flow and c^* indicates the efficiency of the combustion process in the chamber, I_{sp} indicates the over-all efficiency of the rocket motor.

1.3.3
Gun Propulsion

1.3.3.1 Internal Ballistics

The one-dimensional momentum equation for an internal ballistics of gun is represented by[10–12]

$$m_w\frac{du}{dt} = m_w u\frac{du}{dx} = pA_{bi} \tag{1.80}$$

where m_w is the mass of the projectile, u is the velocity, x is the distance, t is the time, p is the pressure, and A_{bi} is the cross-sectional area of the gun barrel. Integration of Eq. (1.80) from 0 to L_b gives

$$m_w\frac{u_{be}^2}{2} = A_{bi}\int_0^{L_b} p\,dx \tag{1.81}$$

where u_{be} is the velocity at the barrel exit and L_b is the effective length of the barrel used to accelerate the projectile. If one assumes an averaged pressure in the barrel, $[p]$, given by

$$[p] = \frac{1}{L_b} \int_0^{L_b} p dx \tag{1.82}$$

the velocity of the projectile is given by

$$u_{be} = \sqrt{\frac{2[p] L_b A_{bi}}{m_w}} \tag{1.83}$$

When the physical dimensions of a barrel is given, the thermodynamic efficiency of the gun propellant is maximized to produce a pressure in the barrel as high as possible with a given propellant mass within a limited time.

1.3.3.2 The Thermochemical Process of Gun Propulsion

Gun propellant burns under a non-constant volume and a non-constant pressure condition. The gas generation rate changes rapidly with time and the temperature changes also simultaneously because of the displacement of the projectile in the combustion chamber in the gun barrel. Though the pressure change is rapid, the linear burning rate is assumed to be expressed by the pressure exponent law, the so called Vieille's law, i.e., $r = ap^n$ where r is burning rate (mm/s), p is pressure (MPa), n is a constant dependent on the propellant composition and a is a constant dependent on the propellant chemical composition and the initial propellant temperature. The fundamental difference between gun propellants and rocket propellants is the zone of burning pressure. Since the burning pressure in guns is extremely high (> 100 MPa), the parameters of this equation are empirically determined. Though rocket propellant burns below 20 MPa, in general, the burning rate expression of gun propellants appears to be similar to that of rocket propellants. The mass burning rate of the propellant is dependent also on the burning surface area of the propellant, which increases and/or decreases as the burning proceeds. The change of burning surface area is determined by the shape and dimensions of the propellant grains used.

The effective work done by gun propellants is the pressure force that acts on the base of the projectile. Thus, the work done by propellant combustion is evaluated by the thermodynamic energy that is represented by

$$f = pv = \mathrm{R}\frac{T_g}{M_g} \tag{1.84}$$

The unit of f is given by MJ/kg. It is evident that a high f value is favorable to gun propellants and is similar to I_{sp} used to evaluate the thermodynamic energy of rocket propellants.

The thermal energy generated by propellant combustion is distributed to various non-effective energies[10]. The energy losses of a caliber gun are approximately

Sensible heat of combustion gas	42 %
Kinetic energy of combustion gas	3 %
Heat loss to gun barrel and projectile	20 %
Mechanical losses	3 %

The remaining part of the energy, 32 %, is used to accelerate the projectile. It is obvious that the major energy loss is the heat exhausted from the gun barrel. This is an unavoidable heat loss based on the thermodynamic law : the pressure in the gun barrel cannot decrease until the combustion gas is at the atmospheric temperature.

References

1 Jeans, J., Introduction to the Kinetic Theory of Gases, The University Press, Cambridge (1959).

2 Dickerson, R. E., Molecular Thermodynamics, W. A. Benjamin, New York (1969), Chapter 5.

3 JANAF Thermochemical Tables, Dow Chemical Co., Midland, Michigan (1960–1970).

4 Liepmann, H. W. and Roshko, A., Elements of Gasdynamics, John Wiley & Sons, New York (1957), Chapter 2.

5 Shapiro, A. H., The Dynamics and Thermodynamics of Compressible Fluid Flow, The Ronald Press Company, New York (1953), Chapter 5.

6 Summerfield, M., The Liquid Propellant Rocket Engine, Jet Propulsion Engines, Princeton University Press, New Jersey (1959), pp. 439–520.

7 Glassman, I. and Sawyer, F., The Performance of Chemical Propellants, Circa Publications, New York (1970), Chapter 2.

8 Sutton, G. P., Rocket Propulsion Elements, 6th edition, John Wiley & Sons, Inc., New York (1992), Chapter 3.

9 Kubota, N., Rocket Combustion, Nikkan Kogyo Press, Tokyo (1995), Chapter 2.

10 Weapons Systems Fundamentals – Analysis of Weapons, U.S. Navy Weapons Systems, NAVWEPS Operating Report 3000, Vol. 2 , 1963.

11 Krier, H. and Adams, M. J., An Introduction to Gun Interior Ballistics and a Simplified Ballistic Code, Interior Ballistics of Guns, edited by Krier, H. and Summerfield, M., Progress in Astronautics and Aeronautics, Vol. 66, AIAA, New York (1979).

12 Gun Propulsion Technology, edited by Stiefel, L., Progress in Astronautics and Aeronautics, Vol. 109, AIAA, Washington DC (1988).

Propellants and Explosives: Thermochemical Aspects of Combustion. Naminosuke Kubota
Copyright © 2002 Wiley-VCH Verlag GmbH & Co. KGaA
ISBNs: 3-527-30210-7 (Hardback); 3-527-60050-7 (Electronic)

2
Thermochemistry of Combustion

2.1
Generation of Heat Energy

2.1.1
Chemical Bond Energy

All materials are composed of atoms which are tightly bonded to each other to form molecules of the materials. When chemical reaction occurs, the materials change to other materials through bond breakage and new bond formation. The chemical bond energy is dependent on the type and energetic state of the atoms based on the electrons of each atom. Though the exact energetic state of the materials should be evaluated by quantum mechanics, an overall energetic state is evaluated by the chemical bond energies determined experimentally.

Typical chemical bonds are either covalent or ionic. These bonds form energetic materials and their combustion products. The gaseous reactants, hydrogen, oxygen, nitrogen, and hydrocarbons, contain covalent bonds, which may be single, double, and/or triple. Many energetic crystalline materials are formed by ionic bonds. The status of the bonds determines the energetics and physicochemical properties of the materials.

The total chemical bond energy between the atoms of a molecule is the energy of the molecule. Bond breakage of a gas molecule occurs by collision between molecules or photochemical energy supplied externally. When a molecule dissociates to atoms, energy is needed to break the chemical bonds and to separate atoms. The chemical bond energy of a molecule A–B is equal to the dissociation energy to form A and B atoms. For example, an H_2O molecule dissociates to form two H atoms and one O atom: $H_2O \rightarrow 2H + O - 912$ kJ/mol. The bond breakage of two O–H bonds occurs by $H_2O \rightarrow H + OH - 494$ kJ/mol and then $OH \rightarrow O + H - 419$ kJ/mol. The first O–H bond breakage requires 494 kJ/mol and the second 419 kJ/mol. The difference, the O–H bond breakage, appears to be 75 kJ/mol. However, the two dissociation processes occur simultaneously for H_2O molecules; the average O–H bond energy appears to be 457 kJ/mol. The chemical bond energy of typical molecules related to combustion is shown in Table 2-1.[1–3]

Table 2-1. Chemical bond energy of energetic materials.

Chemical bond	*Bond energy, kJ/mol*
C – H	411
C – C	358
C = C	599
C ≡ C	812
C – O	350
C = O (ketone)	766
C = O (formaldehyde)	699
C = O (acetaldehyde)	720
C ≡ N	883
H – H	435
O – H	465
O – O	138
N – H	368
N – O	255
N = O	601
N = N	443
N ≡ N	947

2.1.2
Heat of Formation and Heat of Explosion

When reactant R of an energetic material reacts to generate product P, heat is released (or absorbed). Since the chemical bond energy of R is different from that of P, the energy difference between R and P appears as heat. The rearrangement of the molecular structure of R changes the chemical potential. The heat of reaction at constant pressure, represented by Q_p, is equal to the enthalpy change of the chemical reaction:

$$\Delta H = Q_p \tag{2.1}$$

where H is enthalpy, ΔH is the increase of enthalpy by reaction, and the subscript p indicates the condition at constant pressure.

The heat produced by chemical reaction is the "heat of explosion", H_{exp}. H_{exp} is determined by the difference between the heat of formation of reactants, $\Delta H_{f,r}$, and the heat of formation of products, $\Delta H_{f,\mathrm{p}}$, as represented by

$$H_{exp} = \Delta H_{f,\mathrm{r}} - \Delta H_{f,\mathrm{p}} \tag{2.2}$$

H_{exp} : heat of explosion
$\Delta H_{f,\mathrm{r}}$: heat of formation of reactants
$\Delta H_{f,\mathrm{p}}$: heat of formation of products

The heat of formation, ΔH_f is dependent on the chemical structure and chemical bond energy of the molecules comprising the reactants and products. Equation (2.2) indicates that the higher H_{exp} is obtained when higher $\Delta H_{f,\mathrm{r}}$ is used for the reactants and also lower $\Delta H_{f,\mathrm{p}}$ as the products.

2.1.3
Thermal Equilibrium

Though combustion is a very fast exothermic chemical reaction compared with other chemical reactions, the reaction time is finite, and the combustion products are formed after a large number of molecular collisions, which produce also a large number of intermediate molecules. When the time-averaged numbers of molecules and the temperature become constant, the reaction system is said to be in a thermal equilibrium state.[1,2,4]

Gibbs free energy F for one mole of ideal gas is defined in

$$F = h - Ts = e + pV - Ts \tag{2.3}$$

Substituting of Eqs. (1.4), (1.5a), and (1.11) into Eq. (2.3), one gets

$$dF = V\,dp - s\,dT \tag{2.4}$$

by the differentiation of Eq. (2.3). Substitution of the equation of state Eq. (1.5) for one mole of an ideal gas into Eq. (2.4), one gets

$$dF = (\mathrm{R}T/p)dp - s\,dT \tag{2.5}$$

When the temperature of the gas remains unchanged, Eq. (2.5) is represented by

$$dF = \mathrm{R}T\,d\ln p \tag{2.6}$$

Integrating of Eq. (2.6), one gets

$$F - F_0 = \mathrm{R}T\ \ln p \tag{2.7}$$

where F_0 is a standard free energy at temperature T and pressure 1 MPa.

One assumes that the chemical species A, B, C, and D are in a thermal equilibrium state in the case of reversible reactions:

$$\mathrm{aA} + \mathrm{bB} \rightleftharpoons \mathrm{cC} + \mathrm{dD} \tag{2.8}$$

where a, b, c, and d are stoichiometric coefficients of the reversible reaction in the thermal equilibrium state. Based on Eq. (2.7), the change of free energy dF of the reaction is represented by

$$\Delta F - \Delta F_0 = \mathrm{R}T[(\mathrm{c} \ln p_\mathrm{c} + \mathrm{d} \ln p_\mathrm{d}) - (\mathrm{a} \ln p_\mathrm{a} + \mathrm{b} \ln p_\mathrm{b})]$$

$$= \mathrm{R}T \ln (p_\mathrm{c}{}^\mathrm{c}\, p_\mathrm{d}{}^\mathrm{d} / p_\mathrm{a}{}^\mathrm{a}\, p_\mathrm{b}{}^\mathrm{b}) \tag{2.9}$$

where p_a, p_b, p_c, and p_d are the partial pressures of the chemical species A, B, C, and D, respectively, and ΔF_0, is the standard free energy change of the reaction represented by Eq. (2.8). When the reaction is at thermodynamic equilibrium, the free energy change becomes zero, $\Delta F = 0$, and Eq. (2.9) becomes

$$\Delta F_0 = -\mathrm{R}T \ln (p_\mathrm{c}{}^\mathrm{c}\, p_\mathrm{d}{}^\mathrm{d} / p_\mathrm{a}{}^\mathrm{a}\, p_\mathrm{b}{}^\mathrm{b}) \tag{2.10}$$

$$= -\mathrm{R}T \ln K_p \tag{2.11}$$

where K_p is the equilibrium constant defined by

$$K_p = p_\mathrm{c}{}^\mathrm{c}\, p_\mathrm{d}{}^\mathrm{d} / p_\mathrm{a}{}^\mathrm{a}\, p_\mathrm{b}{}^\mathrm{b} \tag{2.12}$$

Substituting Eq. (2.11) into Eq. (2.3), one gets

$$dh_0 - Tds_0 = -\mathrm{R}T \ln K_p \tag{2.13}$$

where dh_0 and ds_0 are the changes of enthalpy and entropy between a standard pressure (1 MPa) and pressure p at temperature T. Thus, the left hand side of Eq. (2.13) is the free energy change between the standard pressure (1 MPa) and pressure p at temperature T. K_p is obtained for each reaction of Eq. (2.8). Since the free energy change is dependent on temperature, not on pressure, K_p is also dependent on temperature only.[4,5] The equilibrium constants of combustion products are tabulated in JANAF Thermochemical Tables.[6] If the reaction is a + b = c + d, the number of molecules involved in the reaction remains unchanged before and after reaction and the equilibrium reaction appears to be pressure insensitive.

2.2
Adiabatic Flame Temperature

The heat of reaction is given by the difference between the heat of formation of the reactants and that of the products. When the temperature of the reactant T_0 becomes the temperature of the product T_1, the energy change due to chemical reaction is represented by the energy conservation law as[4–7]

$$\sum_i n_i[(H_{T1} - H_0^0) - (H_{T0} - H_0^0) + (\Delta H_f)_{T0}]_i$$

$$= \sum_j n_j[(H_{T2} - H_0^0) - (H_{T0} - H_0^0) + (\Delta H_f)_{T0}]_j + \sum_j n_j Q_j \tag{2.14}$$

where H_0^0 is the standard enthalpy at 0 K, n is the stoichiometry of the chemical species involved in the reaction, and the subscript T_1 is the temperature of reactant, T_2 the temperature of product, i the reactant, and j the product. This expression indicates that the energy change is not dependent on the reaction pathway from the reactant to the product.

When the temperatures of the reactants is T_1 and the temperature of the product is T_2, Eq. (2.14) is represented by

$$\sum_i n_i[(H_{T1} - H_{T0}) + (\Delta H_f)_{T0}]_i = \sum_j n_j[(H_{T2} - H_{T0}) + (\Delta H_f)_{T0}]_j + \sum_j n_j Q_j \tag{2.15}$$

where T_0 is the temperature of heat of formation defined, and H is the enthalpy given by

$$H_T - H_{T0} = \int_{T0}^{T} c_p dT \tag{2.16}$$

When $T_0 = 298.15$ K is used as a standard temperature, Eq. (2.16) becomes

$$\sum_i n_i[(H_{T1} - H^0) + \Delta H_f^0]_i = \sum_j n_j[(H_{T2} - H^0) + \Delta H_f^0]_j + \sum_j n_j Q_j \tag{2.17}$$

where H^0 is a standard enthalpy at 298.15 K. JANAF Thermochemical Tables show $H_T - H^0$ values as a function of T for various materials.

When the reaction is conducted under adiabatic conditions, all heat generated $n_j Q_j$ is converted to the enthalpy of the products, and T_2 becomes T_f, defined as the adiabatic flame temperature. Equation (2.17) becomes

$$\sum_i n_i[(H_{T1} - H^0) + (\Delta H_f)_{T0}]_i = \sum_j n_j[(H_{Tf} - H^0) + (\Delta H_f)_{T0}]_j \tag{2.18}$$

One gets two separated equations based on Eq. (2.18) as

$$Q_1 = \sum_i n_i\,(\Delta H_f)_{T0,i} - \sum_j n_j\,(\Delta H_f)_{T0,j} \tag{2.19}$$

$$Q_2 = \sum_j n_j\,(H_{Tf} - H_{T0})_j - \sum_i n_i (H_{T1} - H_{T0})_i \tag{2.20}$$

T_f and n_j are determined at $Q_1 = Q_2$. In case of $T_0 = 298.15$ K, Eqs. (2.19) and (2.20) becomes

$$Q_1^0 = \sum_i n_i(\Delta H_f^0)_i - \sum_j n_j(\Delta H_f^0)_j \tag{2.21}$$

$$Q_2^0 = \sum_j n_j (H_{Tf} - H^0)_j - \sum_i n_i (H_{T1} - H^0)_i \tag{2.22}$$

T_f and n_j are also determined at $Q_1^0 = Q_2^0$. When the temperature of the reactants is 298.15 K, $H_{T1} = H^0$, and then

$$Q_2^0 = \sum_j n_j \int_{298}^{Tf} c_{p,j}\, dT \tag{2.23}$$

is obtained by the use of Eqs. (2.22) and (2.16).

Though the set of equations are nonlinear and complex, computations of T_f and n_j for any combustion reactions are possible as long as the thermochemical data are available. The reaction of $3H_2 + O_2$ at 2 MPa is demonstrated as an example computation to identify the procedure for the determinations of T_f and n_j and to understand the principle of a thermochemical equilibrium and adiabatic flame temperature. First, the following reaction scheme and products are assumed:

$$3H_2 + O_2 \rightarrow n_{H_2O}H_2O + n_{H_2}H_2 + n_H H + n_O O + n_{O_2}O_2 + n_{OH}OH \tag{2.24}$$

The mass of the each chemical species is conserved before and after reaction. For the number of hydrogen atoms,

$$3H_2 = 2n_{H_2O} + 2n_{H_2} + n_H + n_{OH} = 6 \tag{2.25}$$

For the number of oxygen atoms,

$$O_2 = n_{H_2O} + n_O + 2n_{O_2} + n_{OH} = 2 \tag{2.26}$$

The equation of state for each species is given as

$$p_j V = n_j RT \quad \text{and} \quad pV = nRT \tag{2.27}$$

Thus, one gets

$$n_j = p_j V/RT = p_j n/p \tag{2.28}$$

where n is the total number of moles of products. Substituting Eq. (2.28) into Eq. (2.25), one gets

$$2\,p_{H_2O} + 2\,p_{H_2} + p_H + p_{OH} = 6(RT/V) \tag{2.29}$$

$$p_{H_2O} + p_O + 2\,p_{O_2} + p_{OH} = 2(RT/V) \tag{2.30}$$

The chemical species of the products are all in the chemical equilibrium state as

$$1/2\ O_2 \rightleftharpoons O \tag{2.31}$$

$$1/2\ H_2 \rightleftharpoons H \tag{2.32}$$

$$1/2\ O_2 + 1/2\ H_2 \rightleftharpoons OH \tag{2.33}$$

$$H_2 + 1/2\ O_2 \rightleftharpoons H_2O \tag{2.34}$$

As defined in Eq. (2.12), the equilibrium constants for each chemical equilibrium state are

$$K_{p,1} = p_O/p_{O_2}{}^{1/2} \tag{2.35}$$

$$K_{p,2} = p_H/p_{H_2}{}^{1/2} \tag{2.36}$$

$$K_{p,3} = p_{OH}/(p_{O_2}{}^{1/2}\ p_{H_2}{}^{1/2}) \tag{2.37}$$

$$K_{p,4} = p_{H_2O}/(p_{H_2}\, p_{O_2}{}^{1/2}) \tag{2.38}$$

These K_p values are determined by Eq. (2.13) as a function of temperature (see JANAF Thermochemical Tables[6]). There are 7 unknown parameters (T_f, p_{H_2O}, p_{H_2}, p_O, p_H, p_{O_2}, and p_{OH}), and 7 equations: Eqs. (2.18), (2.29), (2.30), (2.35) ~ (2.38). The procedure for the computations is as follows:

(1) Determine $H_{T1} - H_{T0}$ at T_0, T_1, and p from the Theromochemical Tables.

(2) Determine $H_{f,T0}$ from the Thermochemical Tables.

(3) Determine $H_{Tf,1} - H_{T0}$ and $K_{p,j}$ at $T_{f,1}$ (assumed) from the Thermochemical Tables.

(4) Determine p_j (or n_j) at $T_{f,1}$ and p.

(5) Determine Q_1 and Q_2.

(6) If $Q_1 < Q_2$ or $Q_1 > Q_2$, assume $T_{f,2}$. Continue the iterations from (1) to (6) until $Q_1 = Q_2$.

(7) If $Q_1 = Q_2$ at $T_{f,m}$, $T_{f,m}$ is the adiabatic flame temperature, T_f.

The computational process indicates that, for example, Q_1 decreases monotonically with T and Q_2 increases monotonically with T. The adiabatic flame temperature is determined by the interpolation of the computed results. Practical computations are done by the use of computer programs.[8] The results of this example are as follows:

$$T_f = 3360\ \text{K}$$

$$n_{H_2O} = 1.837,\ n_{H_2} = 1.013,\ n_O = 0.013,\ n_H = 0.168,\ n_{O_2} = 0.009, \text{ and } n_{OH} = 0.131$$

The adiabatic flame temperature and mole fractions of different mixture ratios of hydrogen and oxygen reaction are shown in Table 2-2. The maximum adiabatic flame temperature is obtained by the mixture of $2H_2 + O_2$, which is the stoichiometric mixture ratio of hydrogen and oxygen.

Table 2-2. Adiabatic flame temperature and mole fractions of the combustion products of H_2 and O_2 mixtures at 2 MPa.

Reactants	T_f	**Mole fractions**					
	K	H_2O	H_2	O	H	O_2	OH
$H_2 + O_2$	3214	0.555	0.021	0.027	0.009	0.290	0.098
$2\ H_2 + O_2$	3498	0.645	0.136	0.022	0.048	0.042	0.107
$3\ H_2 + O_2$	3358	0.579	0.319	0.004	0.053	0.003	0.042
$4\ H_2 + O_2$	3064	0.479	0.481	0.000	0.030	0.000	0.010

If a condensed material is formed as a combustion product, no equilibrium constant defined by Eq. (2.12) is obtained. For example, the reaction of solid carbon and oxygen produces carbon dioxide:

$$C_{(s)} + O_{2(g)} \rightarrow CO_{2(g)} \tag{2.39}$$

Since solid carbon vaporizes under the vapor pressure of solid carbon, $p_{vp},_C$, the chemical equilibrium constant $K_{p,6}$ is defined as

$$K_{p,6} = p_{CO_2}/(p_{vp,C}\ p_{O_2}) \tag{2.40}$$

However, since the vapor pressure is independent of the reaction system, it is determined as a characteristic value of thermodynamics. The equilibrium constant $K_{p,7}$ is defined as

$$\begin{aligned} K_{p,7} &= K_{p,6} \times p_{vp,C} \\ &= p_{CO_2}/p_{O_2} \end{aligned} \tag{2.41}$$

Thus, $K_{p,7}$ is determined by the vapor pressure and standard free energy. In computations of the first step, it is assumed that no solid species are formed. If the partial pressure is higher than the vapor pressure, the next step computations should include liquid or solid materials. Then, the computation continues to proceed until the conditions are matched.

2.3
Chemical Reaction

2.3.1
Thermal Dissociation

When high temperature products are an equilibrium state, many molecules consisting of the products dissociate thermally. For example, the rotational and vibrational modes of carbon dioxide are excited and their motions become very intense. When temperature is increased, the chemical bonds between carbon atom and oxygen atom are broken. This kind of bond breakage is called thermal dissociation. For example, the dissociation of H_2O becomes evident at about 2000 K and produces H_2, OH, O_2, H, and O at 0.1 MPa. About 50 % of H_2O dissociates at 3200 K and 90 % of H_2O dissociates at 3700 K. The products of H_2, O_2, and OH dissociates to H and O as temperature increases. The fraction of the molecules of the thermal dissociation is suppressed as pressure increases at a constant temperature.

2.3.2
Reaction Rate

Since chemical reaction occurs through molecular collisions, the reaction of the chemical species M_j occurs through molecular collisions and is represented by

$$\sum_{j=1}^{n} \nu_j' \, M_j \rightarrow \sum_{j=1}^{n} \nu_j'' \, M_j \tag{2.42}$$

where ν' and ν'' are the stoichiometric coefficients of the reactant and product, respectively, and n is the number of chemical species involved in the reaction. The reaction rate Ω is expressed by the law of mass action[2,4] as

$$\Omega = k_f \prod_{j=1}^{n} [M_j]^{\nu_j'} \tag{2.43}$$

where $[M_j]$ is the concentration of species M_j and k_f is the reaction rate constant of the reaction shown in Eq. (2.42). The reaction rate constant k_f is determined by statistical theory and is expressed by

$$k_f = Z_c \exp(-E/RT) \tag{2.44}$$

where E is activation energy and Z_c is pre-exponential factor determined by collision theory. The exponential term in Eq. (2.44) is the Boltzmann factor, which indicates the fraction of M_j whose energy is higher than the activation energy E.

The rate of production of the species M_i is expressed by

$$d\,[\mathrm{M}_i]/dt = (\nu_i'' - \nu_i')\,\Omega$$

$$= (\nu_i'' - \nu_i')\,k_f \prod_{j=1}^{n} [\mathrm{M}_j]^{\nu_j'} \tag{2.45}$$

where $\nu_i'' - \nu_i'$ is the stoichiometric factor and t is time. The overall order of the reaction m defined in

$$m = \sum_{j=1}^{n} \nu_j' \tag{2.46}$$

When $m = 1$, the reaction is called a first order reaction, and the reactions of $m = 2$, and 3 are called second order and third order, respectively. When an elementary chemical reaction

$$\mathrm{A} + 2\mathrm{B} \rightarrow 3\mathrm{P}$$

produces 3 moles of P from 1 mole of A and 2 moles of B, the reaction rate in mol/m^3 s is expressed by

$$d[\mathrm{P}]/dt = -3d[\mathrm{A}]/dt = -3/2\ d[\mathrm{B}]dt$$

References

1 Dickerson, R. E., Molecular Thermodynamics, W. A. Benjamin, New York (1969), Chapter 5.

2 Laidler, K. J., Chemical Kinetics, Second Edition, McGraw-Hill Book, New York (1969), Chapter 4.

3 Sarner, S. F., Propellant Chemistry, Reinold Publishing Corporation, New York (1966), Chapter 4.

4 Penner, S. S., Chemistry Problems in Jet Propulsion, Pergamon Press, New York (1957), Chapters 12 and 13.

5 Wilkins, R. L., Theoretical Evaluation of Chemical Propellants, Prentice-Hall, Englewood Cliffs (1963), Chapters 3 – 5.

6 JANAF Thermochemical Tables, The Clearing House for Federal Scientific and Technical Information, U.S. Department of Commerce, Springfield, Virginia.

7 Glassman, I., Combustion, Academic Press, New York (1977), Chapter 1.

8 Gordon, S. and McBridge, B. J., Computer Program for Calculation of Complex Chemical Equilibrium Compositions, Rocket Performance, Incident and Reflected Shocks, and Chapman-Jouguet Detonations, NASA SP-273, 1971.

Propellants and Explosives: Thermochemical Aspects of Combustion. Naminosuke Kubota
Copyright © 2002 Wiley-VCH Verlag GmbH & Co. KGaA
ISBNs: 3-527-30210-7 (Hardback); 3-527-60050-7 (Electronic)

3

Combustion Wave Propagation

3.1

Combustion Reaction

3.1.1

Ignition and Combustion

Combustion phenomena have been studied extensively, and a number of instructive books have been published based on both experiment[1–4] and theory[5]. The definition of combustion is not clear. The combustion of gaseous materials produces heat accompanied by emission from the luminous reaction products. However, an energetic polymer burns very fast by itself and produces heat without luminous emission. When a reactive gas is heated by an external energy source, chemical reactions occur between the molecules of the reactive gas. This reaction initiation process is exothermic and forms high temperature products. This process is said to be an ignition, a part of the combustion phenomena. When the heat produced by this exothermic reaction heats up the unreacted portion of the reactive gas, a successive ignition process is established without external heating. This process is said to be self-sustaining, i.e., combustion. The ignited region between the unburned and burned regions is called a combustion wave which propagates toward the unburned region.

When heat is transferred to the surface of an energetic solid material, the surface temperature and the subsurface temperature are increased simultaneously. When the surface temperature reaches the decomposition or gasification temperature, endothermic and/or exothermic reactions occur on and above the surface. The decomposition gases react to form reaction products accompanied by a high heat release, and the temperature in the gas phase increases. This process is the ignition of the energetic solid material. If this reaction process occurs even after the heat given to the surface is removed, combustion is established. On the other hand, if the exothermic and gasification reactions are terminated after the heat given to the surface has been removed, ignition has failed and combustion is not established.

External heating is needed for ignition, and successive heating is needed from the high-temperature burned portion to the low-temperature unburned portion for combustion. The ignition and combustion of reactive gases and energetic solid materials are fundamentally the same. However, additional physicochemical processes such as phase transition for solid to liquid and/or to gas are needed for energetic solid materials. In the combustion wave, melting, decomposition, sublimation, and/or gasification processes are involved.

3.1.2
Premixed Flame and Diffusion Flame

Any reactants to form combustion products are composed of a mixture of oxidizer and fuel components, and the flame is produced by the reaction of the mixture. Two types of flames are formed when the mixture burns: premixed flame and diffusion flame[1,2]. Premixed flame is formed by the combustion of the two components that are premixed prior to burning in the combustion zone. The neighboring oxidizer and fuel component molecules in the premixed reactants react homogeneously in the combustion zone. The temperature and the concentration of the products increase uniformly in the combustion zone.

When oxidizer and fuel components are separated physically and diffuse into each other in the combustion zone, a diffusion flame is formed. Since the molecular distributions of oxidizer and fuel components are not uniform, temperature and combustion products are also not uniform in the combustion zone. Thus, the reaction rate to produce combustion products is low when compared with the premixed flame, because an additional diffusion process is needed to form the diffusion flame.

3.1.3
Laminar Flame and Turbulent Flame

The characteristics of a reactive gas (a premixed gas) are dependent not only on the type of reactants, pressure, and temperature, but also on the flow conditions. When the flame front of a combustion wave is flat and one-dimensional in shape, the flame is said to be laminar. When the flame front is composed of a large number of eddies which are three-dimensional in shape, the flame is said to be turbulent. Unlike a laminar flame, the combustion wave of a turbulent flame is no longer one-dimensional, and the reaction surface of the combustion wave is increased significantly by the fluid-dynamically induced eddies.

When the same chemical compositions of the reactants are used for each type of flame, the chemical reaction rate is considered to be the same for each. However, the reaction surface area of the turbulent flame is increased because of the nature of eddies, and the overall reaction rate at the combustion wave appears to be much higher than that for the laminar flame. Furthermore, the heat transfer process from the unburned gas to the burned gas at the combustion wave is different because the thermophysical properties such as the thermal diffusivity are higher for the turbulent flame than for the laminar flame. Thus, the speed of a turbulent flame appears to be much higher than that of a laminar flame.

The creation of eddies in a combustion zone is dependent on the nature of flow of the unburned gas, i.e., the Reynolds number. If the upstream flow is turbulent, the combustion zone tends to be turbulent. However, since the transport properties such as viscosity, density, and heat conductivity, are changed by the increased temperature and the force acting on the combustion zone, a laminar flow at the upstream tends to generate eddies in the combustion zone and the flame becomes turbulent. Furthermore, in some cases a turbulent flame accompanied by eddies much larger than the thickness of the combustion wave is formed. Though the local combustion zone seems to be laminar and one-dimensional in nature, the overall characteristics of the flame are not those of the laminar flame.

3.2

Combustion Wave of Premixed Gas

3.2.1

Governing Equations for Combustion Wave

The combustion wave of a premixed gas propagates with a certain velocity into the unburned region (with the flow speed = 0). The velocity is sustained by the thermodynamic and thermochemical characteristics of the premixed gas. Figure 3-1 illustrates a combustion wave which propagates into the unburned gas with the velocity u_1 one-dimensionally at a steady-state condition. If one assumes that the observer of the combustion wave moves with the same speed u_1, the combustion wave appears to be stationary, and the unburned gas then flows into the combustion wave with the velocity $-u_1$. The burned gas leaves downstream of the burned gas region with the speed $-u_2$ with respect to the combustion wave. The thermodynamic characteristics of the combustion wave are described by velocity (u), pressure (p), density (ρ), and temperature (T) of the unburned gas (shown in the subscript 1) and the burned gas (shown in the subscript 2) as illustrated in Fig. 3-1.

The governing equations of the combustion wave are the set of conservation equations of mass, momentum, and energy:

$$\rho_1 u_1 = \rho_2 u_2 = m \tag{3.1}$$

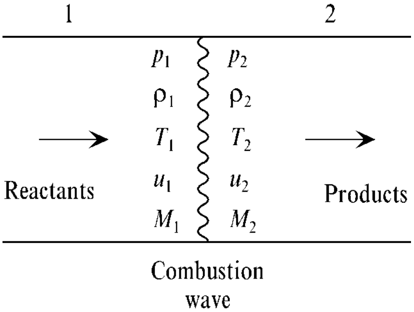

Figure 3-1. Combustion wave propagation.

$$p_1 + \rho_1 u_1^2 = p_2 + \rho_2 u_2^2 \tag{3.2}$$

$$c_p T_1 + \frac{u_1^2}{2} + q = c_p T_2 + \frac{u_2^2}{2} \tag{3.3}$$

where m is the mass flux and q is the heat of reaction per unit mass. These equations are equivalent to Eqs. (1.28), (1.29), and (1.30) for the shock wave except for the additional term of q in Eq. (3.3). The heat of reaction produced in the combustion wave is given by

$$q = h_1^0 - h_2^0 \tag{3.4}$$

The enthalpy is given by the sum of the sensible enthalpy plus chemical enthalpy as

$$h = c_p T + h^0 \tag{3.5}$$

$$c_p T = e + p/\rho \tag{3.6}$$

where h and h^0 are the heats of formation per unit mass at temperature T and at the standard state, respectively.

Equations (3.1) and (3.2) give the velocity u_1 and u_2 as

$$u_1^2 = \frac{1}{\rho_1^2}\left(\frac{p_2 - p_1}{1/\rho_1 - 1/\rho_2}\right) \tag{3.7}$$

$$u_2^2 = \frac{1}{\rho_2^2}\left(\frac{p_2 - p_1}{1/\rho_1 - 1/\rho_2}\right) \tag{3.8}$$

3.2.2
Rankine-Hugoniot Relations

Combining Eqs. (3.1) – (3.4), one gets

$$h_2 - h_1 = \frac{1}{2}(p_2 - p_1)(1/\rho_1 + 1/\rho_2) \tag{3.9}$$

which is termed the Rankine-Hugoniot equation. Since the internal energy e is represented by Eq. (3.6), the Rankine-Hugoniot equation is also expressed by

$$e_2 - e_1 = \frac{1}{2}(p_1 + p_2)(1/\rho_1 - 1/\rho_2) + q \tag{3.10}$$

If the reactant and product are assumed to be in thermodynamic equilibrium, e_1 and e_2 are given as known functions of pressure and density,

$$e_1 = e(p_1,\rho_1) \quad e_2 = e(p_2,\rho_2) \tag{3.11}$$

The Rankine-Hugoniot equation given by Eq. (3.10) or Eq. (3.9) is shown in Fig. 3-2 as a function of $1/\rho$ and p called the Hugoniot curve. The Hugoniot curve for $q = 0$, i.e., no chemical reactions, passes the initial point $(1/\rho_1, p_1)$ and is exactly equivalent to the shock wave described in Chapter 1. When heat q is produced in the combustion wave, the Hugoniot curve shifts to the position shown in Fig. 3-2. It is evident that two different types of combustion are possible on the Hugoniot curve: (1) a detonation, in which pressure and density increase, and (2) a deflagration, in which pressure and density decrease.

Equations (3.1) and (3.2) yield the following relationship, the so-called Rayleigh equation:

$$(p_2 - p_1)/(1/\rho_2 - 1/\rho_1) = -m^2 \tag{3.12}$$

As shown in Fig. 3-3, the two lines of the tangents from the initial point 1 $(1/\rho_1,p_1)$ to the points J and K $(1/\rho_2,p_2)$ on the Hugoniot curve represent the Rayleigh lines which are expressed by[6]

$$\left[\frac{p_2-p_1}{1/\rho_2-1/\rho_1}\right]_J = \left[\frac{\partial p}{\partial\,(1/\rho)}\right]_J = \tan\theta_J \tag{3.13}$$

$$\left[\frac{p_2-p_1}{1/\rho_2-1/\rho_1}\right]_K = \left[\frac{\partial p}{\partial\,(1/\rho)}\right]_K = \tan\theta_K \tag{3.14}$$

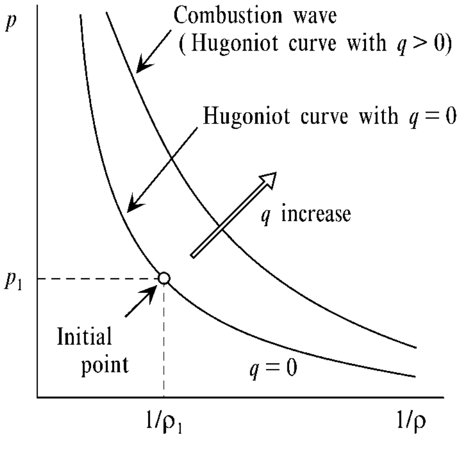

Figure 3-2. Hugoniot curve of combustion wave.

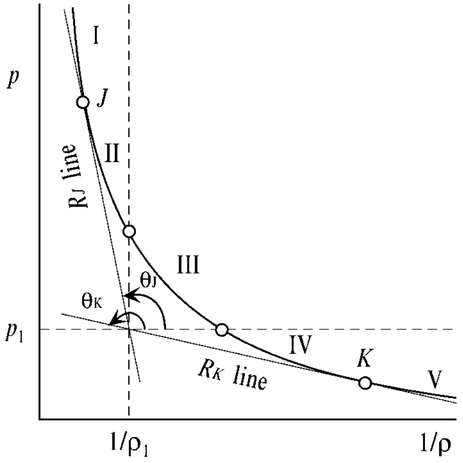

Figure 3-3. Definition of Hugoniot curve for combustion wave.

The mass flow rate given by Eq. (3.1) and the velocity u_2 at point J or K are represented by

$$m = \sqrt{-\tan\theta_J} = \sqrt{-\tan\theta_K} \tag{3.15}$$

$$u_2 = \frac{1}{\rho_2}\sqrt{-\tan\theta_J} \quad \text{at point } J \tag{3.16}$$

$$u_2 = \frac{1}{\rho_2}\sqrt{-\tan\theta_K} \quad \text{at point } K \tag{3.17}$$

3.2.3
Chapman-Jouguet Points

As illustrated in Fig. 3-3, the Hugoniot curve is divided into five regions [1–4]. Since the velocity u_2 expressed by Eq. (2.16) becomes an imaginary value in the region III because $\tan\theta_J$ is a positive value, a combustion wave is physically not possible in Region III. Points J and K are called the Chapman-Jouguet points. Chapman-Jouguet states that the velocity at J on the Hugoniot curve is the minimum value for the propagation velocity u_D relative to the unburned gas, and the velocity at K is the maximum value for the propagation velocity u_d relative to the unburned gas. The entropy of the reaction products varies along the Hugoniot curve. Instructive descriptions of the Chapman-Jouguet relationship are available in [3–5]

Since the Rayleigh line through the point J or K is a tangent to the Hugoniot curve, it is also a tangent to the line of constant entropy through J or K . Thus, the slope of the line of constant entropy is exactly the slope of the Hugoniot curve at J or K[6]. The differentiation of Eq. (3.10) gives

$$de = -\frac{1}{2}(p_1 + p_2)\,d(1/\rho_2) + \frac{1}{2}(1/\rho_1 - 1/\rho_2)\,dp_2 \tag{3.18}$$

The entropy curve is expressed by

$$Tds = de + p_1 d(1/\rho) \tag{3.19}$$

Combining Eqs. (3.15), (3.18), and (3.19), one gets

$$T\left(\frac{\partial s}{\partial p}\right)_{\mathrm{H}} = \left(\frac{1}{\rho_1} - \frac{1}{\rho_2}\right)\left[1 + \frac{m^2}{\partial p/\partial(1/\rho)}\right]_{\mathrm{H}} \tag{3.20}$$

along the Hugoniot curve (H). Since the Raleigh line (R) is a tangent to the Hugoniot curve at points *J* and *K*, $\{\partial p/\partial(1/\rho)\}_{\mathrm{H}} = \{\partial p/\partial(1/\rho)\}_{\mathrm{R}}$, the relationship of

$$\left[\frac{\partial p}{\partial(1/\rho)}\right]_{\mathrm{H}} = -m^2 \tag{3.21}$$

is obtained based on Eqs. (3.13) or (3.15). Substituting Eq. (3.21) into Eq. (3.20), the relationship of $(\partial s/\partial p)_{\mathrm{H}} = 0$ on the Hugoniot curve is obtained, and then $ds = 0$ at *J* and *K* on the Hugoniot curve.

The velocity of sound in the burned gas is expressed by

$$a^2 = \left(\frac{\partial p}{\partial \rho}\right)_s = -\frac{1}{\rho^2}\left[\frac{\partial p}{\partial(1/\rho)}\right]_s \tag{3.22}$$

Using Eq. (3.13), one gets

$$(a_2^2)_J = \left[-\frac{1}{\rho_2^2}\,\frac{p_2 - p_1}{1/\rho_2 - 1/\rho_1}\right]_J = (u_2^2)_J \tag{3.23}$$

Thus, the following relationship is obtained:

$$(u_2)_J = (c_2)_J \quad \text{or} \quad M_2 = 1 \quad \text{at point } J$$

The velocity of the burned gas (u_2) at *J* is equal to the speed of sound in the burned gas (a_2). A similar result is obtained at *K* as

$$M_2 = 1 \quad \text{at point } K$$

The velocity of the burned gas relative to a stationary observer u_p defined as "particle velocity" is given by

$$u_1 = u_D = u_2 + u_p \tag{3.24}$$

Using Eq. (3.1), one gets

$$u_p = u_1(1 - \rho_1/\rho_2) \tag{3.25}$$

Since $\rho_1 < \rho_2$ for a detonation and $\rho_1 > \rho_2$, for a deflagration, the flow field becomes $0 < u_p < u_1$ for detonation, and $u_p < 0$ for deflagration. For detonation, the velocity of the combustion products is less than the detonation wave velocity. For deflagration, the combustion products move away in the opposite direction to that of the deflagration wave.

The line of constant entropy represented by Eq. (1.14), $p\ (1/\rho)^\gamma$ = constant rises with increasing pressure more steeply than the Rayleigh line and less steeply than the Hugoniot curve in Regions I and V, called the strong detonation branch and the strong deflagration branch, respectively. On the other hand, the line of constant entropy rises with increasing pressure less steeply than the Rayleigh line and more steeply than the Hugoniot curve in Regions II and IV, called the weak detonation branch and the weak deflagration branch, respectively. The velocity of the reaction products relative to the reaction front is subsonic behind the combustion wave of Regions I and IV. The velocity is sonic behind a Chapman-Jouguet detonation at *J* or deflagration at *K*, and is supersonic behind the combustion wave of Regions II and V. These characteristics are shown in Fig. 3-4 and are summarized as follows[3–6]:

Region I $p_2 > p_J$: supersonic flow to subsonic flow, strong detonation
Region II $p_2 < p_J$: supersonic flow to supersonic flow, weak detonation
Region III : physically invalidated flow
Region IV $p_2 > p_K$: subsonic flow to subsonic flow, weak deflagration
Region V $p_2 < p_K$: supersonic flow to supersonic flow, strong deflagration

However, Region II and Region V are the regions wherein no physical processes are attainable, as described in [1–4]. In experiments, most deflagration waves are

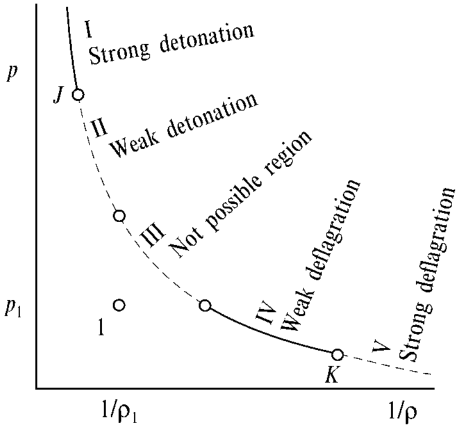

Figure 3-4. Regions of detonation and deflagration in Hugoniot curve.

observed in Region IV in a weak deflagration branch, and most detonation waves are observed in Region I in a strong detonation branch. It must be noted that the relationships of the Hugoniot curve are obtained under idealized conditions: the combustion wave is assumed to be formed under one-dimensional and steady-state flow, and the reactants and products are also assumed to be perfect gases. The realistic phenomena of combustion wave propagation are more complex, being accompanied by thermophysical and thermochemical effects. However, the general characteristics of detonation and deflagration waves are shown in Table 3-1.

Table 3-1. Thermophysical characteristics of deflagration and detonation waves

	Deflagration	*Detonation*
p_2/p_1	< 1	> 1
ρ_2/ρ_1	< 1	> 1
T_2/T_1	> 1	> 1
u_2/u_1	> 1	< 1
M_1	< 1	> 1
M_2	< 1	< 1

In general, the wave propagation velocity in the deflagration branch is termed the flame speed, and that in the detonation branch is termed the detonation velocity.

3.3
Structure of Combustion Wave

3.3.1
Detonation Wave

A detonation wave formed by a reactive gas at a one-dimensional steady-state flow condition is shown in Fig. 3-5. The Hugoniot curve indicates that the pressure, density, and temperature increase rapidly at the front of the detonation wave because of the passage of the shock wave. The energy transfer caused by nonequilibrium molecular collisions occurs from translational energy to rotational energy and to vibrational energy in the shock wave. The increased temperature initiates an exothermic chemical reaction of the reactive gas behind the shock wave and further increases the temperature. The pressure behind the shock wave decreases through a relaxation time and reaches a steady-state condition, the Chapman-Jouguet or CJ point *J* shown in Fig. 3-4. In general, the increase in pressure and temperature through a detonation wave is in the order of $p_2/p_1 = 15–50$, $T_2/T_1 = 10–20$. However, the increase in density is in the order of $\rho_2/\rho_1 = 1.5–2.5$ as shown in Fig. 3-5. The detonation temperature is approximately 400–800 K higher than that of the deflagration temperature because the kinetic energy is converted into pressure and then temperature for the detonation wave.

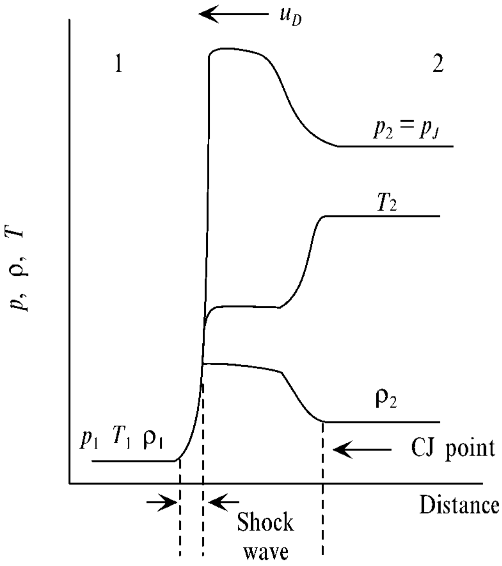

Figure 3-5. Structure of detonation wave and Chapman-Jouguet point.

The structure of a detonation wave proposed by Zeldovich, von Neumann, and Döring (ZND model) is that the pressure at the shock front increases along the Hugoniot curve without chemical reactions and reaches the pressure at the point of the intersection of the Rayleigh line and the Hugoniot curve, the so-called von Neumann spike[3–6], – as shown in Fig. 3-6. Then the pressure decreases along the Rayleigh line to the CJ point *J*, where the detonation velocity reaches the speed of sound

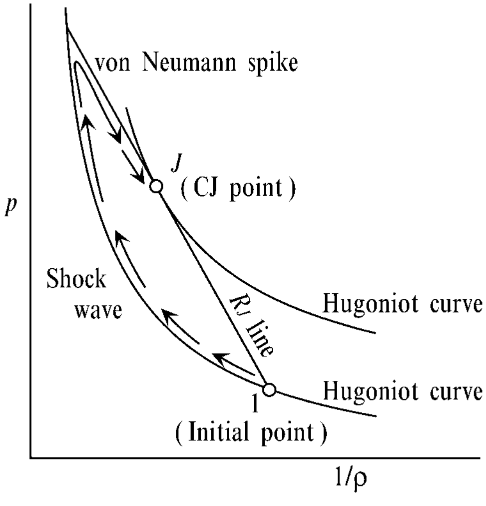

Figure 3-6. Detonation wave formation from shock wave to von Neumann spike, and to Chapman-Jouguet point.

M_2. Experimental observations indicate that the pressure of the detonation front is higher than the pressure at J, but less than the pressure at the point of the intersection of the Rayleigh line and the Hugoniot curve, and finally reaches the pressure at J shown in Fig. 3-6.

The procedure for the computation of the detonation speed is as follows:

(1) Assume a reaction scheme (reactants to products)
(2) Assume T_2.
(3) Assume $1/\rho_2$ and determine p_2 by the use of the equation of state.
(4) Determine p_j (or n_j) at T_2 and p_2 by the same procedure for the determination of T_f described in Section 2.2 of Chapter 2.
(5) Repeat the procedure of (3) and (4) until Eq. (3.9) is satisfied.
(6) Determine u_1 by Eq. (3.7)
(7) Assume a different T_2
(8) Repeat the procedure from (3) to (7) until the minimum value of u_1 is determined.
(9) The minimum value u_1 is the detonation velocity u_D at point J (Chapman-Jouguet detonation velocity).

Computations of the thermochemical values of various combinations of oxidizers and fuels are obtained from [7], and practical computations are done by the use of the computer programs described in [8]. A computational example of detonation characteristics of the gaseous mixture, 2 H_2 + O_2, is shown in Table 3-2 and compared with deflagration characteristics.

Table 3-2. Detonation characteristics of 2 H_2 + O_2

Initial condition	*Detonation*	*Deflagration*
p_1 0.1 MP	p_J 1.88 MPa	p_2 0.1 MPa
T_1 298 K	T_2 3680 K	T_2 3500 K
a_1 538 m/s	a_2 1550 m/s	a_2 1380 m/s
	M_1 5.28	
	u_D 2840 m/s	

Since the detonation velocity is equal to the speed of sound at the CJ point, the u_D is determined by Eqs. (3.24) and (3.25). The temperature of detonation at the CJ point is higher than the temperature of deflagration because of the shock wave compression on the detonation wave.

3.3.2
Deflagration Wave

A deflagration wave formed by a reactive gas at a one-dimensional steady-state flow condition is illustrated in Fig. 3-7. In the combustion wave, temperature increases from the initial temperature of the unburned gas to the ignition temperature and

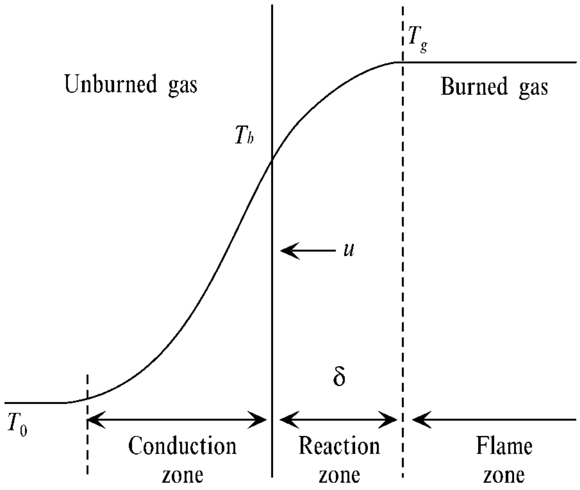

Figure 3-7. Thermal structure of deflagration wave.

then reaches the flame temperature. The heat generated in the reaction zone is transferred back to the unburned gas zone.

The thermal balance of the heat flux transferred back from the reaction zone to the unburned gas zone and the heat given to the unburned gas to increase temperature from the initial temperature T_0 to the ignition temperature T_b is represented by

$$\lambda(dT/dx)_b = c_p\rho u\,(T_b - T_0) \tag{3.26}$$

where T is temperature, x is distance, u is the flow velocity that is equal to the laminar flame speed, ρ is density, c_p is specific heat, λ is thermal conductivity. The subscripts 0 and b indicate the initial condition and the location of the onset of the chemical reaction, respectively. If the temperature in the reaction zone increases linearly, the temperature gradient in the reaction zone is given by

$$(dT/dx)_b = (T_g - T_b)/\delta \tag{3.27}$$

where δ is the thickness of the reaction zone, and T_g is the flame temperature. Combining Eqs. (3.26) and (3.27), one gets

$$\lambda(T_g - T_b)/\delta = c_p\rho u(T_b - T_0) \tag{3.28}$$

and then

$$u = \frac{\lambda}{c_p\rho\delta}\frac{T_g - T_b}{T_b - T_0} \tag{3.29}$$

The reaction rate in the combustion wave is given by

$$[\omega]\delta = \int \omega dx \tag{3.30}$$

and one then gets the relationship $\rho u = [\omega]\,\delta$, where ω is the reaction rate and $[\omega]$ is an averaged value of the reaction rate in the combustion wave. Thus, one gets

$$u = \frac{1}{\rho}\sqrt{\frac{\lambda[\omega]}{c_p}\frac{T_g - T_b}{T_b - T_0}} \tag{3.31}$$

The thickness of the combustion wave is determined to be

$$\delta = \lambda/(c_p \rho u) \tag{3.32}$$

The reaction rate in the combustion wave is expressed by

$$\omega = \rho^m \; [\varepsilon]^{\,m} \, Z \exp(-E/\mathrm{R}T) \tag{3.33}$$

where ε is the mole fraction of the reactant, $[\varepsilon]$ is an averaged value of the mole fraction in the combustion wave, p is pressure, m is the order of the chemical reaction, E is activation energy, R is the universal gas constant, and Z is a constant. Substituting Eqs. (3.33) and (1.5) into Eq. (3.31), the laminar flame speed is represented by

$$u \sim p^{m/2-1} \exp(-E/2\mathrm{R}T) \tag{3.34}$$

where T is assumed to be an averaged value of T_b and T_g. Though the analysis is a simplified one, the characteristics of a laminar flame speed are given. In general, the gas phase reaction is bimolecular and then the order of the chemical reaction is approximately 2. The laminar flame speed appears to be pressure independent. When the mixture of fuel and oxidizer components of a premixed gas is at the stoichiometric ratio, the flame temperature T_g becomes the maximum, and then the laminar flame speed becomes the maximum. When the initial temperature T_0 of a premixed gas is increased, the laminar flame speed is also increased. The laminar flame speed given by Eq. (3.31) is confirmed by observed results. For example, the thickness of the reaction zone of a propane-air mixture is obtained from Eq. (3.32): $u = 350$ mm/s and $\delta = 1.6$ mm.

3.4
Ignition Reaction

3.4.1
Ignition Process

When heat is transferred to a gaseous mixture of oxidizer and fuel components, i.e., a premixed gas, an exothermic reaction occurs and temperature increases. The reaction continues and proceeds into the non-reacted portion of the mixture even after the heat is removed. The amount of heat transferred to the mixture is defined to be the ignition energy. However, when the reaction is terminated after the heat is removed, ignition of the mixture has failed. This is because the heat generated in the combustion zone is not enough to heat up the unreacted portion of the mixture from the initial temperature to the ignition temperature.

Ignition is dependent on various physicochemical parameters such as the type of reactants, reaction rate, pressure, heat transfer process from the external heating to the reactants, and the size or mass of reactants. The rate of heat production is dependent on the heat of formation of the reactants and the products, temperature, and the activation energy. The process of ignition includes external heating and an exothermic reaction by the reactants. Thus, a non-steady heat balance occurs during external heating and self-heating by the exothermic reaction.

3.4.2
Thermal Theory of Ignition

One assumes that a reactive gas is kept in a container and an exothermic reaction occurs. The rate of heat generation of the reactive material q_R (self-heating by the exothermic reaction) is represented, using Eq. (3.33), as

$$
\begin{aligned}
q_R &= QV\omega = QV\rho^m\,[\varepsilon]^{\,m}\,Z\exp(-E/\mathrm{R}T) \\
&= QVA\,p^m\exp(-E/\mathrm{R}T) \qquad (3.35)
\end{aligned}
$$

where V is the volume of the container, Q is the heat of reaction, and A is a constant. Since the heat loss occurs because of the temperature difference between the container surface and that of the surroundings, the heat loss is given by

$$q_L = h_g\,S\,(T - T_0) \qquad (3.36)$$

where S is the surface area of the container, h_g is the heat transfer coefficient from the container surface to the surroundings, and T_0 is the temperature of the surroundings and also the initial temperature of the reactive gas.

Equations (3.35) and (3.36) are illustrated in Fig. 3-8 as a function of temperature. The temperature T_i indicates the ignition temperature of the reactive gas. If the rate of heat generation of the reactant is given by the curve q_{R1}, self-heating occurs at T_0

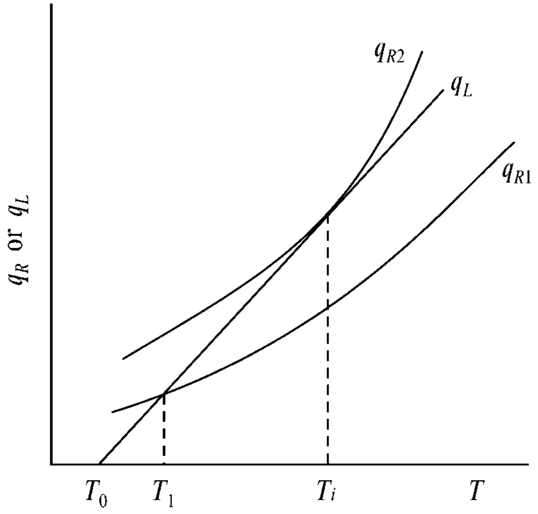

Figure 3-8. Ignition criterion from heat loss and heat gain.

without heat loss and temperature increases toward T_1. However, when the temperature reaches T_1, the rate of heat loss q_L becomes equal to q_{R1}, and then the temperature increase by self-heating is stopped at T_1. Thus, the temperature never reaches the ignition temperature T_i. On the other hand, if the rate of heat generation of the reactant is given by the curve q_{R2}, the self-heating increases the temperature up to T_i because q_{R2} is larger than q_L in the temperature range T_0 to T_i. Since q_{R2} is also larger than q_L in the temperature range above T_i, the self-heating continues, and then ignition occurs.

The ignition criteria of the thermal theory for ignition is then represented by

$$q_L = q_{R2} \quad \text{and} \quad \frac{dq_L}{dT} = \frac{dq_{R2}}{dT} \quad \text{at } T = T_i \tag{3.37}$$

Substituting Eqs. (3.35) and (3.36) into Eq. (3.37), one gets a simplified relationship:

$$T_i - T_0 = \mathrm{R}T_0^2/E \tag{3.38}$$

It is seen from Eqs. (3.35) and (3.38) that the ignition temperature decreases as the density of reactant increases, i.e., as pressure increases.

3.4.3
Flammability Limit

The rate of heat generation of a mixture depends on the ratio of oxidizer and fuel components in the mixture. As the mixture ratio becomes fuel rich or oxidizer rich, the rate of heat generation decreases and the reaction rate decreases also. At a certain mixture ratio, no combustion occurs even if an excess ignition energy is given to the mixture. This is a combustion limit, the so-called flammability limit. Thus, there exist two flammability limits, the lower limit and upper limit, for one reactant consisting of different mixture ratios of the same oxidizer and fuel components. For example, a hydrogen and air mixture burns in the mixture ratio of 0.04 ~ 0.74 by hydrogen volume. The lower limit is 0.04 and the upper limit is 0.74 by volume. The maximum reaction rate and the highest temperature are obtained at the mixture ratio of 0.292, i.e., the stoichiometric ratio of hydrogen to oxygen by volume. In case of a hydrogen and oxygen mixture, the lower limit is 0.04 and the upper limit is 0.94 by volume. The stoichiometric ratio of this mixture is 0.667.

3.5
Combustion Wave of Energetic Materials

3.5.1
Thermal Theory of Burning Rate

A schematic representation of the combustion wave structure of a typical energetic material is shown in Fig. 3-9, and the heat transfer process is shown in Fig. 3-10 as a function of the burning distance and temperature. In zone I (solid phase zone or condensed phase zone), no chemical reactions occur and temperature increases from the initial temperature (T_0) to the decomposition temperature (T_u). In zone II (condensed phase reaction zone), temperature increases from T_u to the burning surface temperature (T_s), where phase change from solid to liquid and/or to gas occurs

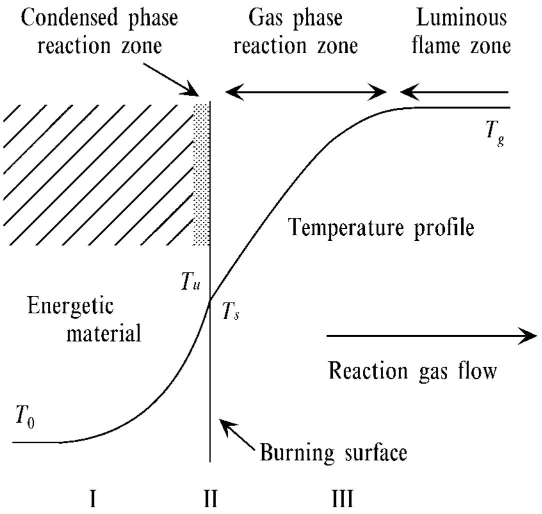

Figure 3-9. Combustion wave structure of an energetic material.

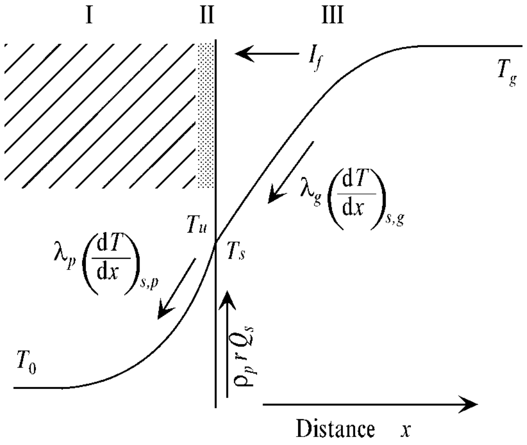

Figure 3-10. Thermal structure and heat feedback process of combustion wave.

and reactive gaseous species are formed and endothermic or exothermic reaction occur. In zone III (gas phase reaction zone), temperature increases rapidly from T_s to the flame temperature (T_g), where exothermic gas phase reaction occurs.

The basic assumptions in the following description of the burning rate model are

1. One-dimensional burning
2. Steady-state burning at a fixed pressure
3. Radiative energy from the gas phase is absorbed at the burning surface.

With reference to Figs. 3-9 and 3-10, the energy and the species equations are:

condensed-phase energy equation :

$$\frac{d}{dx}\left(\lambda_p \frac{dT}{dx}\right) - \rho_p r c_p \frac{dT}{dx} + \omega_p Q_p = 0 \tag{3.39}$$

condensed-phase species equation for species j:

$$\frac{d}{dx}\left(\rho_p D_{p,j} \frac{d\varepsilon_j}{dx}\right) - \rho_p r \frac{d\varepsilon_j}{dx} - \omega_{p,j} = 0 \tag{3.40}$$

gas phase energy equation:

$$\frac{d}{dx}\left(\lambda_g \frac{dT}{dx}\right) - \rho_g u_g c_g \frac{dT}{dx} + \omega_g Q_g = 0 \tag{3.41}$$

gas phase species equation for species i:

$$\frac{d}{dx}\left(\rho_g D_{g,i}\frac{d\varepsilon_i}{dx}\right) - \rho_g u_g \frac{d\varepsilon_i}{dx} - \omega_{g,i} = 0 \tag{3.42}$$

where r is burning rate, Q is heat of reaction, D is diffusion coefficient, and the subscript p is condensed phase, g is gas phase, j is the species in condensed phase, and i is the species in gas phase.

Several additional assumptions are applied to the above equations[9,10]: (1) no endothermic or exothermic reaction is involved within the condensed phase (below the burning surface), (2) the luminous flame zone does not contribute to the conductive heat feedback from the gas phase to the burning surface, and (3) no species diffusion occurs in the condensed phase or in the gas phase. Equations (3.39) and (3.40) are then simplified as follows:

$$\frac{d}{dx}\left(\lambda_p \frac{dT}{dx}\right) - \rho_p r c_p \frac{dT}{dx} = 0 \tag{3.43}$$

$$-\rho_p r \frac{d\varepsilon_j}{dx} - \omega_{p,j} = 0 \tag{3.44}$$

The integration of Eq. (3.43) under the boundary conditions of

$T = T_0$ at $x = -\infty$

$T = T_s$ at $x = 0$

is represented by

$$T(x) - T_0 = (T_s - T_0)\exp(rx/\alpha_p) \tag{3.45}$$

where α_p is the thermal diffusivity of the condensed phase defined as $\alpha_p = \lambda_p/\rho_p c_p$, i.e. it is assumed to be independent of temperature. Figure 3-11 shows the temperature profiles in the condensed phase at r = 2 mm/s, 10 mm/s, and 50 mm/s with the assumptions of T_0 = 325 K, T_s = 600 K, $\lambda_p = 2.10 \times 10^{-4}$ kJ/s m K, ρ_p = 1600 kg/m^3, c_p = 1.47 kJ/kg K, and $\alpha_p = \lambda_p/\rho_p c_p = 8.93 \times 10^{-8}$ m^2/s. The thermal wave thickness in the condensed phase defined as $\delta_p = \alpha_p/r$ is 45 μm, 9 μm, and 1.8 μm at r = 2 mm/s, 10 mm/s, and 50 mm/s, respectively. The temperature gradient in the condensed phase increases as the burning rate increases, i.e., δ_p decreases as the burning rate increases.

Since energetic materials are composed of several chemical ingredients and each molecular structure is complex, numerous gaseous species are produced at the burning surface and their reaction schemes are also complex. Thus, the determination of the gas phase reaction rate for each species j during burning is extremly difficult. The treatment of the gas phase reaction, which determines the temperature gradient just above the burning surface, $\phi = (dT/dx)_{s,g}$, and the heat feedback from

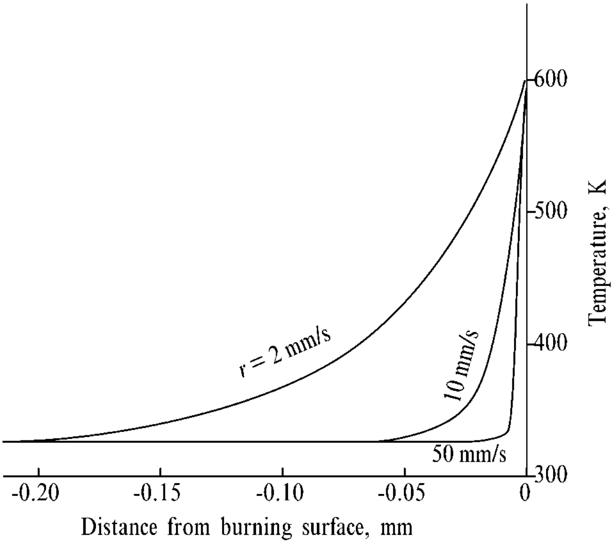

Figure 3-11. Temperature profile in condensed phase of an energetic material.

the gas phase to the condensed phase, $\Lambda_g = \lambda_g\ \phi$, is the basic point which leads to the burning rate equation. In order to gain a fundamental understanding of the heat feedback process in the gas phase, a heat release in the gas phase is assumed to be given by a step function and has a positive constant value ω_g. The model represents the heat flux feedback from the gas phase to the condensed phase by integration of Eq. (3.41) with the boundary condition that heat flux at infinity must be zero. One gets

$$\Lambda_g = Q_g \int_0^\infty \exp(-\rho_g c_g\ u_g\ x/\lambda_g)\omega_g dx \tag{3.46a}$$

In analogy with the condensed phase, the thermal diffusivity in the gas phase is given by $\alpha_g = \lambda_g/\rho_g c_g$, i.e. is assumed to be independent of temperature. The thermal wave thickness in the gas phase δ_g is defined in $\delta_g = \alpha_g/u_g$. Then, Eq. (3.46a) is represented by

$$\Lambda_g = Q_g \int_0^\infty \exp(-u_g\ x/\alpha_g)\omega_g\ dx \tag{3.46b}$$

$$= Q_g \int_0^\infty \exp(-x/\delta_g)\ \omega_g\ dx \tag{3.46c}$$

In general, reaction rates are strongly dependent on the temperature when the activation energy is high. Thus it is assumed that the two major effects of the reaction rate, temperature and concentration of the reactant, tend to cancel each other;

as the reaction proceeds the temperature increases but the concentration of reactants decreases. Furthermore, it is assumed that the resulting constant rate of reaction occurs from the burning surface ($x_i = 0$) throughout the reaction zone in the gas phase ($x = x_g$). Equation (3.46c) becomes, under these approximations,

$$\Lambda_g = \frac{\alpha_0 [\omega_g] Q_g}{r} \left\{ 1 - \exp\left(-\frac{r\,x_g}{\alpha_0} \right) \right\} \tag{3.47a}$$

where $[\omega_g]$ is a positive constant for $x_i < x \leq x_g$ and is zero elsewhere, and $[\omega_g]$ should be considered an average value for the real reaction rate occurring in the gas phase, and $\alpha_0 = \lambda_g / \rho_p c_g$ is defined as the thermal diffusivity at the interface between the condensed phase and the gas phase. The characteristic length L_g^* defined in $L_g^* = \alpha_0 / r = \delta_g$ is substituted into Eq. (3.47a); then one gets

$$\Lambda_g = \frac{\alpha_0 [\omega_g] Q_g}{r} \left\{ 1 - \exp\left(-\frac{x_g}{L_g^*} \right) \right\} \tag{3.47b}$$

When the term in the exponent $x_g / L_g^* \gg 1$, a simplified expression of the heat flux feedback from the gas phase to the solid phase is obtained[10] as

$$\Lambda_g = L_g^* [\omega_g] Q_g \tag{3.48}$$

This asymptote occurs whenever the heat transferred back to the burning surface is small compared to the heat released in the gas phase, which implies that x_g / L_g^* is large enough. Though Eq. (3.48) is not precise, it represents the behavior of burning rate without introducing mathematical complexities and reaction parameters.

The heat flux feedback from zone II to zone I by conduction heat transfer, Λ_p, is given by

$$\Lambda_p = \lambda_p \, (dT/dx)_{s,p} = \rho_p \, c_p \, r \, (T_s - T_0) \tag{3.49}$$

and the heat flux generated in the condensed phase zone at the burning surface, Γ_s, is given by

$$\Gamma_s = \rho_p \, r \, Q_s \tag{3.50}$$

where the subscript s denotes the burning surface and p the condensed phase reaction zone at the burning surface. The boundary conditions for the energy equation in the condensed phase and at the burning surface, respectively, are given as

$$T = T_0 \quad \text{at} \quad x = -\infty$$

$$\Lambda_p = \Lambda_g + \Gamma_s \quad \text{at} \quad x = 0 \tag{3.51}$$

Generally, the reaction rate ω_j of a one-step reaction

$$\sum_{i=1}^{N} \nu_i' \, \mathrm{M}_i \xrightarrow{k_g} \sum_{i=1}^{N} \nu_i'' \, \mathrm{M}_i$$

is represented by

$$\omega_j = \rho_g \frac{d\varepsilon_j}{dt} = \rho_g u_g \frac{d\varepsilon_j}{dx} = (\nu_i'' - \nu_i')k_g \prod_{h=1}^{N} (\rho_g \varepsilon_h)^{\nu_h'} \tag{3.52}$$

where M is the designation of an arbitrary chemical species, N is the number of parallel reaction paths in the gas phase, k_g is the reaction rate constant, ν_i' and ν_i'' are the stoichiometric coefficients for species i as a reactant and j as a product, respectively. Therefore the heat feedback from the gas phase to the burning surface is obtained from Eqs. (3.42), (3.48), and (3.52):

$$\Lambda_g = L_g^* \sum_{i=1}^{N} Q_{g,i}(\nu_i'' - \nu_i')k_g \prod_{h=1}^{N} (\rho_g \varepsilon_h)^{\nu_h'} \tag{3.53}$$

Then, combining Eq. (3.51) with Eq. (3.53), and solving for r one gets:

$$r = \left[\frac{\alpha_0}{\rho_p c_p (T_s - T_0 - Q_s/c_p)} \sum_{i=1}^{N} Q_{g,i}(\nu_i'' - \nu_i')k_g \prod_{h=1}^{N} (\rho_g \varepsilon_h)^{\nu_h'} \right]^{\frac{1}{2}} \tag{3.54}$$

Equation (3.54) is the simplified burning-rate equation. If the reaction rates in the gas phase are known, the burning rate is given in terms of gas density (pressure), burning surface temperature, initial propellant temperature and physical properties of energetic material.

The burning surface temperature is related to the burning rate by an Arrhenius equation which assumes first order decomposition reaction for each reaction species at the burning surface.

$$r = \sum_{j=1}^{K} \varepsilon_j Z_{s,j} \exp(-E_{s,j}/\mathrm{R}T_s) \tag{3.55}$$

where K is the number of assumed parallel, independent gasification reaction paths in the condensed phase. Equations (3.54) and (3.55) can be combined; then the burning rate and burning surface temperature can be obtained for any given set of conditions.

Generally the gas phase reactions in flame models for premixed gases and the gas phase reactions of the burning of energetic materials are assumed to be bimolecular and hence of second order. Then one can express Eq. (3.54) as

$$r = \left[\frac{\alpha_0 Q_g (\varepsilon_g \rho_g)^2 k_g}{\rho_p c_p (T_s - T_0 - Q_s/c_p)} \right]^{\frac{1}{2}} \tag{3.56}$$

The reaction rate constant, k_g, is a function of temperature expressed as:

$$k_g = Z_g \exp(-E_g/\mathrm{R}T_g) \tag{3.57}$$

The perfect gas law is also used to related the assumed spatially constant density to p and T_g:

$$\rho_g = p/RT_g \tag{3.58}$$

Equations (3.57) and (3.58) are substituted into Eq. (3.56); then, the burning rate equation for energetic materials propellant is given under the assumptions described above as

$$r = p\left[\frac{\alpha_0 Q_g \varepsilon_g^2 Z_g \exp(-E_g/\mathrm{R}T_g)}{\rho_p c_p (RT_g)^2 (T_s - T_0 - Q_s/c_p)}\right]^{\frac{1}{2}} \tag{3.59}$$

where T_g is given as

$$T_g = T_0 + Q_s/c_p + Q_g/c_g \tag{3.60}$$

The burning surface decomposition rate, i.e., burning rate, is given from Eq. (3.55) as

$$r = Z_s \exp(-E_s/\mathrm{R}T_s) \tag{3.61}$$

The nonlinear character of the algebraic equations, (3.59) and (3.61), implies the need for an iteration solution.

3.5.2
Flame Standoff Distance

If the reactive gas produced at the burning surface of an energetic material reacts slowly in the gas phase and generates a luminous flame, the distance L_g between the burning surface and the luminous flame front is said to be the flame standoff distance. In the gas phase shown in Fig. 3-8, the temperature gradient appears to be small and the temperature increases relatively slowly. In this case, heat flux by conduction, the first term in Eq. (3.41), is neglected. Similarly, the rate of mass diffusion, the first term is Eq. (3.42), is assumed to be small compared with the rate of mass convection, the second term in Eq. (3.42). Thus, one gets

$$-\rho_g u_g c_g \frac{dT}{dx} + \omega_g Q_g = 0 \tag{3.62}$$

$$-\rho_g u_g \frac{d\varepsilon_g}{dx} - \omega_g = 0 \tag{3.63}$$

The reaction rate for an m th order reaction is given by (ignoring the temperature dependence of ρ_g)

$$\omega_g = \rho_g \frac{d\varepsilon_g}{dt} = \rho_g u_g \frac{d\varepsilon_g}{dx} = -\varepsilon_g^m \rho_g^m Z_g \exp(-E_g/\mathrm{R}T_g) \tag{3.64}$$

Equations (3.62) – (3.64) are combined; then

$$dT/dx = (1/c_g u_g)\, Q_g \varepsilon_g^m \rho_g^{m-1} Z_g \exp(-E_g/\mathrm{R}T_g) \tag{3.65}$$

The mass flow continuity relation between the gas phase and solid is

$$u_g = r\rho_p/\rho_g \tag{3.66}$$

Combining Eqs. (3.65) and (3.66) and the perfect gas law gives

$$dT/dx = (1/c_g \rho_p r)\, Q_g \varepsilon_g^m (RT_g)^{-m} p^m Z_g \exp(-E_g/\mathrm{R}T_g) \tag{3.67}$$

If the burning rate of the energetic material is expressed by

$$r = ap^n \tag{3.68}$$

where n is the pressure exponent of burning rate, Eq. (3.67) is represented by

$$dT/dx = (1/c_g \rho_p a)\, Q_g \varepsilon_g^m (RT_g)^{-m} Z_g \exp(-E_g/\mathrm{R}T_g)\, p^{m-n} \tag{3.69}$$

The temperature gradient, dT/dx, in the gas phase is approximately equal to $\Delta T_g/L_g$, where ΔT_g is the temperature change across the gas phase zone. Thus, the flame standoff distance L_g is represented by

$$L_g = p^{n-m} \frac{\Delta T_g c_g \rho_p a (RT_g)^m}{Q_g \varepsilon_g^m Z_g \exp(-E_g/\mathrm{R}T_g)} \tag{3.70}$$

$$\sim p^{n-m} = p^d \tag{3.70a}$$

3.5.3
Burning Rate Characteristics of Energetic Materials

3.5.3.1 **Pressure Exponent of Burning Rate**

In general, the burning rate of energetic materials increases linearly as pressure increases in a ln p versus ln r plot represented by Eq. (3.68) at constant initial temperature T_0, where r is burning rate and p is pressure. Thus, the pressure sensitivity of the burning rate at a constant initial temperature is defined by

$$n = \left(\frac{\partial \ln r}{\partial \ln p}\right)_{T_0} \tag{3.71}$$

Equation (3.68) is called Vieille's law or Saint Robert's law, and *n*, defined in the pressure exponent, and *a* are dependent on the chemical composition and the initial propellant temperature.

3.5.3.2 **Temperature Sensitivity of Burning Rate**

The burning rate of any energetic materials depends also on the initial temperature of the materials, T_0, even when the burning pressure is kept constant. The temperature sensitivity of burning rate, σ_p, is defined by the change of burning rate when T_0 is changed as

$$\sigma_p = \frac{1}{r}\frac{r_1 - r_0}{T_1 - T_0} \tag{3.72}$$

where r_0 and r_1 are the burning rates at T_0 and T_1, respectively, and *r* is the average burning rate between T_0 and T_1. Thus, the unit of σ_p appears to be K^{-1}. The differential form of Eq. (3.72) is expressed by

$$\sigma_p = \frac{1}{r}\left(\frac{\partial r}{\partial T_0}\right)_p = \left(\frac{\partial \ln r}{\partial T_0}\right)_p \tag{3.73}$$

Using Eq. (3.68) one gets

$$\sigma_p = \left[\frac{\partial \ln(ap^n)}{\partial T_0}\right]_p = \frac{1}{a}\left(\frac{\partial a}{\partial T_0}\right)_p \tag{3.74}$$

The temperature sensitivity of the burning rate defined in Eq. (3.72) is a parameter of considerable relevance in energetic materials.

3.5.4
Analysis of Temperature Sensitivity of Burning Rate

In order to understand the fundamental concept of the cause of temperature sensitivity, the analysis described in this section assumes that the combustion wave is homogeneous and the combustion wave consists of steady-state one-dimensionally successive reaction zones. The gas phase reaction occurs with a one-step temperature rise from the burning surface temperature to the maximum flame temperature. The heat transfer in the combustion wave structure of energetic materials is illustrated in Fig. 3-10. The heat flux feedback from zone III to zone II by conductive heat transfer, $\Lambda_g = \lambda_g\,(dT/dx)_{s,g}$, is given by Eq. (3.46), and the heat flux feedback from zone II to zone I by conduction heat transfer, $\Lambda_p = \lambda_p\,(dT/dx)_{s,p}$, is given by Eq. (3.49). Using the integrated energy equation [Eq. (3.51)] at the burning surface, the burning rate is represented by

$$r = \alpha_s \phi / \psi \tag{3.75}$$

$$\phi = (dT/dx)_{s,g} \quad \psi = T_s - T_0 - Q_s/c_p \tag{3.76}$$

Equation (3.75) indicates that the burning rate of energetic materials is determined to be two parameters: the gas phase parameter ϕ which is determined by the physical and chemical properties in the gas phase, and the condensed phase parameter ψ which is determined by the physical and chemical properties in the condensed phase. When the initial temperature is increased from T_0 to $T_0 + \Delta T_0$, the temperature profile is shown in Fig. 3-12. The burning surface temperature T_s is also increased to $T_s + \Delta T_s$ and the final combustion temperature is increased from T_g to $T_g + \Delta T_g$.

When the logarithmic form of the burning rate equation given by Eq. (3.75) is differentiated with respect to the initial temperature of the energetic material at a constant pressure, the following is derived:

$$(\partial \ln r/\partial T_0)_p = \{\partial \ln \lambda_g (dT/dx)_{s,g}/\partial T_0\}_p - \{\partial \ln \rho_p c_p (T_s - T_0 - Q_s/c_p)/\partial T_0\}_p \tag{3.77}$$

Hence the physical property of $\alpha_s = \lambda_g/\rho_p c_p$, thermal diffusivity at burning surface, is assumed to be independent of T_0, and Eq. (3.77) is written as

$$\begin{aligned} \sigma_p &= (\partial \ln \phi/\partial T_0)_p - (\partial \ln \psi/\partial T_0)_p \\ &= \Phi + \Psi \end{aligned} \tag{3.78}$$

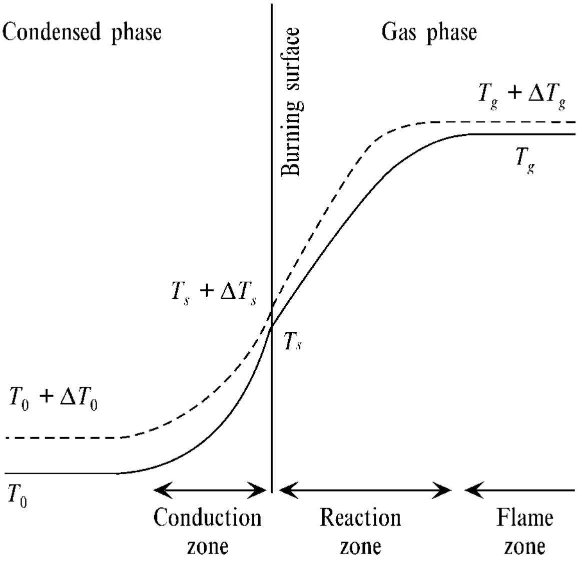

Figure 3-12. Temperature profiles in combustion wave at different initial temperatures of an energetic material.

where $\Phi = (\partial \ln \phi / \partial T_0)_p$ (3.79)

and $\Psi = -(\partial \ln \psi / \partial T_0)_p$ (3.80)

It is shown from Eq. (3.78) that the temperature sensitivity consists of two parameters[11], Φ and Ψ: Φ is the so-called "temperature sensitivity of the gas phase", which is determined by the parameters of gas phase, and Ψ is the so-called "temperature sensitivity of the condensed phase", which is determined by the parameters of condensed phase.

If one assumes that the reaction in the gas phase is given by Eq. (3.48), the heat flux feedback from the gas phase to the burning surface is given by

$$\lambda_g \phi = \alpha_0 [\omega_g] Q_g / r \tag{3.81}$$

Differentiating the logarithmic form of Eq. (3.81) with respect to T_0 at a constant pressure, one gets

$$\begin{aligned}\Phi &= (\partial \ln [\omega_g]\, Q_g / \partial T_0)_p - (\partial \ln r / \partial T_0)_p \\ &= (\partial \ln [\omega_g] / \partial T_0)_p + (\partial \ln Q_g / \partial T_0)_p - \sigma_p \\ &= \Omega + \Theta - \sigma_p \end{aligned} \tag{3.82}$$

where λ_g and α_0 are assumed to be constant and

$$\Omega = (\partial \ln [\omega_g] / \partial T_0)_p \tag{3.83}$$

$$\Theta = (\partial \ln Q_g / \partial T_0)_p \tag{3.84}$$

Thus, one gets the temperature sensitivity expression:

$$\sigma_p = \Omega/2 + \Theta/2 + \Psi/2 \tag{3.85}$$

If one assumes that the reaction rate in the gas phase is given by a one-step m th-order Arrhenius-type reaction given by Eq. (3.64) and substitutes in Eq. (3.83), one gets

$$\Omega = \frac{E_g}{R T_g^2} \left(\frac{\partial T_g}{\partial T_0} \right)_p \tag{3.86}$$

The heat generated in the gas phase can be given by

$$Q_g = c_g (T_g - T_s) \tag{3.87}$$

Substituting Eq. (3.87) in Eq. (3.84), one gets

$$\Theta = \left(\frac{\partial T_g}{\partial T_0} - \frac{\partial T_s}{\partial T_0}\right)_p \frac{1}{T_g - T_s} \tag{3.88}$$

Substituting Eqs. (3.86), (3.88), and (3.80) in Eq. (3.85), one gets

$$\sigma_p = \frac{E_g}{2RT_g^2}\left(\frac{\partial T_g}{\partial T_0}\right)_p + \left(\frac{\partial T_g}{\partial T_0} - \frac{\partial T_s}{\partial T_0}\right)_p \frac{1}{2(T_g - T_s)}$$
$$- \left(\frac{\partial T_s}{\partial T_0} - 1 - \frac{1}{c_p}\frac{\partial Q_s}{\partial T_0}\right)_p \frac{1}{2(T_s - T_0 - Q_s/c_p)} \tag{3.89}$$

Equation (3.89) is the expression of temperature sensitivity of energetic materials based on the analysis of a one-dimensional one-step reaction in the combustion wave.

References

1 Lewis, B. and von Elbe, G., Combustion, Flames and Explosions of Gases, Academic Press, New York (1951).

2 Gaydon, A. G. and Wolfhard, H. G., Flames Their Structure, Radiation and Temperature, Chapman and Hall, London (1960).

3 Strehlow, R. A., Fundamentals of Combustion, International Textbook Company, Scranton, Pennsylvania (1968), Chapter 5.

4 Glassman, I., Combustion, Academic Press, New York (1977), Chapter 5.

5 Williams, F. A., Combustion Theory 2nd edition, Benjamin/Cummings, New York (1985), Chapters 6 and 7, pp. 182–246.

6 Zucrow, M. J. and Hoffman, J. D., Gas Dynamics, John Wiley & Sons, New York (1976), Chapter 9.

7 JANAF Thermochemical Tables, Dow Chemical Co., Midland, Michigan (1960–1970).

8 Gordon, S. and McBridge, B. J., Computer Program for Calculation of Complex Chemical Equilibrium Compositions, Rocket Performance, Incident and Reflected Shocks, and Chapman-Jouguet Detonations, NASA SP-273, 1971.

9 Kubota, N., Ohlemiller, Caveny, L. H., and Summerfield, M., The Mechanism of Super-Rate Burning of Catalyzed Double Base Propellants, AMS Report No. 1087, Aerospace and Mechanical Sciences, Princeton University, Princeton, NJ (1973).

10 Kubota, N., Survey of Rocket Propellants and Their Combustion Characteristics, Fundamentals of Solid-Propellant Combustion, edited by Kuo, K. K., Summerfield, M., Progress in Astronautics and Aeronautics, Vol. 90, Chapter 1, AIAA, Washington DC (1984).

11 Kubota, N., Temperature Sensitivity of Solid Propellants and Affecting Factors: Experimental Results, Nonsteady Burning and Combustion Stability of Solid Propellants, edited by De Luca, L., Price, E. W., and Summerfield, M., Progress in Astronautics and Aeronautics, Vol. 143, Chapter 4, AIAA, Washington DC (1990).

Propellants and Explosives: Thermochemical Aspects of Combustion. Naminosuke Kubota
Copyright © 2002 Wiley-VCH Verlag GmbH & Co. KGaA
ISBNs: 3-527-30210-7 (Hardback); 3-527-60050-7 (Electronic)

4

Energetics of Propellants and Explosives

4.1

Evaluation of Chemical Energy

4.1.1

Heats of Formation of Reactants and Products

Propellants and explosives are designed for an energy density that is as high as possible within limits imposed by mechanical sensitivities, manufacture, physical properties, and combustion characteristics. As shown in Eq. (2.2), $\Delta H_{f,\mathrm{r}}$ is expected to be as high as possible and $\Delta H_{f,\mathrm{p}}$ as low as possible in order to gain high H_{exp}. Tables 4-1 and 4-2 show $\Delta H_{f,\mathrm{r}}$ of typical ingredients used to formulate energetic materials and $\Delta H_{f,\mathrm{p}}$ of typical combustion products of energetic materials at 298 K, respectively.[1–9]

Table 4-1. Heats of formation of energetic materials.

Reactant	***$\Delta H_{f,r}$ (MJ/kg)***
NG	–1.70
NC	–2.60
DEGDN	–2.21
TEGDN	–2.53
TMETN	–1.61
DBP	–3.03
DEP	–7.37
TA	–5.61
2NDPA	–0.01
HMX	+0.25
RDX	+0.27
AP	–2.52
NP	+0.23
KP	–3.12
AN	–4.56
TAGN	–0.281
ADN	–1.22

Table 4-1. Continued.

Reactant	$\Delta H_{f,r}$ ***(MJ/kg)***
HNF	–0.39
CL-20	+0.96
KN	–4.87
Ammonium picrate	–1.50
Diazodinitrophenol	–1.46
Diethyleneglycol	–2.10
Nitroglycol	–1.51
NQ	–0.77
NIBGTN	–0.80
NM	–1.73
Hydrazine nitrate	–2.45
PETN	–1.59
TNT	–0.185
Trinitroanisol	–0.548
TNB	–0.097
TNChloroB	+0.169
Methyl nitrate	–1.91
Tetryl	+0.196
Picric acid	–0.874
Lead azide	+1.66
CTPB	–0.89
HTPB	–0.31
GAP	+0.96
BAMO	+2.46
Cubane	+5.47
B	0
C	0
Al	0
Mg	0
Ti	0
Zr	0

Table 4-2. Heats of formation of combustion products.

Product	$\Delta H_{f,p}$ ***(MJ/kg)***
CO	–3.94
CO_2	–8.94
H_2	0
$H_2O_{(g)}$	–13.42
N_2	0
Al_2O_3	–16.4
B_2O_3	–18.3
MgO	–14.9

Typical materials containing oxygen and nitrogen atoms are nitrate esters such as nitrocellulose (NC) and nitroglycerin (NG). Nitrate esters contain of $–O–NO_2$ chemical bonds in their structures. The oxidizer component is oxygen atoms and the fuel components are carbon and hydrogen atoms. The oxidized combustion products are CO_2 and H_2O, for which $\Delta H_{f,\mathrm{p}}$ are –8.94 MJ/kg and –13.42 MJ/kg, respectively, as shown in Table 4-2[1–9]. The nitrogen atoms in the reactants produce nitrogen gas, for which $\Delta H_{f,\mathrm{p}}$ is zero (Table 4-2).

Table 4-3 shows H_{exp} and the nitrogen concentration N (%) of the typical energetic materials used as major components of propellants and explosives[1–9]. In order to obtain a higher H_{exp} for propellants and explosives, various types of chemicals are mixed such as plasticizers, stabilizers, and reaction rate modifiers. The major chemicals are fuels and oxidizers. The fuels react with the oxidizers to produce heat and gaseous products. Even though the $\Delta H_{f,\mathrm{r}}$ for both fuel and oxidizer is low, a higher H_{exp} is obtained if the oxidizer has a potential to oxidize the fuel effectively. The oxidation reaction, i.e., combustion, produces combustion products of lower $\Delta H_{f,\mathrm{p}}$. It is also shown that the H_{exp} is high for high N (%) materials.

Table 4-3. Heats of explosion and nitrogen concentrations of energetic materials.

Material	*Chemical formula*	*H_{exp}(MJ/kg)*	*N (%)*
NG	$(ONO_2)_3(CH_2)_2CH$	6.32	18.50
NC	$C_{12}H_{14}N_6O_{22}$	4.13	14.14
DEGDN	$(CH_2)_4O(ONO_2)_2$	4.85	14.29
TEGDN	$(CH_2)_6O_2(ONO_2)_2$	3.14	11.67
TMETN	$CH_3C(CH_2)_3(ONO_2)_3$	5.53	16.46
AP	NH_4ClO_4	1.11	11.04
AN	NH_4NO_3	1.60	35.0
NQ	$CH_4N_4O_2$	2.88	53.83
TAGN	$CH_9N_7O_3$	3.67	58.68
HMX	$(NNO_2)_4(CH_2)_4$	5.36	37.83
RDX	$(NNO_2)_3(CH_2)_3$	5.40	37.84
Ammonium picrate	$C_6H_6NO(NO_2)_3$	4.28	22.77
Diazodinitrophenol	$C_6H_2N_2O(NO_2)_2$		26.67
Diethyleneglycol dinitrate	$(ONO_2)_2(CH_2)_4O$	4.85	14.29
Nitroglycol	$(ONO_2)_2(CH_2)_2$	6.83	18.42
Nitroisobutylglycerol trinitrate	$(ONO_2)_3NO_2C(CH_2)_3$	7.15	19.58
NM	CH_3NO_2	4.54	22.96
Hydrazine nitrate	$(NH_2)_2HNO_3$	3.87	44.20
PETN	$(ONO_2)_4(CH_2)_4C$	5.90	17.72
TNT	$(NO_2)_3C_7H_5$	5.07	18.50
Trinitroanisol	$(NO_2)_3C_7H_5O$	4.62	17.29
TNB	$(NO_2)_3C_6N_3$	5.34	19.72
TNChloroB	$(NO_2)_3C_6H_2Cl$		16.98

Table 4-3. Continued.

Material	*Chemical formula*	*H_{exp}(MJ/kg)*	*N (%)*
Methyl nitrate	CH_3ONO_2	6.12	18.19
Tetryl	$(NO_2)_4C_7H_5N$	5.53	24.39
Picric acid	$(NO_2)_3C_6H_2OH$	5.03	18.37
Lead azide	$Pb(N_3)_2$		28.85
CL-20	$(NNO_2)_6(CH)_6$	6.80	38.45

4.1.2
Oxygen Balance

The concentration of oxygen atoms within the oxidizer represented by "oxygen balance : [OB]" is an important parameter to identify the potential of oxidizers. Oxygen balance is the amount of the oxygen molecules remaining after oxidizing hydrogen, carbon, Mg, Al, etc. to produce H_2O, CO_2, MgO_2, Al_2O_3, etc. If excess oxygen molecules remain after the oxidation reaction, the oxidizer is said to have a "positive" oxygen balance. If the oxygen molecules are completely consumed and excess fuel molecules remain, the oxidizer is said to have a "negative" oxygen balance.

Let us consider the reaction of an oxidizer composed of $C_aH_bN_cO_dCl_eS_f$, represented by

$$C_aH_bN_cO_dCl_eS_f \rightarrow$$

$$aCO_2 + 1/2(b-e)H_2O + c/2N_2 + eHCl + fSO_2 - \{(a+f) + 1/4(b-e) - d/2\}O_2$$

The oxygen balance expressed in mass percent is given by

$$[OB] = -\{(a+f) + 1/4(b-e) - d/2\} \times 32/(\text{molecular mass of material}) \times 100\ (\%)$$

For example, NG produces excess oxygen molecules as a combustion product:

$$C_3H_5N_3O_9 \rightarrow 3\ CO_2 + 5/2\ H_2O + 3/2\ N_2 + 1/4\ O_2$$

The oxygen balance of NG is given by

$$[OB]_{NG} = +\ 1/4 \times 32/227 \times 100 = +\ 3.52\,\%$$

The oxygen balance of any mixtures of any type of oxidizer can be obtained by assuming the oxidized products. Table 4-4 also shows the oxygen balance of oxidizers [OB] and the density ρ of energetic materials.

Table 4-4. Oxygen balance and density of energetic materials.

Material	*[OB] (%)*	*ρ (kg/m^3)*
NG	+3.5	1590
NC	–28.7	1670
DEGDN	–40.8	1380
TEGDN	–66.7	1340
TMETN	–34.5	1470
DBP	–224.2	1050
TA	–139.0	1150
AP	+34.0	1950
NP	+71.5	2220
AN	+20.0	1720
ADN	–4.4	1720
HNF	+25.0	1860
NQ	–30.7	1710
TAGN	–33.5	1500
HMX	–21.6	1900
RDX	–21.6	1820
CL-20	–11.0	2040
Ammonium picrate	–52.0	1720
Diazodinitrophenol	–60.9	1630
Diethyleneglycol	–40.8	1380
Nitroglycol	0	1480
NIBGTN	0	1680
NM	–39.3	1140
Hydrazine nitrate	+8.6	1640
PETN	–10.1	1760
TNT	–73.9	1650
Trinitroanisol	–62.5	1610
TNB	–56.3	1760
TNChloroB	–45.3	1800
Methyl nitrate	–10.4	1220
Tetryl	–47.4	1730
Picric acid	–45.4	1770
Lead azide	–5.5	4600

4.1.3
Thermodynamic Energy

The chemical energy generated by the combustion of energetic materials is converted to thermodynamic energy used for propulsion and explosion. As described in Chapter 2, the chemical energy is determined by the chemical structure of the molecules of the energetic materials. However, the thermodynamic energy is determined by the conversion of the heat and combustion products to pressure as described in Chapter 1. The characteristic velocity c^* defined in Eq. (1.74), the specific impulse I_{sp} defined in Eq. (1.76), and the heat of explosion H_{exp} defined in Eq. (2.2) are used to evaluate the thermodynamic energy potential of materials. It is shown that c^* is used to evaluate the energetics in rocket motor, I_{sp} is used to evaluate the overall energetics including the nozzle expansion process, and H_{exp} is used to evaluate the enthalpy potential. In addition, the ratio of the combustion temperature T_g and the molecular mass of the combustion products M_g, defined as $\Theta = T_g/M_g$, is also used to evaluate the energetics of the materials.

Though the thermodynamic energy of propellants and explosives is not determined by the thermodynamic energy of their individual components, it is important to recognize the thermochemical properties through the thermodynamic energy of each component. Table 4-5 shows T_g, M_g, Θ, I_{sp} and the combustion products of the major components used for propellants and explosives obtained by the NASA program computations.[10]

Table 4-5. Thermochemical properties of energetic chemicals (10 MPa).

	T_g K	M_g kg/kmol	Θ kmol K/kg	I_{sp} s
NC (12.6 %N)	2600	24.7	105	233
NG	3300	28.9	114	247
TMETN	2910	23.1	126	256
TEGDN	1390	19.0	73	186
DEGDN	2520	21.8	116	244
AP	1420	27.9	51	160
AN	1260	22.9	55	164
ADN	2060	24.8	83	206
HNF	3120	26.4	118	265
CL-20	3640	27.5	132	281
NP	610	36.4	17	88
RDX	3300	24.3	136	269
HMX	3290	24.3	135	269
TAGN	2310	18.6	124	251

	Major combustion products (moles/mol)								
	O_2	H_2O	CO	O_2	H_2	N_2	OH	HCl	Cl_2
NC (12.6 %N)		0.225	0.147	0.128	0.116	0.111			
NG	0.069	0.280	0.107	0.275	0.014	0.181	0.041		
TMETN		0.263	0.357	0.096	0.140	0.136			
TEGDN		0.110	0.397	0.063	0.335	0.079			
DEGDN		0.253	0.365	0.079	0.190	0.111			
AP	0.287	0.377				0.119		0.197	0.020
NP	0.750					0.125			0.125
AN	0.143	0.571				0.286			
RDX		0.226	0.246	0.082	0.089	0.326			

Table 4-5. Continued.

	Major combustion products (moles/mol)								
	O_2	*H_2O*	*CO*	*O_2*	*H_2*	*N_2*	*OH*	*HCl*	*Cl_2*
HMX		0.227	0.246	0.082	0.089	0.326			
TAGN		0.209	0.098	0.013	0.290	0.389			
HNF	0.098	0.337	0.002	0.125		0.348	0.003		
ADN	0.196	0.339				0.397			
CL-20	0.018	0.137	0.235	0.142	0.028	0.367	0.033		

4.2
Crystalline and Polymeric Materials

4.2.1
Physicochemical Properties of Crystalline Materials

Since the energy density of materials is determined by the intermolecular structure, the energy density of polymeric materials is limited because of the role of chemical bonds which produce elongation properties between atoms. Furthermore, the density of polymeric materials is also limited by the molecular structures. On the other hand, the density of crystalline materials is high because of the three-dimensionally arranged atoms in the molecular structures. The distance between atoms in the crystals is short to form a crystalline structure, which makes the bond energy between atoms high. The different properties of polymeric materials and crystalline mixtures makes high energy density materials used for propellants or explosives. Thus, the choice of polymeric materials and crystalline materials becomes a key element in formulating high-energy propellants or explosives.

The polymeric materials that act as fuels and oxidizers are composed of atoms of nitrogen, oxygen, carbon, and hydrogen. The hydrocarbon structures act as fuel components, and the oxidizer fragments of $–C–NO_2$, $–O–NO_2$, $–O–NO$, or $–N–NO_2$ are attached to the hydrocarbon structure with covalent chemical bonds.

The polymeric materials composed of hydrocarbon structures and nitrogen triple bonds in the shape of $–N=N^-=N^+$ are azide polymers. Azide polymers generate heat when thermally decomposed. The bond breakage of the nitrogen triple bonds forms nitrogen gas and produces heat simultaneously. The chemical bond energy between two nitrogen atoms, $N\equiv N$, is very high, producing energy from the triple bonds. Thus, the azide polymers produce heat without oxidation reactions. As shown in Table 4-3, a higher H_{exp} is obtained by the materials containing higher nitrogen concentrations.

Crystalline materials used as oxidizer components of propellants and explosives decompose thermally to produce gaseous fragments which act as oxidizer fragments. On the other hand, hydrocarbon polymers used as fuel components such as polyurethane and polybutadiene decompose endothermically and generate hydrogen, solid carbon, and other hydrocarbon fragments which act as fuel fragments. The mixtures of the hydrocarbon polymers and the crystalline materials are energetic materials which are gasified by heating and generate both fuel and oxidizer fragments simultaneously. These fragments react exothermically and produce high temperature combustion products. The combustion process of the energetic materials is dependent on various physical and chemical characteristics such as the individual properties of both fuel and oxidizer components, their mixture ratio, particle size of crystalline oxidizers, additives as catalysts and modifiers, and also combustion pressure and initial temperature.

Typical crystalline materials used as oxidizer components are divided into perchlorates, nitrates, nitro-compounds, nitramines, and metal azides. The polymeric materials used as fuel components are divided into nitrate esters, inert polymers, and azide polymers. The combinations of these oxidizer and fuel components give the desired ballistic characteristics of propellants or explosives.

4.2.1.1 **Perchlorates**

The perchlorates used for propellants and explosives are ammonium perchlorate (AP: NH_4ClO_4), nitronium perchlorate (NP: NO_2ClO_4), and potassium perchlorate (KP: $KClO_4$). AP is the major crystalline oxidizer used for composite rocket propellants. The oxygen molecules produced by the decomposition act as an oxidizer when AP particles are mixed with a polymeric fuel component, for example,

$$NH_4ClO_4 + C_mH_n \text{ (hydrocarbon polymer)} \rightarrow CO_2 + H_2O + N_2 + HCl$$

This reaction produces significant amounts of heat and gaseous molecules, which yields high I_{sp}, defined in Eq. (1.76).

Though AP is relatively stable under mechanical shocks, it detonates with a velocity of 3400 m/s when an excess shock is given. A mixture of AP and ammonium nitrate (AN) with a small amount of silicon iron is used as an industrial explosive.

The oxygen concentration in NP is higher than that in other crystalline materials. Thus, the chemical potential as an oxidizer is high when it is combined with a fuel component. Since the theoretical density is 2220 kg/m^3 and the heat of formation is positive, +33.6 kJ/mol, NP is an ideal material as an oxidizer. However, NP is extremely hygroscopic, and hydrolysis forms nitric acid and perchloric acid:

$$NO_2ClO_4 + H_2O \rightarrow HNO_3 + HClO_4$$

NO_2 is formed by the thermal decomposition of NP at about 360 K, which is too low to use it as a practical oxidizer ingredient.

KP is a well-known oxidizer component of pyrolants. Since KP produces potassium oxides and condensed products, the high molecular mass M_g of the combustion products is not favorable for its use as an oxidizer of rocket propellants. A mixture of 75 % $KClO_4$ with 25 % asphalt pitch was used as a rocket propellant named Galcit, and was the original composite propellant used in the 1940s. Though potassium chlorate ($KClO_3$) is also a crystalline oxidizer and has a lower oxygen balance compared with that of KP, $KClO_3$ is more sensitive to mechanical shock and easy to ignite, and is also easy to detonate.

4.2.1.2 **Nitrates**

Typical crystalline nitrates used for propellants and explosives are ammonium nitrate (AN: NH_4NO_3), potassium nitrate (KN: KNO_3), sodium nitrate (SN: $NaNO_3$), pentaerythritol tetranitrate (PETN: $C_5H_8(ONO_2)_4$), and triaminoguanidine nitrate (TAGN: $CH_9N_7O_3$).

Disadvantages of the use of AN in rocket propellants include hygroscopicity and crystal structure transitions at 398 K, 357 K, 305 K, and 256 K. The volumetric changes caused by these transitions affect internal mechanical stresses of the propellant grain, which sometimes damages the grain under temperature cycling conditions. During the propellant processing, humidity control cannot be avoided because of the hygroscopicity. On the other hand, the hygroscopicity and crystal phase transitions give no limitation of the use of AN for dynamites, emulsion explosives or slurry explosives.

Though the oxidation potentials of KN and SN are high, both metal nitrates generate high-M_g combustion products. Thus, the specific impulse becomes low when KN or SN is used for rocket propellants. KN and SN are used as major ingredients of dynamites or pyrotechnics. KN is a well-known material as a major component of black powder.

Unlike other crystalline nitrates, PETN is a crystalline nitrate ester similar to NG and NC. Though PETN is one of the most powerful explosives, no excess oxidizer fragments are formed when it decomposes. Thus, PETN is not used as an oxidizer of propellants.

TAGN contains a relatively high mole fraction of hydrogen, and the oxidizer fragment (HNO_3) of TAGN is attached by an ionic bond in the molecular structure. The molecular mass of the combustion products of TAGN is low because of the high concentration of hydrogen.

4.2.1.3 **Nitro-compounds**

The energetic materials containing –C–NO_2 bonds in their molecular structures are nitro-compounds. Similar to nitrate-compounds, when nitro-compounds are decomposed thermally, NO_2 molecules are formed and act as an oxidizer component. The NO_2 molecules react exothermically with other remaining hydrocarbon fragments and generate a large number of high temperature combustion products. Typical nitro-compounds used for explosives are dinitrotoluene (DNT: $C_7H_6N_2O_4$), trinitrotoluene (TNT: $C_7H_5O_6N_3$), hexanitrostilbene (HNS: $C_{14}H_6O_{12}N_6$), diaminotrinitrobenzene (DATB: $C_6H_5O_6N_5$), triaminonitrobenzene (TATB: $C_6H_6O_6N_6$), diazodinitrophenol (DDNP: $C_6H_2O_5N_4$), hydrazinium nitroformate (HNF: $N_2H_5C(NO_2)_3$), hexanitrobenzene (HNB: $C_{12}H_4N_8O_{12}$), trinitro-2,4,6-phenylmethylnitramine (Tetryl: $C_7H_5O_8N_5$), and 2,4,6-trinitrophenol (Picric acid: $C_6H_3N_3O_7$). The computational molecular design predicts several possible high-energy-density nitro-compounds such as octanitrocubane and tetranitrotetraazacubane.

In general, the energy density of nitro-compounds is high and the sensitivity of detonatability is also high. Thus, nitro-compounds are used as major components of explosives, but not of propellants.

4.2.1.4 **Nitramines**

Nitramines are characterized by –N–NO_2 chemical bonds that are attached to hydrocarbon structures. The bond breakage of N–N produces NO_2, which acts as an oxidizer. The remaining hydrocarbon fragments act as fuel components. Typical nitramines are cyclo-1,3,5-trimethylene-2,4,6-trinitramine (RDX: $C_3H_6O_6N_6$), cyclo-1,3,5,7-tetramethylene-2,4,6,8-tetranitramine (HMX: $C_4H_8O_8N_8$), nitroguanidine (NQ: $CH_4N_4O_2$), hexanitro hexaaza isowurtzitane (CL-20: $(NNO_2)_6(CH)_6$), ammonium dinitramide (ADN: $NH_4N(NO_2)_2$). Some other high-energy density nitramines such as hexanitro hexaaza wurtzitane (HNHAW) and hexanitro hexaaza adamantane (HNHAA) are predicted by a computational molecular design as ingredients of propellants and explosives.

RDX and HMX are known as hexogen and octogen, respectively. The physicochemical properties of RDX and HMX are shown in Tables 4-1, 4-3, and 4-4. Though the density, heat of formation, and heat of explosion are approximately the same for both RDX and HMX, the melting point of HMX is much higher than that of RDX. RDX was synthesized to gain higher energy density than nitroglycerin in order to improve explosive power, and was named from "Research and Development eXplosive". HMX was synthesized to give a higher melting point than that of RDX, and was named "High Melting point eXplosive".

The chemical compositions of RDX and HMX are stoichiometrically balanced when CO, not CO_2, is assumed to be formed as the combustion product:

$$\text{RDX:}\quad C_3H_6O_6N_6 \rightarrow 3\,CO + 3\,H_2O + 3\,N_2$$

$$\text{HMX:}\quad C_4H_8O_8N_8 \rightarrow 4\,CO + 4\,H_2O + 4\,N_2$$

Though the adiabatic flame temperature is 3300 K for RDX and 3290 K for HMX at 10 MPa and no excess oxidizer fragments are produced. Thus, RDX and HMX are not used as oxidizers of propellants.

The overall initial decomposition reaction of HMX is represented by

$$3\,(CH_2NNO_2)_4 \rightarrow 4\,NO_2 + 4\,N_2O + 6\,N_2 + 12\,CH_2O$$

NO_2 and N_2O act as oxidizers and CH_2O acts as fuel component. Since nitrogen dioxide reacts quite rapidly with formaldehyde, the gas phase reaction

$$7\,NO_2 + 5\,CH_2O \rightarrow 7\,NO + 3\,CO + 2\,CO_2 + 5\,H_2O$$

is probably the dominating reaction, being immediately followed by the decomposition reaction. The reaction product NO oxidizes the remaining fuel fragments such as H_2 and CO. However, the oxidation reaction by NO is reported to be slow to produce the final combustion products. The dominating gas phase reaction, determining the burning rate of HMX, is the oxidation reaction by NO_2. A similar combustion process is considered for RDX.

Nitroguanidine (NQ) is a nitramine compound containing one N–NO_2 group in its molecular structure. Unlike cyclic nitramines such as HMX and RDX, the density is not high and the heat of explosion is also not high. However, the M_g of the combustion products is low because of the high mass fraction of H_2 contained within NQ. The addition of NQ particles within a double-base propellant forms a composite propellant termed a triple-base propellant, and is used as a gun propellant.

The molecular structure of ADN is given by $NH_4N(NO_2)_2$, i.e. an ionically bonded positive ionic ammonium group, NH_4^+, and negative ionic dinitramide group, $-N(NO_2)_2^-$ group. Since the oxygen concentration of ADN is relatively high, ADN is used as an oxidizer component of rocket propellants. Though ADN is a crystalline and high-oxygen-concentration material similar to AP and KP, it contains no halogen or metal atoms within the molecular structure, similar to AN. Thus, ADN is used as an oxidizer of smokeless composite propellants. The melting point is about 364 K, accompanied by the latent heat of melting. The onset temperature of the exothermic decomposition is about 432 K, and the reaction is ended at about 480 K without residues. The activation energy for the exothermic decomposition process ranges between 117 kJ/mol and 151 kJ/mol.

4.2.1.5 **Metal Azides**

Lead azide ($Pb(N_3)_2$), sodium azide (NaN_3), and silver azide (AgN_3) are azides of metals. Since these metal azides are very sensitive to mechanical shock and easy to detonate, these are used as pyrolants for initiators and igniters of propellants and explosives.

4.2.2
Physicochemical Properties of Polymeric Materials

Polymeric materials are used as binders to adhere solid particles to each other to formulate composite explosives or composite propellants. The polymeric materials are also used as a part of the fuel ingredients when the crystalline particles are oxidizer-rich. Various types of hydrocarbon polymers are used for polymeric binders.

The viscosity of the polymeric binders is required to be relatively low during the mixing process with crystalline particles in order to attain a uniformly dispersed structure. The curing time is long enough to enable homogeneous mixing to occur. In addition, the elasticity after curing is high enough to give high mechanical strength and elongation characteristics of composite explosives and propellants.

Three types of polymeric materials are used: inert polymers, active polymers, and azide polymers. No exothermic heat is produced when inert polymers are decomposed thermally. On the other hand, exothermic reaction occurs when active polymers and azide polymers are decomposed thermally. Self-sustaining burning is possible when active polymers and azide polymers are ignited.

4.2.2.1 **Nitrate Esters**

Nitrate esters are characterized by the $-O-NO_2$ bonds in their structures. Typical nitrate esters used for propellants and explosives are nitrocellulose (NC), nitroglycerin (NG), triethyleneglycol dinitrate (TEGDN), trimethylolethane trinitrate (TMETN), and diethyleneglycol dinitrate (DEGDN). These nitrate esters are all liquid at room temperature and are used as energetic plasticizers to formulate propellants and explosives. The thermal decomposition of nitrate esters occurs by bond breakage of O–NO_2 and produces NO_2 gas[2]. The remaining hydrocarbon structures are also decomposed and produce aldehydes and other fuel fragments that are oxidized by the NO_2 gas. This oxidation reaction is highly exothermic and generates high temperature combustion products.

NC is an energetic nitropolymer consisting of a hydrocarbon structure with –O–NO_2 bonds as oxidizer fragments. In general, NC is produced from the cellulose, $\{C_6H_7O_2(OH)_3\}_n$, of cotton or wood, which is nitrated using nitric acid (HNO_3) to produce –O–NO_2 groups in the structure.

$$\{C_6H_7O_2(OH)_3\}_n + x\ HNO_3 \rightarrow (C_6H_7O_2)_n(OH)_{3n-x}(ONO_2)_x + x\ H_2O$$

Through this nitration, –OH contained within the cellulose is replaced by –O–NO_2, and the degree of nitration determines the energy content to form high temperature combustion gases. The maximum nitration is obtained when the nitrogen mass becomes 14.14 % within NC. The energy density of NC varies according to the degree of nitration of the cellulose. The nitrogen percentage of NC used as a conventional ingredient of propellants and explosives ranges from 13.3 % N to 11.0 % N. The NC molecule containing 12.6 % N, is represented by $C_{2.20}H_{2.77}O_{3.63}N_{0.90}$, whose heat of formation is $\Delta H_f = -2.60$ MJ/kg. The heat of formation decreases as the degree of nitration decreases, as shown in Table 4-6.

Table 4-6. Heat of formation of nitrocellulose.

% N	13.3	13.0	12.5	12.0	11.5	11.0
ΔH_f (MJ/kg)	–2.39	–2.48	–2.61	–2.73	–2.85	–3.01

NC decomposes by an autocatalytic reaction which evolves NO_2 gas due to the breakage of the weakest bond of –O–NO_2. The reaction between 363 K and 448 K is first order and the activation energy is 196 kJ/mol. The remaining fragments form aldehydes such as HCHO and CH_3CHO. The reaction between NO_2 and aldehydes produces heat and combustion gases.

NG has a relatively low molecular mass, 227.1 kg/kmol, is liquid at room temperature, and becomes a solid state below 286 K[1,2]. Since NG is shock sensitive and easy to detonate, desensitizers are admixed for practical applications. NG is one the major ingredients used for propellants and explosives. Typical examples are double-base propellants mixed with nitrocellulose, and dynamites mixed also with nitrocellulose and/or other crystalline materials. The autocatalytic decomposition of NG, occuring at 418 K, is caused by the bond breakage of –O–NO_2 and evolves NO_2 with an activation energy of 109 kJ/mol. The self-ignition occurs after a critical concentration of NO_2 is achieved at 491 K.

Though nitroglycerin (NG) is a liquid nitrate ester but not a nitropolymer, NG becomes a polymeric material when mixed with plasticizers. Similar to NC, NG is a hydrocarbon structure with –O–NO_2 bonds as oxidizer fragments. The thermal decomposition of NG is fundamentally the same as that of NC, producing NO_2 gas as an oxidizer and aldehydes as fuel components.

4.2.2.2 **Inert Polymers**

Various types of polymers are used to formulate propellants and explosives. The nature of polymers is identified by their chemical bond structure. Two types of copolymers are used to formulate modern propellants and explosives: (1) polyurethane copolymer and (2) polybutadiene copolymer. The chemical bond structures of polyether and polyester are used for polyurethane copolymers. Since the molecular concentration of oxygen is relatively high for polyurethane binder, this class of binder is used to achieve high combustion efficiency with low oxidizer concentration of crystalline materials. On the other hand, the heat of formation of polybutadiene copolymer is high and the molecular concentration of oxygen is low when compared with polyurethane copolymer. This class of binder is used to achieve a high combustion temperature when mixed with crystalline oxidizer particles.

Polybutadiene acrylonitrile (PBAN) is used as the binder of the large booster propellant of the Space Shuttle. Carboxy-terminated polybutadiene (CTPB) and hydroxy-terminated polybutadiene (HTPB) are widely used for modern composite propellants. CTPB and HTPB form a regularly distributed matrix of polymers through a crosslinking reaction. For example, HTPB polymer, $HO–(CH_2–CH=CH–CH_2)_n–OH$, is cured with isophorone diisocyanate (IPDI) to form a polymeric binder. Using this binder, a high loaded density of oxidizer particles is obtained. In order to achieve a superior mechanical property of the propellant grain, a small amount of bonding agent is added to adhere each oxidizer particle to the binder.

Hydroxy-terminated polyester (HTPS) is made of diethylene glycol and adipic acid, and hydroxy-terminated polyether (HTPE) is made of propylene glycol. Hydroxy-terminated polyacetylene (HTPA) is synthesized from butynediol and paraformaldehyde and characterized by acetylenic triple bonds. The terminal OH groups of these polymers are cured with isophorone diisocyanate. Table 4-7 shows the chemical properties of typical polymers used for composite propellants and explosives. All polymers are inert but, except for HTPB polymer, contain relatively high concentrations of oxygen in their molecular structures.

Table 4-7. Chemical properties of polymers used in propellants and explosives.

Polymer	*Chemical formula*	$\xi(O)$	ΔH_f
HTPS	$C_{4.763}H_{7.505}O_{2.131}N_{0.088}$	34.1	–0.550
HTPE	$C_{5.194}H_{9.840}O_{1.608}N_{0.194}$	25.7	–0.302
HTPA	$C_{4.953}H_{8.184}O_{1.843}N_{0.205}$	29.5	–0.139
HTPB	$C_{7.075}H_{10.65}O_{0.223}N_{0.063}$	3.6	–0.058

$\xi(O)$: Oxygen concentration, % by mass
ΔH_f: Heat of formation (298 K), MJ/mol

Polyether prepolymer:
$H{-}(O{-}CH(CH_3){-}CH_2)_n{-}O{-}CH_2{-}CH(CH_3){-}O{-}(CH_2{-}CH(CH_3){-}O)_n{-}H \quad n = 17$
Polyester prepolymer:

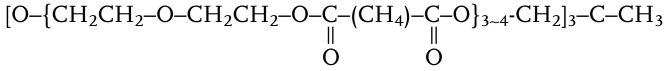

$$[O{-}\{CH_2CH_2{-}O{-}CH_2CH_2{-}O{-}\underset{\underset{O}{\|}}{C}{-}(CH_4){-}\underset{\underset{O}{\|}}{C}{-}O\}_{3\sim4}{-}CH_2]_3{-}C{-}CH_3$$

4.2.2.3 **Azide Polymers**

The materials containing $-N{=}N^- = N^+$ bonds are azides, which produce nitrogen gas accompanied by a significant amount of heat when they are thermally decomposed. Polymeric materials consisting of hydrocarbon structures with $-N{=}N^- = N^+$ bonds are azide polymers characterized by $-N_3$ attached to carbon atoms. Glycidyl azide

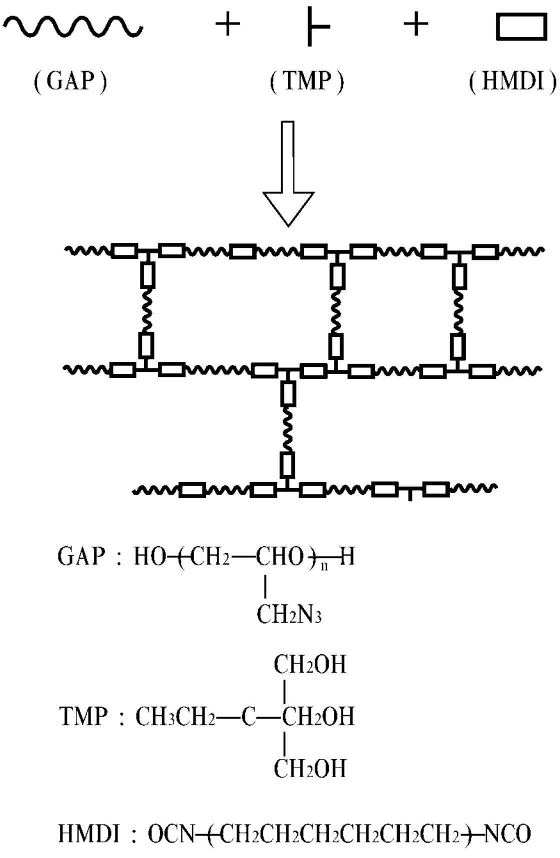

Figure 4-1. Copolymerization process of glycidyl azide polymer.

polymer (GAP: $C_3H_5ON_3$), bis-azide methyl oxetane (BAMO: $C_5H_8ON_6$), 3-azidomethyl-3-methyl oxetane (AMMO: $C_5H_9ON_3$) are typical energetic azide polymers which are used as active binders of propellants and explosives.[4,8,9,11–15]

The decomposition of $-N_3$ bonds within azide polymers generates a significant amount of heat without oxidation reaction by oxygen atoms. The bond breakage of $-N_3$ is an initial step of the reaction accompanied by melting and gasification processes. The formation of gaseous fragments occurs on heating, and numerous chemical species are formed from the reacting surface of the azide polymers. The heat transfer process from the high temperature zone to the reacting surface determines the burning rate of azide polymers.

GAP is synthesized by replacing C–Cl bonds of polyepichlorohydrin with $C-N_3$ bonds[14]. The three nitrogen atoms in the N_3 are attached linearly with ionic and covalent bonds in every GAP monomer unit. The bond energy of N_3 is reported to be 378 kJ per azide group. Since GAP is a liquid at room temperature, it is polymerized to form GAP copolymer by reaction of the terminal –OH groups with hexamethylene diisocyanate (HMDI) and crosslinking with trimethylolpropane (TMP), as shown in Fig. 4-1. The physicochemical properties of GAP prepolymer and GAP copolymer are shown in Tables 4-8 and 4-9, respectively[14].

Table 4-8. Chemical properties of GAP prepolymer.

Chemical formula	$C_3H_5ON_3$
Molecular mass	1.98 kg/mol
Heat of formation at 293 K	0.957 MJ/kg
Flame temperature at 5 MPa	1470 K

Table 4-9. Physicochemical properties of GAP copolymer.

Chemical formula				$C_{3.3}H_{5.6}O_{1.12}N_{2.63}$		
Molecular mass				1.27 kg/mol		
Flame temperature at 5 MPa				1370 K		
Combustion products (mole fractions) at 5 MPa						
N_2	$C_{(s)}$	CO	CO_2	CH_4	H_2	H_2O
0.190	0.298	0.139	0.004	0.037	0.315	0.016

The adiabatic flame temperature of the GAP copolymer is 1370 K at 5 MPa, and large amounts of $C_{(s)}$, H_2, and N_2 are formed as combustion products which are mostly fuel components like $C_{(s)}$, CO, and H_2, and very small amounts of CO_2 and H_2O are formed.

BAMO polymer has two N_3 bonds in every BAMO monomer unit. As shown in Table 4-10, the heat of formation of BAMO is positive, and the adiabatic flame temperature is higher than that of GAP. BAMO monomer is synthesized by replacing C–Cl bonds of 3,3-bis (chloromethyl) oxetane (BCMO) by $C-N_3$ bonds[15]. The molecular mass distribution of the BAMO polymer is distributed in the range 300 to 5 × 10^5, and the main peak is $M_n = 9600$ and $M_w = 26700$ ($M_w/M_n = 2.8$), where M_n is the number-averaged molecular mass and M_w is the mass-averaged molecular mass[15].

Table 4-10. Heat of formation and flame temperature of BAMO prepolymer.

Chemical formula	$(C_5H_8N_6O)_n$
Heat of formation at 293 K	2.46 MJ/kg
Flame temperature at 10 Mpa	2020 K

Since BAMO polymer is a solid at room temperature, it is copolymerized with tetrahydrofuran (THF) in order to form a liquid BAMO copolymer. The terminal OH groups of BAMO-THF copolymer are cured with the NCO groups of hexamethylene diisocyanate (HMDI) and crosslinked with trimethylolpropane (TMP). The energy density of BAMO copolymer is defined as the energy contained within the unit mass of BAMO copolymer. The physicochemical properties of BAMO copolymer are shown in Table 4-11[15].

Table 4-11. Physicochemical properties of BAMO copolymer

Chemical formula	$HO{-}(C_5H_8N_6O)_n{-}(C_4H_8O)_m{-}H$
Molecular mass	2.24 kg/mol (n= 10.4, m= 6.9)
Density	1270 kg/m^3
Heat of formation at 293 K	1.19 MJ/kg
Flame temperature at 10 MPa	1520 K

4.3
Classification of Propellants and Explosives

Propellants and explosives are both composed of high energetic materials to produce high temperature gaseous products. Propellants are used to provide propulsive forces, and explosives are used to provide destructive forces through combustion phenomena. When propellants and explosives are burned in a vessel, the gaseous products in the vessel generate a high pressure which is converted into a propulsive force or a destructive force. Though the energetics of both propellants and explosives are fundamentally the same, the combustion phenomena are different because of the difference in the heat release processes. Propellants burn in the region of the deflagration branch IV and explosives burn in the region of the detonation branch I described in Chapter 3.

The energy produced by a unit volume, defined as the "energy density", is an important property for both propellants and explosives. For rocket and gun propulsions, the aerodynamic drag during flight in the atmosphere increases as the cross-sectional area of these projectiles increases. The reduction in cross-sectional area is favored by reduction of the size of the combustion chamber of the projectiles and by increase in the density of the propellant used. In other words, high energy density is required to gain high volumetric propulsive force.

On the other hand, a high pressure build-up in a closed vessel or an open vessel is required for explosives. When the shell wall of a closed vessel is burst by the pressure, a large number of the shell wall fragments are formed when the rate of pressure rise is high enough to give non-ductile destruction of the shell wall. This fragment formation process is used for bomb and warhead explosions. When explosives are burst in a drilled hole in a rock, high pressure generated in the hole breaks the rock into a large number of small pieces or several blocks. These destructive processes are applied to blasting processes in mines.

When an energetic material burns slowly in a closed shell accompanied by a deflagration wave, not a detonation wave, the shell does not burst until the pressure reaches the limit of the breakage strength of the shell wall. When the shell wall is designed to burst suddenly and to produce fragments, the shock wave generated by the pressure difference between the shell wall and the atmosphere propagates into the atmosphere. In this case, the energetic material behaves as an explosive even though the energetic material burns in the deflagration branch.

Though high pressure is generated when an energetic material burns and produces high temperature gas, the high temperature gas is not the only condition to generate high pressure. When the gas has low molecular mass, high pressure is generated even if the temperature is low, as described in Chapter 1. This is evident from the following example: the reaction between titanium and solid carbon to produce solid titanium carbide:

$$\mathrm{Ti} + \mathrm{C} \rightarrow \mathrm{TiC} + 184\ \mathrm{kJ/mol}$$

Here, the combustion temperature reaches about 3460 K without any pressure rise when the reaction takes place in a closed vessel. This is caused by the reaction occurring without producing gaseous products throughout the reaction. Thus, this class of energetic materials, the so-called “pyrolants”, cannot be used as propellants and explosives. However, the heat produced by pyrolants can be used, for example, to initiate the ignition of propellants or explosives. Thus, energetic materials are classified into two types: one to obtain both high temperature and low molecular mass for use as propellants or explosives, and the other to obtain high temperature and high molecular mass for use as pyrolants.

The materials used for propellants and explosives are classified into two types: (1) energetic materials consisting of chemically bonded oxidizer and fuel components in the same molecule, and (2) energetic composite materials consisting of physically mixed oxidizer and fuel components. Stoichiometrically balanced materials are chosen to obtain high heat release and low molecular mass combustion products. Nitropolymers consisting of nitro-groups and hydrocarbon structures are the energetic materials which produce oxidizer and fuel fragments when decomposed. NC is a typical nitropolymer used as a major component of nitropolymer propellants. Though NG is not a nitropolymer, it also consistes of nitro-groups and hydrocarbon structure and is used with NC to form nitropolymer propellants, the so-called double-base propellants. Double-base propellants are near-stoichiometrically balanced energetic materials and produce high temperature and low molecular mass combustion products. Figure 4-2 (a) shows a rocket flight assisted by the combustion of a double-base propellant. No smoke signature is seen from the rocket nozzle because the combustion products are mainly CO_2, CO, H_2O, and N_2.

The materials containing either excess oxidizer fragments or excess fuel fragments in their chemical structures are also used to formulate energetic composite materials. The mixture of an oxidizer-rich component and a fuel-rich component can form a stoichiometrically balanced material that is used for propellants and explosives. Though ammonium perchlorate (AP) produces oxidizer-rich fragments, the energy density is not high. Polymeric hydrocarbon materials are also low energetic materials. However, when AP particles and a hydrocarbon polymer are mixed together, a stoichiometrically balanced material named an AP composite propellant is formed. In order to increase the specific impulse, aluminum powders are added as a fuel component. Figure 4.2 (b) shows a rocket flight assisted by the combustion of an AP composite propellant. The white smoke signature is seen from the rocket nozzle because the combustion products are mainly HCl, Al_2O_3, CO_2, and H_2O. HCl generates white smoke when combined with H_2O (moisture) in the atmosphere.

The physicochemical properties of explosives are fundamentally equivalent to those of propellants. Explosives are also made of energetic materials such as nitropo-

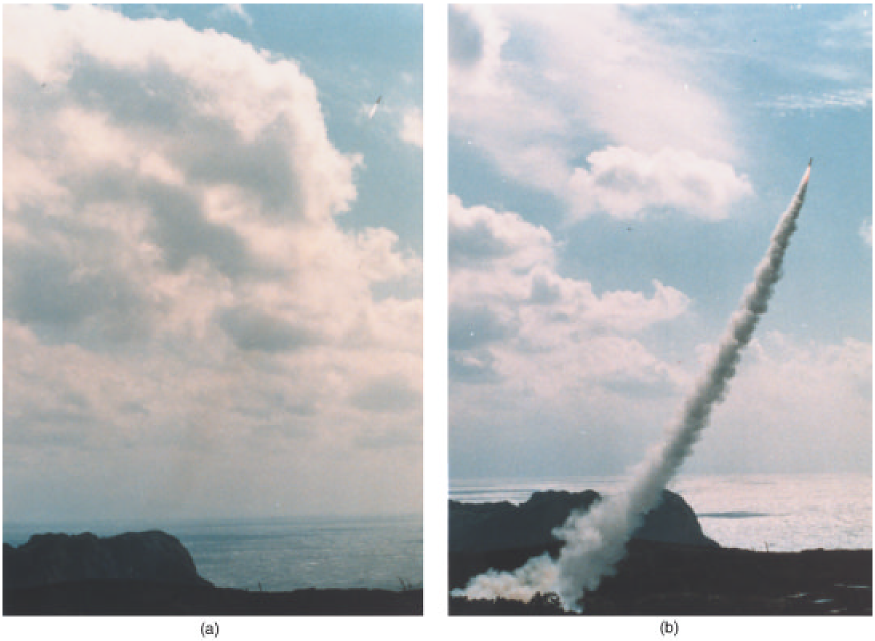
(a) (b)

Figure 4-2. Rocket flight trajectories assisted by (a) NC-NG double-base propellant and (b) aluminized AP composite propellant.

lymers and composite materials composed of crystalline particles and polymeric materials. TNT, RDX, and HMX are typical energetic crystalline materials used for explosives. Furthermore, when ammonium nitrate (AN) particles are mixed with an oil, an energetic explosive named ANFO (ammonium nitrate fuel oil) explosive is formed. AN with water is also an explosive used for industrial and civil engineering. The difference between the materials used for explosives and propellants is not evident. Explosives are used to initiate detonation by mechanical shock or high heat flux. There are no reasons not to detonate for even low energy density materials.

4.4
Formulation of Propellants

When fuel and oxidizer components are bonded chemically in the same molecules, the molecules are chosen to formulate an energetic material. Nitropolymers are composed of $O{-}NO_2$ groups and a hydrocarbon structure. The bond breakage of $O{-}NO_2$ produces NO_2, gaseous species that acts as an oxidizer fragment, and the remaining hydrocarbon structure acts as a fuel fragment. NC is a typical nitropolymer used as a major component of propellants. The propellants composed of NC are termed “nitropolymer propellants”.

Crystalline particles that produce gaseous oxidizer fragments are used as oxidizer components, and hydrocarbon polymers that produce gaseous fuel fragments are used as fuel components. The mixtures of these crystalline particles and hydrocarbon polymers form energetic materials that are termed “composite propellants”. Both oxidizer and fuel components produced at the burning surface of each component mix together to form a stoichiometrically balanced reactive gas in the gas phase.

The polymeric hydrocarbon acts also as a binder for each particle to bond to, forming a propellant grain. Ammonium perchlorate (AP) is a typical crystalline oxidizer and hydroxyl-terminated polybutadiene (HTPB) is a typical polymeric fuel. When AP and HTPB decompose thermally on the propellant surface, oxidizer and fuel gases are produced and diffuse each other, and then react to produce high temperature combustion gases.

An energetic material composed of granulated energetic grains is called a “granulated propellant”. Granulated propellants are used as gun propellants and pyrotechnics. For example, a mixture of crystalline potassium nitrate particles, sulfur, and charcoal forms an energetic granulated material known as black powder. Granulated NC grains are used as a single-base propellant for guns. The granulated single-base, double-base, or triple-base propellants are used as gun propellants. Though the linear burning rate (the burning velocity perpendicular to the propellant burning surface) of granulated propellants is not so high, the mass burning rate (mass generation rate from the entire burning surface of the grains) is very high because of the large burning surface area of the grains. The high mass burning rate of propellants is used for gun propulsion to create a short burn time and high pressure in the barrels. The burning time of granulated propellants in gun tubes is in the order of

10 ms to 100 ms. The mass burning rate of these grains is high because the web thickness is very small compared with that of rocket propellants, and the burning pressure is in the order of 100 MPa to 1000 MPa. Though the physical structures of single-base and double-base granulated grains are essentially homogeneous, these grains burn independently when they burn in combustion chambers. Thus, the flame structures appear to be heterogeneous in nature. The shape of each grain is designed to obtain an adequate pressure versus time relationship during burning.

The mechanical properties of propellants are important to the formulation of the desired propellant grains. During the pressure build-up process in a rocket motor such as during the ignition transient or unstable burning in the chamber or very high pressure (> 1 GPa) in gun tubes, very high mechanical stresses act on the grains. If the internal grain shape is complicated, increased chamber pressure causes a crack in the grain and increases the burning surface area. The increased burning surface area due to an unexpected crack increases the chamber pressure, which can cause a catastrophic explosion of the rocket motor or the gun tube. In general, mechanical properties of propellants are dependent on the environmental temperatures. Elongation properties of propellants become poor at low temperatures (approximately below 200 K). This causes in-depth crack formation when a mechanical stress acts on the grain at low temperatures. On the other hand, strength properties become poor at high temperatures (approximately above 330 K). This causes deformation of the grain when an external force such as acceleration force or gravitational force acts on the grain. Accordingly, the selection of propellant ingredients to form the propellant grain shape is not only dependent on the combustion performance but also the mechanical properties of the formed propellant grain. The design criteria of gun propellants are different from those of rocket propellants. The size and mass of each grain of gun propellants are much smaller than those of rocket propellants. The burning surface area per unit mass of propellant is much larger for gun propellants. Furthermore, the operational combustion pressure is in the order of 1 GPa for gun propellants and 1 – 10 MPa for rocket propellants.

4.5
Nitropolymer Propellants

4.5.1
Single-Base Propellants

Single-base propellants are made of NC that is gelatinized with ethyl alcohol or diethyl ether used as solvents. Small amounts of diphenylamine, $(C_6H_5)_2NH$, are also added as a chemical stabilizer of NC. In some cases, a small amount of K_2SO_4 or KNO_3 is mixed as a flame suppressor. Ethyl alcohol (C_2H_5OH) or diethyl ether ($C_2H_5OC_2H_5$) is mixed with the NC in order to make it soft and give an adequate size and shape of propellant grain. The grain is coated with carbon black to keep the surface smooth. Table 4-12 shows chemical composition, flame temperature, and combustion products of a typical single-base propellant.

Table 4-12. Physicochemical properties of a single-base propellant.

Composition (wt %)				***Temp. (K)***	***Combustion products (mole fractions)***				
NC	DNT	DBP	DPA	T_f	CO_2	CO	H_2O	H_2	N_2
85.0	10.0	5.0	1.0	1590	0.052	0.508	0.130	0.212	0.098

4.5.2
Double-Base Propellants

Double-base propellants are formed by the use of NC that is gelatinized with energetic nitrate esters such as NG, DEGDN, DEGDN, or TMETN. These liquid nitrate esters are used to produce a rigid gel network of plasticized NC and to form a double-base propellant whose physical structure is homogeneous. For example, liquid NG is absorbed by solid NC, making a homogeneous gelatinized material. Though both materials burn by themselves, the propellants composed of NC and NG maintain the desired grain shapes used for rockets and guns and generate the desired temperature and combustion products when they burn.

Dibutylphthalate (DBP), diethylphthalate (DEP), and triacetin (TA) are typical plasticizers and stabilizers used for double-base propellants. These chemicals are used to obtain superior characteristics of propellant grain formation, and to improve mechanical properties, shock sensitivities, and chemical stability. Several types of amines are used as anti-aging agents in double-base propellants. Amines are known to react with gaseous NO_2 which is generated by the bond breakage of the $O–NO_2$ of nitrate esters. This reaction prevents gas formation in the propellant grain and prevents mechanical destruction of the grain. A small amount of 2-nitrodiphenylamine (2NDPA) is commonly added to nitropolymer propellants. The heats of formation of DBP, TA, and 2NDPA are shown in Table 4-1.

4.5.2.1 **NC-NG Propellants**

Double-base propellant is known as smokeless propellant, and is used for guns and rockets. Two major ingredients are used to formulate double-base propellant grain: NC and NG. NG is also a nitrate ester characterized by the $–O–NO_2$ group, and is known as a high explosive. Since NG is liquid at room temperature, NG is absorbed by NC and acts to gelatinize NC to form double-base propellant grain. Table 4-13 shows the chemical ingredients and energetic properties of typical double-base propellants.

NC and NG have oxygen available in the form of $O–NO_2$, which is attached to the organic moiety (e.g., cellulose) from which they are derived. The physicochemical properties of double-base propellants such as energy density, mechanical properties and chemical stability depend on the fractions of NC, NG, stabilizers, plasticizers, and catalysts. Though the energy density is increased by increase in the fraction of NG, the mechanical properties are adverely affected and chemical stability is decreased.

Two types of production method are used to form double-base propellant grains used for rockets and guns: (1) an extrusion method using an external mechanical press and (2) a casting method using finely divided NC powders or NC-NG powders. The extrusion method is used for small grains (< 0.1 kg) for , e.g., guns and pyrotechnics. The casting method is used for large grains (> 1 kg) for, e.g., booster and sustainer rockets. The specific impulse I_{sp} of double-base propellant composed of NC and NG is shown in Fig. 4-3 as a function of the mass fraction of NG, ξ (NG). When ξ (NG) = 1.0, the theoretical maximum I_{sp} of 247 s is obtained at 10 MPa combustion with an ideal expansion process to 0.1 MPa. However, NG is a liquid at room temperature and sensitive to mechanical shock. Practical double-base propellants always need plasticizers and/or stabilizers to be mixed with NG. Since NG is a detonative explosive, ξ (NG) is approximately < 0.5 for conventional double-base propellants. Furthermore, various types of chemicals such as burning rate catalysts, modifiers, and anti-aging agents are added to NC-NG mixtures in order to obtain superior mechanical properties at high and low environmental temperatures and to improve burning rate characteristics.

The mechanical properties and shock sensitivities of double-base propellants are highly dependent on the mixture ratio of NC and NG. Though the specific impulse of double-base propellants increases as the concentration of NG increases, the strength of the propellant decreases. It becomes difficult to keep grain shape when ξ (NG) is as high as 0.6 at room temperature. When ξ (NG) decreases to < 0.4, the elongation properties of double-base propellants become poor. Thus, double-base propellants need to contain desensitizers, stabilizers, and chemicals to improve

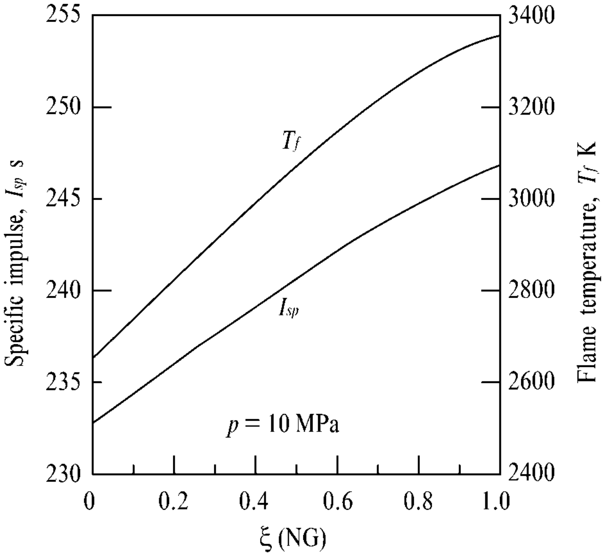

Figure 4-3. Specific impulse and adiabatic flame temperature of NC-NG double-base propellant as a function of the mass fraction of NG.

mechanical properties. In order to gain superior mechanical properties, plasticizers and stabilizers such as dibutylphthalate (DBP: $C_{16}H_{22}O_4$), triacetin (TA: $C_9H_{14}O_6$), ethyl centralite (EC: $CO\{N(C_6H_5)(C_2H_5)\}_2$), or diethylphthalate (DEP: $C_{12}H_{14}O_4$) are added. Typical chemical compositions and thermochemical properties of NC-NG double-base propellant are shown in Table 4-13.

4.5.2.2 **NC-TMETN Propellants**

Since NG is highly shock sensitive, other types of nitrate esters can be used to formulate non-NG double-base propellants. DEGDN, TEGDN, and TMETN are typical examples of energetic nitrate esters which can be replaced by NC. Though these nitrate esters are less energetic than NG, sensitivities to friction and mechanical shock are less than those of NG. Thus, the mass fraction of desensitizers is less than that used with NG during propellant formulation. The physicochemical properties of these nitrate esters are shown in Tables 4-1 to 4-6.

TMETN is liquid at room temperature, and the production process used for NC-NG propellants is used to produce NC-TMETN propellants. Though the energy density of TMETN is lower than that of NG, the shock sensitivity is lower than that of NG and no desensitizers are needed for NC-TMETN propellants. Instead of DEP or TA used as a low energy density plasticizer and stabilizer of NC-NG propellants, TMETN is mixed with TEGDN, which is a dinitrate ester and a relatively high-energy-density material. Thus, the overall energy density of double-base propellants composed of NC-TMETN is equivalent to more than that of NC-NG double-base propellants.

For comparison of NC-NG and NC-TMETN double-base propellants, both chemical compositions and thermochemical properties are listed in Table 4-13. Though the mass ratio of NC/NG (0.80) is much smaller than that of NC/TMETM (1.38), the combustion performance, such as T_f and M_g, appears to be equal, and Θ is 109 kmolK/kg for both propellants. In the case of rocket motor operation, I_{sp} and ρ_p are also approximately equivalent for both propellants.

Table 4-13. Chemical compositions and thermochemical properties of NC-NG and NC-TMETN double-base propellants (10 MPa).

	NC-NG	***NC-TMETN***
Ingredients	wt %	wt %
NC	39.6	53.8
NG	49.4	–
TMETN	–	39.1
DEP	10.0	–
TEGDN	–	7.0
EC	1.0	0.1
ρ_p kg/m^3	1550	1550
T_f K	2690	2570

Table 4-13. Continued.

	NC-NG	*NC-TMETN*
Thermodyamic energy		
M_g kg/kmol	24.6	23.6
Θ kmol K/kg	109	109
I_{sp} s	242	240
Combustion products	mol %	mol %
CO	39.7	39.8
CO_2	12.4	19.4
H_2	11.5	14.3
H_2O	23.8	23.6
N_2	12.4	11.8
OH	0.1	0.0
H	0.2	0.1

4.5.2.3 Nitro-Azide Propellants

Double-base propellants containing azide polymers are termed nitro-azide propellants. DEP used as a plasticizer in double-base propellants is replaced with azide polymers in order to increase the energy density. The compatibility of GAP prepolymer with NG is suitable for desensitizing the mechanical sensitivity of NG and gives superior mechanical properties of the rocket propellant grains formed.

Table 4-14 shows a comparison of the theoretical combustion properties of NC-NG-DEP and NC-NG-GAP propellants at 10 MPa. Though the molecular mass of the combustion products M_g remains relatively unchanged by the replacement of DEP by GAP, the adiabatic flame temperature is increased from 2557 K to 2964 K when 12.5 % of DEP is replaced by 12.5 % of GAP. Thus, the specific impulse I_{sp} is increased from 237 s to 253 s. The density of propellant ρ_p is also an important parameter for evaluating the thermodynamic performance of the propellant. The density is increased from 1530 kg/m^3 to 1590 kg/m^3 by the replacement of DEP with GAP. Since GAP is also compatible with DEP, double-base propellants composed of four major ingredients, NC, NG, DEP, and GAP, are also formulated.

Table 4-14. Chemical compositions and thermochemical properties of NC-NG-DEP and NC-NG-GAP propellants (10 MPa).

	NC-NG-DEP	*NC-NG-GAP*
Ingredients	wt %	wt %
NC	37.5	37.5
NG	50.0	50.0
DEP	12.5	–
GAP	–	12.5

Table 4-14. Continued.

		NC-NG-DEP	***NC-NG-GAP***
Thermodynamic energy			
ρ	kg/m^3	1530	1590
T_f	K	2560	2960
M_g	kg/kmol	24.0	25.0
Θ	kmol K/kg	107	118
I_{sp}	s	237	253
Combustion products		mol %	mol %
CO		41.5	33.7
CO_2		11.0	13.4
H_2		13.4	9.1
H_2O		22.2	25.9
N_2		11.9	16.9

4.5.2.4 **Chemical Materials of Double-Base Propellants**

Though the major components of double-base propellants are NC-NG or NC-TMETN, various additives such as plasticizers, burning rate modifiers, and combustion instability suppressants are also needed. Table 4-15 shows the materials used to formulate double-base propellants.

Table 4-15. Chemical materials used to form double-base propellants.

Plasticizer (oxidizer and fuel):	NG, TMETN, TEGDN, DNT
Plasticizer (fuel):	DEP, DBP, TA, PU
Stabilizer:	EC, 2NDPA, DPA
Plasticizer (energetic fuel):	GAP, BAMO, AMMO
Binder (fuel and oxidizer):	NC
Burning rate catalyst:	PbSa, PbSt, Pb2EH, CuSa, CuSt, LiF
Burning rate catalyst modifier:	C (carbon black, graphite)
Combustion instability suppressant:	Al, Zr, ZrC
Opacifier:	C (carbon black, graphite)
Flame suppressant:	KNO_3, K_2SO_4

4.5.3
Triple-Base Propellants

Triple-base propellants are made by the addition of crystalline nitroguanidine (NQ) within double-base propellants. Since NQ contains a relatively high mole fraction of hydrogen atoms within the molecular structure, the molecular mass of the combustion products becomes low even though the flame temperature becomes low.

Table 4-16 shows the chemical composition, adiabatic flame temperature and thermodynamic work at 10 MPa defined in Eq. (1.84) of a triple-base propellant (NC: 12.6 % N).

Table 4-16. Chemical compositions and properties of triple-base propellants.

Compositions (wt %)				***Flame temp. (K)***	***Thermodynamic work (MJ/kg)***
NC	NG	NQ	EC	T_f	f
28.0	22.8	47.7	1.5	3050	1.09

Figure 4-4 shows the thermodynamic energy f, defined in Eq. (1.84), of single-base, double-base, and triple-base propellants as a function of the combustion temperature, T_f. Though the f value of double-base propellants is high, T_f is also high. In order to suppress gun erosion, T_f is needed to be low. Triple-base propellants are formulated to reduce erosion and give f values as high as possible.

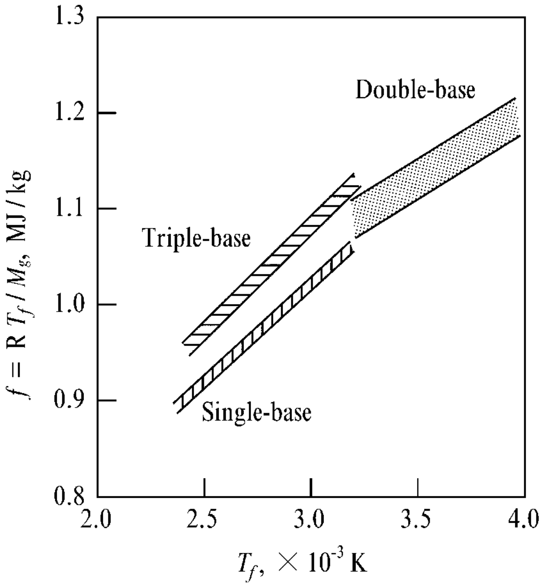

Figure 4-4. Thermodynamic energy of single-, double-, and triple-base propellants.

4.5.4
Composite Modified Double-Base Propellants

Instead of using NQ to formulate triple-base propellants, crystalline AP, HMX, or RDX particles are mixed with nitropolymers to form composite modified double-base (CMDB) propellants. A nitropolymer such as NC-NG or NC-TMETN double-base propellant acts as a base matrix to bond the crystalline particles within the propellant. Thus, the physical structure of CMDB propellants is heterogeneous, and the physicochemical properties are intermediate between composite and double-base propellants in nature, and are widely used because of their great potential in producing high specific impulse and flexibility of burning rate.

Typical crystalline-energetic-particles are AP and nitramines such as HMX and RDX. The use of AP leads to an AP-CMDB propellant and the use of HMX leads to an HMX-CMDB propellant. These particles burn as a monopropellant at the burning surface of the CMDB propellant, and the combustion products react again with the combustion products of the base matrix.

Figure 4-5 shows the adiabatic flame temperature and the specific impulse of AP-CMDB propellants as a function of the mass fraction of AP, ξ (AP) at 10 MPa. The base matrix of NC-NG propellant consists of NC/NG in the ratio = 0.5/0.5. The maximum T_f (3160 K) and I_{sp} (253 s) are obtained at ξ (AP) = 0.5.

Figure 4-6 shows the adiabatic flame temperature of the mixture of an NC-NG double-base propellant as a function of the mass fraction of HMX, ξ (HMX). The base matrix of double-base propellant is composed of NC/NG in the ratio = 0.2/0.8. Since HMX is a stoichiometrically energetic material, HMX acts as an energetic material, not an oxidizer. Accordingly, the flame temperature increases monotonously as ξ (HMX) increases.

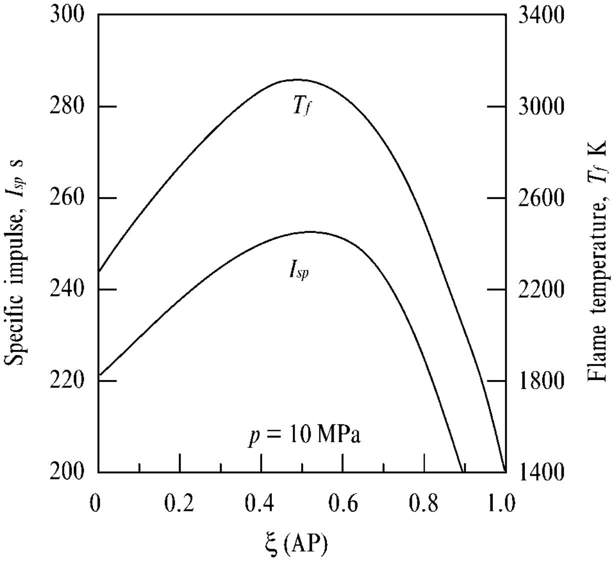

Figure 4-5. Specific impulse and adiabatic flame temperature of AP-CMDB propellant.

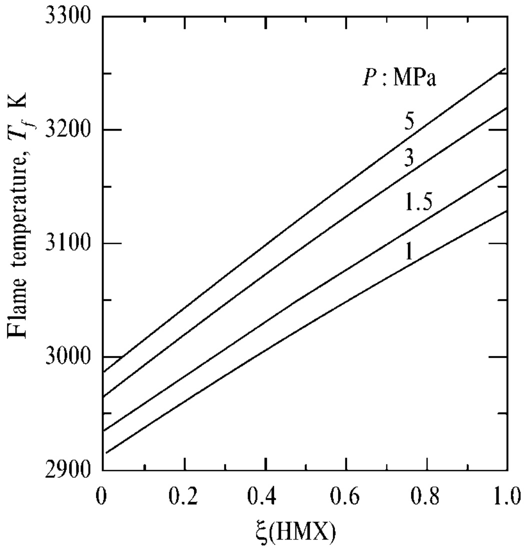

Figure 4-6. Specific impulse and adiabatic flame temperature of HMX-CMDB propellant.

4.6
Composite Propellants

Crystalline materials such as KNO_3, NH_4NO_3, and NH_4ClO_4 are used as oxidizers because of their high concentrations of oxygen atoms in the molecular structures. These materials generate high concentrations of gaseous oxidizing fragments when thermally decomposed. On the other hand, hydrocarbon-based polymeric materials such as polyurethane and polybutadiene generate high concentrations of gaseous fuel fragments when thermally decomposed. Both gaseous fragments diffuse into each other and react to generate heat and combustion products. Thus, the mixtures of crystalline materials and polymeric materials form combustible energetic materials whose physical structures are nonhomogeneous. Thus, the energetic materials are termed composite or heterogeneous propellants. Accordingly, the ballistic properties such as burning rate and pressure sensitivity are not only dependent on the chemical ingredients of oxidizer and fuel, but also the shape and size of the oxidizer particles.

The mechanical properties of composite propellant grains are dependent on the physical and chemical properties of polymeric materials and the additives such as bonding agents, surfactants, crosslinkers, and curing agents. The physical properties such as mechanical strength and elongation are altered by the use of different types of binder, mass fraction, and oxidizer particle size. Low viscosity of the mixed materials is needed to form a stoichiometrically balanced propellant. High concentrations of oxidizer particles and/or aluminum powders are needed to give high specific impulse. Burning rate catalysts or modifiers are also added to obtain a wide range of burning rates.

4.6.1
AP Composite Propellants

4.6.1.1 AP-HTPB Propellants

As shown in Figs. 4-7 and 4-8, T_f and I_{sp} at 10 MPa of AP composite propellants are the highest when the mass fraction of AP, ξ (AP), is 0.98. The maximum I_{sp} is 259 s and the maximum T_f is 3020 K. In order to gain increased I_{sp}, aluminum particles are added as a fuel component. Though the addition of aluminum particles increases M_g, the increase of T_f still gives higher I_{sp}. The effects of the mass fraction of aluminum particles addition, ξ (Al) on I_{sp} and T_f are also shown in Figs. 4-7 and 4-8. Though T_f increases as ξ (Al) increases, the increase of I_{sp} is maximized at about ξ (Al) = 0.20, for example, I_{sp} = 270 s and T_f = 3890 K at ξ (Al) = 0.20.

When AP composite propellant burns, a high mole fraction of aluminum oxides is produced as a combustion product and generates visible smoke. If the smoke is required to be removed for military purposes or fireworks display, aluminum particles cannot be added as a component of AP composite propellants. In addition, a large amount of white smoke is produced even when non-aluminized AP composite propellants burn. This is because the combustion product, HCl, nucleates the condensation of moisture in the atmosphere, and relatively large-sized water drops are formed as fog or mist. This physical process occurs only when the relative humidity in the atmosphere is high, above about 60 %. If the atmospheric temperature is low,

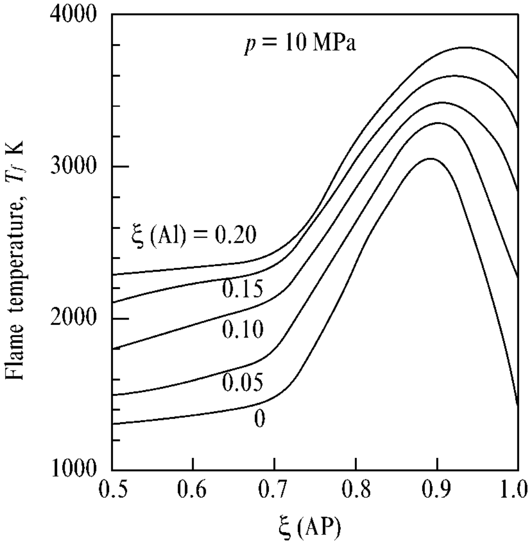

Figure 4-7. Adiabatic flame temperature of aluminized AP-HTPB composite propellants.

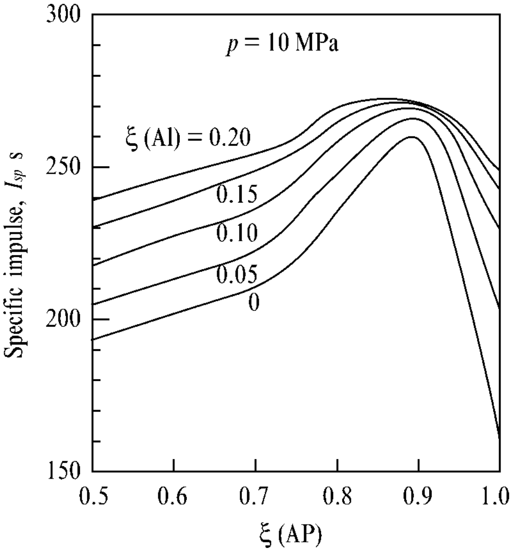

Figure 4-8. Specific impulse of aluminized AP-HTPB composite propellants.

below 260 K, white smoke is also formed by the same process. If the HCl smoke generated by AP combustion needs to be removed, the propellant should be replaced with double-base propellants, or the AP particles should be replaced with other non-halogen- or non-metal-containing oxidizers such as AN, RDX, HMX, ADN, or HNF. When aluminum particles are replaced with magnesium particles, the mole fraction of HCl is reduced significantly because of the formation of MgCl, as a combustion product.

Hydroxy-terminated polybutadiene (HTPB) is considered to be the best binder to achieve high combustion performance and superior elongation properties at low temperatures and also superior strength properties at high temperatures. These properties are difficult to obtain with double-base propellants. HTPB is characterized by an –OH termination of the butadiene polymer. The other type of butadiene polymer is carboxyl-terminated polybutadiene (CTPB), which is cured with an imine or an epoxy resin. It must be noted that CTPB is a little sensitive to humidity, and the aging characteristics are affected by humidity. The prepolymer of HTPB is cured and crosslinked with isophorone diisocyanate (IPDI) to formulate HTPB polymer used as a binder of oxidizer particles. The functionality of HTPB prepolymer is also an important chemical parameter during the process of curing and crosslinking in order to gain superior mechanical properties of HTPB binder. This also affects the aging characteristics of AP-HTPB propellants.

4.6.1.2 AP-GAP Propellants

Azide polymers such as GAP and BAMO are also used to formulate AP composite propellants in order to improve the specific impulse of AP-HTPB propellants. Since azide polymers are energetic materials which burn by themselves, the use of azide polymers as binders of AP particles with or without aluminum particles increases the specific impulse of AP-HTPB propellants. As shown in Fig. 4-9, the maximum I_{sp} 260 s is obtained at ξ (AP) = 0.80 and is approximately 12 % higher than that of AP-HTPB propellants because the maximum loading density of ξ (AP) is approximately 0.86 to formulate AP composite propellants. Since the molecular mass M_g remains high, above ξ (AP) = 0.8, I_{sp} decreases rapidly as ξ (AP) increases.

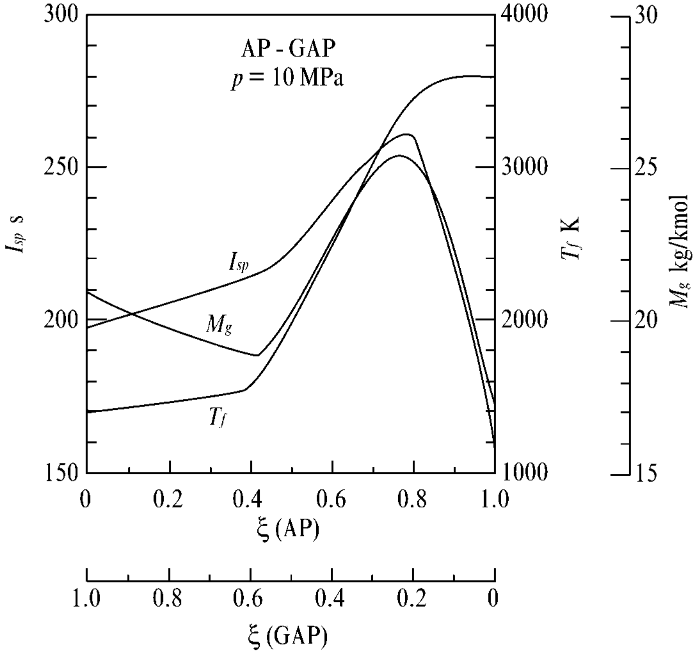

Figure 4-9. Specific impulse, adiabatic flame temperature, and molecular mass of AP-GAP composite propellant.

4.6.1.3 Chemical Materials of AP Composite Propellants

Similar to double-base propellants, various types of materials such as plasticizers, burning rate modifiers, and combustion instability suppressants are added to a mixture of AP and a binder. Table 4-17 shows the materials used to formulate AP composite propellants.

Table 4-17. Chemical materials used to formulate AP composite propellants.

Oxidizer:	AP
Binder (fuel):	HTPB, CTPB, PBAN, HTPE, HTPS, HTPA, PU, PS, PVC
Binder (energetic fuel):	GAP, BAMO, AMMO
Curing and/or crosslinking agent:	IPDI, TDI, PQD, HMDI, MAPO
Bonding agent:	MAPO, TEA, MT-4
Plasticizer:	DOA, IDP, DOP
Burning rate catalyst:	Fe_2O_3, FeO(OH), nBF
Burning rate negative catalyst:	LiF
Negative burning rate modifier:	OXM
Metal fuel:	Al
High energy additive:	RDX, HMX, NQ, CL-20, ADN
Combustion instability suppressant:	Al, Zr, ZrC
HCl suppressant:	Mg, MgAl, $NaNO_3$

4.6.2
AN Composite Propellants

Ammonium nitrate contains a relatively high concentration of oxidizer fragments as shown in Table 4-4. In order to gain an I_{sp} as high as possible, the binder mixed with AN is GAP. However, the maximum I_{sp} and T_f are 238 s and 2400 K at ξ (AN) = 0.85

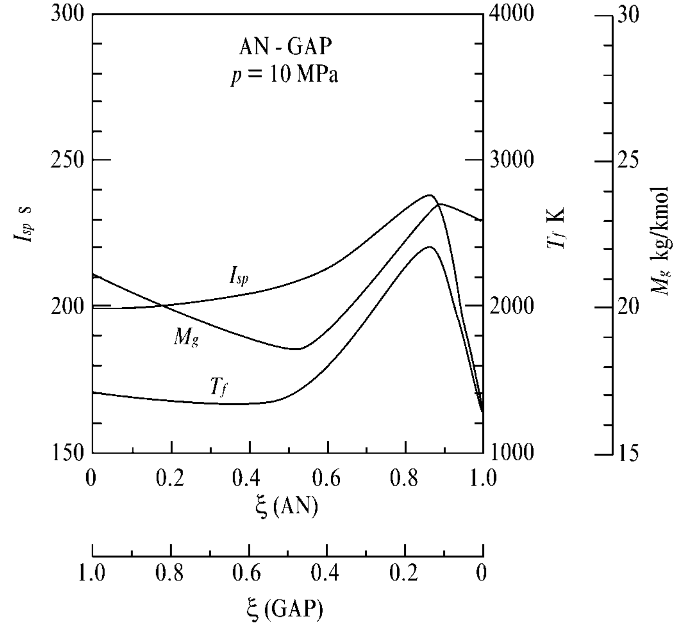

Figure 4-10. Specific impulse, adiabatic flame temperature, and molecular mass of AN-GAP composite propellant.

is obtained as shown in Fig. 4-10. Since AN crystal particles are not like AP, the practical ξ(AN) is less than 0.8 where I_{sp} drops to 225 s and T_f drops also to 2220 K.

4.6.3
Nitramine Composite Propellants

Nitramine composite propellants composed of HMX or RDX particles and polymeric materials offer the advantages of low flame temperature and low molecular mass combustion products, as well as reduced infrared emissions. The reduced infrared emissions result from the elimination of CO_2 and H_2O in the combustion products. To formulate these composite propellants, crystalline nitramine monopropellants such as HMX or RDX are mixed with a polymeric binder. Since both HMX and HMX are stoichiometrically balanced, the polymeric binder acts as a coolant producing low temperature fuel-rich combustion products. This is in contrast to AP composite propellants where the binder surrounding the AP particles acts as a fuel to produce high temperature combustion products.

Similar polymeric binders to those used for AP composite propellants are used for nitramine composite propellants such as HTPB, HTPE, and GAP. The combustion performance and the products of HMX composite propellants are shown in Figs. 4-11 and 4-12, respectively. The binder mixed with HMX particles is GAP, as with AN-GAP propellants shown in Fig. 4-10. Though the maximum T_f and I_{sp} are

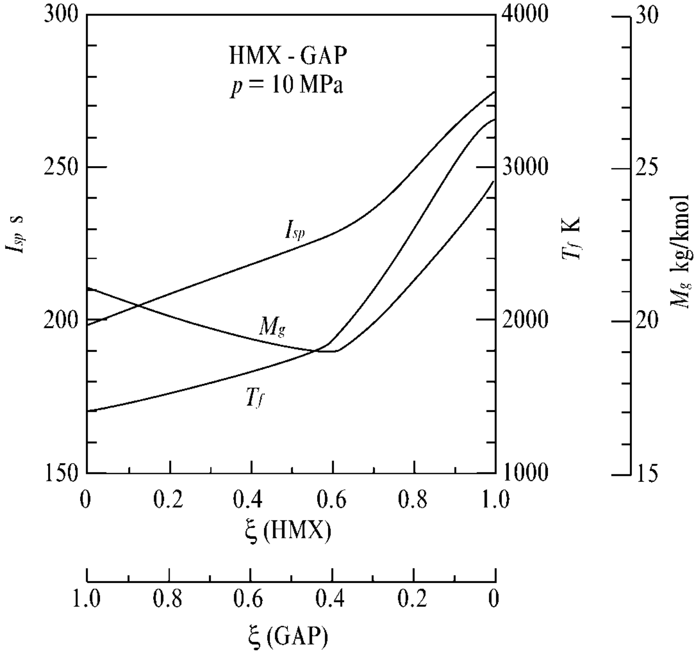

Figure 4-11. Specific impulse, adiabatic flame temperature, and molecular mass of HMX-GAP composite propellant.

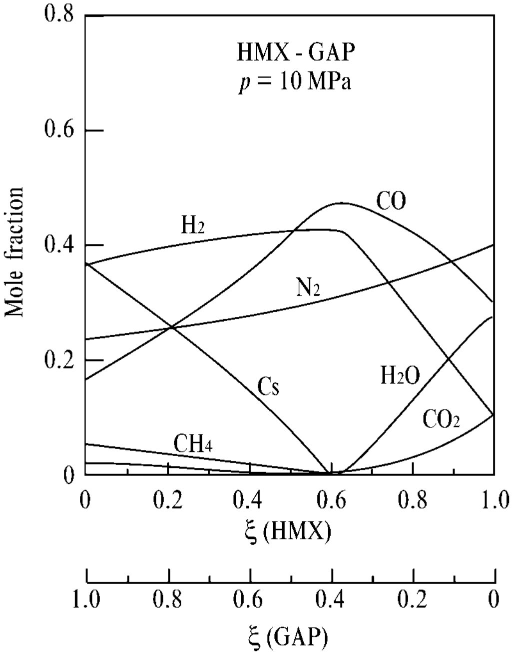

Figure 4-12. Mole fraction of combustion products of HMX-GAP composite propellant.

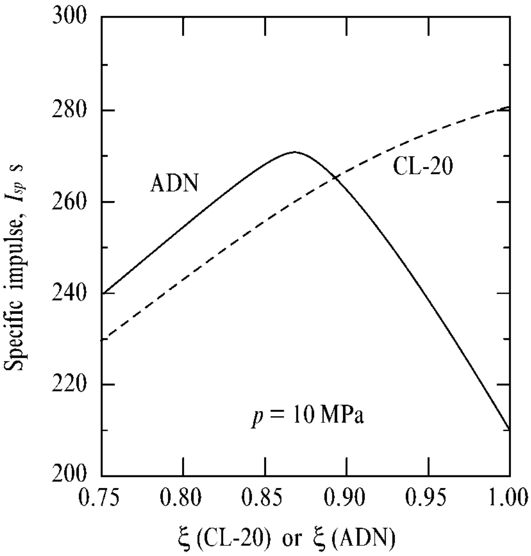

Figure 4-13. Specific impulse of ADN-GAP or CL-20-GAP composite propellant.

obtained at ξ (HMX) = 1.0, the maximum HMX loading is less than ξ (HMX) = 0.80 for practical HMX-GAP propellants where I_{sp} is 250 s and T_f = 2200 K. It is important to note that no H_2O, CO_2, $C_{(s)}$ are formed as combustion products at ξ (HMX) = 0.60. Though the mole fractions of H_2 and N_2 are relatively high, no infrared emission or absorption occurs from these molecules. The emission of CO is not high compared with CO_2 , H_2O, and $C_{(s)}$. The use of this class of propellants reduces infrared emission from rocket exhaust gas significantly.

Figure 4-13 shows the specific impulse of ADN-GAP and CL-20-GAP propellants as a function of the mass fraction of ADN, ξ (ADN) or CL-20, ξ (CL-20). The maximum I_{sp} of 270 s is obtained at ξ (ADN) = 0.87 and the maximum I_{sp} of 280 s is obtained at ξ (CL-20) = 1.00. Since the mass fraction of GAP needed to formulate practical composite propellants is at least ξ (GAP) = 0.13, I_{sp} 270 s is possible for ADN-GAP propellants but only I_{sp} 260 s for CL-20-GAP propellants.

4.6.4
TAGN Composite Propellants

TAGN is a unique energetic material which contains relatively high mole fractions of hydrogen atom. When TAGN is mixed with a polymeric material, it acts as a minor part of the oxidizer and produces fuel-rich combustion products. Figure 4-14 shows I_{sp}, T_f, and M_g of the propellants composed of TAGN and GAP, and Fig. 4-15

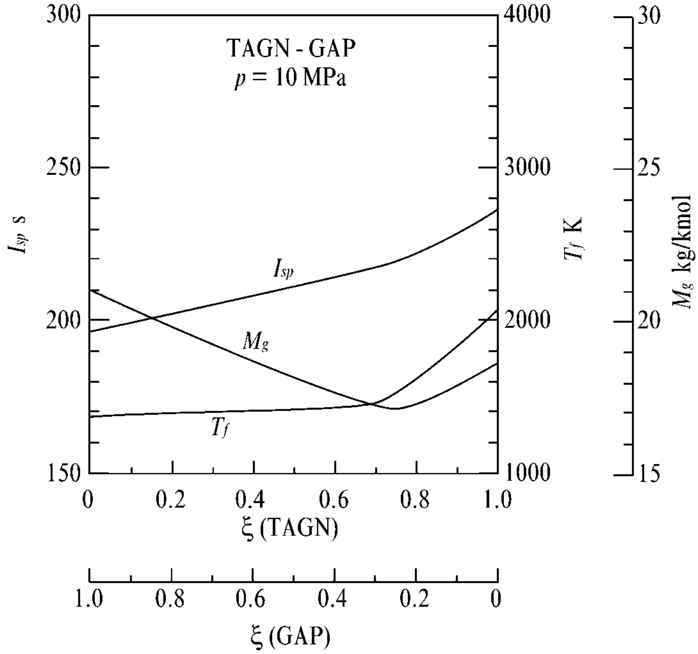

Figure 4-14. Specific impulse, adiabatic flame temperature, and molecular mass of TAGN-GAP composite propellant.

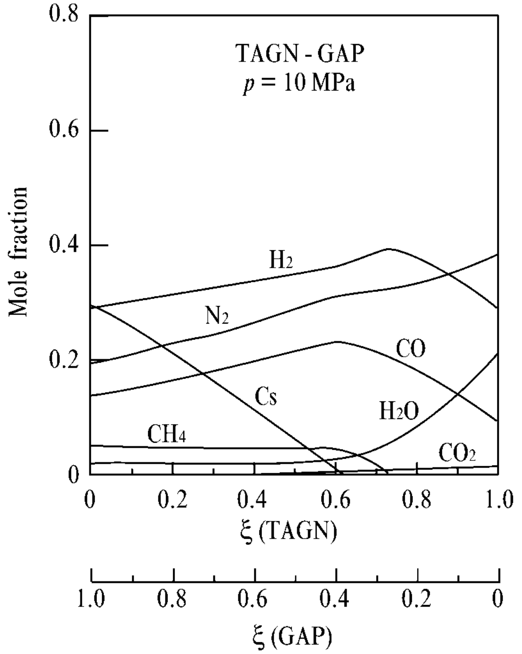

Figure 4-15. Mole fraction of combustion products of TAGN-GAP composite propellant.

shows the combustion products as a function of ξ (TAGN) or ξ (GAP). Since T_f is low, I_{sp} is low, and TAGN-GAP propellants are formulated to use as gas-generating propellants for a ducted rocket engine or gun propellants which reduce gun barrel erosion.

4.6.5
Black Powder

This granulated propellant consists of a number of powdered energetic materials that are packed in a cartridge. These are termed granulated propellants and used for gun propulsion and aerial shell ejection for fireworks. Black powder is a typical granulated propellant used for small sized rockets, guns, and fireworks. Since each particle of black powder has high porosity and small size, the mass burning rate is very high.

Though the theoretical I_{sp} of black powder is less than that of single-base, double-base, and AP-based composite propellants, black power is useful for short-duration operation of simplified propulsive systems. The advantages of black power are: low cost, very low aging effect, simple adjustment of propulsive forces by the adjustment of the quantity.

Black powder is a mechanically mixed material consisting of KN powder (60 % – 80 %), charcoal (10 % – 25 %), and sulfur (8 % – 25 %), which is pressed, granulated, and formed as a packed shape for use. When black powder is ignited, the combustion occurs from the entire granulated surfaces. Thus, the rate of gas production becomes much higher than that of conventional propellants used for rockets. However, this combustion phenomenon is deflagration, not detonation. The burning rate of black powder is not defined like that of rocket propellants because of the nature of the combustion of the granulated material. The overall gas production rate is an important parameter for combustion, which is dependent on each granulated powder and the density of the packed shape. The burning rate of black powder is highly dependent on the particle size of the ingredients. The porosity of charcoal is a dominating factor of the burning rate when the mixture ratio is fixed. The types of wood used as the starting material to produce the charcoal is also an important parameter for the determination of the burning characteristics. Table 4-18 shows a chemical composition of a black powder used for the ejection of the burst-aerial shells of fireworks.

Table 4-18. Chemical compositions and thermochemical properties of black powder.

Ingredient	*wt %*
Potassium nitrate	60 – 80
Charcoal	10 – 25
Sulfur	8 – 25
ρ_p kg/m^3	1200 – 2000
T_f K	1400 – 3200
I_{sp} s	60 – 150

4.7
Formulation of Explosives

Nitroglycerin is used to formulate explosives and is mixed with nitrocellulose as with double-base propellants. However, the mass fraction of NC is 0.06 – 0.08 for explosives and 0.3 – 0.6 for double-base propellants. Though both materials are homogeneous in their physical structures, the energy density of explosives is higher than that of double-base propellants because of the high mass fractions of NG.

Nitroglycol (NGC) has similar physical and chemical properties to those of NG. However, the vapor pressure is too high for it to be used as a major component of propellants and explosives. Nitroglycol is used as an additive to NG to reduce the freezing point of NG and to formulate explosives. However, the shock sensitivity of NG-based explosives is much higher than that of other types.

Additions of crystalline oxidizers such as ammonium nitrate or potassium nitrate to nitrate esters or energetic polymers form composite explosives whose physical structures are heterogeneous. In contrast to homogeneous explosives, the energy density of composite explosives is higher than that of homogeneous explosives.

When explosives are used for warheads of gun projectiles and missiles, the acceleration force acting on the explosives is high and aerodynamic heating due to supersonic flight becomes high also. Thus, the explosives including TNT as a major chemical do not resist high accelerations and heating. Mixtures of polymeric materials and crystalline energetic particles such as HMX, PETN, DATB, and HNS are used as high explosives. The use of polymeric materials improves tensile stress and elongation properties to protect from external mechanical shock and external heating.

4.7.1
Industrial Explosives

4.7.1.1 ANFO Explosives

A mixture of ammonium nitrate and light oil forms a low strength explosive which is used as a blasting compound for mines and industrial engineering. These are named ANFO explosives (ammonium nitrate fuel oil explosives)[3]. A mixture of AN particles (95 %) and light oil (5 %) gives ANFO explosive. Porous AN particles are used to absorb oil effectively and to make grain-shaped ANFO explosives. Since AN is highly hygroscopic in nature, humidity control is needed during the formulation process. The density is in the range 800 – 900 kg/m^3 and the detonation velocity is 2500 –3500 m/s.

4.7.1.2 Slurry Explosives

Slurry explosives consist of saturated aqueous solutions of ammonium nitrate with sensitizing additives[1,3]. Nitrates such as monomethylamine nitrate, ethylene glycol mononitrate, or ethanolamine mononitrate are used as sensitizers. Aluminum powders are also added as energetic materials. Table 4-19 shows a typical chemical composition of a slurry explosive. It is important to include so-called micro-bubbles in the explosives in order to give the initial detonation and produce the subsequent detonation wave. The micro-bubbles are made of glass or polymeric materials.

Slurry explosives have anti-water and anti-humidity characteristics and are fundamentally insensitive to mechanical shock and heat. The strength of detonation is approximately equal to that of NG-NC based explosives. Since slurry explosives are a mixture of aqueous AN and oil, the physical nature is an emulsion and these are also termed emulsion explosives.

Table 4-19. Chemical composition of a slurry explosive.

Ingredient	*wt %*
Water	10
Ammonium nitrate	45
Potassium nitrate	10
Monomethylamine nitrate	30
Aluminum	2
Others	3

4.7.2
Military Explosives

4.7.2.1 TNT Based Explosives

Mixtures of TNT, RDX, and/or AN are used as TNT based explosives. Various additives such as aluminum powders, barium nitrate, and/or some other small amounts of materials are used. The density is in the range 1450 kg/m^3 – 1810 kg/m^3. Aluminum powders are added to give bubble energy when used under water conditions.

4.7.2.2 Plastic Bonded Explosives

Since TNT based explosives have relatively low melting points, the deformation of the explosives or an unexpected ignition occurs when high heat flux is given to warheads by aerodynamic heating of high-supersonic or hypersonic flight. Plastic bonded explosives (PBX) have been developed based on similar chemical processes to those used to develop composite rocket propellants. The crystalline materials such as RDX and HMX are mixed with liquid copolymers such as polystyrene and polybutadiene prepolymers. The mixtures are cast in the warheads under vacuum conditions in order to remove bubbles in the mixtures. Then, the mixtures are crosslinked and cured to give rubber-like properties where mechanical strength and decomposition temperature are much higher than TNT based Composition B.

There are various types of crystalline materials and polymers used to formulate PBX. Table 4-20 shows typical materials used for PBX. Though the polymers used are not the same as those used for propellants, the fundamental concept of the selection of the materials for PBX is the same as that for propellants as shown in Table 4-20.

Table 4-20. Chemical materials used to formulate PBX

Energetic materials (oxidizer):	RDX, HMX, TNT, AP, AN
Polymeric materials (binder and fuel):	Nylon, Viton, Polyester-styrene, HTPB, Polyurethane, Silicone resin
Plasticizers:	Fluoronitropolymer, TEGDN
Fuel:	Al

References

1 Meyer, R., Explosives, VCH Verlag Chemie, Weinheim (1977).
2 Sarner, S. F., Propellant Chemistry, Reinhold Publishing Corporation, New York (1966).
3 Japan Explosives Society, Energetic Materials Handbook, Kyoritsu Shuppan (1999).
4 Chan, M. L., Reed, Jr., R., and Ciaramitaro, D. A., Advances in Solid Propellant Formulations, Solid Propellant Chemistry, Combustion, and Motor Interior Ballistics, edited by Yang, V., Brill, T. B., and Ren, Wu-Zhen, Progress in Astronautics and Aeronautics, Vol. 185, Chapter 1.7, AIAA, Virginia (2000).

5 Doriath, G., Available Propellants, Solid Rocket Technical Committee Lecture Series, AIAA Aerospace Sciences Meeting, Reno, Nevada (1994).

6 Miller, R. R. and Guimont, J. M., Ammonium Dinitramide Based Propellants, Solid Rocket Technical Committee Lecture Series, AIAA Aerospace Sciences Meeting, Reno, Nevada (1994).

7 Kubota, N., Propellant Chemistry, Journal of Pyrotechnics, 11 (2000), pp. 25–45.

8 Sanderson, A., New Ingredients and Propellants, Solid Rocket Technical Committee Lecture Series, AIAA Aerospace Sciences Meeting, Reno, Nevada (1994).

9 Miller, R., Advancing Technologies: Oxidizers, Polymers, and Processing, Solid Rocket Technical Committee Lecture Series, AIAA Aerospace Sciences Meeting, Nevada (1994).

10 Gordon, S. and McBridge, B. J., Computer Program for Calculation of Complex Chemical Equilibrium Compositions, Rocket Performance, Incident and Reflected Shocks, and Chapman-Jouguet Detonations, NASA SP-273, 1971.

11 Beckstead, M. W., Overview of Combustion Mechanisms and Flame Structures for Advanced Solid Propellants, Solid Propellant Chemistry, Combustion, and Motor Interior Ballistics, edited by Yang, V., Brill, T. B., and Ren, Wu-Zhen, Progress in Astronautics and Aeronautics, Vol. 185, Chapter 2.1, AIAA, Virginia (2000).

12 Bazaki, H., Combustion Mechanism of 3-Azidomethyl-3-Methyloxetane (AMMO) Composite Propellants, Solid Propellant Chemistry, Combustion, and Motor Interior Ballistics, edited by Yang, V., Brill, T. B., and Ren, Wu-Zhen, Progress in Astronautics and Aeronautics, Vol. 185, Chapter 2.8, AIAA, Virginia (2000).

13 Komai, I., Kobayashi, K., and Kato, K., Burning Rate Characteristics of Glycidyl Azide Polymer (GAP) Fuels and Propellants, Solid Propellant Chemistry, Combustion, and Motor Interior Ballistics, edited by Yang, V., Brill, T. B., and Ren, Wu-Zhen, Progress in Astronautics and Aeronautics, Vol. 185, Chapter 2.9, AIAA, Virginia (2000).

14 Kubota, N. and Sonobe, T., Combustion Mechanism of Azide Polymer, Propellants, Explosives, Pyrotechnics, Vol. 13, 1988, pp. 172–177.

15 Miyazaki, T. and Kubota, N., Energetics of BAMO, Propellants, Explosives, Pyrotechnics, Vol. 17, 1992, pp. 5–9.

Propellants and Explosives: Thermochemical Aspects of Combustion. Naminosuke Kubota
Copyright © 2002 Wiley-VCH Verlag GmbH & Co. KGaA
ISBNs: 3-527-30210-7 (Hardback); 3-527-60050-7 (Electronic)

5

Combustion of Crystalline and Polymeric Materials

5.1

Combustion of Crystalline Materials

5.1.1

Ammonium Perchlorate (AP)

5.1.1.1 Thermal Decomposition

Experimental studies on the thermal decomposition and combustion processes of AP have been done and their detailed mechanisms have been reported.[1–12] Figure 5-1 shows the thermal decomposition of AP measured by differential thermal analysis (DTA) and thermal gravimetry (TG) with a heating rate of 0.33 K/s. An endothermic peak is seen at 520 K, which is the orthorhombic to cubic crystal structure lattice phase transition whose heat of reaction is –85 kJ/kg without mass loss. An exothermic reaction occurs between 607 K and 720 K accompanied by mass loss. This exothermic reaction occurs through the overall reaction scheme of[1,2]

$$NH_4ClO_4 \rightarrow NH_3 + HClO_4$$

$$HClO_4 \rightarrow HCl + 2\,O_2$$

and produces excess oxygen as an oxidizer. The exothermic peak shifts toward higher temperatures as the heating rate is increased. Figure 5-2 shows the plot of reciprocal temperature versus heating rate; a straight line that determines the activation energy for the exothermic gasification reaction. The activation energy is determined to be 134 kJ/mol. However, the decomposition reaction includes sublimation and melting processes which cannot be identified from the DTA and TG data. Dissociative sublimation occurs when the heating rate is slow compared with the heating rate of a normal burning[5]. This sublimation is endothermic to the extent of 2.1 MJ/kg and is of zeroth order with respect to pressure. The melting of AP occurs at a higher temperature zone, being > 725 K when the heating rate is high.

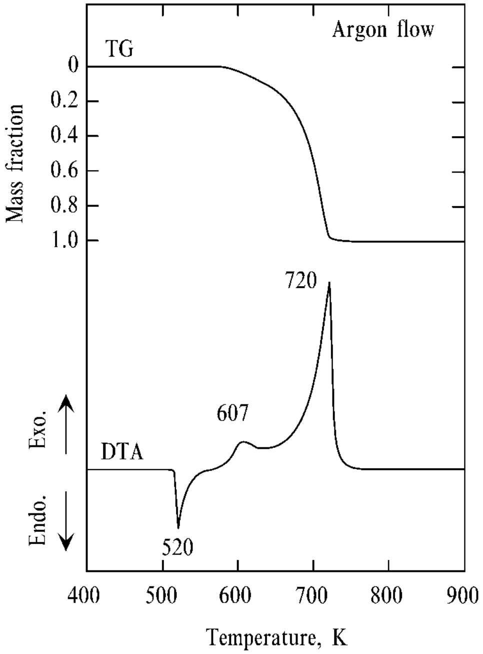

Figure 5-1. Thermal decomposition process of AP measured by thermal gravimetry (TG) and by thermal differential analysis (DTA).

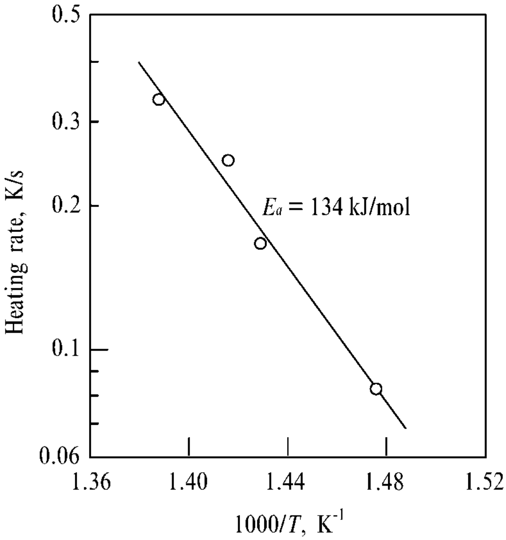

Figure 5-2. Determination of the activation energy of AP decomposition.

5.1.1.2 **Burning Rate**

The mode of degradation of AP was studied first by Bircumshaw and Newman[3]. They found that, below 570 K, only 30 % decomposition occurs, and the remaining 70 % is a porous solid residue chemically identical to the starting AP, which does not react further when pressure and temperature are very low. Above 670 K, no solid residue remains behind. When pressure is increased, pure sublimation is retarded and decomposition reaction is increased. AP degradation involves as a first step dissociative sublimation of a loosely held NH_3:$HClO_4$ complex, and the resulting gaseous NH_3 and $HClO_4$ are liberated.

The burning rate of a pressed strand of AP was discussed as a function of pressure by Arden[1] and Levy and Friedman[2]. The lower pressure limit of AP burning is about 2.7 MPa and the burning rate increases as pressure increases above this.

5.1.1.3 Combustion Wave Structure

When AP which is made as a pressed strand burns, a high temperature flame is formed in the gas phase due to the exothermic reaction between NH_3 and $HClO_4$. Mitani and Niioka measured the gas phase structure above the regressing surface of an AP pellet and found a two-stage flame.[10] The conductive heat from the flame to the burning surface is used to heat up the solid phase from its initial temperature to the surface temperature. At the burning surface, the AP crystals go through an orthorhombic to cubic lattice transition. This endothermic –80 kJ/kg transition occurred at about 513 K. Tanaka and Beckstead made a computation of the condensed phase and gas phase structures of AP by assuming 107 reaction steps and 32 gaseous species.[13] The burning surface temperature and the melt layer thickness were also computed as a function of pressure.

5.1.2
Ammonium Nitrate (AN)

5.1.2.1 Thermal Decomposition

AN melts at 443 K and begins to gasify above 480 K. The decomposition process of AN is dependent on the decomposition temperature. At low temperatures (about 480 K), the gasification process of AN is the endothermic (–178 kJ/mol) reversible reaction represented by[14]

$$NH_4NO_3 \rightleftharpoons NH_3 + HNO_3$$

The decomposition process shifts to an exothermic (37 kJ/mol) gasification reaction as temperature increases

$$NH_4NO_3 \rightarrow N_2O + 2\,H_2O$$

and the overall decomposition reaction of AN then appears to be

$$NH_4NO_3 \rightarrow N_2 + 2\,H_2O + 1/2\,O_2$$

This reaction is highly exothermic (119 kJ/mol) and produces oxygen molecules which act as an oxidizer. Though the ignition of AN is difficult because of the endothermic reaction at the initial stage, AN becomes highly inflammable in the high pressure region and also becomes detonatable when heated much above 550 K. Furthermore, the inflammable characteristics of AN are dependent on impurities or additives.

5.1.3
HMX

5.1.3.1 Thermal Decomposition

A detailed literature summary and discussions of the thermal decomposition of HMX are presented by Boggs[15], and the general picture of the decomposition processes of HMX may be understood from [15]. When HMX is heated slowly, a single-stage mass loss process is observed: the mass loss begins at 550 K and rapid gasification reaction occurs at 553 K. No solid residue remains above 553 K. Two endothermic peaks and one exothermic peak are seen: the first endothermic peak at 463 K is the crystal transformation from β to δ and the second endothermic peak at 550 K is the phase change from solid to liquid. The exothermic peak at 553 K is caused by the reaction accompanied by gas phase reaction.

A thermally degraded HMX sample which is obtained by the interrupted decomposition at the 50 % mass loss condition (the heating is stopped at 552 K and the sample is cooled down to the room temperature, 293 K) is identified as a recrystallized material[16]. Gasification reaction of the thermally degraded HMX begins at 550 K and rapid decomposition occurs at 553 K, which is equivalent to the thermal decomposition process of nondegraded HMX. However, the endothermic peak observed at 463 K is not seen for the degraded HMX. The results of an infrared (IR) analysis of β-HMX, δ-HMX, and the degraded HMX show that the degraded HMX is equivalent to δ-HMX, which implies that the endothermic reaction of the phase change from solid to liquid observed at 550 K is caused by δ-HMX.

5.1.3.2 Burning Rate

Since HMX is a fine crystalline particle, it is difficult to measure its linear burning rate. When a large HMX single crystal (approximately 10 mm × 10 mm × 20 mm) is ignited by an electrically heated wire attached to the top of the crystal, the HMX crystal is ignited and then broken immediately into fragments because of the thermal stress created in the crystal. As a result, no steady burning of the crystal is possible, and no linear burning rate exists for HMX because the heat conduction rate from the ignited surface to the inside of the crystal is faster than the surface regressing rate (burning rate). A breakage of HMX crystal structure occurs due to the thermal stress caused by the temperature difference in the crystal.

When a pressed pellet made of HMX particles is ignited from the top, it burns steadily without breaking the pellet. The thermal stress created within the pressed pellet is relaxed at the interface of the HMX particles within the pellet. Furthermore, the density of the pressed pellet is at most 95 % of the theoretical HMX density and the thermal stress given to the crystal is absorbed by the voids between the HMX particles. The burning rate of an HMX sample made of a pressed pellet is shown in Fig. 5-3. The pressed pellet is a mixture of β-HMX particles, 33 % 20 μm dia and

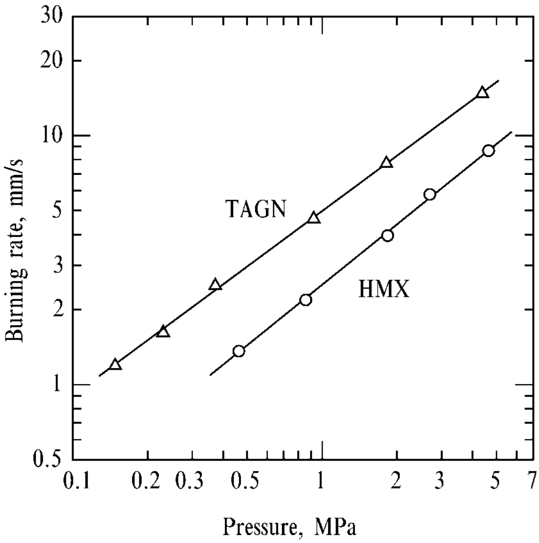

Figure 5-3. Burning rates of HMX and TAGN showing that the burning rate of HMX is lower than that of TAGN.

67 % 200 μm dia. The pellets are 8 mm in diameter and 7 mm long, and the density is 1700 kg/m^3, which is 89 % of the theoretical maximum density (1900 kg/m^3). The burning rate of the HMX pellets increases linearly in a ln p versus ln r plot. The pressure exponent of the burning rate is 0.66 at the initial temperature 293 K.

5.1.3.3 Gas Phase Reaction

The overall initial decomposition reaction of HMX is represented by[17,18]

$$3\ (CH_2NNO_2)_4 \rightarrow 4\ NO_2 + 4\ N_2O + 6\ N_2 + 12\ CH_2O$$

Since nitrogen dioxide reacts quite rapidly with formaldehyde[15,19,20], the gas phase reaction represented by

$$7\ NO_2 + 5\ CH_2O \rightarrow 7\ NO + 3\ CO + 2\ CO_2 + 5\ H_2O$$

is probably the dominating reaction and is immediately followed by the initial decomposition reaction. The reaction between NO_2 and CH_2O is highly exothermic and faster than the reaction rates of the other gaseous species.

The products generated by the reactions shown above react again in the later stage, i.e., NO and N_2O act as oxidizers, and H_2 and CO act as fuels. The reactions involving NO and N_2O are represented by[20]

$$2\,NO + 2\,H_2 \rightarrow N_2 + 2\,H_2O$$

$$2\,NO + 2\,CO \rightarrow N_2 + 2\,CO_2$$

$$2\,N_2O \rightarrow 2\,NO + N_2$$

The overall reactions involving NO and N_2O take place slowly and are trimolecular.[20] The reaction rate is very slow at low pressure and increases rapidly as pressure increases.

5.1.3.4 Combustion Wave Structure and Heat Transfer

Typical flame structures of HMX pellets are shown in Fig. 5-4 as a function of pressure. A thin luminous flame sheet stands some distance from the burning surface and a reddish flame is produced above this luminous flame sheet. The flame sheet approaches the burning surface as pressure increases[16]. When the pressure is < 0.18 MPa, the luminous flame sheet is blown away from the burning surface, as shown in Fig. 5-4 (a). As pressure increases, the luminous flame sheet rapidly approaches the burning surface. However, it becomes very unstable above the burning surface and forms a wave-shaped flame sheet in the pressure range between 0.18 MPa and 0.3 MPa, as shown in Fig. 5-4(b). At further increased pressure, above 0.3 MPa, the luminous flame sheet becomes stable and one-dimensional just above the burning surface, as shown in Fig. 5-4(c).

The combustion wave of HMX is divided into three zones: crystallized solid phase (zone I), solid and/or liquid condensed phase (zone II), and gas phase (zone III). A schematic representation of the heat transfer process in the combustion wave is shown in Fig. 5-5. In zone I, the temperature increases from the initial temperature T_0 to the decomposition temperature T_u without reaction. In zone II, the temperature increases from T_u to the burning surface temperature T_s (interface of the condensed phase and the gas phase). In zone III, the temperature increases rapidly from T_s to the luminous flame (the flame sheet shown in Fig. 5-4) temperature. Since the condensed phase reaction zone is very thin (~0.1 mm), T_s is approximately equal to T_u.

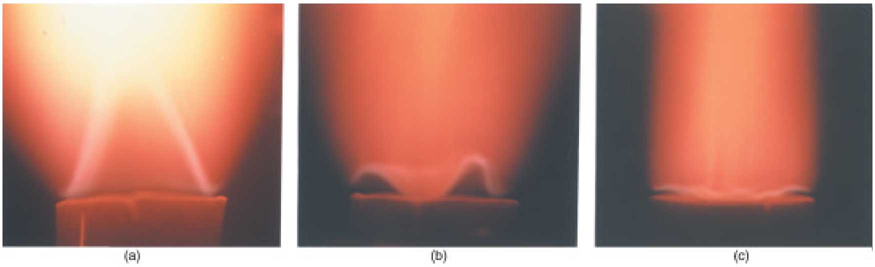

Figure 5-4. Flame photographs of HMX at three different pressures : (a) 0.18 MPa, (b) 0.25 MPa, and (c) 0.30 MPa.

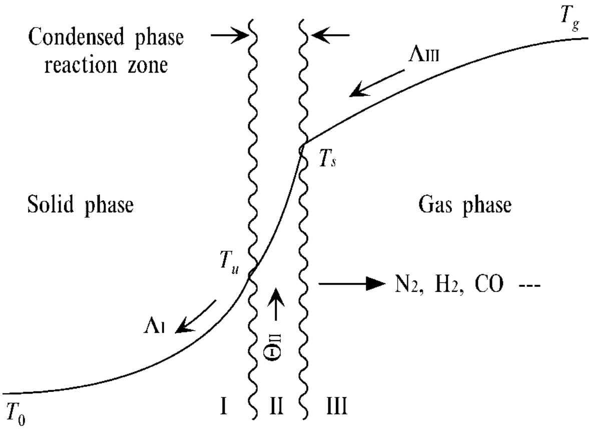

Figure 5-5. Heat transfer model of the combustion wave of an energetic material.

The heat flux transferred back from zone III to zone II, Λ_{III}, is given by

$$\Lambda_{III} = \lambda_{III}\left(\frac{dT}{dx}\right)_{III} \tag{5.1}$$

and the heat flux produced in zone II, Θ_{II}, is given by

$$\Theta_{II} = \rho_I\, r\, Q_{II} \tag{5.2}$$

where Q_{II} is the heat of reaction in zone II. The heat balance equation at the burning surface is represented by

$$\Theta_{II} = \rho_I\, r\, c_I\, (T_s - T_0) - \Lambda_{III} \tag{5.3}$$

The temperature gradient in zone III, $(dT/dx)_{III}$, increases as pressure increases, represented by $(dT/dx)_{III} \sim p^{0.7}$. However, T_s remains relatively constant (~ 700 K) in the pressure range between 0.1 MPa and 0.5 MPa. Using the physical parameter values of HMX, $\rho_I = 1700$ kg/m^3, $c_I = 1.30$ kJ/kgK, and $\lambda_{III} = 8.4 \times 10^{-5}$ kW/mK, Q_{II} is determined as 300 kJ/kg.

Figure 5-6 shows the heat flux produced in zone II and the heat flux transferred back from zone III to zone II as a function of pressure. Θ_{II} is approximately equal to Λ_{III}, both of which increase with increasing pressure represented by $\Lambda_{III} \sim p^{0.75}$ and $\Theta_{II} \sim p^{0.65}$. It is evident from Eq. (5.2) that the pressure sensitivity of Θ_{II} is approximately equal to that of the burning rate. Then, the pressure sensitivity of the HMX burning rate ($\sim p^{0.66}$) is dependent on Λ_{III}, i.e., the pressure sensitivity of the gas phase reaction[16].

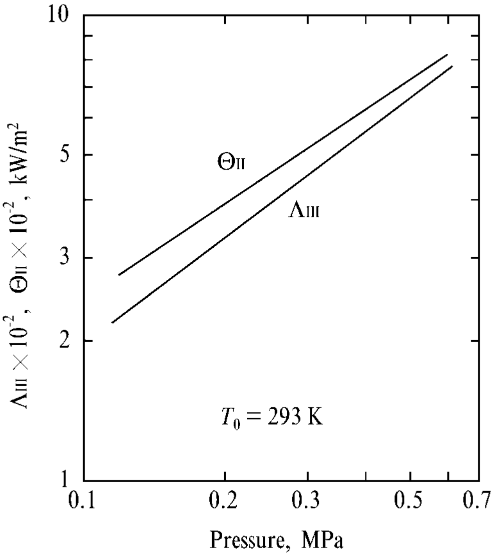

Figure 5-6. Heat flux transferred back from gas phase to burning surface and heat flux produced at burning surface.

5.1.4
Triaminoguanidine Nitrate (TAGN)

5.1.4.1 Thermal Decomposition

The thermal decomposition of TAGN consists of a three-stage heat generation and mass loss process, and is measured by thermogravimetry[21]. The first stage corresponds to the exothermic rapid reaction between the 0 % mass loss (488 K) and 27 % mass loss (498 K), the second stage corresponds to the relatively slow endothermic reaction between the 27 % mass loss (498 K) and 92 % mass loss (573 K), and the third stage corresponds to the very slow endothermic reaction between 92 % mass loss (573 K) and 100 % mass loss (623 K). The endothermic peak at 488 K is caused by the phase change from solid to liquid. The exothermic rapid reaction at the first stage is the process representing the nature of the energetics of TAGN.

A thermally treated TAGN which is obtained by the interrupted decomposition at 27 % mass loss decomposes without the exothermic peak observed at the first stage of TAGN. This indicates that the major energetic fragment of TAGN is used up at the first stage decomposition reaction accompanied by 27 % mass loss. The molecular structure of guanidine nitrate (GN: $CH_6N_4O_3$) is similar to that of TAGN except for the three amino groups in TAGN. The endothermic peak at 487 K is the phase change from solid to liquid and a very slow reaction occurs after this phase change. The major decomposition of GN begins at about 530 K and is complete at 539 K (70 % mass loss). The remaining 30 % mass fraction decomposes endothermically at higher temperatures. Though GN is also an energetic material (T_f = 1370 K and ΔH_f = −3.19 MJ/kg), consisting of the oxidizer fragment (HNO_3) attached by an ionic bond and fuel fragments, neither a rapid gasification reaction nor an exothermic reaction occurs. This is a significant contrast when compared with the decomposition process of TAGN. Thus, one can conclude that the HNO_3 attached to the molecular structure of TAGN is not the fragment to produce the exothermic rapid reaction at the first stage decomposition process[21].

Since the weakest chemical bond in the TAGN molecule is the N–N bond (159 kJ/mol), the initial bond breakage is at amino groups. The NH_2 radicals attached to the TAGN molecule split off. The mass fraction of $3(NH_2)$ within the TAGN molecule is 0.288 which is approximately equal to the observed mass loss fraction (0.27) at the first stage decomposition process. The chemical enthalpy difference between TAGN and GN is 344 kJ/mol, and the energy released by the reaction of NH_2 radicals, producing N_2 and H_2, is 168 kJ/mol[21]. This energy is the heat produced at the first stage decomposition process of TAGN.

5.1.4.2 **Burning Rate**

Since TAGN consists of crystalline particles, the burning rate of TAGN is measured using pressed pellets. The burning rate of TAGN is shown in Fig. 5-3 as a function of pressure. Each pressed pellet is made using TAGN particles 5μm in diameter, and the density of the pellets is 1470 kg/m^3, which is 0.98 % of the theoretical maximum density. The burning rate increases linearly in a ln p versus ln r plot and the pressure exponent n is 0.78, which is equivalent to the pressure exponent of HMX, as also shown in Fig. 5-3 for a reference. The burning rate of TAGN is almost double that of HMX at the same pressure, even though the energy density of TAGN is lower than that of HMX, as shown in Table 4-5.

5.1.4.3 **Combustion Wave Structure and Heat Transfer**

The luminous flame of TAGN stands some distance from the burning surface as shown in Fig. 5-7. The luminous flame front approaches the burning surface when pressure is increased, similarly to the luminous flame front of HMX as described

Figure 5-7. Flame photograph of TAGN burning at 0.2 MPa showing that the luminous flame front stands some distance above the burning surface.

Section 5.1.3 in this chapter. The flame standoff distance versus pressure in a log-log plot is represented by

$$L_g = ap^d \tag{5.4}$$

where d is –1.00. Based on the analysis given by Eq. (3.70), the overall reaction rate in the gas phase $[\omega_g]$ is expressed as

$$[\omega_g] = \frac{\rho_p r}{L_g} \tag{5.5}$$

$$\sim p^{n-d} \sim p^m \tag{5.6}$$

The reaction rate increases linearly in a ln $[\omega_g]$ versus ln p plot. The overall order of the reaction in the gas phase is given by the relationship $m = n - d$, and is determined to be 1.78. This indicates that the reaction rate in the gas phase of TAGN is less pressure sensitive than that of other propellants, for example, $m = 2.5$ for double-base propellants[21].

The heat transfer process in the combustion wave of TAGN consists of three zones, as in the case of HMX, which is illustrated in Fig. 5-5: Zone I is the solid phase, where temperature increases exponentially from the initial temperature T_0 to the decomposition temperature T_u without chemical reaction. Zone II is the condensed phase, where which temperature increases from T_u to the burning surface temperature T_s with an exothermic reaction. Zone III is the gas phase, where temperature increases rapidly from T_s to the final combustion temperature T_g with an exothermic reaction.

The results of the temperature measurements in the combustion wave indicate that T_u is about 750 K and T_s is about 950 K, both of which are relatively unchanged when pressure is increased. The thickness of the condensed phase reaction zone II and the heat flux feedback from zone III to zone II, Λ_{III} , increase as pressure increases. The heat flux in zone II (Θ_{II}) is approximately 13 times higher than that in zone III (Λ_{III}) at 0.3 MPa. The heat of reaction in zone II (Q_{II}) is determined to be 525 kJ/kg. It is obvious that Q_{II} of TAGN is approximately 75 % higher than Q_{II} of HMX. Thus, the higher burning rate of TAGN compared with that of HMX shown in Fig. 5-3 is caused by the higher Q_{II} of TAGN compared with that of HMX even though the adiabatic flame temperature of TAGM is about 1000 K lower than that of HMX. Detailed discussions on the decomposition and combustion of TAGN are described in [21].

5.2
Combustion of Polymeric Materials

5.2.1
Nitrate Esters

The simplest nitrate ester is methylnitrate, which has the chemical structure CH_3ONO_2. The decomposition process is given by[19,22]

$$CH_3ONO_2 \rightarrow CH_3O + NO_2 \qquad Q_p = -147\ \text{kJ/mol}$$

$$\rightarrow CH_2O + 1/2H_2 + NO_2 \qquad Q_p = -34\ \text{kJ/mol}$$

$$\rightarrow CO,\ H_2O,\ NO,\ H_2,\ N_2,\ N_2O,\ CH_2O,\ CO_2$$

The first two reaction schemes are endothermic, but the overall reaction is exothermic and the final flame temperature is 1800 K. The observed pressure dependence of the burning rate follows a second order rate law; the overall activation energy is consistent with the oxidation reaction by NO_2, which is the slowest and rate-controlling step.

The primary step in the decomposition of ethylnitrate ($C_2H_5ONO_2$) is again the breaking of the $C_2H_5O–NO_2$ bond[23], and the decomposition rate obeys a first order law. The decomposition process of ethylene glycol dinitrate is[22]:

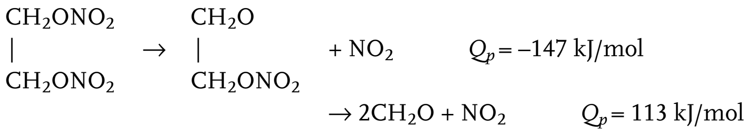

$$\begin{array}{l} CH_2ONO_2 \\ | \\ CH_2ONO_2 \end{array} \rightarrow \begin{array}{l} CH_2O \\ | \\ CH_2ONO_2 \end{array} + NO_2 \qquad Q_p = -147\ \text{kJ/mol}$$

$$\rightarrow 2CH_2O + NO_2 \qquad Q_p = 113\ \text{kJ/mol}$$

The breaking of one $O–NO_2$ bond gives a free radical which decomposes to formaldehyde and nitrogen dioxide. When butane-2,3-diol dinitrate is decomposed at atmospheric pressure, nitrogen dioxide and acetaldehyde are formed[24]. However, these react rapidly to form nitric oxide within a distance of 2 mm from the decomposing surface. The decomposition of butane-1,4-diol dinitrate produces nitrogen dioxide, formaldehyde, and ethylene. The steep temperature increase and the rapid concentration decrease of nitrogen dioxide and formaldehyde are observed within 1 mm of the decomposing surface. It is proposed[24] that the dinitrate decomposes to produce equal amounts of aldehyde and nitrogen dioxide:

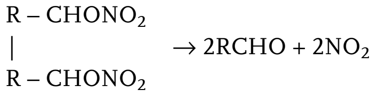

$$\begin{array}{l} R - CHONO_2 \\ | \\ R - CHONO_2 \end{array} \rightarrow 2RCHO + 2NO_2$$

NO_2 is then converted to NO by the oxidation reaction with RCHO.

As is evident from the experimental measurements, most kinds of nitrate esters appear to decompose to NO_2 and C–H–O species with the breaking of the O-NO_2 bond as the initial stage. A strong heat release occurs in the gas phase near the decomposing surface due to NO_2 reduction to NO with the accompanying oxidation of C–H–O species to H_2O, CO, and CO_2. NO reduction, however, is slow, and the reaction is not observed in the decomposition of some nitrate ester systems. Even when the reaction occurs, the heat release does not contribute to the heat feedback to the surface because the reaction occurs remote far from the surface.

The decomposition process is divided basically into three stages for simple nitrate esters:

Stage 1. $RNO_2 \rightarrow NO_2$ + organic molecules (mainly aldehydes)

Stage 2. NO_2 + organic products of stage 1

$\rightarrow NO + H_2, CO, CO_2, H_2O$, etc. at low pressure

Stage 3. NO + H_2, CO etc. $\rightarrow N_2, CO_2, H_2O$, etc. at high pressure

Stage 2 occurs at high or low pressure.

The decomposition process of double-base propellants is autocatalytic, NO_2 being evolved first and then reacting to increase the rate of nitrogen dioxide evolution[25]. The first step of the decomposition is the breaking of the RO–NO_2 bond, followed by the production of complex organic gases[26].

The reaction of formaldehyde and nitrogen dioxide mixtures occurs very rapidly at temperatures above 430 K, NO_2 is reduced almost quantitatively to nitric oxide, and the aldehyde is oxidized to carbon monoxide, dioxide, and water. The order of reaction is unity with respect to both reactants[27]. The flame velocity is independent of pressure and the maximum velocity is 1.40 m/s for a mixture containing 43.2 % HCHO (mol %). The velocity depends significantly upon the mixture ratio; for example, it drops to about half this value for a mixture containing 60 % HCHO. The flame velocity of the mixture of CH_3CHO and NO_2 is also highly dependent on the mixture ratio, about 0.1 m/s at 37 % CH_3CHO and 0.04 m/s at 60 % CH_3CHO.

No reaction between H_2 and NO occurs over a wide range of mixture ratios at 0.1 MPa. This reaction occurs above temperatures of nitric oxide dissociation, except in the presence of some radicals[28]. The mixtures of CO and NO are also difficult to ignite, and only mixtures rich in NO are ignited at 1700 K.

5.2.2
Glycidyl Azide Polymer (GAP)

5.2.2.1 Thermal Decomposition and Burning Rate

The terminal OH groups of GAP prepolymer are cured with the NCO groups of hexamethylene diisocyanate (HMDI) and crosslinked with triethylolpropane (TMP) in order to form GAP copolymer consisting of 84.8 % GAP prepolymer, 12.0 % HMDI, and 3.2 % TMP as shown in Fig. 4-1. The thermochemical data for GAP copolymer, obtained by differential thermal analysis (DTA) and thermal gravimetry (TG), are shown in Fig. 5-8. The exothermic peak, accompanied by mass loss between 475 K and 537 K, is attributed to the decomposition and gasification reactions. Two-stage gasification reaction occurs: the first stage occurs rapidly, accompanied by heat liberation and the second stage occurs relatively slowly without heat liberation[29]. The activation energy of the first stage exothermic gasification is 174 kJ/mol.

A thermally degraded GAP copolymer is made at 532 K with $\beta = 0.25$, where β is the mass fraction loss obtained by thermal degradation[29]. The exothermic peak is reduced and the first stage reaction is complete at 529 K with $\beta = 0.21$ as shown in Fig. 5-8. The thermally degraded GAP copolymer which is obtained by the interruption of heating at the end of the first stage reaction (537 K with $\beta = 0.42$) shows no exothermic peak. The exothermic reaction of GAP copolymer occurs only in the

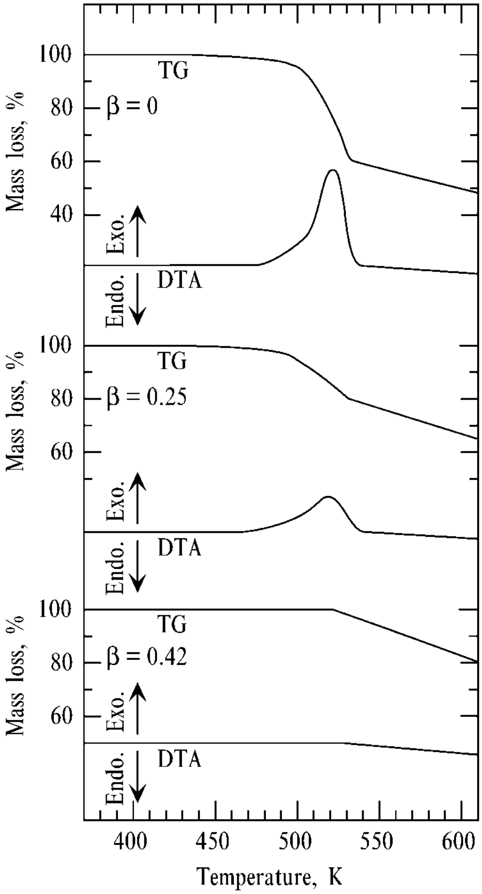

Figure 5-8. Decomposition of thermally degraded GAP showing that the exothermic peak is decreased as the mass fraction of degradation increases.

early stage of decomposition and no exothermic reaction occurs by the gasification of the remaining mass.

The fraction of nitrogen atoms in GAP copolymer decreases linearly as β increases as shown in Fig. 5-9. The mass fraction of 0.68 nitrogen atoms contained in the first stage reaction process ($\beta < 0.41$) and the remaining mass fraction of 0.32 nitrogen atoms is gasified in the second stage reaction process ($\beta > 0.41$). Similarly to the liberation of the nitrogen atoms, the fractions of hydrogen, carbon, and oxygen atoms in GAP copolymer are also liberated linearly as β increases in the range $\beta < 0.41$.

Infrared analysis of GAP copolymer before and after thermal degradation by TG shows that the absorption of the nitrogen triple bond is seen for GAP copolymer ($\beta = 0.0$) in the region of the wave number 2150 cm^{-1}[29]. The nitrogen triple bond absorption is eliminated completely by the thermal degradation ($\beta = 0.41$). The $-N_3$ bonds within GAP copolymer decompose thermally above 537 K to produce N_2. Thus, the gasification of GAP copolymer observed at the first stage occurs by splitting off of the two nitrogen atoms accompanied by heat liberation. The remaining C–H–O molecular fragments decompose at the second stage without heat liberation.

The burning rate of GAP copolymer increases linearly as pressure increases in a ln *p* versus ln *r* plot as shown in Fig. 5-10. The pressure exponent of the burning rate at a constant initial temperature defined in Eq. (3.71) is 0.44. The temperature sensitivity of the burning rate defined in Eq. (3.73) at a constant pressure is 0.010 K^{-1}.

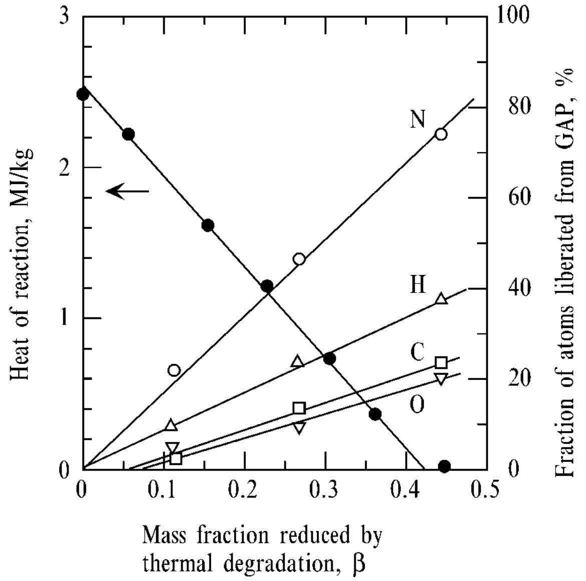

Figure 5-9. Heat of reaction and fraction of atoms liberated from GAP by thermal degradation.

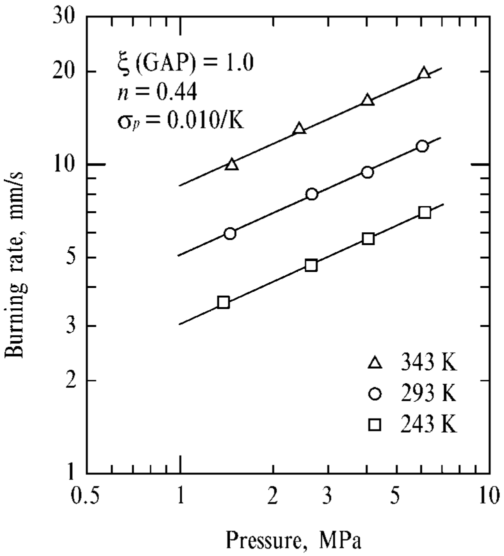

Figure 5-10. Burning rate of GAP copolymer at three different temperatures.

5.2.2.2 Combustion Wave Structure

The combustion wave of GAP copolymer is divided into three zones: zone I is a nonreactive heat conduction zone, zone II is a condensed phase reaction zone, and zone III is a gas phase reaction zone in which final combustion products are formed. Decomposition reaction occurs at T_u in zone II, and gasification reaction is complete at T_s in zone II. This reaction scheme is similar to that of HMX or TAGN shown in Fig. 5-5.

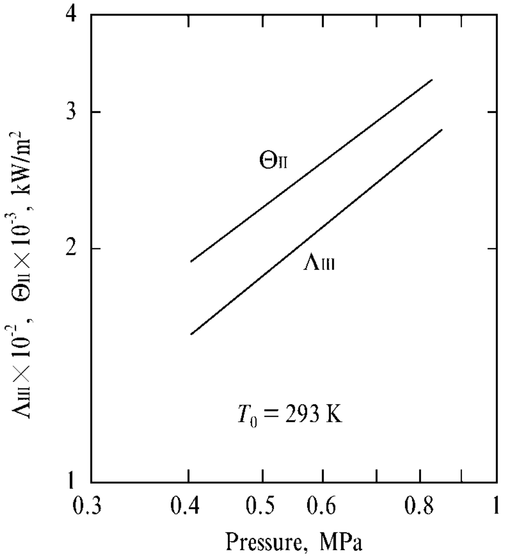

Figure 5-11. The heat flux transferred back from the gas phase to the burning surface and the heat flux produced at the burning surface of GAP copolymer as a function of pressure.

Using Eqs. (5.1) and (5.2), the heat flux in zone II (Θ_{II}) and the heat flux in zone III (Λ_{III}) are determined by temperature profile data in the combustion wave. As shown in Fig. 5-11, both Θ_{II} and Λ_{III} increase linearly as pressure increases in a log – log plot : $\Theta_{II} \sim p^{0.75}$ and $\Lambda_{III} \sim p^{0.80}$. The heat of reaction in zone II (Q_{II}) is determined to be 624 kJ/kg[29]. It is noted that the heat of reaction in zone II of HMX is 300 kJ/kg even though the adiabatic flame temperature of HMX is 1900 K higher than that of GAP copolymer. Furthermore, Λ_{III} of GAP is the same order as Λ_{III} of HMX; however, Θ_{II} of GAP is approximately 10 times larger than Θ_{II} of HMX shown in Fig. 5-6.

5.2.3
Bis-azide methyl oxetane (BAMO)

5.2.3.1 Thermal Decomposition and Burning Rate

When BAMO is heated, an exothermic gasification reaction occurs and is complete when the mass-fraction loss reaches 0.35 as shown in Fig. 5-12. During this gasification process, scission of the two nitrogen triple bonds within BAMO occurs and produces nitrogen gas accompanied by heat release[30]. The remaining part continues to gasify without exothermic reaction at a higher temperature region. For reference, the thermal decomposition process of BCMO is also show in Fig. 5-12. No exothermic reaction occurs during the gasification process. Figure 5-13 shows the decomposition temperature T_d and the exothermic peak temperature T_p as a function of the heating rate of BAMO. Both T_d and T_p shift to a higher temperature region in a ln (θ/T^2) versus $1/T$ plot when the heating rate (θ) is increased. The activation energy of the decomposition is 158 kJ/mol[30].

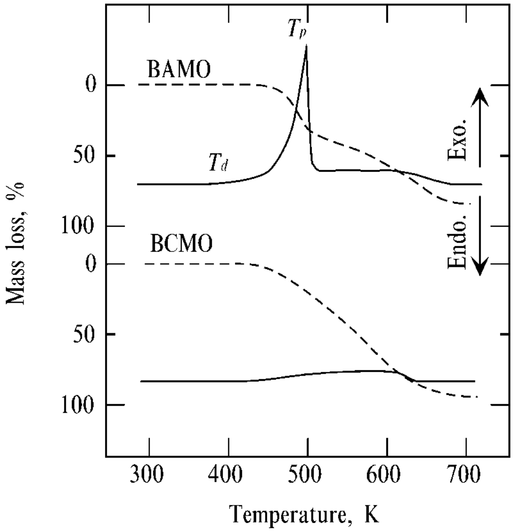

Figure 5-12. BAMO containing of C–N_3 bonds decomposes with rapid heat release accompanied by 0.35 mass fraction loss. On the other hand, BCMO containing of C–Cl bonds decomposes relatively smoothly without heat release.

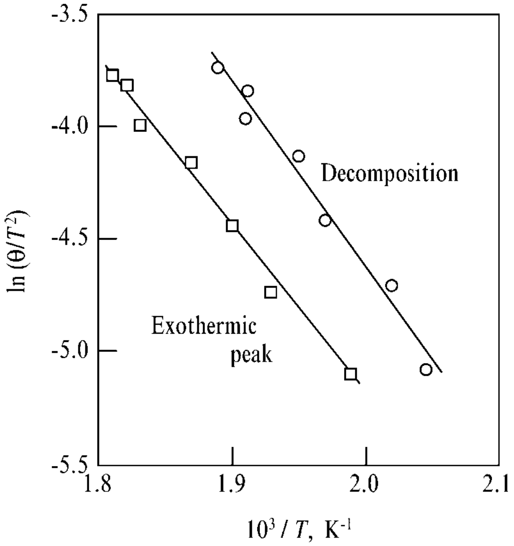

Figure 5-13. Exothermic peak temperature and decomposition temperature of BAMO shift to higher temperature when heating rate is increased.

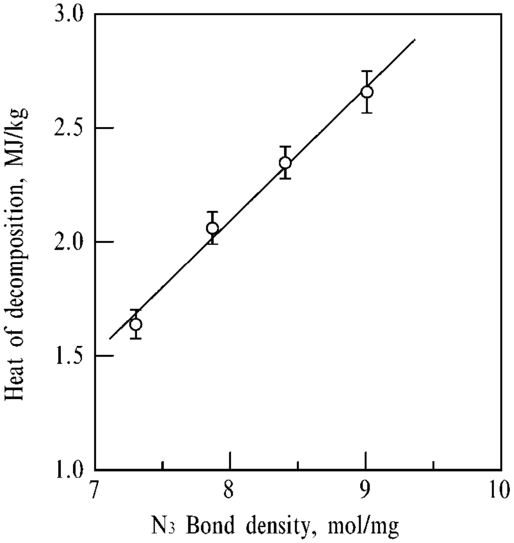

Figure 5-14. Heat of decomposition increases as N3 bond density within BAMO copolymer increases.

The heat of decomposition, Q_d, of BAMO copolymer composed of different levels of N_3 bond density, $\xi(N_3)$, is shown in Fig. 5-14 as a function of $\xi(N_3)$ within BAMO copolymer. BAMO prepolymer is copolymerized by THF. The N_3 bond density is varied by the change of the mass fraction ratio of BAMO prepolymer and THF.

The relationship between Q_d MJ/kg and $\xi(N_3)$ mol/mg measured by a differential scanning calorimeter (DSC) is represented by[31]

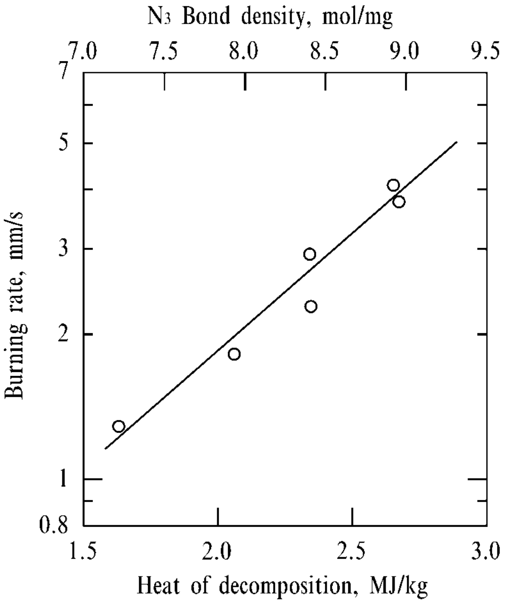

Figure 5-15. Burning rate of BAMO copolymer increases with increasing heat of decomposition and also with increasing N_3 bond density.

$$Q_d = 0.6\,\xi(N_3) - 2.7 \tag{5.7}$$

The heat of decomposition increases linearly as N_3 bond density increases.

The condensed phase reaction zone of a burning-interrupted BAMO copolymer is identified by infrared (IR) spectra analysis. In the nonheated zone, the absorptions of N_3, C–O, C–H, and N–H bonds are seen. In the surface reaction zone (0–0.5 mm below the burning surface), the absorption of N_3 bonds is eliminated. However, the absorptions of C–O, C–H, and N–H bonds remain as observed in the nonheated zone. This suggests that an exothermic reaction occurs by decomposition of N_3 bonds at the subsurface- and surface-reaction zones[30].

The burning rate at $T_0 = 293$ K of BAMO copolymer is shown in Fig. 5-15 as a function of Q_d and $\xi(N_3)$. The linear dependence of the burning rate, r mm/s, in the semi-log plot at 3 MPa is represented by

$$r = 1.84 \times 10^{-4} \exp\,(1.14Q_d) \tag{5.8}$$

The burning rates of BAMO copolymer composed of BAMO/THF = 70/30, 60/40, and 50/50 are shown in Fig. 5-16 as a function of pressure[31]. The burning rate increases linearly in a ln p versus ln r plot as pressure increases at constant T_0. The burning rate is highly sensitive to the mixture ratio of BAMO and THF. Furthermore, the burning rate of BAMO copolymer is also sensitive to T_0. The burning rate of BAMO/THF = 60/40 increases drastically when T_0 is increased at p = constant as shown in Fig. 5-17. The burning rate is represented by

$$r = 0.55 \times 10^{-3}\, p^{0.82} \text{ at } T_0 = 243 \text{ K}$$

$$r = 2.20 \times 10^{-3}\, p^{0.61} \text{ at } T_0 = 343 \text{ K}$$

The temperature sensitivity of burning rate defined in Eq. (3.73) is 0.0112/K at 3 MPa.

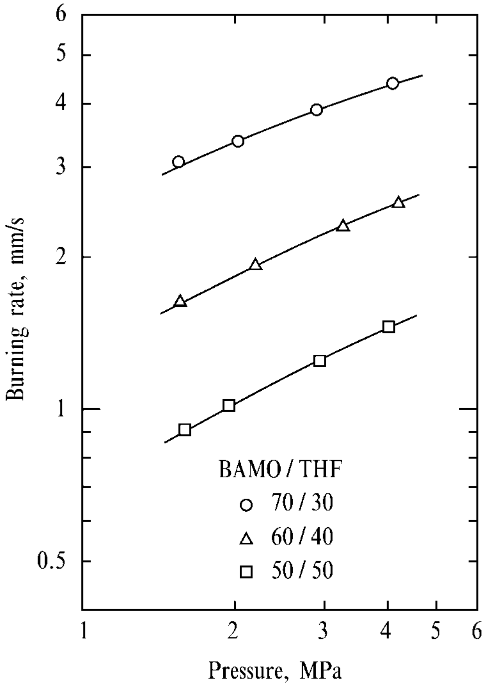

Figure 5-16. Burning rate of BAMO/THF copolymer increases as the mass fraction of BAMO increases at constant pressure.

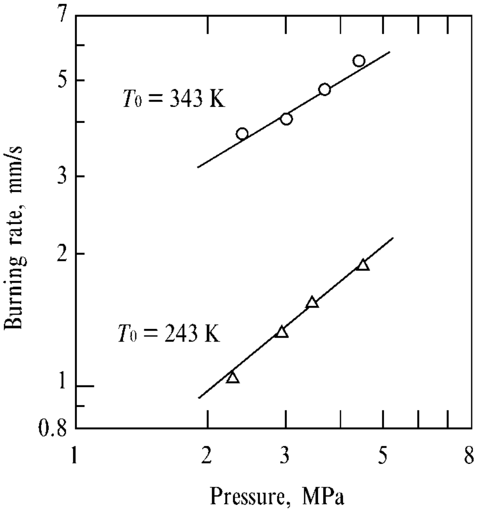

Figure 5-17. Effect of initial temperature on burning rate of BAMO/THF = 60/40 copolymer.

5.2.3.2 Combustion Wave Structure and Heat Transfer

During BAMO copolymer burning in a pressurized inert atmosphere gaseous and carbonaceous solid fragments are formed exothermically at the burning surface. The temperature in the combustion wave of BAMO copolymer increases from the initial temperature T_0 to the burning surface temperature T_s, and to the flame temperature T_f. The burning surface temperature of BAMO copolymer composed of BAMO/THF = 6/4 increases as T_0 increases at constant pressure $p = 3$ MPa : $T_s = 700$ K at $T_0 = 243$ K and $T_s = 750$ K at $T_0 = 343$ K. The effect of T_0 on T_s defined in $(dT_s/dT_0)_p$ is determined to be 0.50[31].

As shown in Fig. 5-18, the temperature gradient in the gas phase at $T_0 = 243$ K and $p = 3$ MPa is a maximum at the burning surface, decreases with distance from the burning surface and becomes zero at about 1.1 mm from the burning surface. When the initial temperature T_0 is increased from 243 K to 343 K, the temperature gradient increases and becomes zero at about 0.7 mm from the burning surface.

The energy conservation equation in the gas phase at steady-state burning is given by Eq. (3.41). If one assumes that the physical properties of λ_g and c_g are constant in the gas phase, Eq. (3.41) can be represented by[31,32]

$$q_d(x) + q_v(x) + q_c(x) = 0 \tag{5.9}$$

$$q_d(x) = \lambda_g \, d^2T/dx^2 : \text{heat flux by conduction} \tag{5.10}$$

$$q_v(x) = -m \, c_g \, dT/dx : \text{heat flux by convection} \tag{5.11}$$

$$q_c(x) = Q_g \omega_g(x) : \text{heat flux by chemical reaction} \tag{5.12}$$

The overall reaction rate in the gas phase $[\omega_g]$ can be represented by

$$[\omega_g] x_g = \int_0^\infty \omega_g(x) dx = m \tag{5.13}$$

Using the burning rate data shown in Fig. 5-17 and the temperature gradient data shown in Fig. 5-18, the heat fluxes given by Eqs. (5.10) – (5.12) are determined as a function of burning distance. As shown in Fig. 5-18, $q_c(x)$ is highest at the burning surface and decreases as the distance increases for both low and high initial temperatures[31]. The convective heat flux $q_c(0)$ at 343 K is 3.3 times higher than the $q_c(0)$ at 243 K, and the reaction distance to complete the gas phase reaction is 1.1 mm for $T_0 = 243$ K and 0.7 mm for $T_0 = 343$ K. Using the data of Figs. 5.17 and 5.18 and Eq. (5.13), $[\omega_g]$ at 3 MPa is determined to be 1.58×10^3 kg/m^{3}s at $T_0 = 243$ K and 7.62×10^3 kg/m^{3}s at $T_0 = 343$ K.

By substitution of T_s data obtained experimentally into Eqs. (3.75) and (3.76), one gets[31]

$Q_s = 457$ kJ/kg at $T_0 = 243$ K

$Q_s = 537$ kJ/kg at $T_0 = 343$ K

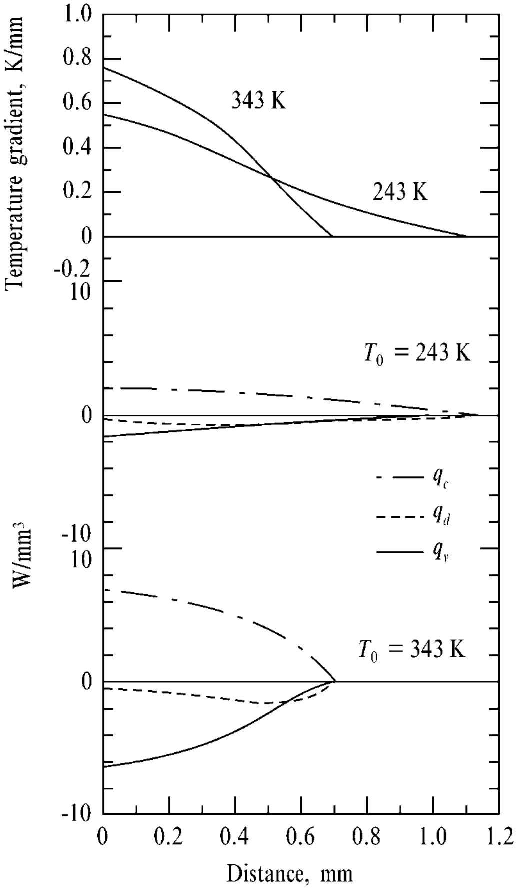

Figure 5-18. Temperature gradient, conductive heat flux, convective heat flux, and heat flux by chemical reaction as a function of distance from burning surface at 3 MPa (initial temperature : 243 K and 343 K) for BAMO/THF = 60/40 copolymer.

Substituting T_s and Q_s data into Eqs. (3.75) and (3.76), the temperature sensitivity of the gas phase Φ defined in Eq. (3.79) and of the solid phase Ψ defined in Eq. (3.80) are determined to be 0.0028 K^{-1} and 0.0110 K^{-1}, respectively: Ψ is approximately four times greater than Φ. The computed σ_p represented by the sum of Φ and Ψ is determined to be $\sigma_p = 0.014\,K^{-1}$ which is approximately equal to the σ_p obtained by burning rate experiments. The heat of reaction at the burning surface is the dominant factor affecting the temperature sensitivity of the burning rate of BAMO copolymer.

References

1 Arden, E. A., Powling, J., and Smith, W. A.W., Observations on the Burning Rate of Ammonium Perchlorate, Combustion and Flame, Vol. 6, No. 1, 1962, pp. 21–33.

2 Levy, J. B. and Friedman, R., Further Studies of Ammonium Perchlorate Deflagration, Eighth Symposium (International) on Combustion, The Williams & Wilkins, Baltimore (1962), pp. 663–672.

3 Bircumshaw, L. L. and Newman, B. H., The Thermal Decomposition of Ammonium Perchlorate I, Proceedings of Royal Society, Vol. A227, No. 1168, 1954, pp. 115–132, and also Bircumshaw, L. L. and Newman, B. H., The Thermal Decomposition of Ammonium Perchlorate II, Proceedings of Royal Society, Vol. A227, No. 1169, 1955, pp. 228–241.

4 Jacobs, P. W. M. and Pearson, G. S., Mechanism of the Decomposition of Ammonium Perchlorate, Combustion and Flame, Vol. 13, 1969, pp. 419–429.

5 Jacobs, P. W. M. and Whitehead, H. M., Decomposition and Combustion of Ammonium Perchlorate, Chemical Reviews, Vol. 69, 1969, pp. 551–590.

6 Jacobs, P. W. M. and Powling, J., The Role of Sublimation in the Combustion of Ammonium Perchlorate Propellants, Combustion and Flame, Vol. 13, 1969, pp. 71–81.

7 Hightower, J. D. and Price, E. W., Combustion of Ammonium Perchlorate, Eleventh Symposium (International) on Combustion, The Combustion Institute, Pittsburgh, PA (1967), pp. 463–470.

8 Guirao, C. and Williams, F. A., A Model for Ammonium Perchlorate Deflagration Between 20 and 100 atm, AIAA Journal, Vol. 9, 1971, pp. 1345–1346.

9 Beckstead, M. W., Derr, R. L., and Price, C. F., The Combustion of Solid Monopropellants and Composite Propellants, Thirteenth Symposium (International) on Combustion, The Combustion Institute, Pittsburgh, PA (1971), pp. 1047–1056.

10 Mitani, T. and Niioka, T., Double Flame Structure in AP Combustion, Twentieth Symposium (International) on Combustion, The Combustion Institute, Pittsburgh, PA (1984), pp. 2043–2049.

11 Manelis, G. B. and Strunin, V. A., The Mechanism of Ammonium Perchlorate Burning, Combustion and Flame, Vol. 17, 1971, pp. 69–77.

12 Brill, T. B., Brush, P. J., and Patil, D. G., Thermal Decomposition of Energetic Materials 60. Major Reaction Stages of a Simulated Burning Surface of NH_4ClO_4, Combustion and Flame, Vol. 94, 1993, pp. 70–76.

13 Tanaka, M. and Beckstead, M. W., A Three Phase Combustion Model of Ammonium Perchlorate, AIAA 96–2888, 32nd AIAA Joint Propulsion Conference, AIAA, Reston, VA (1996).

14 Sarner, S. F., Propellant Chemistry, Reinhold Publishing Corporation, New York (1966).

15 Boggs, T. L., The Thermal Behavior of Cyclotrimethylenetrinitramine (RDX) and Cyclotetramethylenetetranitramine (HMX), Fundamentals of Solid-Propellant Combustion, edited by Kuo, K. K. and Summerfield, M., Progress in Astronautics and Aeronautics, Vol. 90, Chapter 3, AIAA, New York (1984).

16 Kubota, N., Combustion Mechanism of HMX, Propellants, Explosives, Pyrotechnics, Vol. 14, 1989, pp. 6–11.

17 Suryanarayana, B., Graybush, R. J., and Autera, J. R., Thermal Degradation of Secondary Nitramines: A Nitrogen Tracer Study of HMX, Chemistry and Industry, Vol. 52, 1967, p. 2177.

18 Kimura, J. and Kubota, N., Thermal Decomposition Process of HMX, Propellants and Explosives, Vol. 5, 1980, pp. 1–8.

19 Fifer, R. L., Chemistry of Nitrate Ester and Nitramine Propellants, Fundamentals of Solid-Propellant Combustion, edited by Kuo, K. K. and Summerfield, M., Progress in Astronautics and Aeronautics, Vol. 90, Chapter 4, AIAA, New York (1984).

20 Hinshelwood, C. N., The Kinetics of Chemical Change, Oxford University Press, Oxford, 1950.

21 Kubota, N. , Hirata, N., and Sakamoto, S., Combustion Mechanism of TAGN, Twenty-first Symposium (International) on Combustion, The Combustion Institute, Pittsburgh, PA (1986), pp. 1925–1931.

22 Adams, G. K. and Wiseman, L. A., The Combustion of Double Base Propellants, Selected Combustion Problems, Butterworth's Scientific Publications, London, 1954, pp. 277–288.

23 Adams, G. K., The Chemistry of Solid Propellant Combustion: Nitrate Ester of Double Base Systems, Proceedings of the Fourth Symposium on Naval Structural Mechanics, Purdue University, Lafayette, IN (1965), pp. 117–147.

24 Powling, J. and Smith, W. A. W., The combustion of the Butane-2,3- and 4-Diol Dinitrates and Some Aldehyde-Nitrogen Dioxide Mixtures, Combustion and Flame, Vol. 2, No.2, 1958, pp. 157–170.

25 Hewkin, D. J., Hicks, J. A., Powling, J. and Watts, H., The Combustion of Nitric Ester-Based Propellants: Ballistic Modification by Lead Compounds, Combustion Science and Technology, Vol. 2, 1971, pp. 307–327.

26 Robertson, A. D. and Napper, S. S., The Evolution of Nitrogen Peroxide in the Decomposition of Guncotton, Journal of Chemical Society, Vol. 91, 1907, pp. 764–786.

27 Pollard, F. H. and Wyatt, P. M. H., Reactions Between Formaldehyde and Nitrogen Dioxide; Part III, The determination of Flame Speeds, Transactions of Faraday Society, Vol. 46, No. 328, 1950, pp. 281–289.

28 Sawyer, R. F. and Glassman, I., The Reactions of Hydrogen with Nitrogen Dioxide, Oxygen, and Mixtures of Oxygen and Nitric Oxide, Twelfth Symposium (International) on Combustion, The Combustion Institute, Pittsburgh, PA (1969), pp. 469–479.

29 Kubota, N. and Sonobe, T., Combustion Mechanism of Azide Polymer, Propellants, Explosives, Pyrotechnics, Vol. 13, 1988, pp. 172–177.

30 Miyazaki, T. and Kubota, N., Energetics of BAMO, Propellants, Explosives, Pyrotechnics, Vol. 17, 1992, pp. 5–9.

31 Kubota, N., Combustion of Energetic Azide Polymers, Journal of Propulsion and Power, Vol. 11, No. 4, 1995, pp. 677–682.

32 Kubota, N., Propellant Chemistry, Journal of Pyrotechnics, 11 (2000), pp. 25–45.

Propellants and Explosives: Thermochemical Aspects of Combustion. Naminosuke Kubota
Copyright © 2002 Wiley-VCH Verlag GmbH & Co. KGaA
ISBNs: 3-527-30210-7 (Hardback); 3-527-60050-7 (Electronic)

6

Combustion of Double-Base Propellants

6.1

Combustion of NC-NG Propellants

6.1.1

Burning Rate Characteristics

Since the discovery of double-base propellants, also referred to as smokeless powder, numerous investigators have attempted to improve and control their burning characteristics. In the early twentieth century, it was established that the burning rates of many double-base propellants obey a relationship known as Vieille's Law represented by Eq. (3.68), in which the burning rate is proportional to the pressure raised to a power n , known as the pressure exponent of burning rate. Accordingly, extensive experimental and theoretical studies have been done on the combustion of double-base propellants and a number of combustion models have been proposed which describe the combustion wave structure and burning rate characteristics. Some of these results are summarized in Refs. [1–6]. The combustion model was presented first by Crawford, Huggett and McBrady[7], and theoretical models were proposed by Rice and Ginell[8], and Parr and Crawford[9]. The models describe the fundamental process of burning and the rate-determining domains. The photographic observation of the flame structure was done by Heller and Gordon[10] first and then by Kubota[11], Eisenreich[12] and Aoki and Kubota[13].

In the burning process, some oxidizer from the nitrate group, released by thermal decomposition, reacts with the other molecular decomposition products to produce heat. In examining the details of this process, one seeks to understand how they translate into the global characteristics of double-base propellants such as pressure dependency of the burning rate. Typical burning rates of double-base propellants are shown in Figs. 6-1 and 6-2. The burning rate of each propellant increases linearly as pressure increases in a log (pressure) versus log (burning rate) plot. Though the burning rate increases as the energy density (H_{exp}) contained within the propellant increases at the same pressure, the pressure exponent of burning rate n is 0.64 and appears to be independent of H_{exp} (ranging from 3.47 MJ/kg to 4.59 MJ/kg).

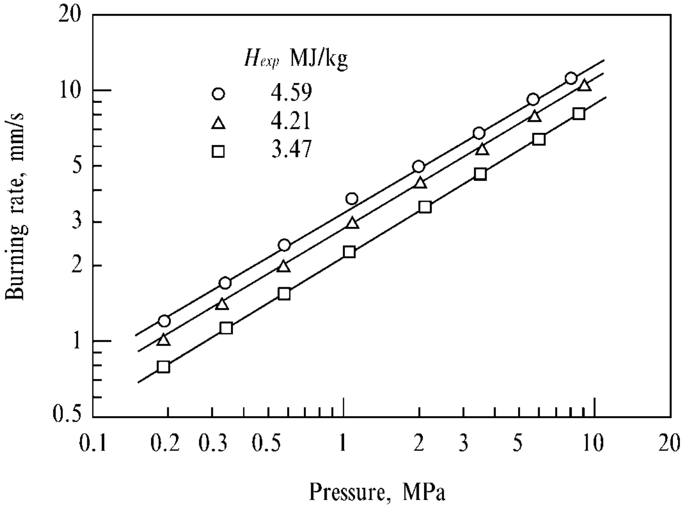

Figure 6-1. Burning rate increases with increasing energy density of NC-NG double-base propellant at constant pressure: the pressure exponent remains unchanged when the energy density is changed.

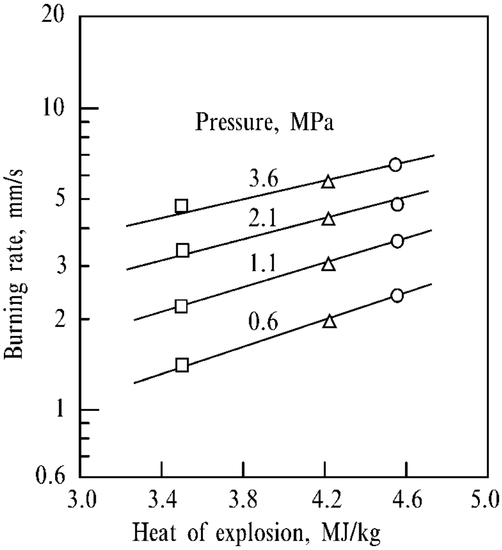

Figure 6-2. Burning rate of NC-NG double-base propellant increases as the heat of explosion increases at constant pressure.

6.1.2
Combustion Wave Structure

The combustion wave of a double-base propellant consists of the following five successive zones as shown in Fig. 6-3, (I) heat conduction zone, (II) solid phase reaction zone, (III) fizz zone, (IV) dark zone, and (V) flame zone[7,10,13,14]:

(I) Heat conduction zone: Though a thermal effect is given by heat conduction from the burning surface, no chemical changes occur. The temperature increases from the initial propellant temperature T_0 to the onset temperature of the solid phase reaction T_u.

(II) Solid phase reaction zone: Nitrogen dioxide and aldehydes are produced in the thermal degradation process. This reaction process occurs endothermically in the solid phase and/or at the burning surface. The interface between the solid phase and the burning surface is composed of a solid/gas and/or solid/liquid/gas thin layer. The nitrogen dioxide fraction exothermically oxidizes the aldehydes at the interface layer. Thus the overall reaction in the solid phase reaction zone appears to be exothermic. The solid phase reaction zone is very thin, and the temperature is approximately equal to the burning surface temperature T_s.

(III) Fizz zone: The major fractions of nitrogen dioxide, aldehydes and other C–H–O and C–H species react to produce nitric oxide, carbon monoxide, water, hydrogen, and carbonaceous materials. This reaction process occurs very rapidly in the early stages of the gas phase reaction zone just above the burning surface.

(IV) Dark zone: Here, the oxidation reactions between the products formed in the fizz zone reaction occur. Nitric oxide, carbon monoxide, hydrogen, and carbonac-

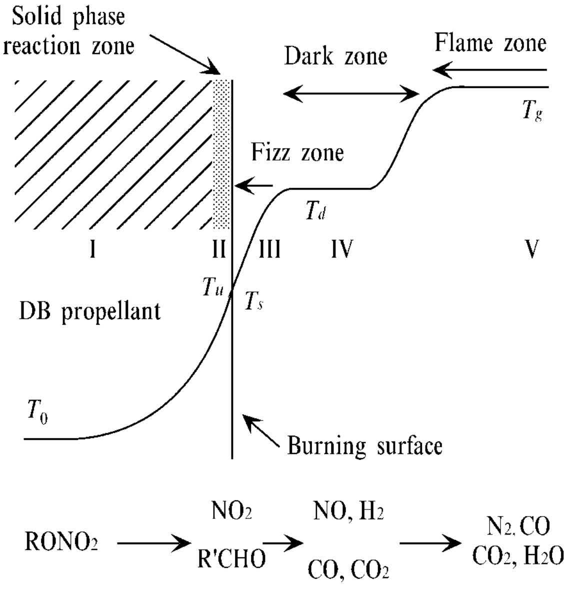

Figure 6-3. Combustion wave structure of double-base propellant.

eous fragments react to produce nitrogen, carbon dioxide, water, etc. These exothermic reactions occur very slowly and only if the temperature or pressure is high enough.

(V) Flame zone: The dark zone reaction occurs rapidly, after an induction time, and produces the flame zone where the final combustion products are formed, and the combustion products reach the thermal equilibrium state. When pressure is low, below about 1 MPa, no flame zone is produced because the reduction reaction of nitric oxide is too slow to produce nitrogen.

The solid phase reaction zone is also termed the subsurface reaction zone or condensed phase reaction zone. The dark zone reaction is the induction zone to produce the flame zone. Thus, the dark zone is also termed the "preparation zone" to produce the luminous flame. Since the flame zone is luminous, it is also termed the "luminous flame zone".

Photographic observations of the flame structure are useful to understand the overall characteristics of double-base propellant combustion. Figure 6-4 shows the flame photographs of a double-base propellant at three different pressures. The propellant strand burns in a chimney-type strand burner pressurized with nitrogen gas. The dark zone is clearly distinguishable between the burning surface and the luminous flame zone. The dark zone of length L_d defined as the distance between the burning surface and the luminous flame front (the fizz zone length L_z is included in L_d since $L_d \gg L_z$), decreases as pressure increases, i.e., the luminous flame approaches the burning surface as pressure increases.

The thermal structure of the combustion wave of double-base propellants is understood from the temperature profile traces in the combustion wave. In the solid phase reaction zone, the temperature in the solid phase increases rapidly from the initial temperature T_0 to the onset temperature of the solid phase reaction zone, T_u

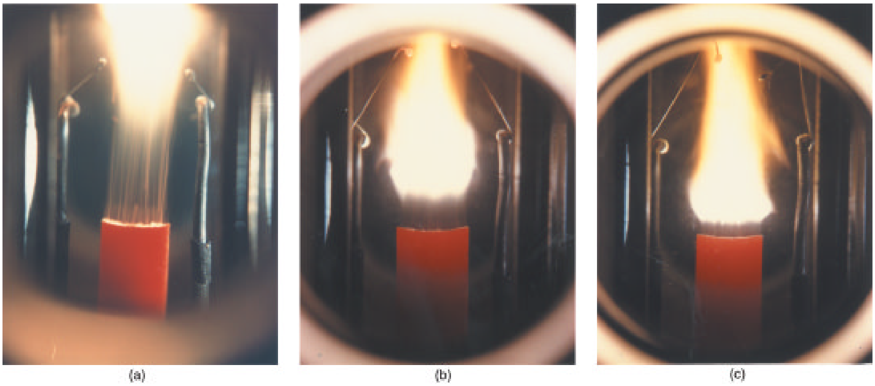
(a) (b) (c)

Figure 6-4. Typical flame photographs of NC-NG double-base propellant:

	p (MPa)	r (mm/s)
(a)	1.0	2.2
(b)	2.0	3.1
(c)	3.0	4.0

just below the burning surface temperature T_s. The Temperature continues to increase rapidly from T_s to the temperature at the end of the fizz zone T_d which is equivalent to the beginning of the temperature of the dark zone. In the dark zone, the temperature increases relatively slowly and the thickness of the dark zone is much greater than that of the solid phase reaction zone or the fizz zone. Between the dark zone and the flame zone, the temperature increases rapidly again and reaches the maximum flame temperature T_g in the flame zone, i.e., the adiabatic flame temperature T_f.

Thus, the combustion wave structure of double-base propellants appears to be a two-stage gas phase reaction: the fizz zone and the dark zone. The thickness of the fizz zone is actually dependent on the chemical kinetics of the gaseous species evolved at the burning surface which in turn is dependent on pressure. The thickness decreases with increased pressure, resulting in an increased temperature gradient. Therefore the rate of heat input by conduction from the gas phase to the solid phase increases with increasing pressure. The length of the dark zone, i.e., the flame standoff distance, decreases also as pressure increases. Subsequently, the luminous flame front approaches the burning surface as shown in Fig. 6-4. When the lengths of both the fizz zone and the dark zone decrease because of the increase of pressure, the burning rate increases simultaneously[10,13].

Since the energy contained per unit mass in a double-base propellant can be altered by changing the mass fraction of NO_2, propellants with varying energy content are formulated using three methods[13]: (1) changing the concentration of plasticizer at constant mixture ratio of NC and NG, (2) changing the mixture ratio of NC/NG, and (3) changing the concentration of nitrate group in NC. Table 6-1 shows the chemical compositions and properties of NC-NG propellants made by method (1). The mixture ratio of NC/NG is kept at 1.307 for the propellants listed. The energy content is changed by the addition of DEP. The mass fraction of NO_2, $\xi(NO_2)$, and the mass fraction of NO, $\xi(NO)$, contained in the propellants are varied from 0.466 to 0.403 and from 0.304 to 0.263, respectively. The adiabatic flame temperature, T_g, is varied from 2760 K to 1880 K.

Table 6-1. Propellant compositions (wt %) and chemical properties.

NC	*NG*	*DEP*	*2NDPA*	*$\xi(NO_2)$*	*$\xi(NO)$*	*T_g K*	*H_{exp} MJ/kg*
53.0	40.5	4.0	2.5	0.466	0.304	2760	4.36
51.3	39.3	7.0	2.4	0.452	0.295	2560	4.22
50.2	38.4	9.0	2.4	0.442	0.288	2420	3.95
48.0	36.7	13.0	2.3	0.422	0.275	2150	3.49
45.8	35.0	17.0	2.2	0.403	0.263	1880	2.98

Figure 6-5 shows the burning rate characteristics as a function of $\xi(NO_2)$. The burning rate increases linearly as pressure increases in ln p versus ln r plots and also increases as $\xi(NO_2)$ increases. The effect of the addition of the plasticizer, DEP, on the burning rate is evident, i.e., the burning rate decreases as the energy content

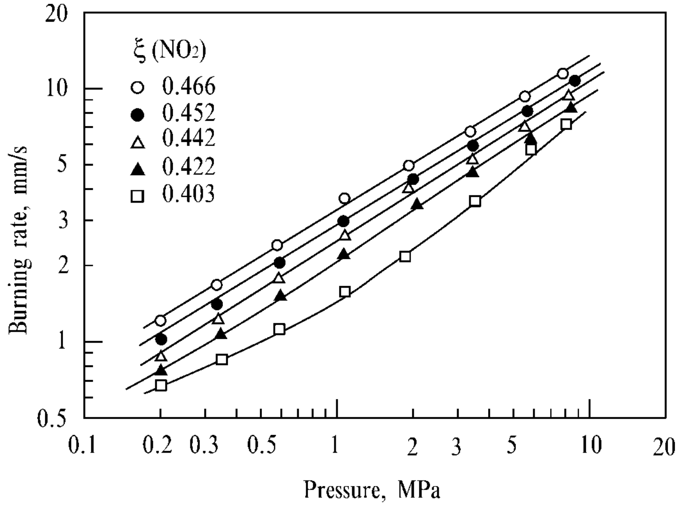

Figure 6-5. Burning rate of double-base propellants increases as pressure increases at constant ξ(NO_2).

(energy density) decreases at constant pressure. The pressure exponent remains unchanged even when the concentration of the plasticizer is changed (n = 0.62), except for the propellant designated by H_{exp} = 2.98 MJ/kg for which the pressure exponent is 0.45 in the low pressure region (below 1.8 MPa) and 0.78 in the high pressure region (above 1.8 MPa).

Since the energy density of double-base propellants is directly correlated with ξ(NO_2), the burning rate shown in Fig. 6-5 is plotted as a function of ξ(NO_2) at different pressures[13]. As shown in Fig. 6-6, the burning rate increases linearly as ξ(NO_2) increases in a ξ(NO_2) versus ln r plot. Combining the results shown in Figs. 6-5 and 6-6, one gets the burning rate expression represented by

$$r = 0.62 \exp\{10.0\,\xi(NO_2)\}\, p^{0.62} \tag{6.1}$$

for the propellants listed in Table 6-1.

Since the final gas phase reaction to produce a luminous flame zone is initiated by the reaction in the dark zone, the reaction time is determined from the dark zone length L_d, i.e., the flame standoff distance. Figures 6-7 and 6-8 show the results for the dark zone length and dark zone temperature, T_d, of the propellants listed in Table 6-1, respectively. The luminous flame front approaches the burning surface and the dark zone length decreases as pressure increases for the propellants. There is no clear difference between the propellants with respect to the dark zone length and the pressure exponent of the dark zone, $d = n - m$, defined in Eq. (3.70) is determined to be approximately –2.0. The overall order of the reaction in the dark zone is also determined to be m= 2.6 for all the propellants. However, the dark zone temperature increases as pressure increases at constant ξ(NO_2) and also increases as ξ(NO_2) increases at constant pressure.

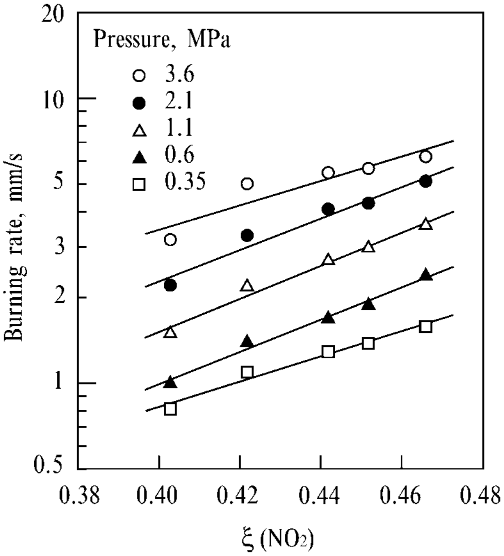

Figure 6-6. Burning rate of double-base propellants increases as ξ(NO_2) at constant pressure.

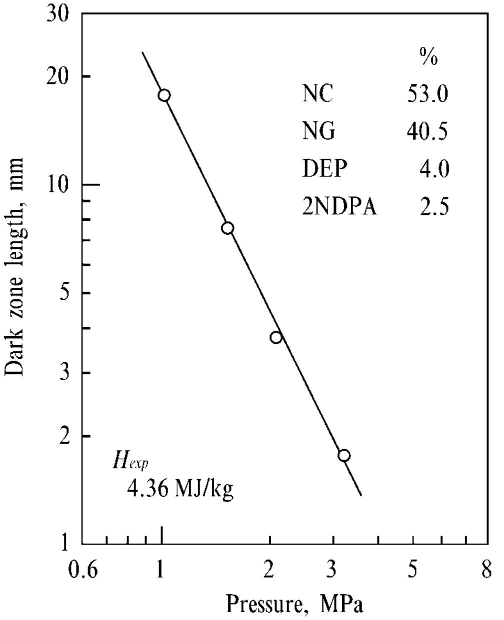

Figure 6-7. Dark zone length (flame standoff distance) decreases as pressure increases.

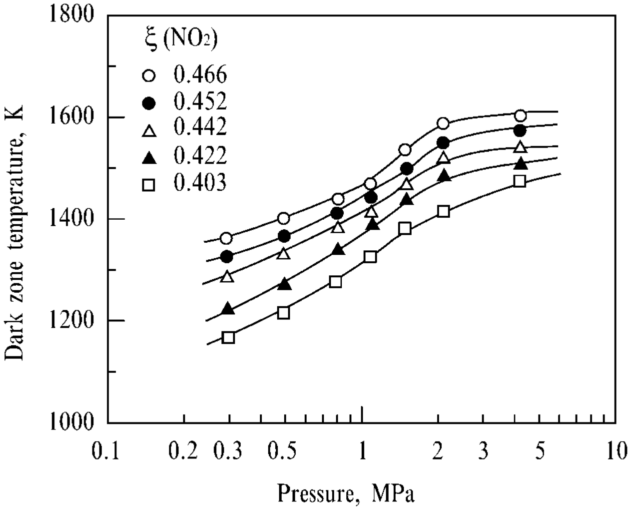

Figure 6-8. Dark zone temperature (temperature at the end of fizz zone) increases as pressure increases and also increases as $\xi(NO_2)$ increases at constant pressure.

The reaction time to produce the luminous flame, τ_d, is given by

$$\tau_d = L_d / u_d \tag{6.2}$$

where L_d is the dark zone length and u_d is the reactive gas velocity in the dark zone. The dark zone velocity is obtained by the mass continuity relationship as

$$u_d = (\rho_p / \rho_d)\, r \tag{6.3}$$

where ρ_d is the density in the dark zone. Using the equation of state, Eq. (1.5), and Eqs. (6.2) and (6.3), τ_d is obtained as

$$\tau_d = pL_d / rR_d\, T_d \tag{6.4}$$

where R_d is the gas constant in the dark zone. Since the dark zone reaction to produce the luminous flame is dependent on the reaction involving NO, not NO_2, the reaction time in the dark zone is plotted as a function of $\xi(NO)$ at different pressures. As is clearly shown in Fig. 6-9, τ_d decreases rapidly as $\xi(NO)$ increases at constant pressure and also decreases as pressure increases at constant $\xi(NO)$. Figure 6-10 shows the relationship between the dark zone temperature and the reaction time in the dark zone plotted as $1/T_d$ versus $\ln(1/\tau_d)$ at different pressures. The activation energy of the dark zone reaction is determined to be 34 ± 2 kJ/mol from the slope of the plotted lines.

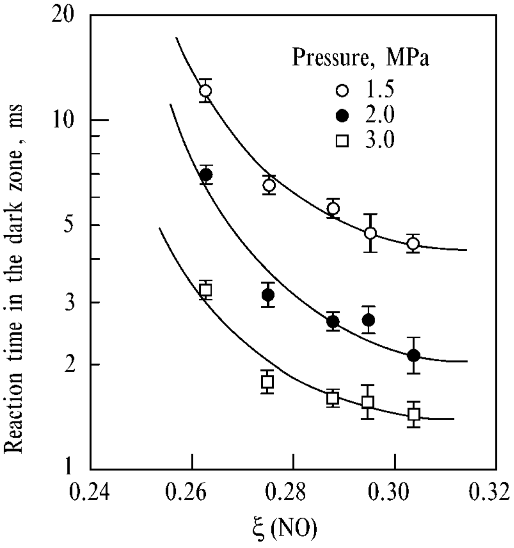

Figure 6-9. Reaction time in the dark zone decreases as ξ(NO) increases at constant pressure.

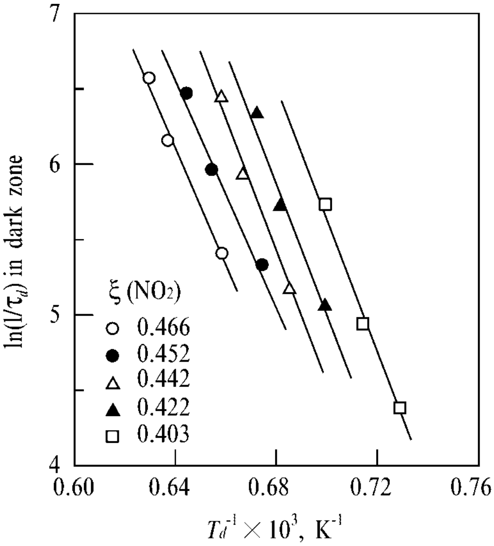

Figure 6-10. Determination of the activation energy in the dark zone at different energy densities of double-base propellants.

The rate of temperature increase in the fizz zone, $(dT/dt)_{f,s}$, indicates the heating rate due to an exothermic reaction in the fizz zone. As shown in Fig. 6-11, the logarithem of the heating rate increases linearly in a plot of ln $(dT/dt)_{f,s}$ versus ξ(NO_2) at 2.0 MPa. The reaction time in the fizz zone, τ_f, is also obtained from a similar relationship to Eq. (6.4) adapted to the fizz zone reaction. Figure 6-12 shows τ_f versus ξ(NO_2) at 2.0 MPa. The logarithm of the reaction time decreases linearly as ξ(NO_2) increases in a plot of lnτ_f versus ξ(NO_2) represented by

$$\tau_f = 2.36 \exp\{-22.0\, \xi(NO_2)\} \qquad (6.5)$$

The heat flux feedback from the fizz zone to the burning surface, $(\lambda_g dT/dx)_{f,s}$, is also computed from the temperature data in the fizz zone. Figure 6-13 shows $(\lambda_g dT/dx)_{f,s}$ (kW/m^2) as a function of $\xi(NO_2)$ at 2.0 MPa, that is represented by

$$(\lambda_g dT/dx)_{f,s} = 4.83 \exp\{10.2\, \xi(NO_2)\} \qquad (6.6)$$

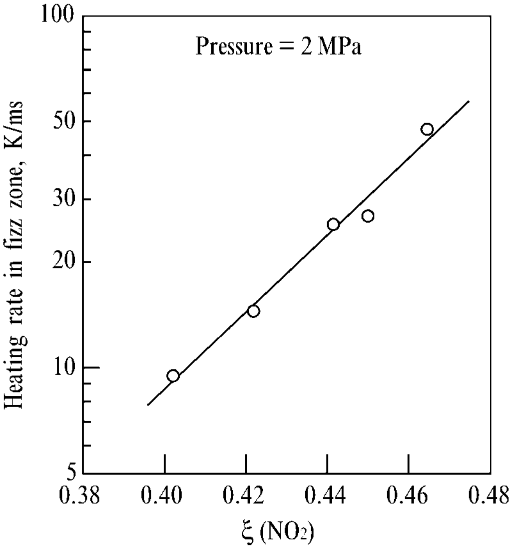

Figure 6-11. Heating rate in the fizz zone increases as $\xi(NO_2)$ increases.

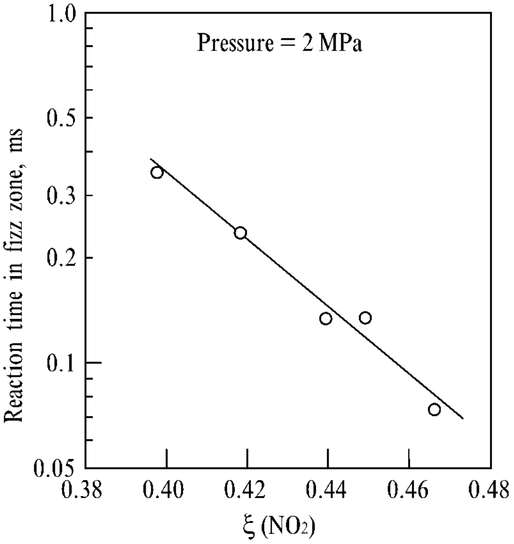

Figure 6-12. Reaction time in the fizz zone decreases as $\xi(NO_2)$ increases.

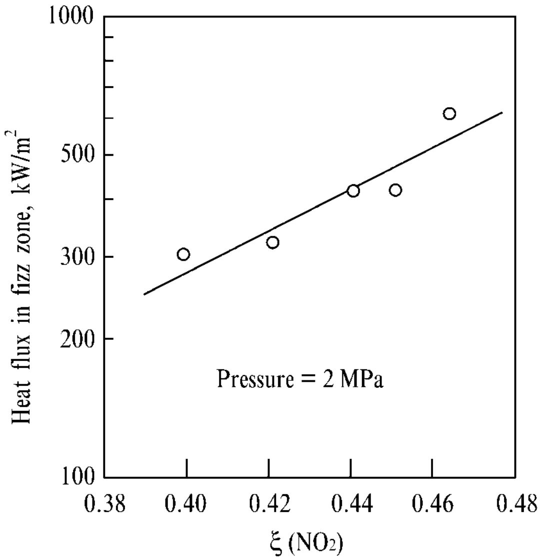

Figure 6-13. Heat flux in the fizz zone increases as ξ(NO_2) increases.

The heat flux feedback from the gas phase to the condensed phase increases as ξ(NO_2) increases, and the burning rate thus increases as the energy density of double-base propellants increases as shown in Figs. 6-1 and 6-2.

6.1.3
Temperature Sensitivity of Burning Rate

The temperature profile in the combustion wave of a double-base propellant is altered when the initial propellant temperature T_0 is increased to $T_0 + \Delta T_0$ as shown in Fig. 6-14. The burning surface temperature T_s is also increased to $T_s + \Delta T_s$ and the temperature of the succeeding gas phase zones, the dark zone from T_d to $T_d + \Delta T_d$, and the final flame temperature from T_g to $T_g + \Delta T_g$. If the burning pressure is low (below about 1 MPa), no luminous flame is formed above the dark zone. The final flame temperature is T_d at low pressures. The burning rate is determined by the heat flux transferred back from the fizz zone to the burning surface and the heat flux produced at the burning surface. The analysis of the temperature sensitivity of double-base propellants described in Section 3.5.4 in Chapter 3 is applied.

Figure 6-15 shows the burning rate and temperature sensitivity of two types of double-base propellants[15]: high energy and low energy propellants. The chemical compositions are shown in Table 6-2. Since DEP is a low energy material, DEP is added to the high energy propellant to formulate the low energy propellant. The burning rates of the high and low energy propellants are approximately straight

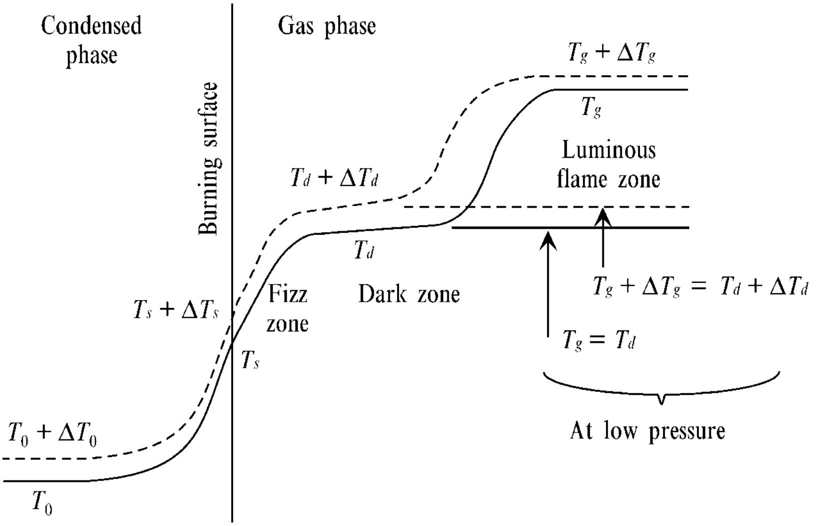

Figure 6-14. Combustion wave structure of a double-base propellant at different initial propellant temperatures and at high- and low-pressures.

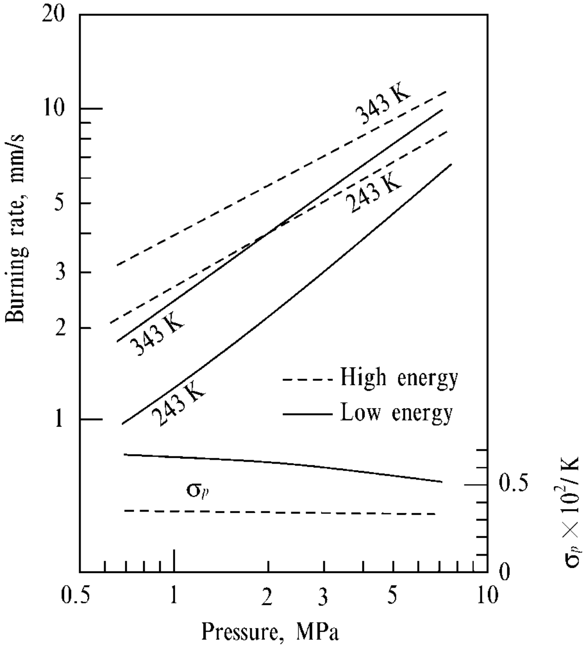

Figure 6-15. Burning rate and temperature sensitivity of high- and low-energy double-base propellants.

lines in a ln p versus ln r plot. The pressure exponents are 0.58 and 0.87 for the high and low energy propellants, respectively. When the initial propellant temperature T_0 is increased from 243 K to 343 K, the burning rate is increased for both propellants. The temperature sensitivity σ_p is 0.0034 K^{-1} for the high energy and is 0.0062 K^{-1} for the low energy propellant at 2 MPa.

Table 6-2. Chemical compositions (wt %) and adiabatic flame temperatures of high and low energy propellants.

Propellant	*NC (12.2 % N)*	*NG*	*DEP*	*T_g (K)*
High energy	55.6	40.4	4.0	2720
Low energy	50.4	36.6	13.0	2110

The dark zone temperature T_d increases with increasing pressure at constant T_0 and also increases with increasing T_0 at constant pressure for both propellants as shown in Fig. 6-16. Though the burning surface temperature T_s increases with increasing T_0, the heat of reaction at the burning surface Q_s remains constant for both propellants. Furthermore, the heat of reaction is approximately the same for the high and low energy propellants. The temperature gradient in the fizz zone increases as T_0 increases at constant pressure and also increases for both propellants. However, the temperature gradient of the high energy propellant is approximately 50 % higher than that for the low energy propellant. The higher temperature gradient implies that the heat flux transferred back from the fizz zone to the burning surface is higher, and the burning rate thus becomes higher for the high energy propellant than for the low energy propellant. The activation energy in the fizz zone is 109 kJ/mol for the high energy propellant and 193 kJ/mol for the low energy propellant.

Substituting the temperature, activation energy in the fizz zone, and burning rate data shown in Fig. 6-16 into Eqs. (3.86), (3.88), and (3.80), the temperature sensitivity of the gas phase, Φ, defined in Eq. (3.79) and the temperature sensitivity of the condensed phase, Ψ, defined in Eq. (3.80) are obtained as[15]

$$\sigma_p = \Phi + \Psi$$

$$0.37 = 0.21 + 0.16 \times 10^{-2}\ /\text{K for the high energy propellant}$$
$$0.64 = 0.41 + 0.23 \times 10^{-2}\ /\text{K for the low energy propellant}$$

The temperature sensitivity of the burning rate consists of 60 % Φ and 40 % Ψ. The lower σ_p of the high energy propellant is due to the lower activation energy and higher temperature in the fizz zone when compared with these values for the low energy propellant.

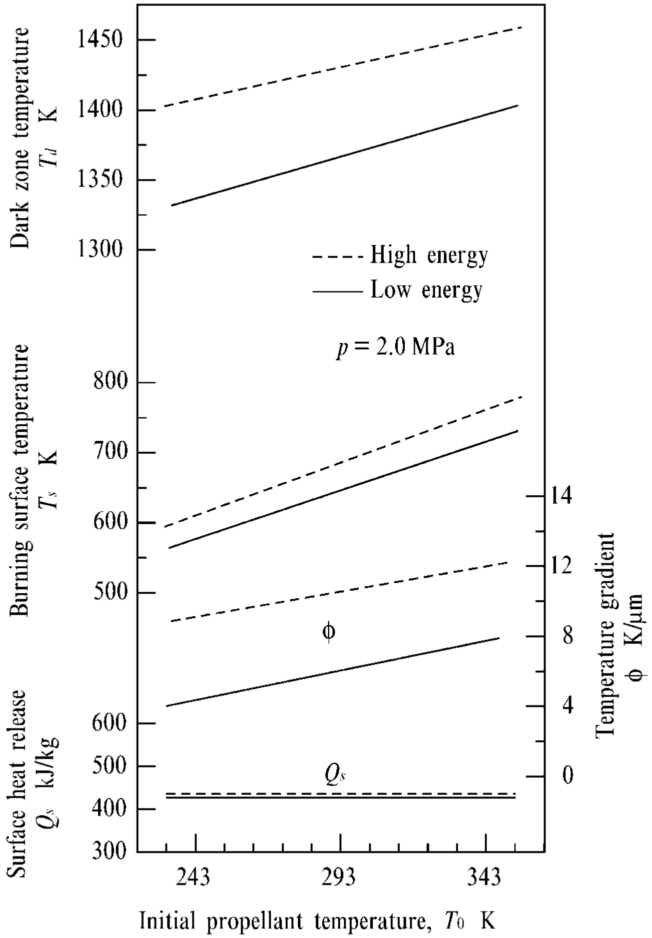

Figure 6-16. Dark zone temperature, burning surface temperature, surface heat release, and temperature gradient in the fizz zone of high- and low-energy double-base propellants as a function of initial propellant temperature.

6.2
Combustion of NC-TMETN Propellants

6.2.1
Burning Rate Characteristics

Figure 6-17 shows a typical example of the comparison of the burning rates of two propellants composed of NC-TMETN and NC-NG. The chemical compositions

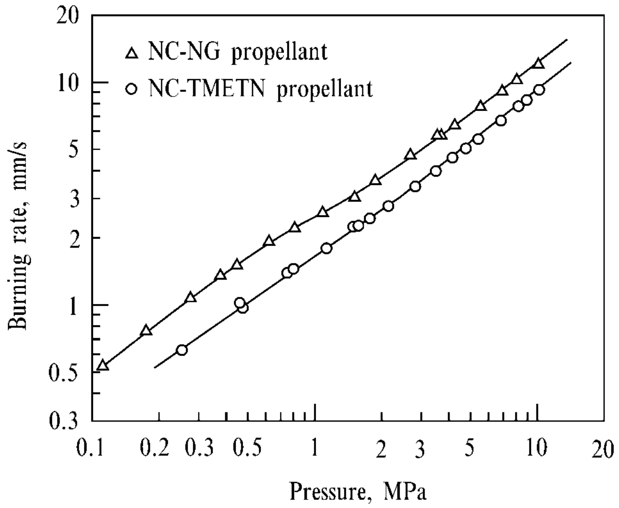

Figure 6-17. Burning rates of NC-NG and NC-TMETN double-base propellants as a function of pressure.

(wt %) and thermochemical properties are shown in Table 6-3. The energy densities of the two propellants are approximately equivalent.

Table 6-3. Chemical compositions and thermochemical properties of NC-NG and NC-TMETN propellants.

	NC-NG	*NC-TMETN*
Ingredients	***wt %***	***wt %***
NC	39.6	53.8
NG	49.4	
TMETN		39.1
DBP	10.0	
TEGDN		7.0
DPA	1.0	
EC		0.1
T_g K	2690	2570
M_g kg/kmol	24.6	23.5
I_{sp} s	242	240

Table 6-3. Continued.

Combustion products	*mole fraction*	*mole fraction*
CO	0.397	0.398
CO_2	0.124	0.104
H_2	0.115	0.143
H_2O	0.238	0.236
N_2	0.124	0.118
H	0.002	0.001

The burning rate of NC-NG propellant is higher than that of NC-TMETN propellant in the pressure range 0.1–10 MPa. However, the pressure exponent appears to be $n = 0.74$ for both propellants. The fundamental burning rate characteristics of NC-TMETN propellants are equivalent to those of NC-NG propellants[10].

6.2.2
Combustion Wave Structure

Since both TMETN and TEGDN are liquid nitrate esters at room temperature, the fundamental thermochemical properties are equivalent to those of NG. The burning rate and the pressure exponent of NC-NG and NC-TMETN propellants appear to be approximately equivalent. The burning process and the combustion wave structure of NC-TMETM appear to be equivalent to those of NC-NG also. The flame structure of NC-TMETN consists of two-stage reaction zones: fizz zone, dark zone, and luminous flame zone as shown in Fig. 6-3. The major oxidizer fragment is NO_2 in the fizz zone and a rapid temperature rise is due to the exothermic reduction of NO_2. In the dark zone, a slow reaction oxidation by NO generates the flame zone at some distance from the burning surface. Accordingly, the burning rate is dependent on the heat flux transferred back from the fizz zone to the burning surface and the heat flux generated at the burning surface. The temperature sensitivity of burning rate and the catalyst action on the combustion zone are equivalent to those of NC-NG propellants[10].

6.3
Combustion of Nitro-Azide Propellants

6.3.1
Burning Rate Characteristics

The burning rate of nitro-azide propellants composed of NC, NG, and GAP is shown in Fig. 6-18. As a comparison, the burning rate of double-base propellants

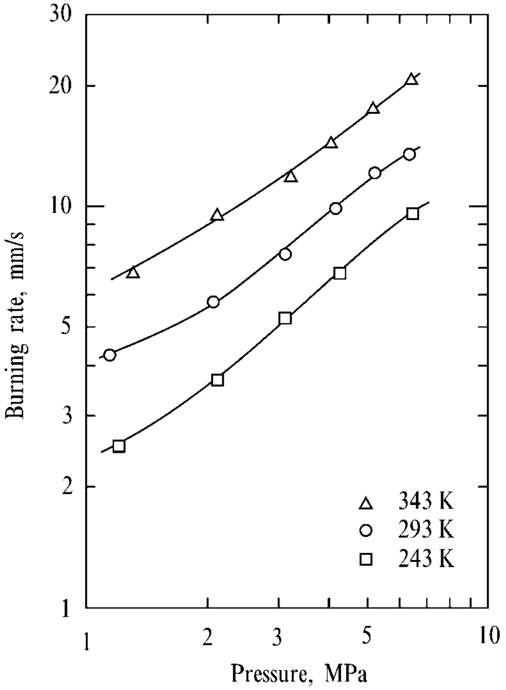

Figure 6-18. Burning rate of a nitro-azide (NC-NG-GAP) propellant at different initial propellant temperatures showing high temperature sensitivity.

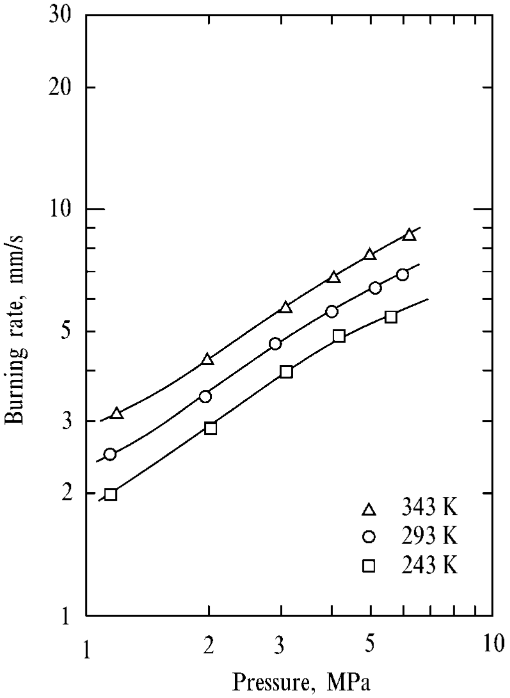

Figure 6-19. Burning rate of a double-base (NC-NG-DEP) propellant at different initial propellant temperatures showing low temperature sensitivity.

composed of NC, NG, and DEP is shown in Fig. 6-19. The chemical compositions of both propellants are shown in Table 6-4. The adiabatic flame temperature is increased from 2560 K to 2960 K when 12.5 % of DEP is replaced with the same amounts of GAP. The specific impulse is also increased from 237 s to 253 s by the same replacement of DEP with GAP.

Table 6-4. Chemical compositions and physicochemical properties (at 10 MPa) of NC-NG-DEP and NC-NG-GAP propellants

	NC-NG-GAP	***NC-NG-DEP***
Ingredients	***wt %***	***wt %***
NC	50.0	50.0
NG	40.0	40.0
GAP	12.5	
DEP		12.5
T_g K	2960	2560
M_g kg/kmol	25.0	24.0
I_{sp} s	253	237
Combustion products	***mole fraction***	***mole fraction***
CO	0.337	0.414
CO_2	0.134	0.110
H_2	0.091	0.134
H_2O	0.259	0.222
N_2	0.169	0.119

Though both propellants contain the same amount of NC and NG, the burning rate of NC-NG-GAP is increased approximately 70 % by the replacement of DEP with GAP at $T_0 = 293$ K. The pressure exponent of the burning rate remains relatively unchanged, $n = 0.7$, by the replacement of DEP with GAP. However, the temperature sensitivity of the burning rate defined in Eq. (3.73) is increased significantly from 0.0038 K^{-1} to 0.0083 K^{-1}.

6.3.2
Combustion Wave Structure

The combustion wave of NC-NG-GAP propellant consists of successive two-stage reaction zones[16]. The first gas phase reaction occurs at the burning surface and the temperature increases rapidly in the fizz zone. The second zone is the dark zone which separates the luminous flame zone from the burning surface. Thus, the luminous flame stands some distance above the burning surface. This structure is equivalent to that of the NC-NG double-base propellants described in this section. The temperature in the dark zone is increased from 1400 K to 1550 K at 3 MPa when DEP is replaced with GAP. Though the reaction time in the dark zone is shortened by the replacement of GAP, the flame standoff distance is increased because of the increased flow velocity in the dark zone. The overall order of the chemical reaction determined by the relationship $d = m - n$ is determined as $d = -1.7$ and $n = 2.4$ for NC-NG-DEP and $d = -1.7$ and $n = 2.5$ for NC-NG-GAP propellants[16]. The results indicate that the basic chemical mechanism in the gas phase, which involves the reduction of NO to N_2, remains unchanged by the replacement of DEP with GAP. However, the increased burning rate and temperature sensitivity of the burning rate when DEP is replaced with GAP indicate that the rate control process of the burning rate is changed by the increased surface heat release Q_s of GAP similar to the high burning rate and high temperature sensitivity of the burning rate of GAP[16] as described in Section 5.2 in Chapter 5.

6.4
Catalyzed Double-Base Propellants

6.4.1
Super-Rate, Plateau, and Mesa Burning

During the Second World War, the accidental discovery was made that the use of lead compounds as lubricants in the propellant extrusion process resulted in a greatly increased pressure exponent of burning rate at low pressures, as manifested in an increased burning rate in this range. Investigation of this phenomenon brought to light the fact that the presence of small quantities of a variety of lead compounds creates similar increases in burning rate at low pressures. Further exploration of this “super-rate burning” phenomenon led to the discovery of the “plateau burning” region and the “mesa burning” region.

It was soon realized that platonized propellants, with their reduced temperature sensitivity in the plateau and mesa burning range, could be used effectively to minimize the sensitivity of the performance of a rocket to the temperature of the environment. Much work has been devoted to understanding the mechanism of plateau and mesa burning, with a view to optimizing the performance characteristics of rocket motors.

The super-rate, plateau and mesa burning characteristics of catalyzed double-base propellants are defined in Fig. 6-20. The first published reference to the latter was from the Allegheny Ballistics Laboratory (ABL) in 1948[10]. Since then, extensive work has been carried out, largely with metal compounds, in developing super-rate, plateau and mesa burning propellants for practical use. For a time it appeared that the addition of a wide variety of metal compounds increased the burning rate. However, the increases in burning rate so obtained were insignificant compared with the increases obtained when lead compounds were added to propellants. Furthermore, it was recognized that metal compounds other than lead compounds did not give plateau and mesa burning in the pressure range of rocket combustion. Thereafter, the search for metal compounds giving plateau burning was focused largely on lead

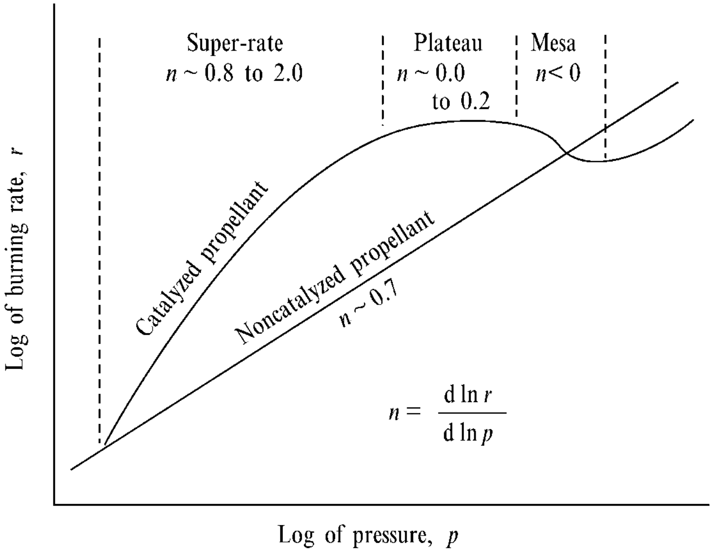

Figure 6-20. Definition of super-rate, plateau, and mesa burnings of a catalyzed double-base propellant.

compounds; it was soon discovered that most lead compounds in adequate amounts give plateau type burning[10].

The pressure exponent of burning rate is commonly used to evaluate the effectiveness of catalysts in producing plateau and mesa burning[17–21]. The pressure exponent is approximately zero for plateau burning and negative for mesa burning, as shown in Fig. 6-20. The pressure exponent and the domain of super-rate, plateau and mesa burning are greatly dependent upon the physical and chemical properties of lead compounds, properties such as quantity, particle size, and chemical structure. Several kinds of lead compounds, such as $PbBr_2$, PbI_2, and $PbCl_2$, do not yield a reduced pressure exponent. Aliphatic lead salts give plateau burning at low pressures with low burning rate, while aromatic lead salts give plateau burning at high pressures with high burning rates[10].

6.4.2
Combustion Mechanisms of Super-Rate Burning

6.4.2.1 Burning Rate Characteristics

Figure 6-21 shows a typical set of burning rates of a catalyzed and a noncatalyzed NC-NG double-base propellants. The burning rate of the noncatalyzed propellant composed of NC 53 %, NG 40 %, and DEP 7 %, increases linearly as pressure increases in a ln p versus ln r plot. When the propellant is catalyzed with 1.5 % lead salicylate (PbSa), 1.5 % lead 2-ethylhexoate (Pb2EH), and graphite 0.2 %, the burning rate increases drastically (super-rate burning) at the low pressure region below 5 MPa, becomes pressure insensitive (plateau burning) between 5 MPa and 7 MPa,

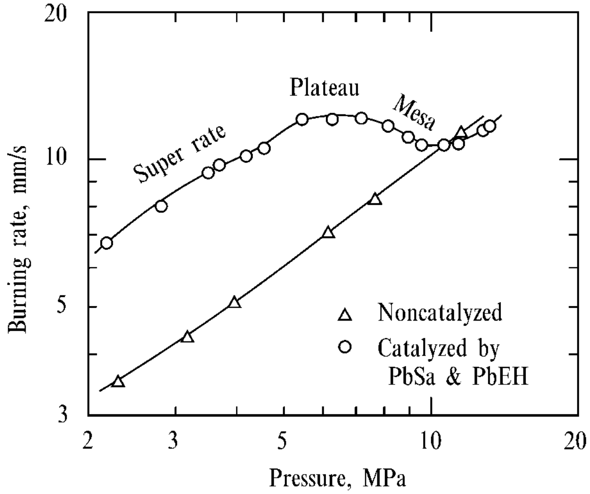

Figure 6-21. A typical burning rate of a platonized double-base propellant.

and decreases as pressure increases (mesa burning) between 7 MPa and 11 MPa. The burning rate returns to the burning rate of the noncatalyzed propellant above 11 MPa where the effect of the addition of the catalysts diminishes[10].

Figure 6-22 shows a comparison of the burning rates of catalyzed NC-NG and NC-TMETN propellants. As shown in Table 6-5, the chemical compositions of both

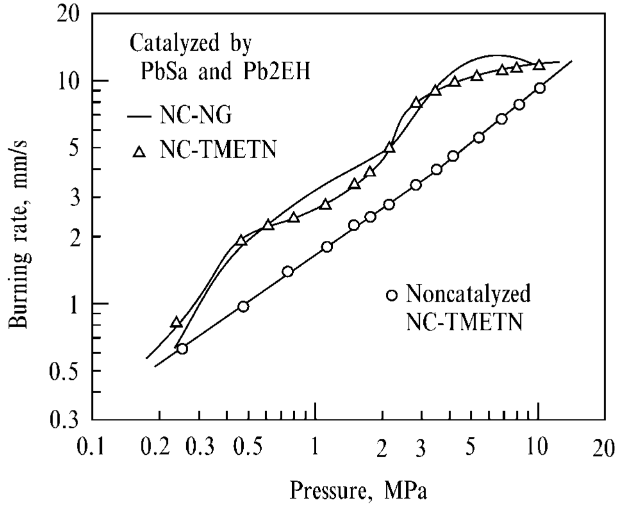

Figure 6-22. Burning rates of catalyzed NC-NG and NC-TMETN double-base propellants: two platonized regions for both propellants by the addition of two lead compounds.

propellants are catalyzed with the same types and the same amounts of catalysts. The burning rates of noncatalyzed NC-NG and NC-TMETN propellants are shown in Fig. 6-17. The energy densities of the two catalyzed propellants are approximately equivalent to each other.

Table 6-5. Chemical compositions of catalyzed NC-TMETN and NC-NG double-base propellants (wt %).

Propellant	*NC*	*TMETN*	*TEGDN*	*NG*	*DEP*	*EC*	*PbSa*	*Pb2EH*
NC-TMETN	50.0	40.4	7.1			0.1	1.2	1.2
NC-NG	50.0			37.1	9.5	1.0	1.2	1.2

The burning rate curves show approximately similar characteristics: at low pressures no super-rate burning occurs for either propellant. Since two kinds of lead catalysts are added to both propellants, two super-rate and two plateau burning zones are seen for both propellants in the same pressure regions. Around 0.5 MPa the maximum super-rate burning is formed, and again relatively high super-rate burning takes place at about 4 MPa. Above 10 MPa super-rate burning is not longer evidenced and burning rates of the two catalyzed propellants are almost the same as those for the noncatalyzed propellants. Though the burning rate versus pressure relationships of NC-NG and NC-TMETN are not quite the same because of small differences in the chemical structure and energy levels of the propellants, the burning characteristics of NC-NG and NC-TMETN propellants are similar, and the action of the catalysts in producing super-rate, plateau, and mesa burning are the same for both propellants.

With super-rate and plateau burning, the temperature sensitivity decreases when pressure is increased; moreover, the lowest temperature sensitivity always appears at the upper end of the plateau burning region, i.e., in the mesa burning region[10]. At pressures above that of mesa burning, greatly increased temperature sensitivity is observed. A further observation indicates that, between certain initial propellant temperatures, there is negative temperature sensitivity in the mesa burning region of some propellants. No negative temperature sensitivity has been reported in the super-rate region.

Plateau burning characteristics are dependent on the chemical component and type of catalysts. The effects of aromatic lead and copper salts on burning rate behavior are shown in Fig. 6-23. The addition of PbSa (1 %) increases the burning rate in the range 0.1 MPa to 7 MPa and produces plateau and mesa burning above 7 MPa. CuSa (1 %) increases the burning rate below 3 MPa and decreases the burning rate above 6 MPa. When PbSa (1 %) and CuSa (1 %) are mixed together, an enhanced super-rate is formed in the region between 0.7 MPa and 6 MPa, and plateau and mesa burning are formed above 7 MPa. An effect on burning rate of coupling between the PbSa and CuSa catalysts occurs. Burning rate does not increase when additional PbSa or CuSa is admixed; apparently the rate accelerating effect is saturated,

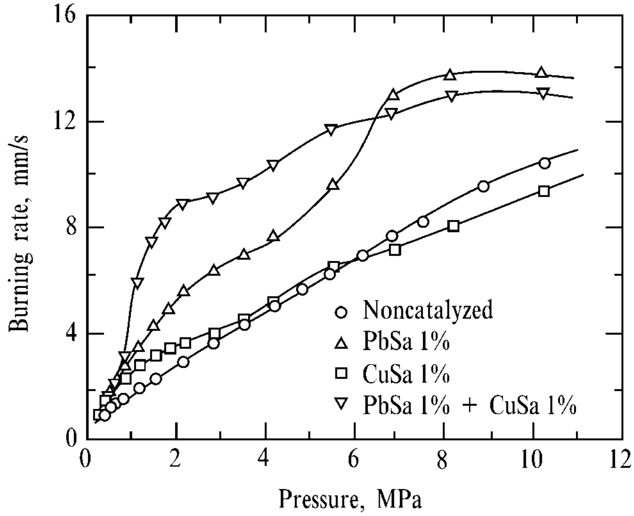

Figure 6-23. Various types of plateau burning by the addition of different types of catalysts.

The effect of the addition of metallic lead and copper powders on super-rate burning is shown in Fig. 6-24. Pb powder is more effective than Cu powder in increasing the burning rate. When these powders are mixed into the noncatalyzed propellant, there is no drastic burning rate increase, i.e., no super-rate burning is observed. However, when PbO powder (1 %) is added, the burning rate is increased approximately 250 %, i.e., there is super-rate burning.

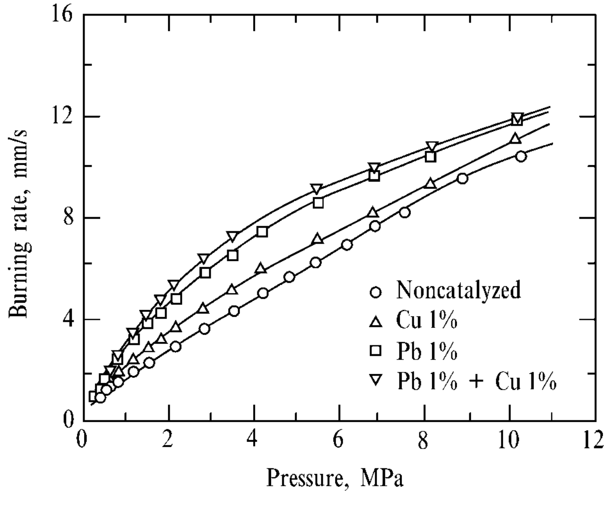

Figure 6-24. Burning rate of double-base propellant increases by the addition of metallic copper and/or lead powders.

Higher lead salt concentrations shift the region of plateau burning to lower pressures, and this also occurs when carbon powder is added to plateau-burning propellants. Above 0.5 % carbon, the plateau slope increases with increasing carbon content at a less-than-proportional rate, and the relative increase of plateau pressure falls off. Above 1 % carbon the plateau disappears. Small-particle carbon powder apparently result in higher burning rates, but, with particles greater than 0.1 μm in size, little or no rate increase is observed. Preckel observed a similar effect on plateau burning when hydrated alumina or acetylene black was added to plateau propellants. However, titanium oxide, magnesium oxide and levigated alumina are not effective in this regard. Solid carbon is not the only catalyst to enhance super-rate burning; there are others such as copper salicylate. The effectiveness of solid carbon in enhancing super-rate burning increases as the specific area of the carbon particles (ca. 0.01–1.0 μm) is increased.

Investigation of the effects of metal oxides showed that the burning rates of the propellants containing Fe_2O_3, Co_2O_3, CuO, ZnO, SnO_2, and Al_2O_3 increased linearly with pressure, i.e., no plateau and mesa burning was observed. PbO was the only metal oxide to produce super-rate, plateau and mesa burning. The increased burning rate at low pressure with PbO was much higher than that with other metal oxides. The burning rate of the basic propellant was reduced by the addition of MgO and NiO over the entire pressure range in which the tests were conducted. Finally, it is reported that metallic nickel powder decreases the burning rate at low pressures and causes a slight increase at high pressures.

The effectiveness of lead compounds in producing super-rate burning decreases as the propellant's heat of explosion increases[10]. This implies that propellants with a lower content of NG or lower nitrated NC are strongly influenced by lead compounds.

The propellants composed of NC-NG and HMX show super-rate and plateau burning rate characteristics as shown in Fig. 6-25[20]. The chemical compositions on noncatalyzed and catalyzed propellants are shown in Table 6-6.

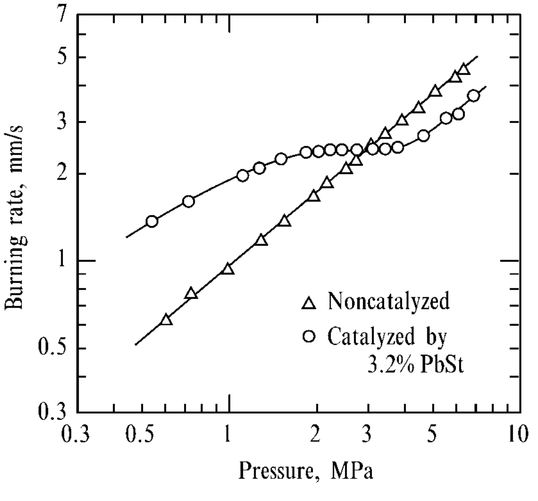

Figure 6-25. Plateau burning of a wide pressure range (1.6 MPa–3.6 MPa) by the addition of 3.2 % PbSt.

Table 6-6. Chemical composition of super-rate and plateau burning propellant (wt %).

NC	*NG*	*HMX*	*DEP*	*SOA*	*PbSt*
42	18	22	8	6.8	3.2

The noncatalyzed burning rate (without 3.2 % PbSt) gives approximately a straight line in a ln p versus ln r plot. The pressure exponent n is 0.85 in the pressure range 0.6–7 MPa. When the noncatalyzed propellant is catalyzed with 3.2 % PbSt, super-rate burning at low pressures (< 1.6 MPa) are significantly greater than in the case of the noncatalyzed propellant. A wide range plateau burning of 2.4 mm/s occurs at pressures between 1.6 MPa and 3.6 MPa. Above the plateau burning region, the burning rate and pressure exponent increase again with increasing pressure[20].

6.4.2.2 Combustion Wave Structure

The flame structures of the noncatalyzed and catalyzed propellants shown in Fig. 6-25 are similar except for the flame standoff distance, i.e., dark zone length, as shown in Fig. 6-26. The dark zone lengths of both propellants decrease with increas-

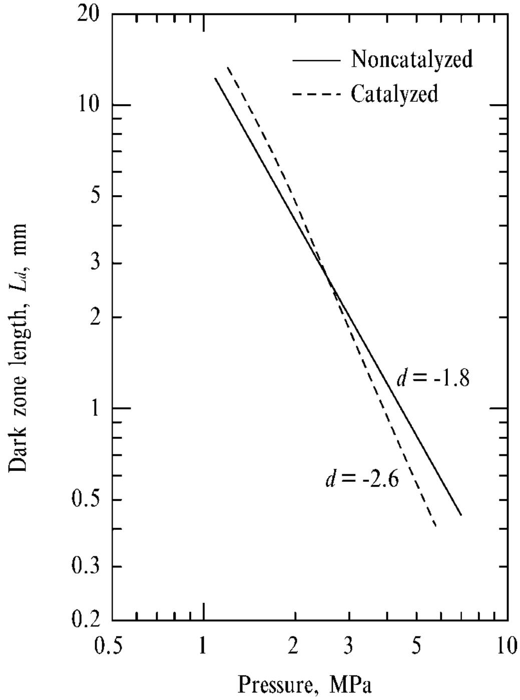

Figure 6-26. The luminous flame front of the patonized propellant approaches more rapidly than that of the noncatalyzed propellant when pressure is increased in the plateau pressure region.

ing pressure which is represented by Eq. (5.4). The dark zone pressure exponent m of the noncatalyzed propellant is –1.8 throughout the pressure range from 1.2–5 MPa. On the other hand, the exponent of the catalyzed propellant is –2.0 in the super-rate region below 1.6 MPa and –2.6 in the plateau region between 1.6 MPa and 3.6 MPa.

The overall order of the reaction in the dark zone defined in Eq. (5.6) is 2.6 for each propellant whether it contains the catalyst or not. The value remains unchanged for the catalyzed propellant not only in the super-rate region ($n = 0.5$ and $d = -2.0$) but also in the plateau region ($n = 0.0$ and $d = -2.6$). This suggests that the reaction mechanism in the dark zone, which involves the reduction of NO to N_2, remains unchanged by the addition of the catalyst. It should be noted that while the burning rate is constant in the plateau region, the luminous flame of the catalyzed propellant stands at a slightly greater distance from the burning surface and approaches the burning surface more rapidly than in the case of the noncatalyzed propellant when the pressure is increased. The luminous flame reaction occurs too far away from the burning surface to cause the observed plateau burning rate. Accordingly, the conductive heat flux from the luminous flame is not responsible for plateau burning, as it is in the case of normal burning.

The temperature at the end of the fizz zone, i.e., at the beginning of the dark zone, of the catalyzed propellant is approximately 1400 K, which is slightly higher than at for the noncatalyzed propellant. The temperature gradient just above the burning surface φ, i.e., in the fizz zone, is significantly different for the two propellants, as shown in Fig. 6-27. The slope increases linearly with pressure in a ln φ_n vs ln p plot for the noncatalyzed propellant. The catalyzed propellant exhibits a significantly different temperature gradient behavior from that of the noncatalyzed propel-

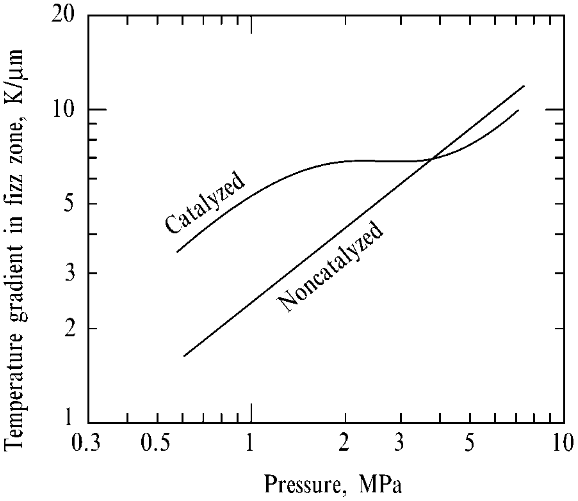

Figure 6-27. Temperature gradient in the fizz zone increases in the super-rate burning region and remains unchanged in the plateau pressure region.

lant. In the super-rate burning region, φ_c is increased, more than doubled, by the addition of the catalyst. In the plateau region, φ_c becomes nearly pressure independent where the burning rate is constant. The gradient is represented by $\varphi_n = b_n\, p^{0.85}$ for the noncatalyzed propellant and by $\varphi_c = b_c\, p^{0.0}$ for the catalyzed propellant[20]. The subscripts n and c denote the noncatalyzed and the catalyzed propellants, respectively. These pressure exponents are approximately equal to the pressure exponent of the burning rate, n, for each of the propellant burning rates. In other words, the burning rate behavior is governed by the conductive heat feedback from the fizz zone to the propellant burning surface.

The effect of catalyst activity of burning rate defined by

$$\eta_r = \frac{r_c - r_n}{r_n} \tag{6.7}$$

while the catalyst activity in the fizz zone is defined by

$$\eta_f = \frac{\tau_{f,n} - \tau_{f,c}}{\tau_{f,n}} \tag{6.8}$$

where τ_f is the reaction time in the fizz zone. If one assumes that $\varphi = (T_d - T_s)/L_f$ where L_f is the fizz zone length, one gets

$$\eta_f = 1 - \frac{\varphi_n r_n}{\varphi_c r_c} \tag{6.9}$$

The catalyst activity in the dark zone is also defined by

$$\eta_{\mathrm{d}} = \frac{\tau_{d,n} - \tau_{d,c}}{\tau_{d,n}} \tag{6.10}$$

$$= 1 - \frac{r_n L_{d,c}}{r_c L_{d,n}}$$

where τ_d is the reaction time in the dark zone, which is given by Eq. (6.2).

If the catalyst acts in the fizz zone or in the dark zone, $\eta_{f,c}$ or $\eta_{d,c}$ becomes smaller than $\eta_{f,n}$ or $\eta_{d,n}$, respectively. As shown in Fig. 6-28, the behavior of η_f corresponds to the behavior of η_r. Both catalyst activities have positive values in the super-rate region and decrease with increasing pressure in the plateau region, and finally both values become negative above 3 MPa. This indicates that the catalyst acts as a positive catalyst in the fizz zone, increasing the burning rate below 3 MPa, but acts as a negative catalyst reducing the burning rate, above 3 MPa. On the other hand, η_d is approximately zero in all regions, super-rate, plateau, and mesa burning. There is action of the catalyst in the dark zone and no effect on burning rate[20].

Experimental results indicate that various phenomena occur on platonized propellants[10,21]. When lead catalysts are added to high energy double-base propellants, no super-rate burning occurs. Lead catalysts act effectively on the low energy double-base propellants. On the other hand, lead catalysts are known to retard the reaction rate of aldehyde oxidation. Carbonaceous materials are formed on the burning sur-

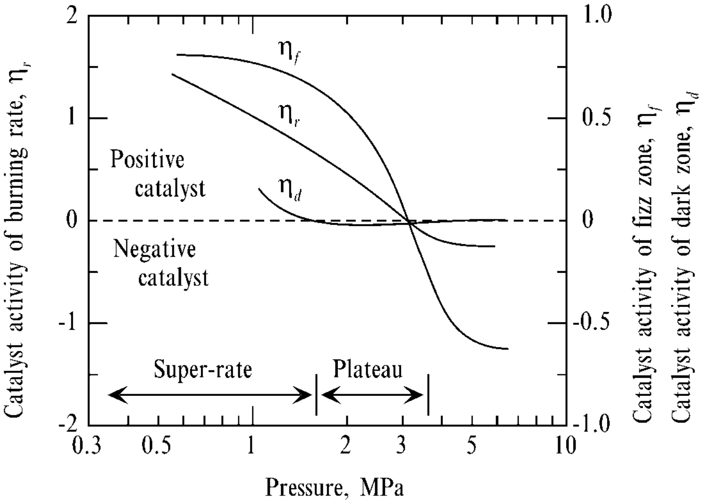

Figure 6-28. Catalyst activity in fizz zone decreases rapidly in the plateau pressure region and becomes negative above the pressure region where the burning rate of the catalyzed propellant is lower than that of the noncatalyzed propellant.

face during super-rate burning and are diminished when super-rate burning diminishes. The following combustion mechanisms are considered to explain the observed super-rate, plateau, and mesa burning : the initial action of the catalysts is in the condensed phase and the reaction process at the burning surface and the succeeding reaction pathways in the gas phase are also altered. Because of the formation of carbonaceous materials, the equivalence ratio of the fuel and oxidizer components shifts toward stoichiometric. The reaction rate in the gas phase is accelerated by the change in the stoichiometry. The heat flux transferred back from the fizz zone to the burning surface increases and super-rate burning occurs. Furthermore, the conductive heat is also increased by the increased average heat conductivity in the fizz zone caused by the carbonaceous materials formed in the fizz zone. As the burning rate increases in the high pressure region, the formation of carbonaceous materials diminishes and then the super-rate burning also diminishes and becomes plateau burning. This negative catalytic reaction by lead compounds is considered to produce mesa burning.

6.4.3
LiF Catalyzed Double-Base Propellants

Super-rate burning occurs when lithium fluoride (LiF) is mixed with NC-NG or NC-TMETN double-base propellants. As shown in Fig. 6-29, the burning rate of the propellant catalyzed by 2.4% LiF and 0.1% C increases drastically in the pressure region between 0.3 MPa and 0.5 MPa. This super-rate burning effect diminishes gradually as pressure increases above 0.5 MPa. The noncatalyzed propellant is a conventional NC-NG double-base propellant composed of 55% NC, 35% NG, and 10% DEP. The maximum burning rate increase is about 230% at 0.5 MPa.

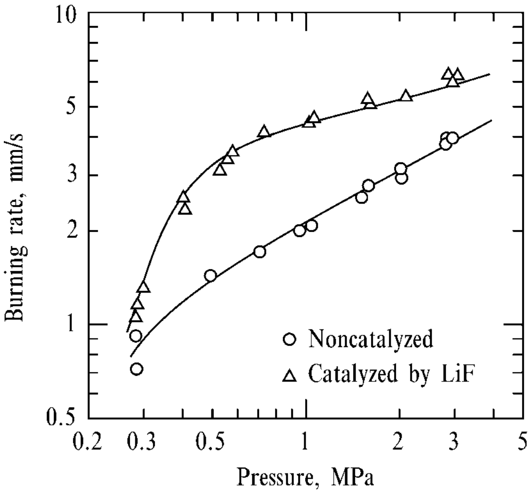

Figure 6-29. Super-rate burning of a LiF catalyzed double-base propellant.

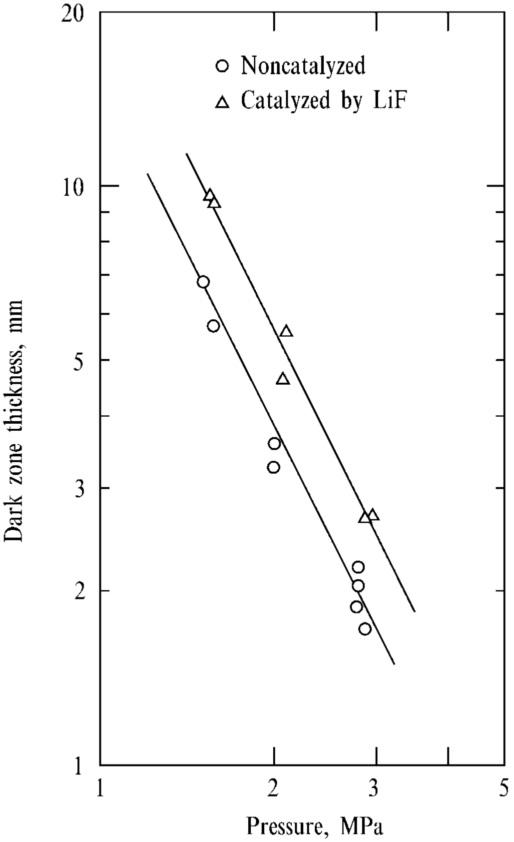

Figure 6-30. Flame standoff distance is increased by the addition of LiF in the super-rate burning region.

The dark zone length of LiF-catalyzed propellants is increased by the addition of LiF in the region of super-rate burning, similarly to the case of Pb-catalyzed propellants, as shown in Fig. 6-30. Table 6-7 shows the dark zone length and reaction timeτ_g in the dark zone to produce the luminous flame in two pressure regions, 1.5 MPa and 3.0 MPa. The reaction time defined in Eq. (6.2) remains relatively unchanged and no significant effect on the dark zone reaction is seen on addition of LiF and C.

Table 6-7. Dark zone length and reaction time in the dark zone for noncatalyzed and catalyzed propellants.

Propellant	p MPa	r mm/s	L_g mm	T_d K	τ_g ms
Noncatalyzed	1.5	2.6	6.1	1100	8.7
	3.0	3.9	1.8	1100	3.0
Catalyzed	1.5	4.9	9.1	1200	6.4
	3.0	5.9	2.7	1200	2.5

The temperature gradient in the fizz zone just above the burning surface increases from 1.9 K/μm to 2.5 K/μm at 0.7 MPa when 2.4 % LiF and 0.1 % C are added. The gas phase reaction rate in the fizz zone and the heat flux feedback from the fizz zone to the burning surface are increased by the addition of the catalysts. However, no effect of addition of the catalysts is seen in the dark zone.

The gas phase and burning surface structures of the LiF-catalyzed propellant are very similar to those of Pb-catalyzed propellants to create super-rate burning. When super-rate burning occurs by the addition of LiF, large amounts of carbonaceous materials are formed on the burning surface. The carbonaceous materials disappear at high pressure regions, where super-rate burning disappears simultaneously. The site and mode of action of LiF on double-base propellants are the same as those of Pb compounds on double-base propellants.

6.4.4
Ni Catalyzed Double-Base Propellants

Metallic nickel is known to be a catalyst in promoting the reduction of NO when NO reacts with aldehyes or hydrocarbon gases[22], since the primary reaction in the dark zone of double-base propellants is NO reduction to N_2. The small amounts of fine Ni particles or organic nickel compounds are added to a double-base propellant to increase the reaction rate in the dark zone.

Figure 6-31 shows the effect of the addition of Ni particles on the burning rate of a double-base propellant. The double-base propellant is composed of 44.0 % NC, 43.0 % NG, 11.0 % DEP, and 2.0 % EC as a reference propellant. This propellant is catalyzed with 1.0 % Ni particles (2 μm in diameter). No burning rate change is seen on addition of Ni particles[22]. However, the flame structure is altered significantly

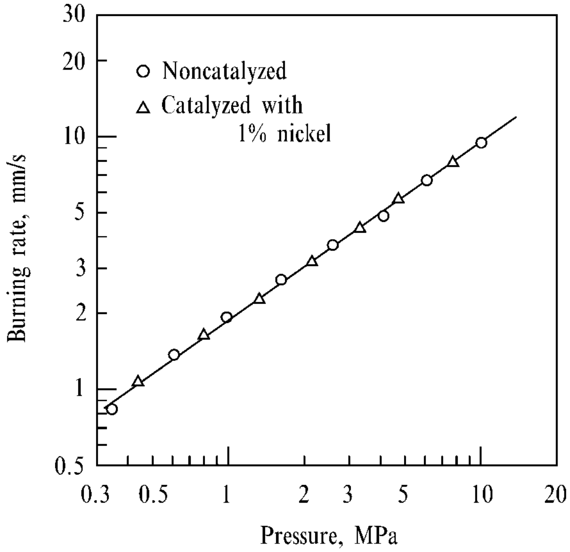

Figure 6-31. Burning rate remains unchanged by the addition of nickel powder.

by this addition. The flame standoff distance between the burning surface and the luminous flame front is shortened, as shown in Fig. 6-32. Though the flame standoff distance of the reference propellant is about 8 mm at 1.5 MPa and decreases rapidly as pressure increases (1 mm at 4.0 MPa), the flame standoff distance of the catalyzed propellant with Ni remains unchanged (0.3 mm) when pressure is increased.

The temperature in the dark zone of the reference propellant is approximately 1300 K at 0.3 MPa and increases as pressure increases (1500 K at 2.0 MPa). A significant increase in temperature for the catalyzed propellant is seen because the dark zone is occupied by the high-temperature luminous flame zone. However, the temperature gradient in the fizz zone just above the burning surface (0.2–0.3 mm from the burning surface) remains unchanged when Ni particles are added. This indicates that the heat flux feedback from the fizz zone to the burning surface is also unchanged. The Ni particles act only on the dark zone reaction, not on the fizz zone or the condensed phase reactions. Thus the burning rate remains unchanged by the addition of the Ni particles[22].

As described in Section 6.4, lead catalysts act on the condensed phase and fizz zone reactions, not on the dark zone reaction, and increase the burning rate. On the contrary, Ni catalysts act on the dark zone reaction, but not on the condensed phase or fizz zone reactions, and do not increase the burning rate. No luminous flame is produced when double-base propellants burn, for example, at 0.5 MPa. However, when catalyzed propellants with metallic Ni or organic Ni compounds burn, a luminous flame is produced just above the burning surface at the same pressure.

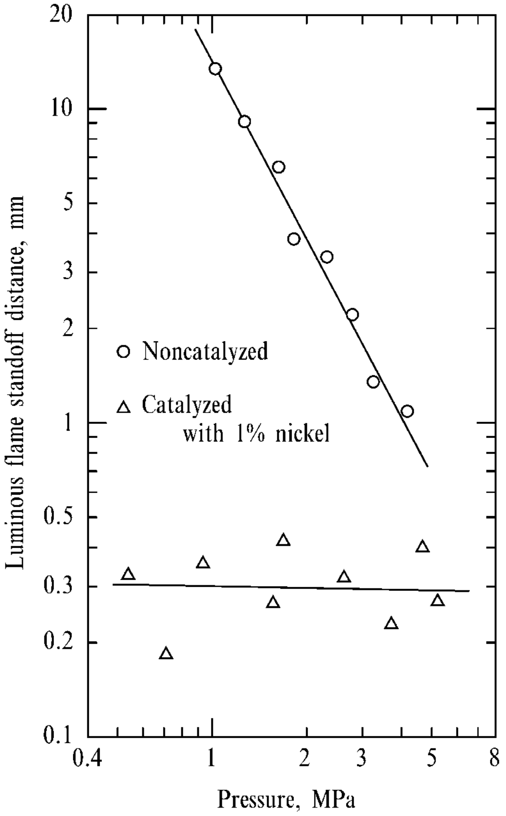

Figure 6-32. Flame standoff distance is decreased significantly by the addition of nickel powder even though the burning rate remains unchanged (see Fig. 6-31).

References

1 Fifer, R. L., Chemistry of Nitrate Ester and Nitramine Propellants, Fundamentals of Solid-Propellant Combustion, edited by Kuo, K. K. and Summerfield, M., Progress in Astronautics and Aeronautics, Vol. 90, Chapter 4, AIAA, New York (1984).

2 Kubota, N., Flame Structure of Modern Solid Propellants, Nonsteady Burning and Combustion Stability of Solid Propellants, edited by De Luca, L., Price, E. W., and Summerfield, M., Progress in Astronautics and Aeronautics, Vol. 43, Chapter 4, AIAA, Washington DC (1990).

3 Lengelle, G., Bizot, A., Duterque, J., and Trubert, J. F., Steady-State Burning of Homogeneous Propellants, Fundamentals of Solid-Propellant Combustion, edited by Kuo, K. K. and Summerfield, M., Progress in Astronautics and Aeronautics, Vol. 90, Chapter 7, AIAA, New York (1984).

4 Huggett, C., Combustion of Solid Propellants, Combustion Processes, High Speed Aerodynamics and Jet Propulsion Series, Vol. 2, Princeton University Press, Princeton, NJ (1956), pp. 514–574.

5 Timnat, Y. M., Advanced Chemical Rocket Propulsion, Academic Press, New York (1987).

6 Lengelle, G., Duterque, J., and Trubert, J. F., Physico-Chemical Mechanisms of Solid Propellant Combustion, Solid Propellant Chemistry, Combustion, and Motor Interior Ballistics, edited by Yang, V., Brill, T. B., and Ren, Wu-Zhen, Progress in Astronautics and Aeronautics, Vol. 185, Chapter 2.2, AIAA, Virginia (2000).

7 Crawford, B. L., Huggett, C., and McBrady, J. J., The Mechanism of the Double Base Propellants, Journal of Physical and Colloid Chemistry, Vol. 54, No. 6, 1950, pp. 854–862.

8 Rice, O. K. and Ginell, R., Theory of Burning of Double-Base Rocket Propellants, Journal of Physical and Colloid Chemistry, Vol. 54, No. 6, 1950, pp. 885–917.

9 Parr, R. G. and Crawford, B. L., A Physical Theory of Burning of Double-Base Rocket Propellants, Journal of Physical and Colloid Chemistry, Vol. 54, No. 6, 1950, pp. 929–954.

10 Heller, C. A. and Gordon, A. S., Structure of the Gas Phase Combustion Region of a Solid Double Base Propellant, Journal of Physical Chemistry, Vol. 59, 1955, pp. 773–777.

11 Kubota, N., The Mechanism of Super-Rate Burning of Catalyzed Double Base Propellants, AMS Report No. 1087, Aerospace and Mechanical Sciences, Princeton University, Princeton, N J (1973).

12 Eisenreich, N., A Photographic Study of the Combustion Zones of Burning Double Base Propellant Strands, Propellants and Explosives, Vol. 3, 1978, pp. 141–146.

13 Aoki, I. and Kubota, Combustion Wave Structures of High and Low Energy Double-Base Propellants, AIAA Journal, Vol. 20, No. 1, 1982, pp. 100–105.

14 Beckstead, M. W., Model for Double-Base Propellant Combustion, AIAA Journal, Vol. 18, No. 8, 1980, pp. 980–985.

15 Kubota, N. and Ishihara, A., Analysis of The Temperature Sensitivity of Double-Base Propellants, Twentieth Symposium (International) on Combustion, The Combustion Institute, Pittsburgh, PA (1984), pp. 2035–2041.

16 Nakashita, G. and Kubota, N., Energetics of Nitro/Azide Propellants, Propellants, Explosives, Pyrotechnics, Vol. 16, 1991, pp. 171–181.

17 Preckel, R. F., Ballistics of Catalyst Modified Propellants, Bulletin of Fourth Meeting of the Army-Navy Solid Propellant Group, Armour Research Foundation, Illinois Institute of Technology, Chicago (1948), pp. 67–71.

18 Hewkin, D., J., Hicks, J. A., Powling, J., and Watts, H., The Combustion of Nitric Ester-Based Propellants: Ballistic Modification by Lead Compounds, Combustion Science and Technology, Vol. 2, 1971, pp. 307–327.

19 Eisenreich, N. and Pfeil, A., The Influence of Copper and Lead Compounds on the Thermal Decomposition of Nitrocellulose in Solid Propellants, Thermochemica Acta, Nol. 27, 1978, pp. 339–346.

20 Kubota, N., Determination of Plateau Burning Effect of Catalyzed Double-Base Propellant, Seventeenth Symposium (International) on Combustion, The Combustion Institute, Pittsburgh, PA (1979), pp. 1435–1441.

21 Kubota, N., Ohlemiller, T. J., Caveny, L. H., and Summerfield, M., Site and Mode of Action of Platonizers in Double Base Propellants, AIAA Journal, Vol. 12, No. 12, 1974, pp. 1709–1714; also Kubota, N., Ohlemiller, T. J., Caveny, L. H., and Summerfield, M., The Mechanism of Super-Rate Burning of Catalyzed Double Base Propellants, Fifteenth Symposium (International) on Combustion, The Combustion Institute, Pittsburgh, PA (1973), pp. 529–537.

22 Kubota, N., Role of Additives in Combustion Waves and Effect on Stable Combustion Limit of Double-Base Propellants, Propellants and Explosives, Vol. 3, 1978, pp. 163–168.

Propellants and Explosives: Thermochemical Aspects of Combustion. Naminosuke Kubota
Copyright © 2002 Wiley-VCH Verlag GmbH & Co. KGaA
ISBNs: 3-527-30210-7 (Hardback); 3-527-60050-7 (Electronic)

7
Combustion of Composite Propellants

7.1
AP Composite Propellants

7.1.1
Burning Rate and Combustion Wave Structure

Ammonium perchlorate (AP) is the crystalline oxidizer most widely used to formulate composite propellants for rockets. Unlike double-base propellants, AP composite propellants are not used as gun propellants because the combustion products of AP composite propellants generate a high mass fraction of hydrogen chloride (HCl), which acts to oxidize and erode the interior surface of gun barrels.

Extensive experimental and theoretical studies have been done on the decomposition and combustion of AP composite propellants in order to achieve a wide spectrum of burning rates[1–13]. The combustion mode of AP-HTPB composite propellants is controlled by the diffusion the process of the decomposed gases of the AP particles and the surrounding HTPB at burning surface[1–2,4–10,12]. The AP particles decompose to produce perchloric acid, $HClO_4$, and the HTPB binder decomposes to produce hydrocarbon fragments and hydrogen[9]. These decomposed gases react and produce heat on and above the burning surface. As shown in Fig. 7-1, an endothermic reaction takes place involving pyrolysis of the binder to form gaseous products (fuel) and the dissociative sublimation and/or decomposition of AP to form ammonia and perchloric acid at the burning surface. The fuel and oxidizer components diffuse and mix together above the burning surface to form diffusional flamelets and/or premixed flame and produce final combustion products such as CO, CO_2, H_2O, HCl, and N_2.

The temperature in the condensed phase increases from the initial propellant temperature T_0 to the burning surface temperature T_s by the conductive heat feedback from the burning surface. Then, the temperature increases in the gas phase because of the exothermic reaction above the burning surface and reaches the final combustion temperature T_g. Since the physical structure of AP composite propellants is highly heterogeneous, the temperature fluctuates from time to time and also from location to location. The temperature profile in Fig. 7-1 is shown as a time-averaged profile. This is in clear contrast with double-base propellants shown in

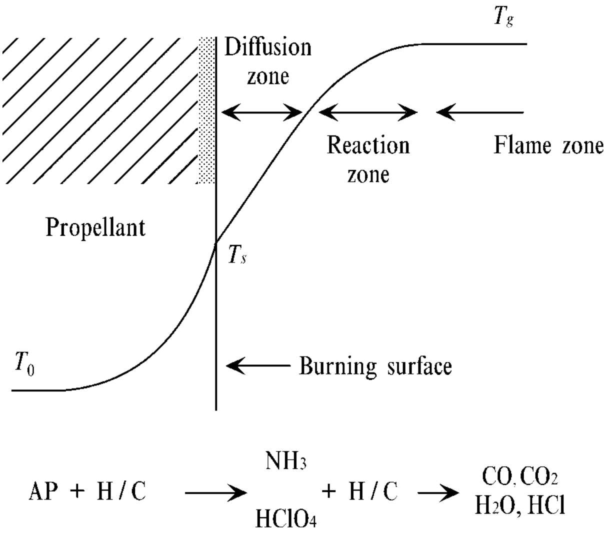

Figure 7-1. Combustion wave structure of an AP composite propellant.

Fig. 6-3. Thus, the burning rate of AP composite propellants depends largely on the particle size of AP[3,11], the mass fraction of AP and the type of binders[3,12].

7.1.1.1 Effect of AP Particle Size

Figure 7-2 shows the effect of the particle size of AP on burning rate[3]. The propellants are composed of AP 80%, ξ(AP = 0.80), and HTPB 20% by mass. The AP particles are bimodal large sized AP of mixture ratio 350 μm/200 μm = 4/3 and bimodal small sized AP of mixture ratio 15 μm/3 μm = 4/3. The burning rate of the small sized AP propellant is more than double that of the large sized AP propellant. The pressure exponent of the burning rate is 0.47 for the large sized AP propellant and 0.59 for the small sized AP propellant.

Figure 7-3 shows the effect of the particle size of AP on the burning rate of unimodal AP composite propellants[3]. The burning rate increases as the particle size of the AP, d_0, decreases. However, the effect of the particle size on the burning rate diminishes as pressure increases. Though the mass fraction of AP, ξ(AP), is 0.65, and these propellants are highly fuel rich, the effect of AP particle size on burning rate is evident.

7.1.1.2 Effect of Binder

Figure 7-4 shows the effect of ξ(AP) on burning rate of AP-HTPB composite propellants[3]. The chemical compositions of the propellants are shown in Table 7-1. The burning rate of the propellant composed of ξ(0.86) is higher than that of ξ(0.80) at constant pressure. However, the pressure exponent is 0.60 for both ξ(0.86) and ξ(0.80) propellants and the burning rate is represented by $r \sim p^{-0.6}$.

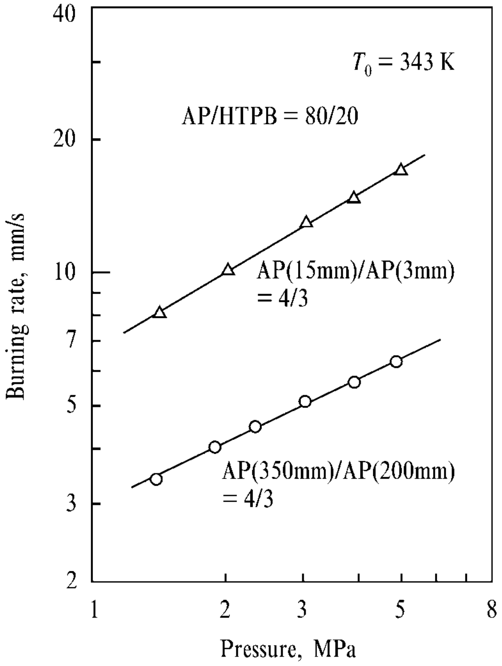

Figure 7-2. Effect of AP particle size (bimodal) on burning rate.

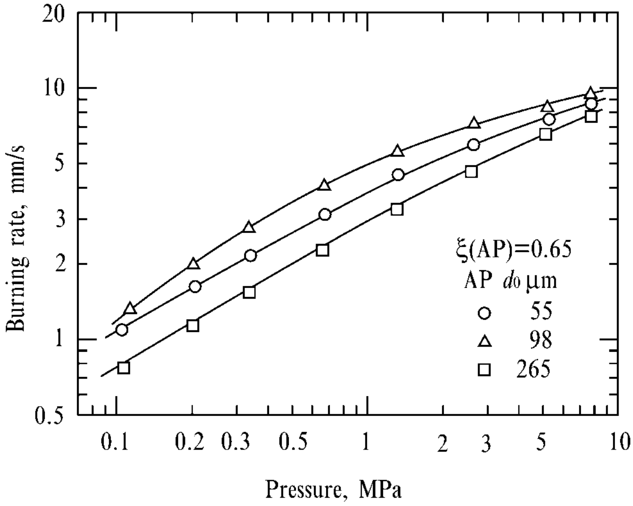

Figure 7-3. Effect of AP particle size (single-modal) on burning rate.

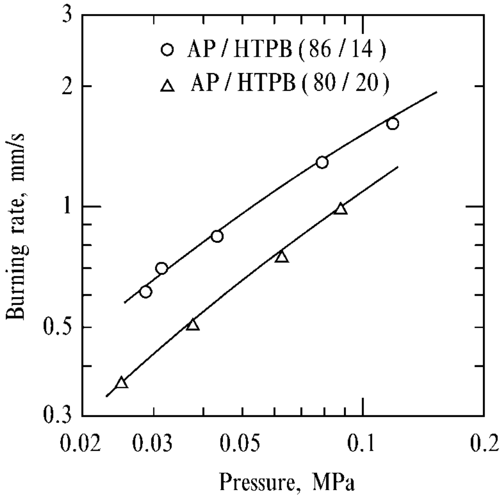

Figure 7-4. Effect of mass fraction of AP on burning rate.

Table 7-1. Chemical compositions of AP-HTPB propellants (wt%).

Propellant	*AP (c)*	*AP (f)*	*HTPB*	*T_g K*
AP/HTPB (86/14)	43	43	14	2680
AP/HTPB (80/20)	40	40	20	2310

HTPB : $C_{7.057}H_{10.647}O_{0.223}N_{0.063}$
AP (c) : $d_0 = 200$ μm and AP (f) : $d_0 = 20$ μm
T_g : adiabatic flame temperature at 0.1 MPa

Figure 7-5 shows the flame photographs of $\xi(0.86)$ propellant at pressures 0.07 MPa (a) and 0.1 MPa (b). A bluish flame is formed on the burning surface. The thickness of the bluish flame is decreased with increasing pressure. The relationship between the thickness of the bluish flame, δ_g, and pressure, p, is represented by $\delta_g \sim p^{-0.6}$: 0.5 mm at 0.02 MPa and 0.2 mm at 0.1 MPa. The reddish flame is seen above the bluish flame. On the other hand, no bluish and reddish flames are seen when $\xi(0.80)$ propellant burns at pressure 0.1 MPa as shown in Fig. 7-5 (c). The flame is entirely yellowish which is caused by the fuel-rich diffusion flame generated by the decomposed gases of the binder and the AP particles[8]. In fact, the flame temperature of the propellant of $\xi(0.86)$ is higher than that of $\xi(0.80)$ as shown in Table 7-1. Since the flame photographs are taken with a relatively long exposure time (1/60 s), the thickness of the bluish flame appears to be a time-averaged value of the numerous diffusion-type flamelets which are generated by the decomposed gases of the binder and the AP particles.

The heat flux transferred back from the gas phase to the burning surface is dependent on the temperature gradient in the gas phase, since the temperature gradient

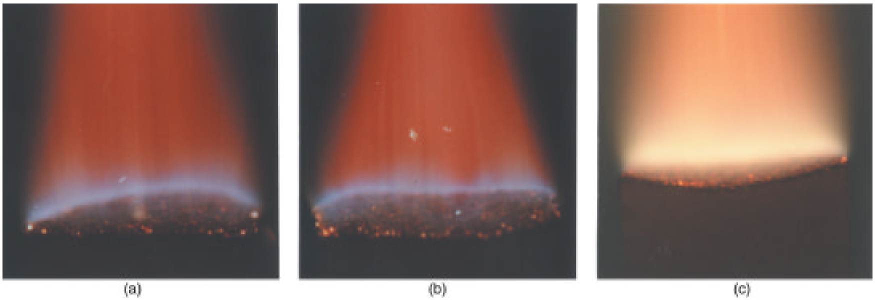

Figure 7-5. Flame photographs of AP-HTPB composite propellants at low pressures:

	Mass fraction		p	r
	AP	HTPB	MPa	mm/s
(a)	0.86	0.14	0.07	1.2
(b)	0.86	0.14	0.10	1.5
(c)	0.80	0.20	0.10	1.0

is inversely proportional to the thickness of the reaction zone in the gas phase. Since the reaction in the gas phase is completed at the upper end of the bluish flame, the heat flux defined in Λ_{III} shown in Fig. 5-5 is proportional to $\Lambda_{\mathrm{III}} \sim 1/\delta_g \sim p^{0.6}$. The observed pressure dependency of burning rate, $r \sim p^{0.6}$ is caused by the pressure dependency of the reaction rate in the bluish flame[8].

7.1.1.3 **Temperature Sensitivity**

Figures 7-6 and 7-7 show the burning rate of AP-HTPB composite propellants at 243 K and 343 K. The propellants are composed of bimodal fine or coarse AP particles with or without catalysts. The catalyst is 2,2-bis (ethylferrocenyl) propane (BEFP). The chemical compositions of the propellants are shown in Table 7-2. All burning rates increase linearly in a ln p versus ln r plot in the pressure range 1.5–5 MPa, and also increase with increasing initial propellant temperature at constant pressure[13]. The burning rate increases with decreasing AP particle size, and the temperature sensitivity decreases with decreasing AP particle size, i.e., with increasing burning rate.

Table 7-2. Chemical compositions of AP composite propellants (wt%).

Propellant	*Binder*	*AP particle size (μm)*				*Catalyst*
	HTPB	*400*	*200*	*20*	*3*	*BEFP*
AP(fn)	20			40	40	
AP(cn)	20	40	40			
AP(fc)	20			40	40	1.0
AP(cc)	20	40	40			1.0

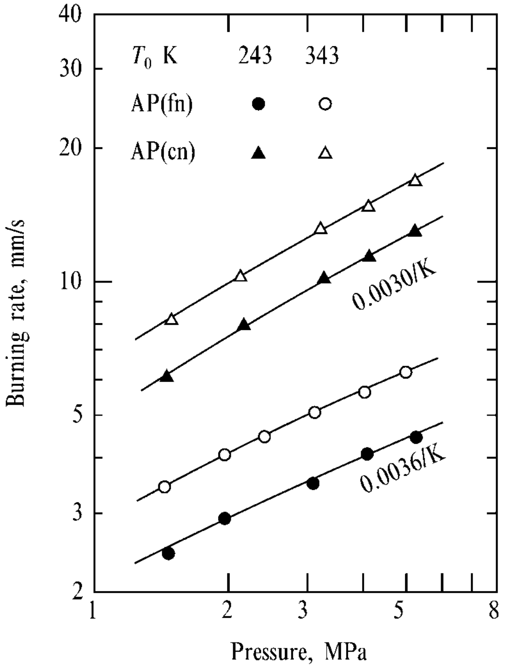

Figure 7-6. Burning rate and temperature sensitivity of AP-HTPB composite propellants composed of fine or coarse AP particles.

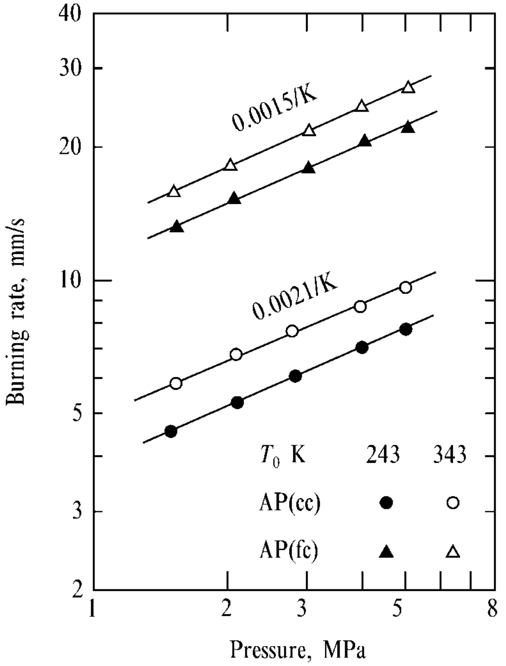

Figure 7-7. Burning rate and temperature sensitivity of catalyzed AP-HTPB composite propellant with BEFP composed of fine or coarse AP particles.

Figure 7-7 shows the effect of the addition of burning rate catalyst on burning rate. The burning rates of both propellants are increased significantly by the addition of 1.0 % BEFP. BEFP acts more effectively on the burning rate of a propellant consisting of fine AP particles than on that of a propellant consisting of coarse AP particles. The temperature sensitivity of the fine propellant with 1.0 % BEFP is lower than that of the coarse propellant with 1.0 % BEFP.

The relationship between temperature sensitivity and burning rate is shown in Fig. 7-8 as a function of AP particle size and burning rate catalyst (BEFP)[13]. The

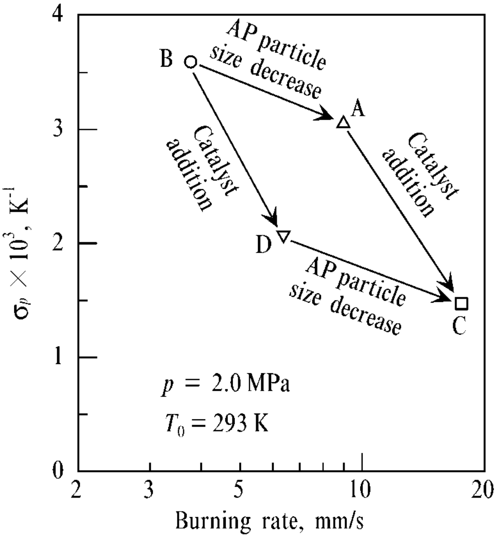

Figure 7-8. Temperature sensitivity characteristics of AP-HTPB composite propellants.

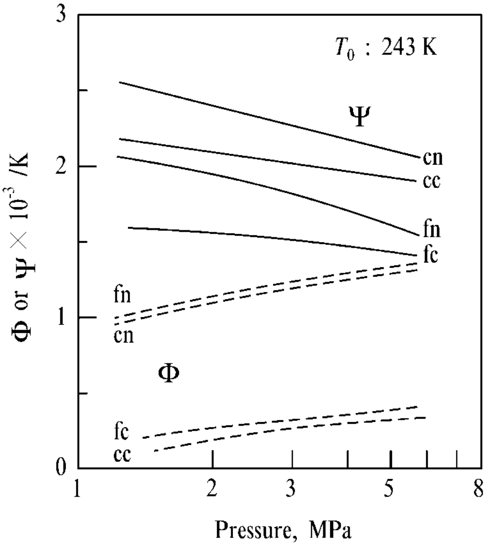

Figure 7-9. Temperature sensitivities of gas phase and condensed phase of AP composite propellants.

temperature sensitivity decreases when the burning rate is increased either by the addition of fine AP particles or by the addition of BEFP. The results of the temperature sensitivity analysis shown in Fig. 7-9 indicate that the temperature sensitivity of the condensed phase Ψ defined in Eq. (3.80) is higher than that of the gas phase Φ defined in Eq. (3.79). In addition, Φ becomes very small when the propellant is catalyzed. The temperature sensitivity of AP-HTPB propellants depends largely on the reaction process in the condensed phase.

7.1.2
Catalyzed AP Composite Propellants

7.1.2.1 Iron Catalysts

The burning rate of AP composite propellants is increased by the addition of catalysts which act to increase the rate of decomposition of AP particles within the propellants. Since catalysts act on the surface of AP particles, the total surface area of catalyst particles at a fixed concentration is an important factor in achieving high catalyst efficiency. Though very fine iron oxides are used to increase the burning rate of AP composite propellants, organic iron compounds act more effectively because of the formation of iron oxide molecules during decomposition. Typical iron compounds are ferric oxides (Fe_2O_3 and Fe_3O_4), hydrated ferric oxide [FeO(OH)], *n*-butyl ferrocene (nBF), di-n-butyl ferrocene (DnBF), BEFP, and iron acetate. Organic iron compounds are also bonded chemically within polymers such as polybutadienes and polyesters. Figures 7-6 and 7-7 show typical examples of the action of catalyst on burning rate[13]. The burning rate is increased approximately twofold by the addition of 1 % BEFP for both small and large sized AP propellants. In general, the degree of the burning rate increase is proportional to the amounts of the catalysts when the catalyst additions are less than about 3 % and the effect of the addition of the catalysts saturates at about 5 %.

Though copper oxides are effective catalysts for increasing the burning rate of AP composite propellants, the thermal stability of the propellants is lowered and spontaneous ignition occurs. Organic boron compounds such as carborane and *n*-hexyl carborane (n-HC) are also effective catalysts. The burning rate of AP-HTPB propellants is increased from 1 mm/s to 9 mm/s at 7 MPa by the addition of 13 % n-HC as shown in Fig. 7-10. The pressure exponent is relatively unchanged by the addition of n-HC in the wide pressure range from 2 MPa to 10 MPa. Since the amount of n-HC mixed with the propellant is 13 % by mass, the boron atoms within the n-HC are considered to act as a fuel component in the combustion wave. The thermal decomposition of n-HC forms boron atoms that are oxidized by the AP decomposed fragments to produce heat at the burning surface. The increased heat flux enhances the decomposition of the AP particles and the binder on the burning surface.

The friction sensitivity of AP composite propellants increases significantly when organic iron and organic boron compounds are added. The ignition of AP composite propellants is correlated to the friction sensitivity and the burning rate of propellants[14]. As a result, effective catalysts such as n-HC, ferrocene, and copper oxides are very sensitive to mechanical friction. The propellants containing these catalysts can easily ignite during their manufacturing.

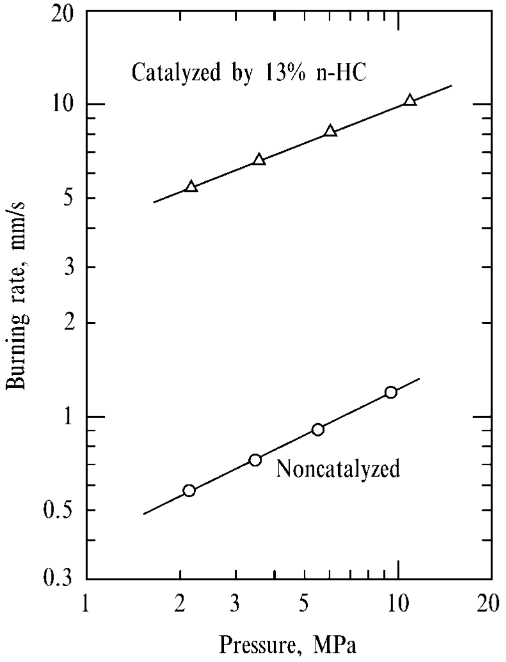

Figure 7-10. Burning rate of an n-HC catalyzed AP composite propellants showing that the burning rate is increased drastically but the pressure exponent remains unchanged by the addition of the catalyst.

7.1.2.2 **LiF Negative Catalyst**

7.1.2.2.1 **Reaction of AP with LiF**

The thermal decomposition process of AP particles is altered significantly when 10 % LiF is admixed as shown in Fig. 7-11. The decomposition of AP particles without LiF begins at about 570 K and 50 % mass loss occurs at 667 K, which corresponds to the exothermic peak. The TG curve consists of a two-stage mass loss process. The first stage corresponds to the first exothermic reaction at 635 K and the second to the second exothermic reaction in the high temperature region between 723 K and 786 K observed in DTA experiments.

When 10 % LiF is added to the AP particles, an endothermic peak is observed at 516 K. However, the exothermic peak of 725 K is lowered to 635 K. An endothermic reaction occurs between 520 K and 532 K. An additional exothermic peak is observed at the higher temperature region between 720 K and 790 K.

An endothermic peak at 525 K is observed when lithium perchlorate ($LiClO_4$: LP) is thermally decomposed. The endothermic reaction is caused by the phase change of $LiClO_4$ from solid to liquid phase. As the temperature is increased, the melted $LiClO_4$ begins to decompose at about 680 K and rapid mass loss decomposition occurs in the temperature range between 720 K and 790 K. This decomposition is similar to the decomposition of the AP particles with 10 % LiF.

The mass loss of the first stage decomposition of the AP particles with 10 % LiF is 56.7 %, and that of the second-stage decomposition is 28.5 %. The residue remain-

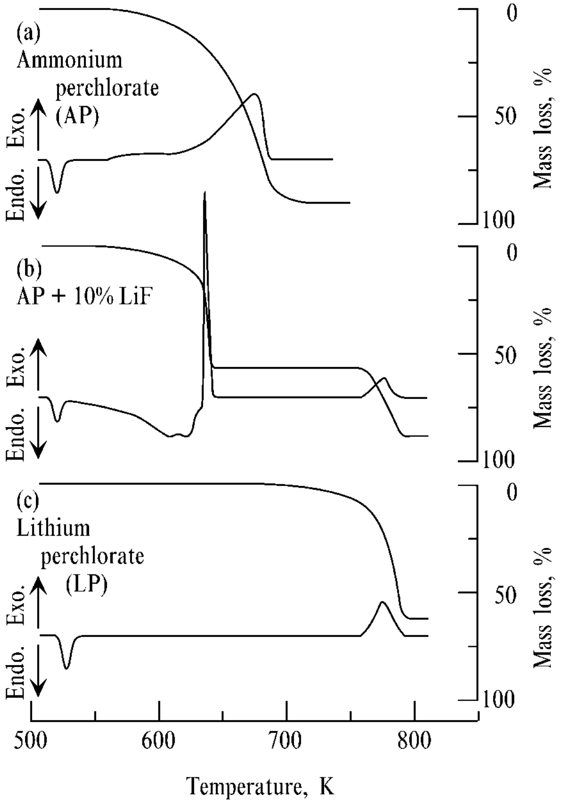

Figure 7-11. Thermal decomposition processes of AP, AP + 10% LiF, and lithium perchlorate.

ing above 790 K is 14.8%. As shown in Fig. 7-12, the two-stage decomposition process is summarized as follows:

(1) primary endothermic reaction

$$1.0\ NH_4ClO_{4\ (s)} + 0.503\ LiF_{\ (s)} \rightarrow 0.497\ NH_4ClO_{4\ (l)} + 0.503\ NH_4F_{\ (g)} + 0.503\ LiClO_{4\ (l)}$$

(2) first-stage decomposition

$$\rightarrow 0.497\ NH_{3\ (g)} + 0.497\ HClO_{4\ (g)} + 0.503\ LiClO_{4\ (l)}$$

(3) second-stage decomposition

$$\rightarrow 1.06\ O_{2\ (g)} + 0.503\ LiCl_{(s)}$$

where $_{(s)}$, $_{(l)}$, and $_{(g)}$ denote solid, liquid, and gas, respectively.

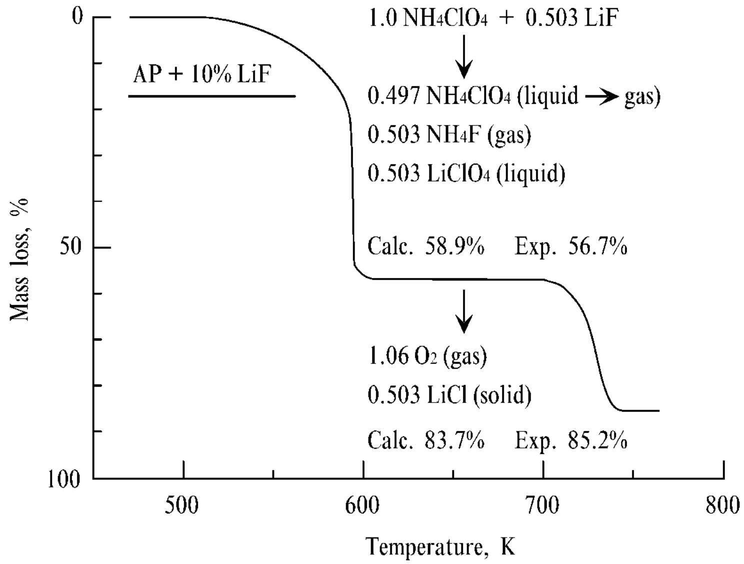

Figure 7-12. Two-stage decomposition process of AP + 10 % LiF measured by thermogravimetry.

The decomposition process of the AP particles is largely altered by the addition of LiF. After the rapid decomposition and gasification reactions at about 630 K, an undecomposed liquefied residue remains. This residue is the same material as that observed in the temperature range between 640 K and 720 K. When the temperature is increased further, the liquefied residue decomposes again at about 750 K and produces a solid residue at 790 K. This solid residue is determined by chemical analysis to be LiCl.

7.1.2.2.2 **Combustion Wave Structures with and without LiF**

The burning rate characteristics of AP composite propellants with and without LiF are shown in Fig. 7-13. Though the burning rate without LiF increases as pressure increases, with LiF the burning rate decreases as the concentration of LiF increases at constant pressure. Further increase of the LiF concentration at a given pressure eventually results in self-extinction of the propellant[15]. Thus, one can state that LiF not only decreases the burning rate but also inhibits steady-state combustion at or below a certain pressure.

The temperature gradient just above the burning surface is shown in Fig. 7-14 for the noncatalyzed propellant and that catalyzed with LiF 0.5 % as a function of burning rate. The conductive heat flux feedback from the gas phase to the burning surface remains relatively unchanged by the addition of 0.5 % LiF. The burning rate reduction by the addition of LiF is due to the altered condensed phase reaction of the AP particles. When both propellants are quenched during burning by rapid pressure decay, no AP particles are seen on the quenched catalyzed propellant with

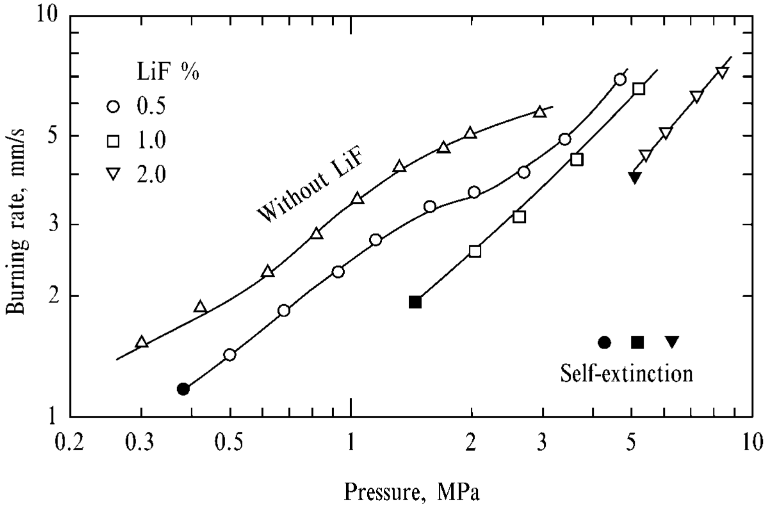

Figure 7-13. Burning rate of LiF catalyzed AP composite propellants showing that the burning rate decreases and the pressure of self-interruption increases as the concentration of LiF increases.

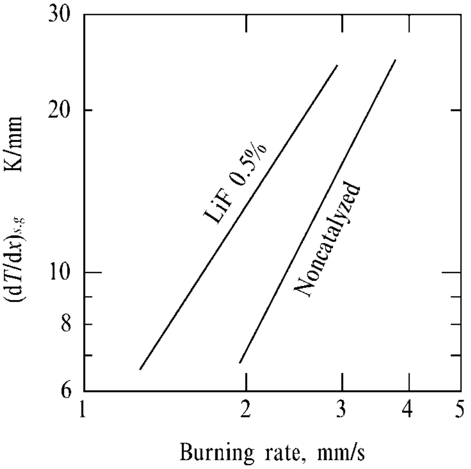

Figure 7-14. Temperature gradient in the gas phase just above the burning surface of noncatalyzed and 0.5 % LiF catalyzed AP composite propellants.

0.5 % LiF as shown in Fig. 7-15. All AP particles on the burning surface decompose during the process of the pressure decay. LiCl particles remain on the quenched burning surface, which is consistent with the results obtained in the DTA and TG experiments[15].

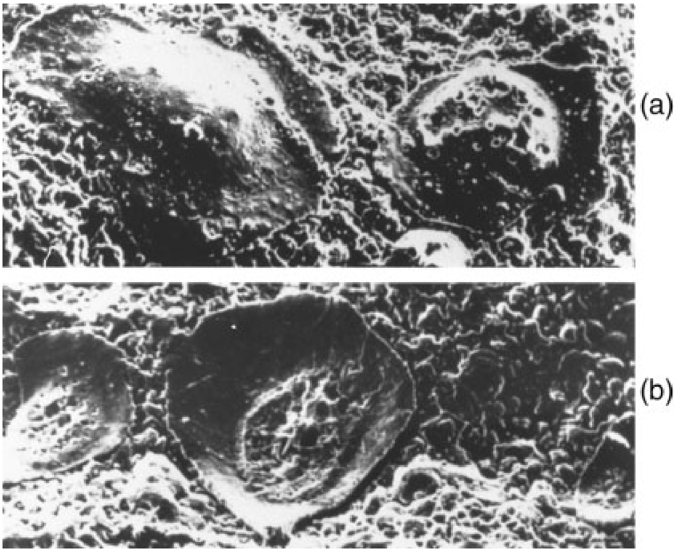

Figure 7-15. Scanning electron microphotographs of quenched AP composite propellant burning surfaces without LiF (a) and with 0.5 % LiF (b) obtained by a pressure decay from 2MPa to 0.1 MPa: the width of each photograph is 0.60 mm.

7.2
Nitramine Composite Propellants

7.2.1
Burning Rate Characteristics

7.2.1.1 Effect of Nitramine Particle Size

When RDX and HMX particles are mixed with polyurethane binder, RDX and HMX composite propellants are formed[1,16–21]. The burning rate versus pressure on a $\ln p$ versus $\ln r$ plot results in a straight line for both propellants. The burning rate of RDX propellant is higher than that of HMX propellant for an equal nitramine mass fraction, $\xi(\mathrm{RDX}) = \xi(\mathrm{HMX}) = 0.80$, at the same pressure, and the pressure exponents of HMX and RDX propellants are 0.64 and 0.55, respectively[17]. When the mass fraction of RDX or HMX is increased from 0.80 to 0.85, both burning rates are increased, and the pressure exponent is increased from 0.55 to 0.60 for RDX propellant. However, the burning rate is less dependent on the particle size of RDX or HMX for both propellants when the bimodal mixture ratio of large and small sized is inversed: 120 μm/ 2 μm= 7/3 and 3/7 for RDX propellants and 225 μm/20 μm= 7/3 and 3/7 for HMX propellants.

7.2.1.2 **Effect of Binder**

The effects of four types of binders, HTPS, HTPE, HTPA, and HTPB on burning rate of HMX composite propellants are shown in Fig. 7-16. The physicochemical properties of these binders are shown in Table 4-7. Each propellant is composed of 80 % HMX and 20 % binder and the HMX particles are a bimodal mixture of large sized (220 μm in diameter) 70 % and small sized (20 μm in diameter) 30 %. The oxygen concentration of HTPS is the highest and that of HTPB is the lowest in the four types of binders[19]. The adiabatic flame temperatures of HTPS, HTPE, HTPA, and HTPB propellants are 1940 K, 1910 K, 2040 K, and 1800 K, respectively.

All the burning rates are approximately straight lines in a ln p versus ln r plot, and the pressure exponent is in the rang 0.62–0.73. With the exception of HTPB propellant, the order of the burning rate is correlated with the order of the adiabatic flame temperature, whereas HTPB exhibits the highest burning rate even though the adiabatic flame temperature is the lowest. The temperature sensitivity of burning rate defined in Eq. (3.73) is 0.0022 K^{-1} for RDX-HTPA and 0.0039 K^{-1} for RDX-HTPS propellants[19].

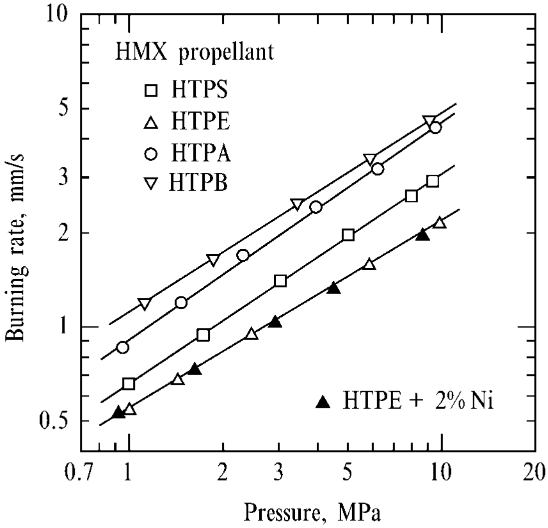

Figure 7-16. Burning rates of HMX composite propellants composed of HTPS, HTPE, HTPA, and HTPB binders.

7.2.2
Combustion Wave Structure

Since the physical structure of nitramine composite propellants is heterogeneous, the combustion wave structure is considered to be also heterogeneous, as in the case of AP composite propellants. However, the difference between AP propellant and RDX propellant is evident in Figs. 7-17 (a) and (b). The luminous flame produced above the burning surface is almost attached the burning surface of the AP propellant (a). On the other


(a) (b)

Figure 7-17. Flame photographs of AP composite propellant (a) and RDX composite propellant (b) showing that the luminous flame front of RDX composite propellant is distended from the burning surface:

	Mass fraction			p	r
	AP	RDX	PU	MPa	mm/s
(a)	0.80		0.20	2.0	5.3
(b)		0.80	0.20	2.0	1.1

hand, the luminous flame stands some distance above the burning surface of the RDX propellant (b). The flame standoff distance between the burning surface and the luminous flame front is similar to the dark zone of double-base propellants[17]. However, the burning surface of the RDX propellant composed of HTPB binder is covered with carbonaceous fragments, and the gas phase is then heterogeneous. Thus, the luminous flame is produced attached to the carbonaceous fragments and also the burning surface. The carbonaceous fragments are attributed to the low concentration of oxygen, 3.6 %, in the HTPB binder, whereas the concentration of oxygen in the HTPS, HTPE, and HTPA binders is > 25 %, as shown in Table 4-7.

The combustion wave structure of RDX composite propellants is homogeneous and the temperature in the solid phase and in the gas phase increases relatively smoothly when compared with AP composite propellants. The temperature increases rapidly on and just above the burning surface (in the dark zone near the burning surface) and the temperature gradient at the burning surface is high. The temperature in the dark zone increases slowly. However, the temperature increases rapidly again at the luminous flame front. The combustion wave structure of RDX and HMX composite propellants composed of nitramines and hydrocarbon polymers is very similar to that of double-base propellants composed of nitrate esters[17].

The flame standoff distance L_d defined in Eq. (3.70) decreases as pressure increases, and the pressure exponent of the flame standoff distance is $d = -1.9 \sim -2.3$ for RDX and HMX propellants. The overall order of the reaction in the dark zone is determined to be $m = 2.5 \sim 2.8$. This is approximately equal to the overall order of the reaction in the dark zone of double-base propellants, $m = 2.5$, which indicates that the reaction pathway in the dark zone of nitramine composite propellants is approximately equal to that of double-base propellants.

The decomposition products of RDX and HMX contain relatively high concentrations of NO_2 at the initial stage. Exothermic reaction between the NO_2 and other decomposed fragments from RDX occurs at the burning surface. The decomposed gas produced from the binder diffuses into the exothermic reaction and the temperature then increases rapidly at the burning surface. The reduction of NO_2 produces NO, which reacts again exothermically to produce the luminous flame zone. Since the reaction involving NO is known to be slow and highly pressure dependent, the luminous flame stands well away from the burning surface. However, the luminous flame front approaches the burning surface rapidly when pressure is increased. This reaction is also caused by the reduction of NO to N_2, as in to the reaction process of double-base propellants.

RDX and HMX are stoichiometrically balanced materials and no excess oxidizer fragments are produced in the combustion products. The binders surrounding the nitramine particles are not fuel components, in contrast to the binders of AP composite propellants. Figure 7-18 shows a set of microphotographs of a RDX-PU propellant before burning (a) and after quenching (b). The quenched burning surface shows a finely divided recrystallized RDX dispersed homogeneously on the surface. The RDX particles and the binder melt and diffuse into each other, and form an energetic mixture on the burning surface during burning[17]. The energetic mixture acts as a homogeneous propellant much like a double-base propellant. The decomposed gas ejected from this energetic mixture forms a homogeneous gas phase structure and produces successive reaction zones: dark zone and luminous flame zone.

As discussed in Section 6.4.4 in Chapter 6, metallic nickel is known to act as a catalyst to promote the reaction between NO and hydrocarbon gases. As in the case of double-base propellants, nickel powders act on the gas phase reaction of nitramine composite propellants. Though the addition of metallic nickel powders (0.1 μm in diameter, 2.0 %) to the HMX-HTPE propellant, the burning rate remains unchanged, as shown in Fig. 7-16. However, the dark zone between the burning surface and the luminous flame front is eliminated completely, and the luminous flame approaches the burning surface when nickel powders are admixed. The NO molecules produced by the reduction of NO_2 at the burning surface react with hydrocarbon gases produced by the decomposition of HTPE binder. This reaction is

Figure 7-18. Scanning electron microphotographs of RDX composite propellant surface before combustion (a) and after quenching (b) by rapid pressure decay from the burning at 2 MPa.

enhanced by the addition of the nickel powders. However, the heat flux feedback from the gas phase to the burning surface remains unchanged because the enhanced NO reduction does not affect the NO_2 reduction at the burning surface, as in the case of the NO_2 reduction in the fizz zone of double-base propellants.

7.2.3
HMX-GAP Propellants

7.2.3.1 Physicochemical Properties of Propellants

Though no excess oxidizer fragments are formed when HMX burns, high temperature combustion products are formed. As shown in Fig. 5-3, the burning rate of HMX is very low even though the flame temperature is high[22]. On the other hand, the burning rate of GAP is very high even though the flame temperature is low, as shown in Fig. 5-10. The mixture of HMX particles with GAP forms HMX-GAP propellants, whose burning rate characteristics are different compared with other types of propellants such as double-base propellants and AP composite propellants.

The physicochemical properties of the propellants for which $\xi(HMX) = 0.4$, 0.6, and 0.8 are shown in Table 7-3. Since the energy density of HMX is higher than that of GAP, the adiabatic flame temperature of HMX-GAP propellant increases as $\xi(HMX)$ increases.

Table 7-3. Physicochemical properties of HMX-GAP composite propellants.

ξ(HMX)	*0.4*	*0.6*	*0.8*
Flame temperature at 5 MPa T_g (K)	1628	1836	2574
Molecular mass M_g (kg/kmol)	19.2	18.9	21.1
Density ρ_p (kg/m^3)	1460	1580	1770

7.2.3.2 Burning Rate and Combustion Wave Structure

The burning rates of GAP-HMX propellant for which $\xi(HMX) = 0.8$ increases linearly with pressure in a $\ln p$ versus $\ln r$ plot as shown in Fig. 7-19. The pressure exponent increases and the temperature sensitivity decreases as $\xi(HMX)$ increases (Fig. 7-20). The burning rate of GAP binder (Fig. 5-10) is higher than that of HMX (Fig. 5-3) even though the flame temperature of GAP binder is 1800 K lower than that of HMX (see Tables 4-5 and 4-8). The burning rate of GAP-HMX propellants is shown in Fig. 7-21 as a function of $\xi(HMX)$ at different pressures. The burning rate decreases as $\xi(HMX)$ increases in the range $\xi(HMX) < 0.6$ and increases as $\xi(HMX)$ increases in the range $0.6 < \xi(HMX)$.

The gas phase reaction of HMX-GAP propellants occurs with two-stage zones[22]: at the first-stage reaction zone the temperature increases rapidly on and just above the burning surface. At the second-stage reaction zone the temperature increases, also rapidly, at some distance from the burning surface. In the preparation zone

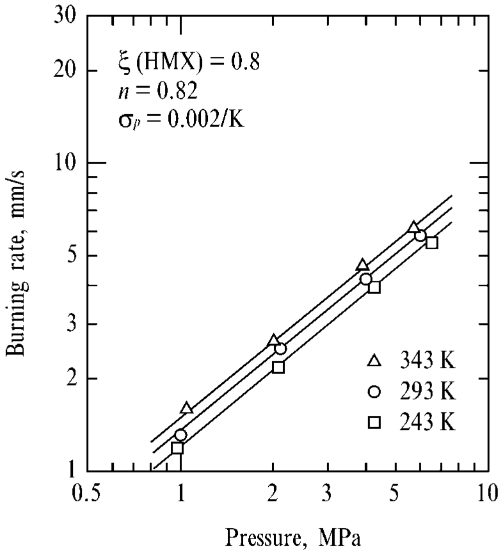

Figure 7-19. Burning rate and temperature sensitivity of HMX composite propellant.

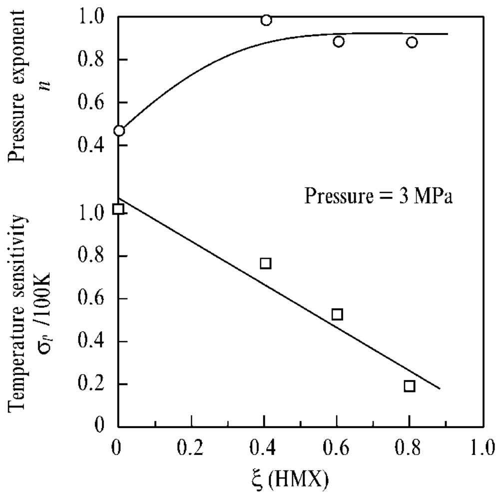

Figure 7-20. Pressure exponent and temperature sensitivity of HMX composite propellant as a function of ξ(HMX).

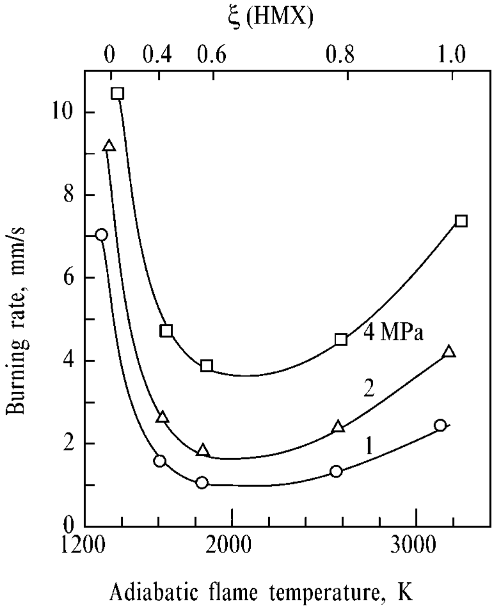

Figure 7-21. Burning rate of HMX composite propellant as a function of adiabatic flame temperature or ξ(HMX) showing the existence of the minimum burning rate at about ξ(0.6).

between the first stage and the second stage the temperature increases very slowly. At the second-stage reaction zone, a luminous flame is produced. The flame stand-off distance, L_g, of the propellant ξ(0.8) decreases linearly as pressure increases in a $\ln L_g$ versus $\ln p$ plot, as shown in Fig. 7-22 (noncatalyzed propellant).

The overall reaction rate in the second-stage reaction zone (preparation zone), ω_g, is determined by Eq. (5.5). The computed results show that the reaction rate increases linearly as pressure increases in a $\ln \omega_g$ versus $\ln p$ plot. Since the burning rate is represented by Eq. (3.75), ϕ and ψ defined in Eq. (3.76), are obtained. As shown in Eq. (3.75), the burning rate increases as ϕ increases and also ψ decreases. The burning surface temperature and the temperature gradient at the burning surface are approximately 695 K and 2.3×10^6 K/m at 0.5 MPa, respectively. The heat flux transferred back from the gas phase to the burning surface is 190 kW/m^2. In the computations of ϕ and Q_s, the physical parameter values used are: $\lambda_g = 8.4 \times 10^{-5}$ kW/mK, $\rho_p = 1770$ kg/m^3, and $c_p = 1.30$ kJ/kgK. Substituting $T_0 = 293$ K, $T_s = 695$ K, and $\phi = 2.3 \times 10^6$ K/m into Eqs. (3.75) and (3.76), Q_s of the propellant composed of ξ(0.8) is determined to be 369 kJ/kg. The results indicate that ϕ and Q_s play dominant roles in the determination of the burning rate of GAP-HMX composite propellants[22].

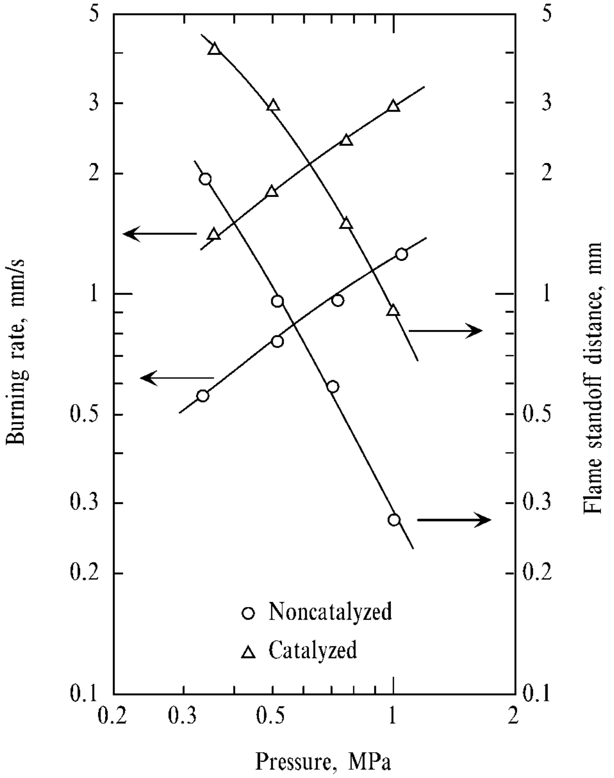

Figure 7-22. Burning rate and flame standoff distance of noncatalyzed and catalyzed GAP-HMX composite propellants.

7.2.4
Catalyzed Nitramine Composite Propellants

Lead compounds are effective in increasing the burning rate (super-rate burning) of double-base propellants. A similar super-rate burning effect is observed when lead compounds are added to composite propellants consisting of nitramine particles and polymeric binder. Though the chemical structures and properties of nitramines are different from those of nitrate esters, super-rate burning effects are obtained by the use of the same lead compounds.

7.2.4.1 Super-Rate Burning of HMX Composite Propellants

The super-rate burning rates of HMX-HTPE and HMX-HTPS propellants are shown in Figs. 7-23 and 7-24, respectively. The basic chemical compositions and physicochemical properties of the noncatalyzed HMX-HTPE and HMX-HTPS propellants are the HMX-HTPE and HMX-HTPS propellants shown in Fig. 7-16, respectively. The catalysts, 2.4% PbSt and 0.4% carbon, are mixed with each noncatalyzed

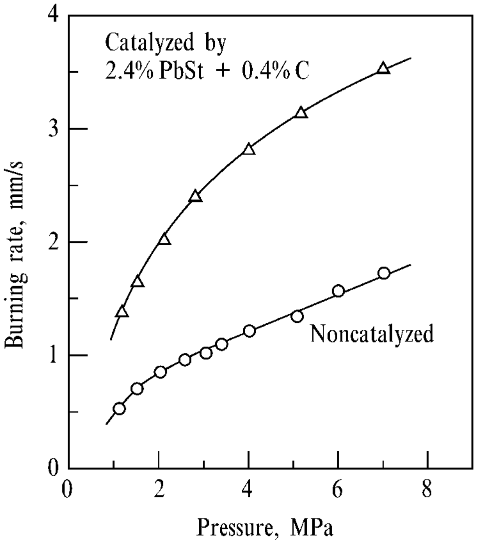

Figure 7-23. Super-rate burning of catalyzed HMX-HTPE composite propellant.

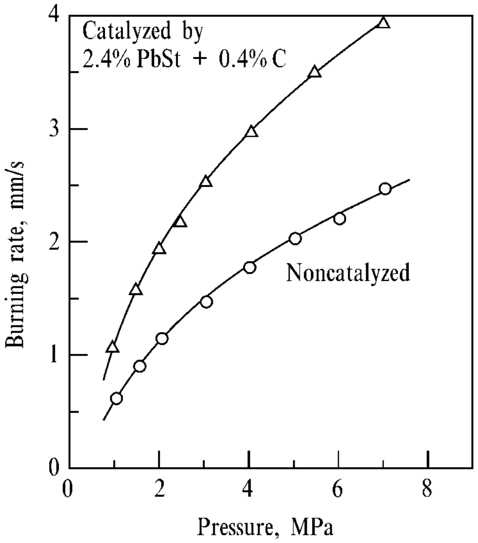

Figure 7-24. Super-rate burning of catalyzed HMX-HTPS composite propellant.

propellant. The nature of the super-rate burning observed in HMX-inert polymer propellants is similar to that of the super-rate burning of double-base propellants[23].

In order to differentiate between the roles of PbSt and C in super-rate burning, the burning rates of propellant with 2.4% PbSt added and propellant with 0.4% C added are measured. As shown in Fig. 7-25, a very small increase of burning rate is seen for both propellants. When 1.2% PbSt and 0.2% C are mixed together, super-rate burning occurs[23]. The degree of the super-rate burning is increased when the amount of both additives is doubled. Lead stearate acts as a super-rate burning cata-

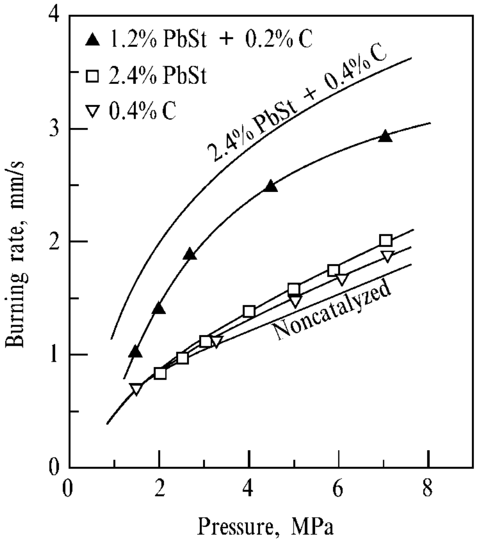

Figure 7-25. Effect of catalyst on super-rate burning of HMX-HTPE composite propellant.

lyst and C acts as a catalyst modifier. Both additives are needed together to obtain a high degree of super-rate burning.

Though the physicochemical properties of HTPE and HTPS are different, the super-rate burning effects appear to be similar. However, the degree of the effect is dependent on the type of binder used. As with double-base propellants, the combustion wave structure of both propellants are homogeneous even though the propellant structures are heterogeneous and the luminous flames are produced above the burning surfaces.

7.2.4.2 Super-Rate Burning of HMX-GAP Propellants

A typical super-rate burning of an HMX-GAP composite propellant is shown in Fig. 7-26. The lead catalyst is a mixture of lead citrate (LC: PbCi), $Pb_3(C_6H_5O_7)_2 \cdot xH_2O$, and carbon black (CB). The catalyzed HMX-GAP propellant consists of 19.4 % GAP, 78 % HMX, 2.0 % LC, and 0.6 % CB. GAP cured with 12.0 % hexamethylene diisocyanate (HMDI) and crosslinked with 3.2 % trimethylolpropane (TMP) is used to formulate GAP binder. The HMX particles are finely divided crystallized β HMX of bimodal particle size distribution (70 % of 2 μm and 30 % of 20 μm in diameter).

Super-rate burning occurs only when LC and CB mixed together within the HMX-GAP propellants[22]. Figure 7-27 shows the effect of mixing LC and/or CB into GAP binder. No effect of the addition of LC and/or CB on burning rate is seen. Furthermore, when these additives are mixed together into HMX pressed pellets, also no effect on burning rate is seen. These experimental facts indicate that super-rate burning of HMX-GAP propellants occurs only when HMX, GAP, a lead compound, and carbon are mixed together.

Figure 7-28 shows a set of flame photographs of the HMX-GAP propellants with and without catalysts. The luminous flame front of the noncatalyzed propellant is

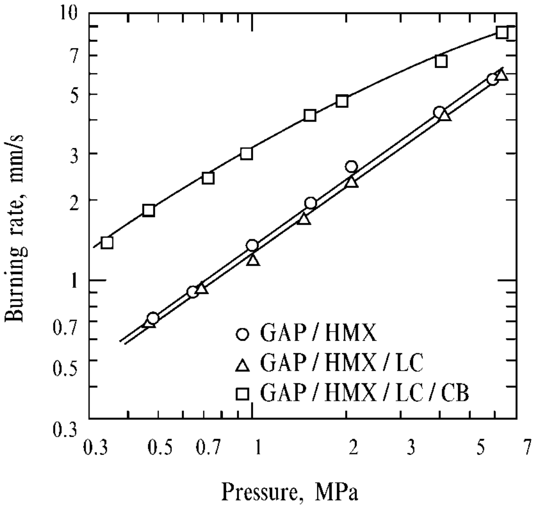

Figure 7-26. Effect of catalyst on super-rate burning of HMX-GAP composite propellant.

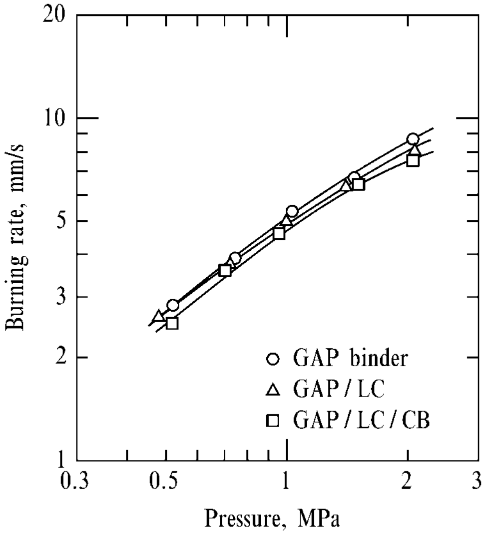

Figure 7-27. Effect of catalyst on burning rate of GAP copolymer showing no burning rate increase by the addition of lead citrate and/or carbon black.

almost attached to the burning surface at 0.5 MPa (a). When the propellant is catalyzed, the luminous flame is distended from the burning surface at the same pressure (b). Since the heat flux transferred back from the gas phase and the heat of reaction at the burning surface are increased, the flow velocity is increased in the gas phase[23]. Thus, the reaction distance to produce the luminous flame is increased. It is evident that the heat flux transferred back from the luminous flame front to the burning surface has a negligible effect on burning rate. Carbonaceous materials are formed in the region of super-rate burning as in the case of catalyzed

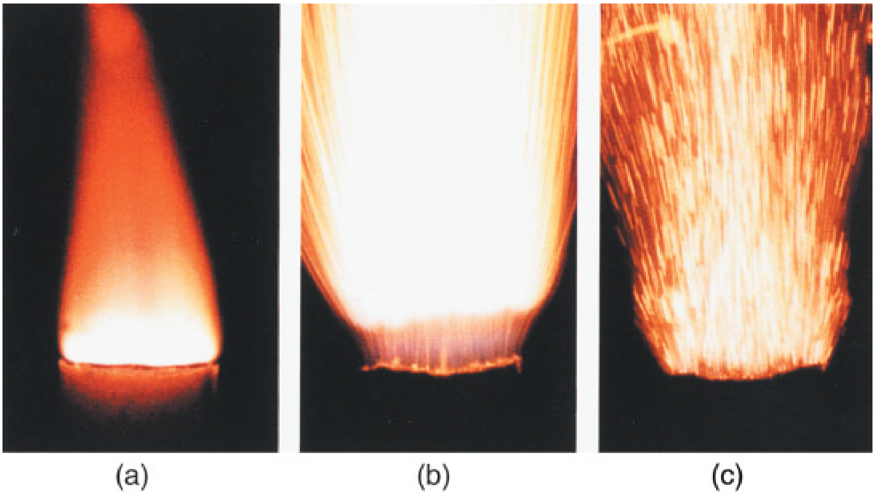

Figure 7-28. Flame photographs of catalyzed and noncatalyzed HMX-GAP composite propellants:

	Mass fraction			p	r
	HMX	GAP	Cat.	MPa	mm/s
(a)	0.80	0.20	0	0.5	0.8
(b)	0.80	0.20	0.03	0.5	1.9
(c)	0.80	0.20	0.03	1.5	4.1

double-base propellants. When pressure is increased to 1.5 MPa, the luminous flame front is blown down to the downstream and numerous carbonaceous particles are ejected from the burning surface (c).

7.3
TAGN Composite Propellants

7.3.1
TAGN-GAP Composite Propellants

As shown in Fig. 5-3, TAGN burns very rapidly even though the flame temperature is low. When TAGN is mixed with a polymeric material, a unique burning rate is observed. Unlike AP composite propellants, TAGN composite propellants are fuel rich and the flame temperature is low. However, the energy density of composite propellants composed of TAGN and GAP is relatively high because of the high concentration of hydrogen[24]. As shown in Table 7-4, the energy density of the propellant with TAGN, mass fraction $\xi(0.2)$ mixed with GAP is approximately equivalent to the propellant composed of HMX, $\xi(0.2)$, mixed with GAP. The physicochemical properties of TAGN-GAP and HMX-GAP (as a reference) are shown in Table 7-4.

The thermodynamic potential Θ defined by T_g/M_g is approximately the same for both TAGN-GAP and HMX-GAP composite propellants.

Table 7-4. Physicochemical properties of TAGN-GAP and HMX-GAP propellants.

	TAGN-GAP	*HMX-GAP*
ξ(TAGN) or ξ(HMX)	ξ(0.2)	ξ(0.2)
Flame temperature at 5 MPa T_g (K)	1380	1480
Molecular mass M_g (kg/kmol)	19.5	19.8
Density ρ_p (kg/m^3)	1320	1400
Θ (kmolK/kg)	70.8	74.7

7.3.2
Burning Rate and Combustion Wave Structure

The burning rate of TAGN-GAP propellant of ξ(0.2) is shown in Fig. 7-29. The pressure exponent is 0.95 and the temperature sensitivity is 0.010 K^{-1}. When TAGN and GAP are mixed together, the burning rate is lowered by less than that of each ingredient, i.e., GAP copolymer shown in Fig. 5-10 and TAGN shown in Fig. 5-3. However, when the mass fraction of TAGN is increased, the burning rate increases in the low pressure region and the pressure exponent decreases, as shown in Fig. 7-30.

The burning surface of TAGN-GAP propellants is heterogeneous because of the decomposition of TAGN particles and GAP. In the region of low ξ(TAGN) (below

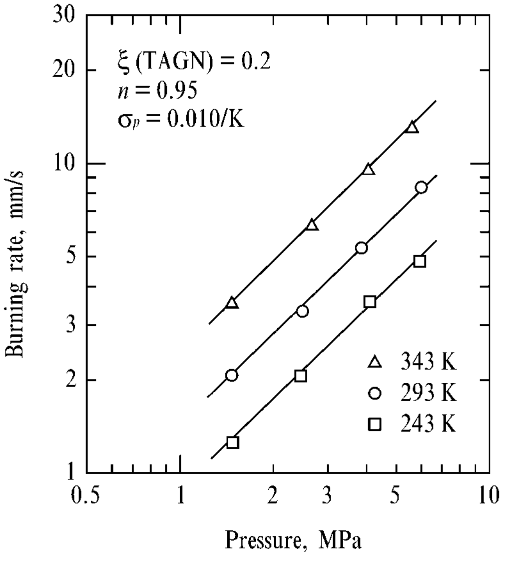

Figure 7-29. Burning rate and temperature sensitivity of TAGN-GAP composite propellant composed of ξ(0.2).

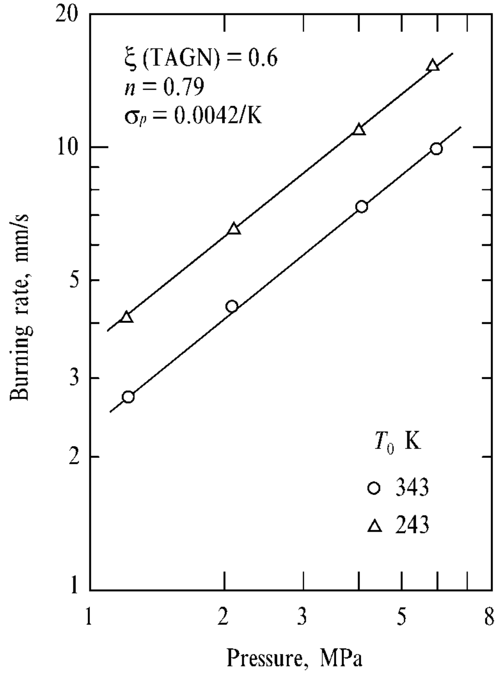

Figure 7-30. Burning rate and temperature sensitivity of TAGN-GAP composite propellant composed of ξ(0.6).

about 0.3), the combustion wave is similar to that of GAP copolymer. In the region of high ξ(TAGN) (above about 0.7), the luminous flame stands some distance above the burning surface as in the ease of the TAGN flame shown in Fig. 5-7. Since the heat flux generated at the burning surface is high for both TAGN and GAP, the burning rate of TAGN-GAP propellants is controlled by the rate of heat release at the burning surface.

7.4
Composite Modified Double-Base Propellants

Since the energy contained within double-base propellants is limited because of the limited energies of nitrocellulose (NC) and nitroglycerin (NG), addition of ammonium perchlorate or energetic nitramine particles such as HMX and RDX increases the combustion temperature and specific impulse. Extensive experimental studies have been done on the combustion characteristics of composite modified double-base (CMDB) propellants containing AP, RDX or HMX particles[25,27–31], and several models have been proposed to describe the burning rates of these propellants[25,27,28].

AP-CMDB propellants burn with a different mode from that of nitramine-CMDB propellants, namely that of AP composite propellants, a diffusion-flame mode. On the other hand, nitramine-CMDB propellants burn with a mode of double-base propellants, a premixed-flame mode. The AP particles mixed with a double-base propellant supply an oxidizer to the double-base propellant used as a base matrix. Though HMX and RDX are stoichiometrically balanced materials and produce high temperature combustion gases, in contrast to AP particles, no excess oxidizer fragments are produced from the nitramine particles. The nitramine particles supply heat to the base matrix. Accordingly, the combustion wave structures and burning rate characteristics of nitramine-CMDB propellants are different from those of AP-CMDB propellants[25].

7.4.1

AP-CMDB Propellants

7.4.1.1 Flame Structure and Combustion Mode

With the addition of AP particles to a double-base matrix, very fine luminous flamelets are formed from each AP particle at the burning surface and diffuse into the dark zone of the base matrix. As the number of AP particles mixed with the base matrix increases, the number of flamelets increase also and the dark zone is replaced with the luminous flame.

When large sized spherical AP particles (d_0 = 3 mm in diameter) are mixed, large sized flamelets are also formed in the dark zone[25]. Close observation of the AP particles at the burning surface reveals that a transparent bluish flame of low luminosity forms above each AP particle. This flame is an ammonia-perchloric acid flame whose products are oxidizer rich, which is also observed in AP composite propellants at low pressures, as shown in Fig. 7-5. The bluish flame is generated a short distance from the AP particle with a temperature up to 1300 K. Surrounding the bluish flame, a yellowish luminous flame stream is formed. This yellowish flame is produced by the diffusion of the decomposed gases of the AP and the double-base matrix. Since the decomposition gas of the base matrix is fuel-rich and the temperature in the dark zone is about 1500 K, the diffusion between the products of the AP and the matrix shifts in equivalence ratio toward stoichiometric, resulting in increased reaction rate and flame temperature. The flame structure of an AP-CMDB propellant is illustrated in Fig. 7-31. When the mass fraction of AP is increased, the dark zone of the base matrix is eliminated almost completely and the luminous flame approaches the burning surface, as shown in Fig. 7-32 (a). For reference, the flame structure of an RDX-CMDB propellant is also shown in Fig. 7-32 (b). Since RDX consists of stoichiometrically balanced crystalline particles, no diffusional flamelets are formed above the burning surface. The decomposed gases of RDX particles diffuse and mix with the decomposed gases of the base matrix and form a reactive homogeneous gas which reacts to produce a premixed flame above the burning surface. As in the case of double-base propellants, the luminous flame is distended from the burning surface for both RDX- and HMX-CMDB propellants[25].

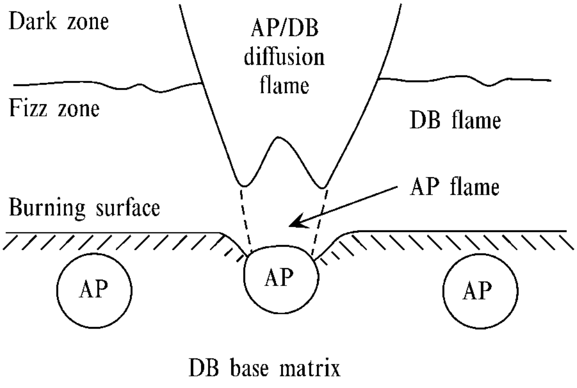

Figure 7-31. Flame structure of AP-CMDB propellant.

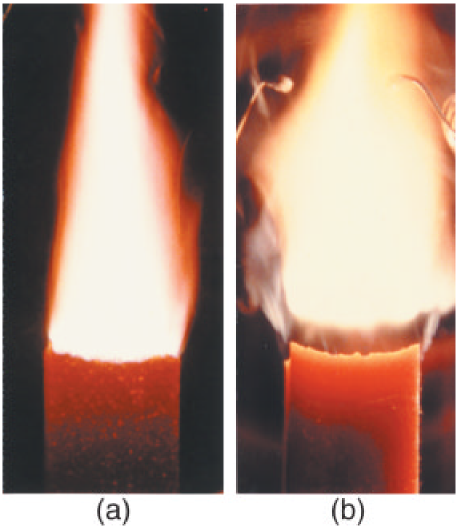

Figure 7-32. Flame photographs of AP-CMDB propellant (a) and RDX-CMDB propellant (b) showing that the luminous flame front of RDX-CMDB propellant is distended from the burning surface:

	Mass fraction			p	r
	AP	RDX	DB matrix	MPa	mm/s
(a)	0.30		0.70	2.0	9.0
(b)		0.30	0.70	2.0	2.2

7.4.1.2 **Burning Rate Models**

The burning rate of spherical AP particles mixed within a double-base propellant is expressed as a function of the initial AP particle size and pressure as follows:

$$r_{\mathrm{AP}} = \kappa \frac{p^{0.45}}{d_0^{0.15}} \tag{7.1}$$

where r_{AP} is the burning rate of AP particles, p is pressure, d_0 is the initial AP particle size, and κ is a constant determined experimentally as $\kappa = 0.38$. Equation (7.1) is similar to the expression obtained by Barrere and Nadaud, where the burning of AP spheres was obtained in gaseous fuel environments[26].

In order to derive a simplified burning rate expression for AP particles, it is assumed that the area of fastest regression has an effective region of thickness, η, around each AP particle, independent of particle size. The effective region is also assumed to burn at the same rate as the AP particle in the DB matrix. This effective thickness is found experimentally to be

$$\frac{\pi}{6} w(d_0 + 2\eta)^3 = \xi \tag{7.2}$$

$$w = \frac{6\rho_{DB}}{\pi d_0^3 (\rho_{AP}/\varphi_{AP} + \rho_{DB} - \rho_{AP})} \tag{7.3}$$

where ξ is the volumetric fraction of the AP-CMDB propellant which burns with the same rate as the AP particle in the DB matrix, and w is the number of AP particles in unit volume of the propellant, φ is mass fraction, and the subscripts AP and DB are AP particle and DB matrix, respectively.

The critical mixture of AP when excess AP particles begin to appear is approximately a 30 % mixture of 18 µm AP particles with the DB matrix. Thus, the effective thickness is derived from Eqs. (7.2) and (7.3) as $\eta = 5$ µm, with ξ assumed to be unity.

As the combustion zones of AP-CMDB propellants are highly heterogeneous physically and chemically, it is assumed that the burning surface of the DB matrix regresses at different rates for two different regions: (1) the area remote from the AP particles where the heat feedback from the gas phase to the burning surface is due only to the DB flame, and (2) the area adjacent to the AP particles which is influenced by heat feedback from the AP/DB diffusion flame. When the areas of fastest regression at the interface between the AP particles and the DB matrix begin to overlap, the base matrix binding some of the AP particles is eroded and some of the burning AP particles are ejected into the gas phase. These AP particles are called "excess AP particles".

The regression rate of region (1) is regarded to be the same as the regression rate represented by Eqs. (3.57)–(3.60). The burning rate equations are obtained under the assumptions that the gas phase reaction takes place at a constant rate and is second-order over the fizz zone, and the luminous flame is too far from the surface to influence the burning rate. The regression rate is also expressed by a one-step Arrhenius-type reaction rate given by Eq. (3.61).

Region (2) is assumed to regress at approximately the same rate as the AP particles, as given by Eq. (7.1). Thus, the burning rate of AP-CMDB propellants r_A is determined as the fractionally weighted sum of the two different regression rates,

$$r_A = \frac{1}{\xi/r_{AP} + (1-\xi)/r_{DB}} \tag{7.4}$$

The results of the calculations are shown in Fig. 7-33. The assumed values for the physical constants and reaction kinetics are listed in [25]. The burning rate increases with increasing pressure, and also increases with increasing concentration and

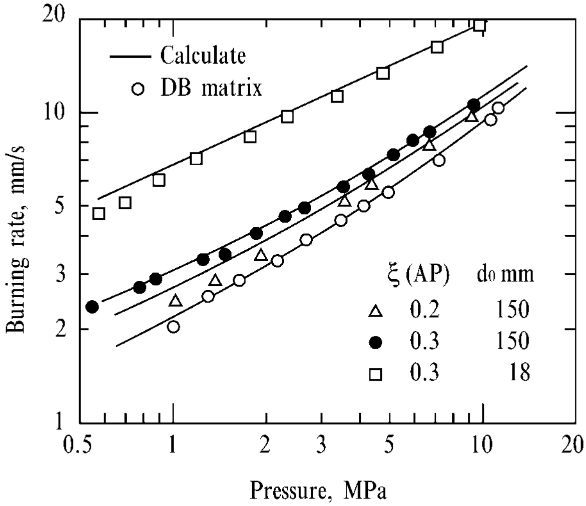

Figure 7-33. Computed and experimental burning rates of AP-CMDB propellants.

decreasing particle size of AP particles. These calculated results compare favorably with the experimental results that are also shown in Fig. 7-33. The calculated burning surface temperature of the DB matrix varies from 621 K at 1 MPa to 673 K at 8 MPa. The temperature sensitivity decreases as pressure increases ($\sigma_p = 0.0056\,K^{-1}$ at 8 MPa)[25].

7.4.2
HMX-CMDB Propellants

7.4.2.1 Flame Structure and Combustion Mode

The decomposed gases produced by HMX particles and the base matrix (double-base propellant) diffuse and mix together and produce relatively homogeneous gases on and above the burning surface of the HMX-CMDB propellant. Since the primary ingredients of double-base propellants are nitrate esters such as NC and NG, the energy density of double-base propellants is represented by the number of $O{-}NO_2$ chemical bonds contained within the unit mass of propellant. The breaking of $O{-}NO_2$ bonds produces NO_2 and aldehydes and C–H–O species. The NO_2 acts as an oxidizer component and reacts with the aldehydes and the remaining C–H–O species, which act as fuel components. This reaction is highly exothermic, and the burning rate of double-base propellants is determined by this reaction process. Thus, the burning rate of double-base propellants is correlated with $\xi(NO_2)$[27, 31].

The chemical structure of HMX is $(CH_2)_4(N{-}NO_2)_4$ and the decomposed fragments of $N{-}NO_2$ bonds produce nitrogen oxides such as NO_2, NO, and oxide radicals. These nitrogen oxides are considered to act as oxidizer components and the remaining C–H–O fragments act as fuel components. These oxidizer and fuel components react to produce high temperature combustion products in the gas phase.

Since ξ(NO_2) contained within the unit mass of HMX is higher than that of double-base propellants, the overall gas-phase reaction is enhanced by the addition of HMX. The physical structure of double-base propellants is homogeneous because of the gelatinized nature of the mixture of NC, NG, and stabilizers. Though the addition of HMX crystalline particles makes the physical structure of HMX-CMDB propellants heterogeneous, the gas phase structure is homogeneous because the decomposed gases from the HMX particles and the base matrix diffuse and mix together above the burning surface and react at some distance above the burning surface to produce the luminous flame. The gas phase structure of HMX-CMDB propellants is similar to that of RDX-CMDB propellants as shown in Fig. 7-32 (b).

Figure 7-34 shows the adiabatic flame temperature and the heat of explosion of HMX-CMDB propellants as a function of ξ(NO_2) under thermal equilibrium conditions. The adiabatic flame temperature, T_g, and the heat of explosion increases as ξ(NO_2) increases, i.e., ξ(NO_2) increases with increasing ξ(HMX). The base matrix is composed of the mass fractions of NC 0.25, NG 0.65, and DEP 0.10. The nitrogen concentration of the nitrocellulose used is 12.2 %, the mass fraction of NO_2 contained within the base matrix is ξ(NO_2 : 0.496), and the heat of explosion is 4.76 MJ/kg.

Figure 7-35 shows the relationship between ξ(NO_2) and the mole fraction of combustion products at 1 MPa. Though the mole fraction of CO, H_2O, and CO_2 decreases with increasing ξ(NO_2), the mole fraction of N_2 increases with ξ(NO_2). The mole fraction of H_2 remains relatively unchanged in the range of the mass fraction of HMX, ξ(HMX) = 0.0 ~ 0.444.

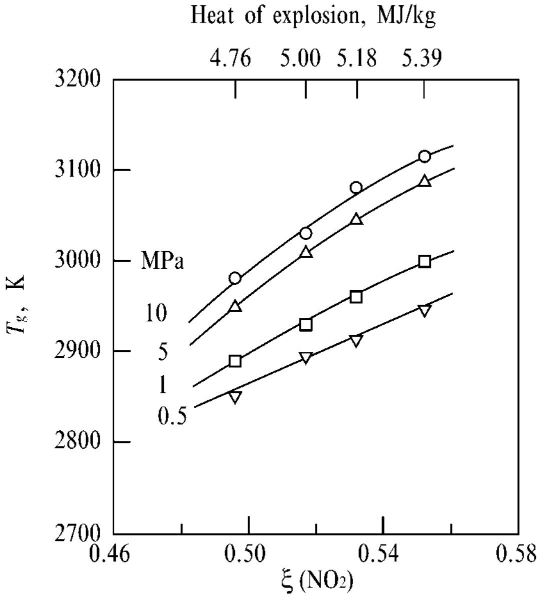

Figure 7-34. Adiabatic flame temperature of HMX-CMDB propellants as a function of ξ(NO2) or het of explosion.

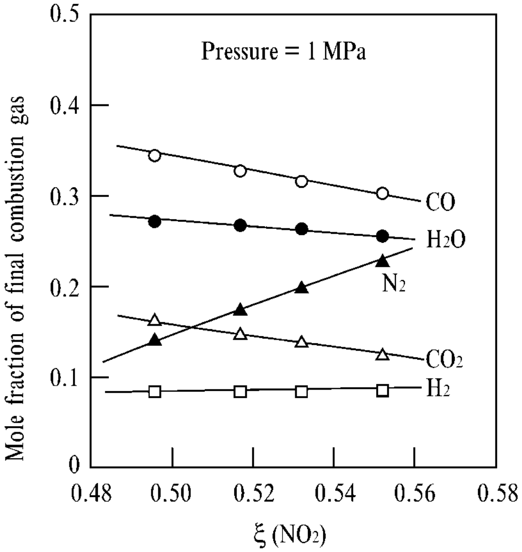

Figure 7-35. Mole fraction of final combustion gas of HMX-CMDB propellant as a function of ξ(NO2).

7.4.2.2 Burning Rate Characteristics

The burning rate of a double-base propellant increases with increasing energy density of propellant at constant pressure. In contrast, the burning rate of HMX-CMDB propellants decreases as ξ(HMX) increases, as shown in Fig. 7-36, which implies that the burning rate of HMX-CMDB propellants decreases with increasing energy density of propellant at constant pressure[27,29–31]. The HMX particles mixed are of β crystal shape and the mean particle diameter is 20 μm. Though the burning rate of

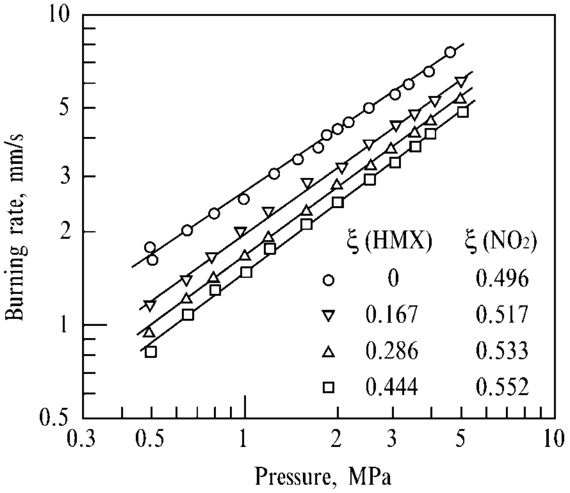

Figure 7- 36. Burning rates of HMX-CMDB propellants composed of different mass fraction of HMX.

AP-CMDB propellants increases as ξ(AP) increases and is highly dependent on the size of the admixed AP particles, the burning rate is less dependent on the size of the admixed HMX particles[25].

Figure 7-37 shows the relationship between burning rate and ξ(NO_2) at different pressures[28]. The burning rate decreases linearly as ξ(NO_2) increases at a constant pressure in a ξ(NO_2) versus ln *r* plot. The burning rate is represented by

$$r = c \exp \{a\, \xi(NO_2)\}\, p^{n} \tag{7.5}$$

where *r* (mm/s) is burning rate and *a* is constant, *p* (MPa) is pressure, *n* is pressure exponent, and *c* (mm/s) is constant when the initial propellant temperature T_0 is given. The pressure exponent is less dependent on ξ(NO_2) and pressure. The parameters of the burning rate given by Eq. (7.5) are $a = -5.62$, $c = 38.3$ mm/s, and $n = 0.70$ at $T_0 = 293$ K.

Since the reaction rate in the gas phase is dependent on the mole fractions of reactive gases, the fundamental reaction pathway in the gas phase of double-base propellants remains relatively unchanged by the addition of HMX particles. On the other hand, the burning rate of double-base propellants increases as ξ(NO_2) increases at constant pressure as discussed in Chapter 6. The gas phase structure of HMX-CMDB propellants is similar to that of double-base propellants shown in Fig. 6-4. A luminous flame stands above the burning surface and the flame standoff distance decreases as pressure increases. The region between the burning surface and the flame front of the luminous flame zone is also named the dark zone. The flame standoff distance (the dark zone length) decreases with increasing ξ(HMX) at con-

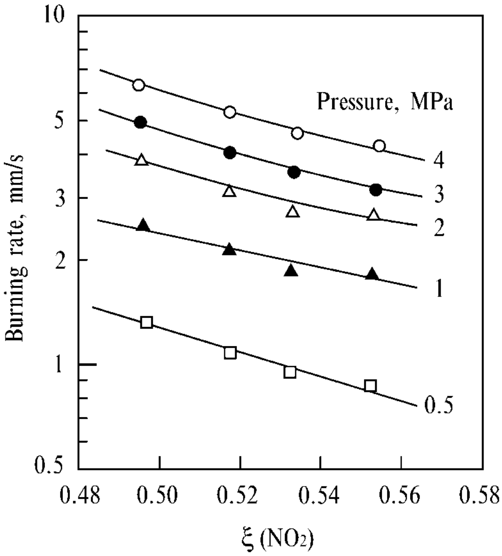

Figure 7-37. Burning rate of HMX-CMDB propellant as a function of ξ(NO_2).

stant pressure. The homogenous nature in the gas phase of a double-base propellant remains unchanged even when crystalline HMX particles are mixed within the double-base propellant[27,31].

When an HMX-CMDB propellant burns steadily, the temperature in the condensed phase increases exponentially from the initial temperature T_0 to the burning surface temperature T_s, as shown in Fig. 6-3. A rapid temperature rise occurs above the burning surface and reaches the temperature in the dark zone T_d . The temperature is relatively constant up to a certain distance from the burning surface and increases again further downstream in the gas phase. The thermal structure of HMX-CMDB propellants appears to be similar to that of homogeneous double-base propellants even though HMX-CMDB propellants are heterogeneous.

Figure 7-38 shows the relationship between T_g and T_d at different burning pressures. The dark zone temperature T_d decreases as T_g (the adiabatic flame temperature) increases. The addition of HMX decreases T_d, which is the temperature of an intermediate reaction zone, i.e., the dark zone. On the other hand, T_d increases slightly with increasing pressure at a constant $\xi(NO_2)$ as shown in Fig. 7-39. The burning rate is correlated with T_d, as shown by the straight line ln r versus T_d plot shown in Fig. 7-40. The burning rate increases with increasing T_d at constant $\xi(NO_2)$, i.e., the burning rate increases as pressure increases[31]. Figure 7-41 shows the burning rate as a function of the adiabatic flame temperature T_g. The burning rate decreases as T_g increases, which implies that the burning rate decreases as the energy density of HMX-CMDB propellants increases.

As in the case of double-base propellants, the burning rate of HMX-CMDB propellants is determined by the heat flux transferred back from the gas phase to the solid phase and the heat flux generated at the burning surface. The temperature gradient in the fizz zone of HMX-CMDB propellants, $\phi = (dT/dx)_{f,s}$, is shown in

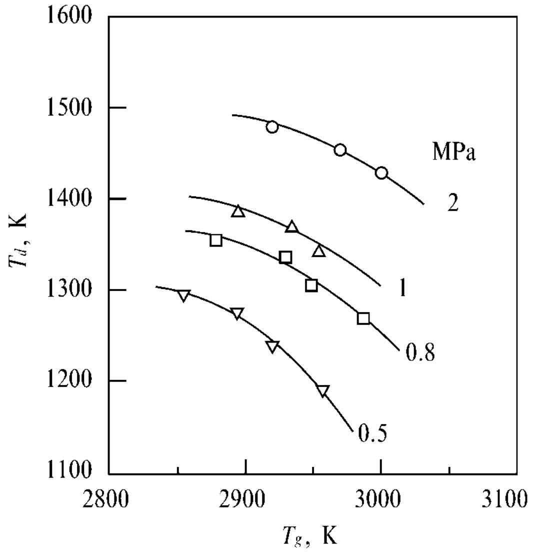

Figure 7-38. Dark zone temperature versus adiabatic flame temperature at different pressures.

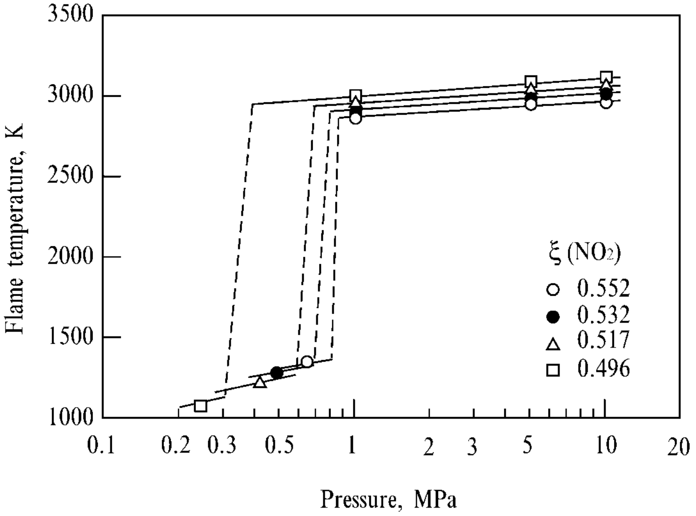

Figure 7-39. Temperature distribution in gas phase of HMX-CMDB propellant as a function of $\xi(NO_2)$.

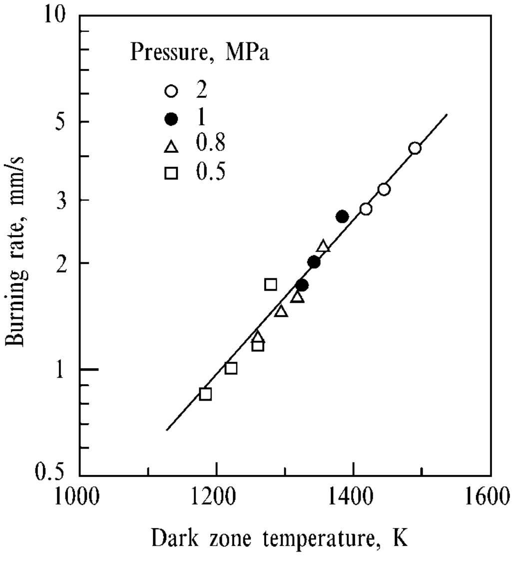

Figure 7-40. Burning rate versus dark zone temperature of HMX-CMDB propellant at different pressures.

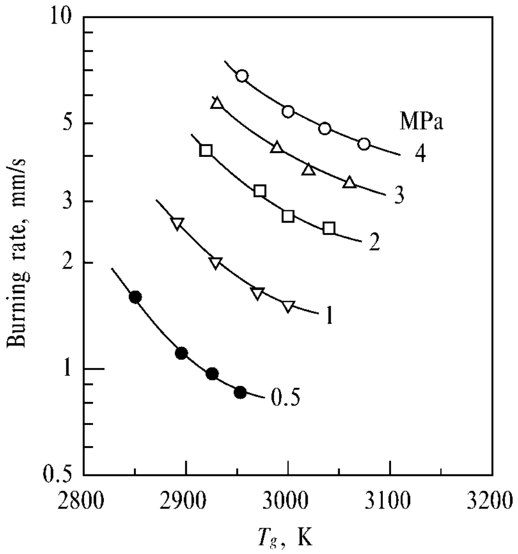

Figure 7-41. Burning rate versus adiabatic flame temperature of HMX-CMDB propellant at different pressures showing that the burning rate decreases as the adiabatic flame temperature increases.

Fig. 7-42 as a function of the dark zone temperature, where T is temperature, x is distance, and the subscript f,s is the fizz zone above the burning surface. As T_d increases, ϕ increases linearly in a ln ϕ versus T_d plot. The heat flux transferred back from the fizz zone to the burning surface is the dominant factor in determining the burning rate[27,31]. In fact, the relationship between the burning rate and ϕ shown in Fig. 7-42 is also similar to the relationship between the burning rate and T_d shown in Fig. 7-40.

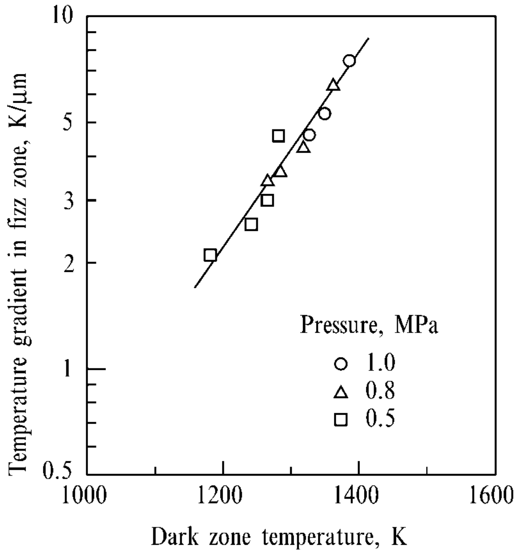

Figure 7-42. Temperature gradient in fizz zone versus dark zone temperature of HMX-CMDB propellant at different pressures showing that the heat flux transferred back to the burning surface increases as the dark zone temperature increases.

Important results are that the dark zone temperature (T_d) decreases even though the flame temperature (T_g) is increased by the increase of $\xi(NO_2)$ at constant pressure as shown in Fig. 7-38. Furthermore, ϕ decreases also as $\xi(NO_2)$ increases, and thus the burning rate decreases as $\xi(NO_2)$ increases, i.e., the burning rate of HMX-CMDB propellants decreases as ξ(HMX) increases at a constant pressure. The observed burning rate characteristics of HMX-CMDB propellants are understood without consideration of the diffusional process and the chemical reaction between the decomposed gases of the base-matrix and the HMX particles. This is a significant difference from the burning rate characteristics of AP-CMDB propellants.

The heat release due to the decomposition of the HMX particles occurs relatively independently from the decomposition of the base matrix used. The overall heat release at the burning surface of HMX-CMDB propellant is represented by[25]

$$Q_{s,\mathrm{CMDB}} = \xi(\mathrm{HMX})Q_{s,\mathrm{HMX}} + \{1 - \xi(\mathrm{HMX})Q_{s,\mathrm{DB}}\} \tag{7.6}$$

where $Q_{s,\mathrm{CMDB}}$, $Q_{s,\mathrm{HMX}}$, and $Q_{s,\mathrm{DB}}$ are the heat release at the burning surface of the unit mass of HMX-CMDB propellants, HMX particles, and the base matrix, respectively. Equation (7.6) indicates that the overall heat release of HMX-CMDB propellant is the mass-averaged heat release of the HMX particles and the base matrix.

The temperature sensitivity of gas phase Φ defined in Eq. (3.79) and the temperature sensitivity of the condensed phase Ψ defined in Eq. (3.80) are obtained from the data of the burning surface temperature T_s, the temperature in the fizz zone T_g, the activation energy in the fizz zone E_g, the heat of reaction at the burning surface Q_s, the temperature gradient in the fizz zone ϕ, and the burning rate r. Figure 7-43 shows the temperature sensitivity of the burning rate of HMX-CMDB propellants as

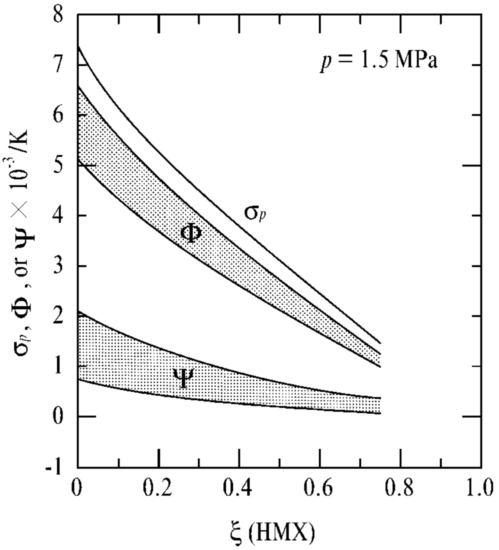

Figure 7-43. Temperature sensitivity of burning rate decreases as ξ(HMX) increases and Φ (gas phase) has a greater effect on σ_p than Ψ (condensed phase).

a function of ξ(HMX). The temperature sensitivity decreases as ξ(HMX) increases, and the temperature sensitivity of the burning rate consists of 70 % Φ and 30 % Ψ.

7.5
Smokeless Composite Propellants

7.5.1
AN Composite Propellants

AN composite propellants containing mass fractions of AN, ξ(AN), ranging from 0.70 to 0.80 with PU binder are studied extensively and various ballistic properties have been utilized in smokeless rocket propellants[32]. Since the propellants are made with halogen-free ingredients, no smoke is produced from the exhaust rocket nozzle theoretically. However, the specific impulse is too low to use for advanced rocket propulsion. Furthermore, the phase transition of AN particles reduces the mechanical properties of the propellant grains and the production capability is affected by humidity. The process for mixing the AN and the binder is restricted because of the crystal shape of AN particles. Small-sized AN propellant grains are made as pressed grains with mass fractions of ξ(0.85) or more to obtain smokeless combustion products. This class of propellant grains is used as gas generating propellants.

The burning rate of AN propellants is rather limited, ranging from 0.8 mm/s to 10 mm/s at 7 MPa. The burning rate is less dependent on the AN particle size because the AN particles melt and mix with the melted PU binder on the burning surface[32]. The decomposed gas produced at the burning surface is premixed in nature and forms a premixed-type luminous flame above the burning surface. The luminous flame stands some distance above the burning surface, as in the case of double-base propellants. In contrast, AP propellants produce a diffusion-type luminous flame on and just above the burning surface.

Combustion catalysts are needed to achieve complete combustion, e.g. chromium compounds such as chromium trioxide (Cr_2O_3), ammonium dichromate ($(NH_4)_2Cr_2O_7$) and copper chromite ($CuCr_2O_4$). Carbon (C) is also added as a burning rate modifier with the combustion catalysts. The burning rate is also changed by NiO used as a phase transition stabilizer of AN crystals[21]. The pressure exponent without catalysts is approximately 0.8 at ξ(0.8) and is reduced to 0.5–0.6 by the addition of the catalysts. The specific impulse is increased approximately 10 s by the replacement of PB or PU binder with GAP, as shown in Fig. 4-10. The burning rate is also increased by exothermic nature of GAP.

The addition of AP particles within AN-PU propellants increases the burning rate and reduces the pressure exponent without catalysts. The specific impulse is also increased from 225 s to 235 s at 10 MPa by the replacement of 30 % AN by the same amount of AP. However, the smokeless nature is eliminated because of the production of HCl, and these propellants are classified as reduced smoke propellants.

7.5.2
ADN, CL-20, and HNF Composite Propellants

The ballistic properties of ADN, CL-20, and HNF as monopropellants and composite propellants used as oxidizers have been studied extensively[33–39]. Since ADN, CL-20, and HNF produce excess oxygen in their combustion products, these are used as oxidizer crystals of composite propellants. Though the pressure exponent of ADN and CL-20 is approximately 0.7[38], about the same value as that of HMX and RDX when burned as pressed pellets, the pressure exponent of HNF is about 0.85–0.95[39].

When these oxidizer particles are mixed with binders such as HTPB, nitro-polymers, and GAP, the burning rate decreases as the mass fraction of ADN or HNF particles increases[34]. Though the temperature sensitivity of ADN composite propellant is quite high in the low pressure region, 0.005 K^{-1} at 1 MPa, it decreases as pressure increases, 0.0023 K^{-1} at 10 MPa[38]. However, the temperature sensitivity of HNF composite propellant is about 0.0018 K^{-1} in the pressure range 1 MPa–10 MPa[38]. The burning surface of ADN and HNF composite propellants is covered with melt layer when PU binder is used, and the luminous flame stands some distance above the burning surface for both propellants[36], as in the case of HMX composite propellants[19].

When HNF or ADN particles are mixed with a GAP copolymer with aluminum particles, an HNF-GAP or ADN-GAP composite propellant is formed, respectively. A higher specific impulse is obtained theoretically than the specific impulse of aluminized AP-HTPB composite propellants[37]. However, the ballistic properties of ADN, CL-20, and HNF composite propellants such as pressure exponent, temperature sensitivity, combustion instability, and mechanical properties are needed to be improved drastically.

References

1 Lengelle, G., Duterque, J. and Trubert, J. F., Physico-Chemical Mechanisms of Solid Propellant Combustion, edited by Yang, V., Brill, T. B., and Wu-Zhen Ren, Progress in Astronautics and Aeronautics, Vol. 185, Chapter 2.2, AIAA, Washington DC (2000).

2 Ramohalli, K. N. R., Steady-State Burning of Composite Propellants, Fundamentals of Solid-Propellant Combustion, edited by Kuo, K. K. and Summerfield, M., Progress in Astronautics and Aeronautics, Vol. 90, Chapter 8, AIAA, New York (1984).

3 Kubota, N., Temperature Sensitivity of Solid Propellants and Affecting Factor: Experimental Results, Nonsteady Burning and Combustion Stability of Solid Propellants, edited by De Luca, Price, E. W., and Summerfield, M., Progress in Astronautics and Aeronautics, Vol. 143, Chapter 4, AIAA, Washington DC (1992).

4 Beckstead, M. W., Derr, R. L., and Price, C. F., Model of Composite Solid-Propellant Combustion Based on Multiple Flames, AIAA Journal, Vol. 8, No. 12, 1970, pp. 2200–2207.

5 Hermance, C. E., A Model of Composite Propellant Combustion Including Surface Heterogeneity and Heat Generation, AIAA Journal, Vol. 4, No. 9, 1966, pp. 1629–1637.

6 Summerfield, M., Sutherland, G. S., Webb, W. J., Taback, H. J. and Hall, K. P., The Burning Mechanism of Ammonium Perchlorate Propellants, ARS Progress in Astronautics and Rocketry, Vol. 1, Solid Propellant Rocket Research, Academic Press, New York (1960), pp. 141–182.

7 Boggs, T. L., Derr, R. L. and Beckstead, M. W., Surface Structure of Ammonium Perchlorate Composite Propellants, AIAA Journal, Vol. 8, No. 2, 1970, pp. 370–372.

8 Kuwahara, T. and Kubota, N., Low Pressure Burning of Ammonium Perchlorate Composite Propellants, Combustion Science and Technology, Vol. 47, 1986, pp. 81–91.

9 Steinz, J. A., Stang, P. L., and Summerfield, M., The Burning Mechanism of Ammonium Perchlorate-Based Composite Solid Propellants, AMS Report No. 830, Aerospace and Mechanical Sciences, Princeton University, Princeton, NJ (1969).

10 Price, E. W., Handley, J. C., Panyam, R. R., Sigman, R. K., and Ghosh, A., Combustion of Ammonium Perchlorate-Polymer Sandwiches, Combustion and Flame, Vol. 7, No. 7, 1963.

11 Bastress, E. K., Modification of the Burning Rates of Ammonium Perchlorate Solid Propellants by Particle Size Control, Ph.D. Thesis, Department of Aeronautical Engineering, Princeton University, Princeton, NJ (1961).

12 Kubota, N., Kuwahara, T., Miyazaki, S., Uchiyama, K., and Hirata, N., Combustion Wave Structure of Ammonium Perchlorate Composite Propellants, Journal of Propulsion and Power, Vol. 2, No. 4, 1986, pp. 296–300.

13 Kubota, N. and Miyazaki, S., Temperature Sensitivity of Burning Rate of Ammonium Perchlorate Propellants, Propellants, Explosives, Pyrotechnics, Vol. 12, 1987, pp. 183–187.

14 Bazaki, H. and Kubota, N., Friction Sensitivity Mechanism of Ammonium Perchlorate Composite Propellants, Propellants, Explosives, Pyrotechnics, Vol. 16, 1991, pp. 43–47.

15 Kubota, N. and Hirata, N., Inhibition Reaction of LiF on the Combustion of Ammonium Perchlorate Propellants, Twentieth Symposium (International) on Combustion, The Combustion Institute, Pittsburgh, PA (1984), pp. 2051–2056.

16 Beckstead, M. W. and McCarty, K. P., Modeling Calculations for HMX Composite Propellants, AIAA Journal, Vol. 20, No. 1, 1982, pp. 106–115.

17 Kubota, N., Combustion Mechanisms of Nitramine Composite Propellants, Eighteenth Symposium (International) on Combustion, The Combustion Institute, Pittsburgh, PA (1981), pp. 187–194.

18 Cohen, N. S. and Price, C. F., Combustion of Nitramine Propellants, AIAA Journal, Vol. 12, No. 10, 1975, pp. 25–42.

19 Kubota, N., Physicochemical Processes of HMX Propellant Combustion, Nineteenth Symposium (International) on Combustion, The Combustion Institute, Pittsburgh, PA (1982), pp. 777–785.

20 Beckstead, M. W., Overview of Combustion Mechanisms and Flame Structures for Advanced Solid Propellants, edited by Yang, V., Brill, T. B., and Wu-Zhen Ren, Progress in Astronautics and Aeronautics, Vol. 185, Chapter 2.1, AIAA, Washington DC (2000).

21 Klager, K. and Zimmerman, G. A., “Steady Burning Rate and Affecting Factors: Experimental Results”, Nonsteady Burning and Combustion Stability of Solid Propellants, edited by De Luca, L., Price, E. W., and Summerfield, M., Progress in Astronautics and Aeronautics, Vol. 143, Chapter 3, AIAA, Washington DC (2992); also Kubota, N., Sonobe, T., Yamamoto, A, and Shimizu, H., Burning Rate Characteristics of GAP Propellants, Journal of Propulsion and Power, Vol. 6, No. 6, 1990. pp. 686–689.

22 Kubota, N. and Sonobe, T., Burning Rate Catalysis of Azide/Nitramine Propellants, Twenty-third Symposium (International) on Combustion, The Combustion Institute, Pittsburgh, PA (1990), pp. 1331–1337.

23 Kubota, N. and Hirata, N., Super-Rate Burning of Catalyzed HMX Propellants, Twenty-first Symposium (International) on Combustion, The Combustion Institute, Pittsburgh, PA (1986), pp. 1943–1951.

24 Kubota, N., Hirata, N., and Sakamoto, S., Combustion Mechanism of TAGN, Twenty-first Symposium (International) on Combustion, The Combustion Institute, Pittsburgh, PA (1986), pp. 1925–1931.

25 Kubota, N. and Masamoto, T., Flame Structures and Burning Rate Characteristics of CMDB Propellants, Sixteenth Symposium (International) on Combustion, The Combustion Institute, Pittsburgh, PA (1976), pp. 1201–1209.

26 Barrere, N. and Nadaud, L., Tenth Symposium (International) on Combustion, The Combustion Institute, Pittsburgh, PA (1965), pp. 1381–1389.

27 Kubota, Energetics of HMX-Based Composite Modified Double-Base Propellant Combustion, Journal of Propulsion and Power, Vol. 15, No. 6, 1999, pp. 759–762.

28 Swaminathan, V. and Soosai, M., On the Burning Rate Characteristics of CMDB Propellants, Propellants and Explosives, Vol. 4, 1979, pp. 107–111.

29 Yano, Y. and Kubota, N., Combustion of HMX-CMDB Propellants (I), Propellants, Explosives, Pyrotechnics, Vol. 10, 1985, pp. 192–196; also Yano, Y. and Kubota, N., Combustion of HMX-CMDB Propellants (II), Propellants, Explosives, Pyrotechnics, Vol. 11, 1986, pp. 1–5.

30 Kubota, N. and Okuhara, H., Burning Rate Temperature Sensitivity of HMX Propellants, Journal of Propulsion and Power, Vol. 5, No. 4, 1989, pp. 406–410.

31 Aoki, I., Burning Rate Characteristics of Double-Base and CMDB Propellants, Ph.D. Thesis, Department of Aeronautics, University of Tokyo, Tokyo (1998).

32 In-house Report (unpublished), Daicel Chemical Industries, Tokyo (1966 – 1968).

33 Chan, M. L., Reed Jr., R., and Ciaramitaro, D. A.. Advances in Solid Propellant Formulations, Solid Propellant Chemistry, Combustion, and Motor Interior Ballistics, edited by Yang, V., Brill, T. B., and Wu-Zhen Ren, Progress in Astronautics and Aeronautics, Vol. 185, Chapter 1.7, AIAA, Washington DC (2000).

34 Takishita, Y. and Shibamoto, H., In-house Report (unpublished), Hosoya Pyrotechnics Co., Tokyo (1999).

35 Price, E. W., Chakravarthy, S. R., Freeman, J. M., and Sigman, R. K., Combustin of Propellants with Ammonium Dinitramide, AIAA-98–3387, AIAA, Reston, Virginia (1998).

36 Korobeinichev, O. P., Kuibida, L. V., and Paletsky, A. A., Development and Application of Molecular Mass-Spectrometry to the Study of ADN Combustion Chemistry, AIAA-98-0445, AIAA, Reston, Virginia (1998).

37 Gadiot, G. M. H. J. L., Mul, J. M., Meulenbrugge, J. J., Korting, P. A. O. G., Schnorhk, A. J., and Schoyer, H. F. R., New Solid Propellants Based on Energetic Binders and HNF, IAF-92-0633, 43rd Congress of the International Astronautical Federation, Paris (1992).

38 Atwood, A. I., Boggs, T. L., Curran, P. O., Parr, T. P., and Hanson-Parr, D. M., Burn Rate of Solid Propellant Ingredients, Part 1: Pressure and Initial Temperature Effects, and Part 2: Determination of Burning Rate Temperature Sensitivity, Journal of Propulsion and Power, Vol. 15, No. 6, 1999, pp. 740–752.

39 Louwers, J., Gadiot, G. M. H. J. L, Breqster, M. Q., Son, S. F., Parr, T., and Hanson-Parr, D., Steady-State Hydrazinium Nitroformate (HNF) Combustion Modeling, Journal of Propulsion and Power, Vol. 15, No. 6, 1999, pp. 772–777.

Propellants and Explosives: Thermochemical Aspects of Combustion. Naminosuke Kubota
Copyright © 2002 Wiley-VCH Verlag GmbH & Co. KGaA
ISBNs: 3-527-30210-7 (Hardback); 3-527-60050-7 (Electronic)

8
Combustion of Explosives

8.1
Detonation Velocity and Pressure

As discussed in Section 3.2.3 of Chapter 3, the derivative of the Hugoniot curve is equal to the derivative of the isentropic curve at point *J*. Then, Eq. (3.13) becomes

$$\left[\frac{\partial p}{\partial(1/\rho)}\right]_H = \left[\frac{\partial p}{\partial(1/\rho)}\right]_s = \frac{p_2-p_1}{1/\rho_2-1/\rho_1} \tag{8.1}$$

The logarithmic form of Eq. (1.14) gives the specific heat ratio during isentropic change as[1,2]

$$\gamma = -\left[\frac{\partial \ln p}{\partial \ln (1/\rho)}\right]_s = \frac{1-p_1/p_2}{\rho_2/\rho_1-1} \tag{8.2}$$

The pressure p_J at the Chapman-Jouguet (CJ) point is obtained using Eqs. (3.12) and (8.2) as[2]

$$p_J = \frac{\rho_1 u_D^2+p_1}{\gamma+1} \tag{8.3}$$

Since p_J is much larger than p_1 in the case of a detonation wave, Eq. (8.3) becomes

$$p_J = \frac{\rho_1 u_D^2}{\gamma+1} \tag{8.4}$$

The characteristic values at the CJ point are also obtained from Eqs. (8.2) and (8.4) as[1]

$$\rho_J = \frac{\gamma+1}{\gamma}\rho_1 \tag{8.5}$$

$$u_p = \frac{1}{\gamma+1} u_D \tag{8.6}$$

The specific heat ratio γ expressed by Eq. (8.2) is determined to be 2.85 for high explosives by statistical detonation experiments. Thus, Eqs. (8.4) – (8.6) are[1]

$$p_J = 0.26\rho_1 \, {u_D}^2 \tag{8.7}$$

$$\rho_J = 1.35\rho_1 \tag{8.8}$$

$$u_p = 0.26 \, u_D \tag{8.9}$$

Though the theoretical detonation velocity and pressure at the CJ point are given by very simplified expressions, the computed results are confirmed by measurement results for RDX and TNT based explosives[1] (Cp-B indicates Composition B) as shown in Table 8-1. The calculated detonation velocity is obtained by Eq. (8.7).

Table 8-1. Detonation velocity and pressure at the CJ point.

			RDX	*TNT*	*Cp-B*	*Cp-B*	*Cyclotol*
ρ		(kg/m^3)	1767	1637	1670	1713	1743
u_D		(m/s)	8639	6942	7868	8018	8252
p_J	by experiments	(GPa)	33.79	18.91	27.2	29.22	31.25
p_J	by Eq. (8.7)	(GPa)	34.5	20.7	27.2	29.0	31.2

8.2
Density and Detonation Velocity

8.2.1
Energetic Explosive Materials

Table 8-2 shows the measured detonation velocity and density of various types of energetic explosive materials based on the data in [2] and [3]. The detonation velocity at the CJ point is computed by the use of Eq. (8.7). The detonation velocity increases as the density increases and also the heat of explosion increases. Ammonium nitrate (AN) is an oxidizer-rich material, and the adiabatic flame temperature is low compared with that of other materials. Thus, the detonation velocity is low and therefore the detonation pressure at the CJ point is low compared with that of other energetic materials. However, when AN particles are mixed with a fuel component, the detonation velocity increases. On the other hand, when HMX or RDX is mixed with a fuel component, the detonation velocity decreases because HMX or RDX is a stoichiometrically balanced material and the addition of fuel components within HMX or RDX decreases the adiabatic flame temperature. Thus the detonation velocity is decreased.

Table 8-2. Detonation velocity, detonation density, and computed detonation pressure at the CJ point of energetic materials.

	ρ kg/m^3	u_D m/s	p_J GPa
Ammonium picrate	1720	7150	2.33
Diazodinitrophenol	1630	7000	2.12
Diethyleneglycol	1380	6600	1.59
NG	1591	7600	2.44
Nitroglycol	1480	7300	2.09
NQ	1710	8200	3.05
NIBGTN	1680	7600	2.57
NM	1138	6290	1.19
Hydrazine nitrate	1640	8690	3.29
HMX	1900	9100	4.17
RDX	1818	8750	3.69
PETN	1760	8400	3.29
TNT	1654	6900	2.09
Trinitroanisol	1610	6800	1.52
TNB	1760	7300	2.49
TNChloroB	1797	7200	2.47
Methyl nitrate	1217	6300	1.28
Tetryl	1730	7570	2.63
Picric acid	1767	7350	2.53
AN	1720	2700	0.33
Lead azide	4600	5300	3.43

8.2.2
Industrial Explosives

8.2.2.1 ANFO Explosives

A mixture of ammonium nitrate and light oil forms a low strength explosive which is used as a blasting compound for mines and in industrial engineering. This class of explosives is named ANFO explosives (ammonium nitrate fuel oil explosives). The density of ANFO explosives is 800–900 kg/m^3 and the detonation velocity is 2500–3500 m/s. The sensitivity to initial detonation is very low, and the handling of ANFO explosives is thus easier than that of other industrial explosives.

8.2.2.2 Slurry Explosives

A mixture of ammonium nitrate and water forms a low strength explosive known as a slurry explosive. In order to obtain a subsequent detonation propagation after detonation initiation, micro-balloons made of glass or plastics are also added to the explosives. During detonation propagation within the explosives, an adiabatic compression is given by the destruction of the micro-balloons.

8.2.3
Military Explosives

The explosives used for military purpose are different from those used for industry. Not only thermomechanical power for destruction but also various other characteristics are required. Experimental tests, such as slow cook-off, fast cook-off, bullet impact, and sympathetic explosion tests must be cleared by the requirements of insensitive munition (IM). The aerodynamic heating of warheads on flight projectiles is also an important factor in the design of warheads.

8.2.3.1 TNT Based Explosives

TNT is one of the important materials used for not only explosives for industry but also military explosives for blasting charges. Since metals are not corroded by TNT, it is cast directly into metal cases as well as pressed into warhead shells. In order to gain high explosive characteristics, TNT is mixed with other materials, such as AN, Tetryl, PETN, Al powder, and nitramine particles[2]. The mixture of TNT and AN is named Amatol has a TNT/AN mass fraction ratio ranging from 0.5/0.5 to 0.2/0.8. The mixture of TNT and AN is melted and then cast. The mixture of TNT and Al named Tritonal has a mass fraction ratio of TNT/Al = 0.8/0.2. The mixture of TNT and HMX is named Octol composed of the mass fraction ratio of TNT/HMX ranging from 0.3/0.7 to 0.25/0.75. The maximum detonation velocity, 8600 m/s, is obtained when the density is 1800 kg/m^3.

The mixture of TNT and RDX is named Composition A when compressed with a small amount of wax. The detonation velocity is approximately 8100 m/s. When TNT and RDX are cast together with a wax, the mixture is named Composition B. The mass fraction ratio is TNT/RDX = 0.4/0.6 with 0.1 % wax. The density is in the range 1600–1750 kg/m^3 and the detonation velocity is about 8000 m/s. The melting point of TNT is 353.8 K, which is too low for its use in warhead charges under conditions of supersonic or hypersonic flight (Mach number > 5). Deformation of charges occurs because of the aerodynamic heating.

8.2.3.2 Plastic-Bonded Explosives

In general, PBX is used for the warheads of rockets and guns. Thus, the detonation pressure (p_J) represented by Eq. (8.7) is a more important parameter than other properties. Since the measurement of the detonation velocity u_D is easier and more accurate than the measurement of p_J, the performance evaluations are done by u_D which is converted to p_J by the use of Eq. (8.7). Table 8-3 shows u_D and ρ data, and gives the computed detonation pressure at the CJ point of HMX-PBX and RDX-PBX.

As shown in Table 8-3, the detonation velocity is highly dependent on the density of the PBX, while in turn, the increase in the mass fraction of HMX or RDX increases the density[4]. When the mixture of nylon powders and HMX particles is pressed to form a desired shape of an explosive, a high density HMX-PBX is formed. However, the process of formation is sensitive to pressurization and mechanical shock.

Though the density of aluminized PBX is high, the measured detonation velocity is low when compared with nonaluminized PBX. Since HMX and RDX are stoichiometrically balanced materials, no extra oxygen is available to oxidize the aluminum particles. The aluminum particles are oxidized by CO molecules in the combustion products of HMX or RDX. Furthermore, the oxidation of the aluminum particles takes a much longer time than that of the crystalline HMX or RDX particles. The aluminum particles do not react in the detonation wave but react downstream of the CJ point shown in Fig. 3-5. Thus, no increase in the detonation velocity occurs even if the density of the PBX is increased by the addition of aluminum particles. However, when an aluminized PBX is used in water, the high temperature aluminum particles react with water to produce hydrogen gas and thus produce bubbles in the water. The bubbles generate additional pressure and a shock wave in the water.

Table 8-3. Detonation velocity, density, and pressure at the CJ point of HMX-PBX and RDX-PBX.

Composition	*Mass fraction ratio*	ρ *kg/m³*	u_D *m/s*	p_J *GPa*
(a) HMX-PBX				
HMX/Nylon	0.95/0.05	1800	8670	3.59
HMX/Nylon	0.86/0.14	1730	8390	3.23
HMX/Polystyrene	0.82/0.18	1670	7980	2.82
HMX/HTPB	0.82/0.18	1640	8080	2.84
HMX/GAP	0.82/0.18	1670	8010	2.84
HMX/Al/Polystyrene	0.59/0.23/0.18	1800	7510	2.69
(b) RDX-PBX				
RDX/HTPB	0.86/0.14	1650	8120	2.89
RDX/Al/HTPB	0.71/0/17/0.12	1750	7700	2.75

8.3
Applications of Detonation Phenomena

As described in Chapter 3, the detonation characteristics are followed by the Rankine-Hugoniot relationship and the detonation velocity is obtained at the Chapman-Jouguet point. Though the detonation characteristics of explosives are fundamentally the same as those of premixed gases, the physicochemical processes of explosives are more complex because the shock wave propagation in the explosives is largely different from that of premixed gases.

Since detonative explosives are kept in various types of vessels used for different objectives such as warheads, bombs, and industrial mines and civil engineering, the performance of the explosives is dependent not only on the chemicals and mass of explosives but also the physical shape of explosives. When a detonation is initiated at a point in an explosive charge, the detonation wave propagates spherically in all directions. When a detonation is initiated at a point at one end of an explosive charge, the detonation wave propagates semi-spherically in the charge. Thus, the strength of the detonation wave in the charge or the shock wave in the atmosphere created by the detonation decreases rapidly as the distance from the detonation initiation point increases. However, the shock wave created by detonation of a shaped charge propagates in a certain direction because of a shock-wave interaction phenomenon, the so called "Munroe effect". When the opposite side of the charge is made as a cone shape and the surface of the cone is made of copper plate (liner), an axi-symmetrically concentrated jet is formed by the molten copper liner. The explosive energy is converted to the kinetic energy of the jet. The important parameters of the jet formation are the shape of liner, liner material, and the cone angle. Tetryl pellet is used to initiate detonation of the main explosives. A drawn copper liner is used as a cone of angle 42° and the outer surface is machined precisely. The shaped jet formed by the molten copper liner is ejected along the center line of the original cone.

References

1 Engineering Design Handbook, Principles of Explosive Behavior, AMPC 706–180, US Army Material Command, Washington, DC (1972).

2 Energetic Materials Handbook, Japan Explosives Society, Kyoritsu Shuppan, Tokyo (1999).

3 Meyer, R., Explosives, Verlag Chemie, Weinheim (1977).

4 Explosives Journal, No. 27, NOF Corporation, Tokyo (1993).

Propellants and Explosives: Thermochemical Aspects of Combustion. Naminosuke Kubota
Copyright © 2002 Wiley-VCH Verlag GmbH & Co. KGaA
ISBNs: 3-527-30210-7 (Hardback); 3-527-60050-7 (Electronic)

9

Combustion in a Rocket Motor

9.1

Combustion Phenomena in a Rocket Motor

9.1.1

Propellant Combustion in a Rocket Motor

Rocket propellants are used to generate high-temperature and high-pressure combustion products in a rocket motor. The design of a rocket motor must achieve the desired pressure versus burning time curve, so as to obtain the required thrust versus time curve. Two types of propellant burning are used, as shown in Fig. 9-1: internal burning type and end burning type. Internal burning is used to obtain a high thrust and a short burning time and end burning is used to obtain a low thrust and a long burning time. Some combinations of internal and end burnings are used to obtain a medium thrust and medium burning time. However, there exists a "not possible zone" in the thrust versus burning time relationship as shown in Fig. 9-2 because of the limited burning rate characteristics of propellants.

Since the burning rate of propellants is dependent on burning pressure, the mass balance between the mass generation rate in the chamber and the mass discharge

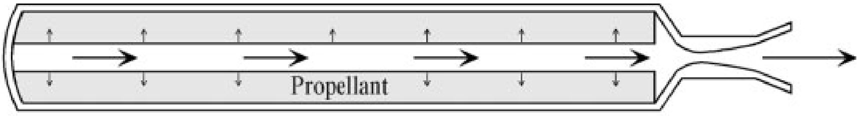

Internal burning type rocket motor

End burning type rocket motor

Figure 9-1. Propellant burning in rocket motor.

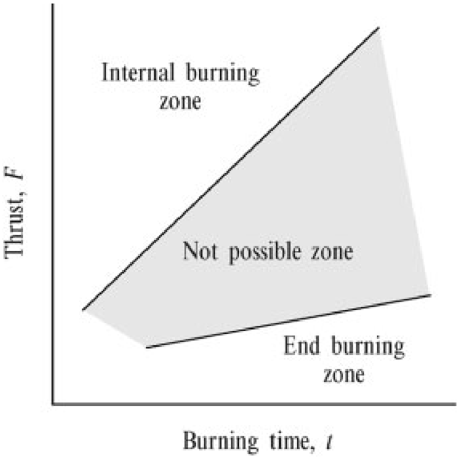

Figure 9-2. Zones of burning in rokket motor.

rate from the nozzle is determined by pressure[1–4]. In addition, the propellant burning rate of a rocket motor is affected by various phenomena which change the mass balance relationship. Figure 9-3 shows typical combustion phenomena encountered in a rocket motor from pressure build-up by ignition to pressure decay by combustion completion.

When a propellant grain is ignited, convective, conductive, and/or radiative heat transfer to the unburned portion of the propellant grain occur. If an excess heat flux is supplied, the propellant grain generates an excess of combustion gas and an overpressure is created, i.e., an abnormal ignition occurs. Immediately after ignition of an internal burning grain shown in Fig. 9-1, the gas flow velocity along the flow direction is high and the heat flux transferred from the combustion gas flow to the grain surface is also high. As a result, the burning rate of the grain perpendicular to the flow direction increases drastically, i.e., an erosive burning occurs. Then, the

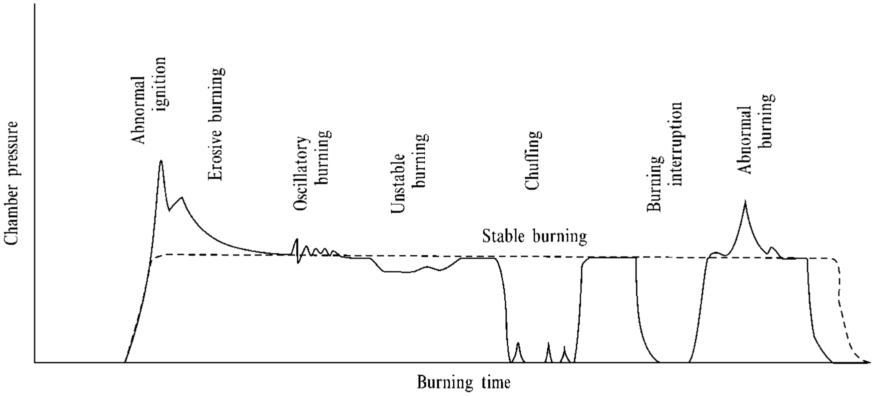

Figure 9-3. Combustion phenomena in rocket motor from ignition to combustion completion.

pressure in the rocket motor increases abnormally. The erosive burning diminishes soon after the port area of the internal burning increases.

When a propellant grain burns with an internal burning, pressure oscillation is generated in the rocket motor. If the strength of the pressure oscillation is high, the rocket motor is damaged. If the pressure exponent of the burning rate is high, unstable burning such as low frequency pressure oscillation, chuffing, and burning interruption occurs.

9.1.2
Stability Criteria of Rocket Motor

When a propellant burns in a rocket motor as shown in Fig. 9-4, the mass generation rate in the chamber, $\dot{m}_g$, is given by

$$\dot{m}_g = \rho_p A_b r \tag{9.1}$$

where A_b is the burning surface area and ρ_p is the density of the propellant. The mass discharge rate from the nozzle, $\dot{m}_d$, is given by Eq. (1.60) and is represented by

$$\dot{m}_d = c_D A_t p_c \tag{9.2}$$

where A_t is the nozzle throat area, c_D is the nozzle discharge coefficient given by Eq. (1.61), and p_c is the chamber pressure. The rate of mass accumulation in the chamber, $\dot{m}_c$, is given by

$$\dot{m}_c = \frac{d(\rho_g V_c)}{dt} \tag{9.3}$$

where V_c is the free volume of the chamber, ρ_g is the density of the combustion gas in the chamber, and t is time. The mass balance in the rocket motor is expressed by

$$\dot{m}_g = \dot{m}_c + \dot{m}_d \tag{9.4}$$

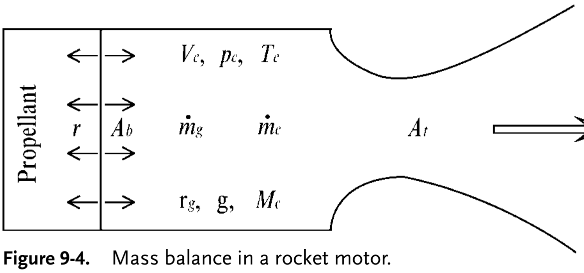

Figure 9-4. Mass balance in a rocket motor.

One assumes that V_c and T_c are constant, and the burning rate is expressed by Eq. (3.68) during a pressure transient in a rocket motor. Eq. (9.4) is represented by[4]

$$\frac{L^*}{RT_c}\frac{d\,p_c}{dt} - K_n\rho_p a p_c^n + c_D p_c = 0 \tag{9.5}$$

where $L^* = V_c / A_t$, $K_n = A_b / A_t$, $R = \mathrm{R}/M_c$. M_c, is molecular mass, and the combustion gas is an ideal gas given by Eq. (1.5). The transient pressure in the rocket motor is obtained by the integration of Eq. (9.5) as

$$p_c(t) = \left[\left(p_i^{1-n} - \frac{a\rho_p K_n}{c_D}\right)\exp\left(\frac{(n-1)RT_c c_D}{L^*}\right)t + \frac{a\rho_p K_n}{c_D}\right]^{\frac{1}{1-n}} \tag{9.6}$$

where p_i is the initial pressure in the rocket motor. The final pressure when $t \rightarrow \infty$ is obtained as

(1) $n > 1$ $: p_i < p_{eq}$ $p_c \rightarrow 0$

$: p_i > p_{eq}$ $p_c \rightarrow \infty$

(2) $n = 1$ $p_c \rightarrow p_i$

(3) $n < 1$ $p_c \rightarrow p_{eq}$

where p_{eq} is the equilibrium pressure obtained when the time dependent term shown in Eq. (9.5) is negligible, and the mass balance is expressed by

$$\rho_p A_b r = c_D A_t p_c \tag{9.7}$$

Substituting Eq. (3.68) into Eq. (9.7), one gets the chamber pressure under steady state conditions as

$$p_{eq} = p_c = \left(\frac{a\rho_p}{c_D}\frac{A_b}{A_t}\right)^{\frac{1}{1-n}} \tag{9.8}$$

As shown in Fig. 9-5, the chamber pressure is given as a crossover point $\dot{m}_g$ and $\dot{m}_d$ in a pressure versus $\dot{m}_g$ or $\dot{m}_d$ plot. It is evident that stable combustion occurs only under the condition of

$$\frac{d(c_D A_t p)}{dp} > \frac{d(\rho_p A_b a p^n)}{dp} \tag{9.9}$$

Substituting Eq. (9.8) into Eq. (9.9) at $p = p_c$, one gets the stability criterion as

$$n < 1 \tag{9.10}$$

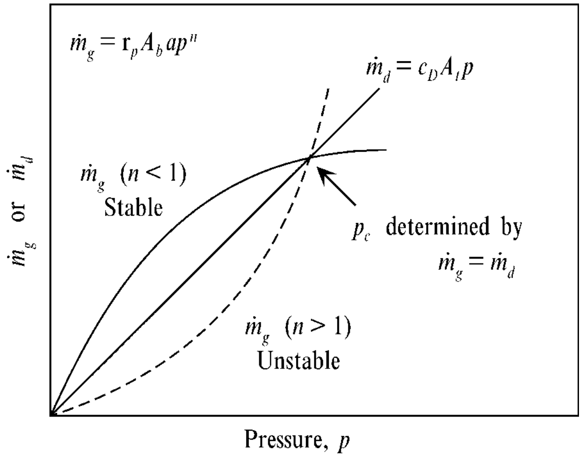

Figure 9-5. Mass balance principle and stable burning point in a rocket motor.

The characteristic time in combustion chamber τ_c is defined, based on Eq. (9.6), as

$$\tau_c = \frac{L^*}{(n-1)RT_c c_D} \tag{9.11}$$

If the pressure in a rocket motor changes during the time interval τ, the pressure transient is considered to be steady state combustion when $\tau > \tau_c$, and is nonsteady state combustion when $\tau < \tau_c$.

9.1.3
Temperature Sensitivity of Pressure in a Rocket Motor

The change of burning rate by the change of initial propellant temperature changes the equilibrium pressure p_c in a rocket motor. Thus, one needs to introduce the temperature sensitivity of pressure in the combustion chamber, π_k , similar to the definition of σ_p :

$$\pi_k = \frac{p_1 - p_0}{p} - \frac{1}{T_1 - T_0} \quad \text{at constant } K_n \tag{9.12}$$

where p_1 and p_0 are the pressures in the combustion chamber at T_1 and T_0, respectively[1]. Thus, the unit of temperature sensitivity of pressure appears to be K^{-1}. Since K_n is defined as the ratio of the burning surface area of propellant and the nozzle throat area, $K_n = A_b/A_t$, $K_n =$ constant indicates a fixed physical dimension of a rocket motor. The differential form of Eq. (9.12) is expressed by

$$\pi_k = \frac{1}{p}\left(\frac{\partial p}{\partial T_0}\right)_{Kn} = \left(\frac{\partial \ln p}{\partial T_0}\right)_{Kn} \tag{9.13}$$

Substituting Eq. (9.8) into Eq. (9.13) and using Eq. (3.74), one gets

$$\pi_k = \frac{1}{a}\frac{1}{1-n}\left(\frac{\partial a}{\partial T_0}\right)_p = \frac{\sigma_p}{1-n} \tag{9.14}$$

Reduction of temperature sensitivity of burning rate defined in Eq. (3.73) increases the combustion stability in rocket motors, which results in improved ballistics. Figure 9-6 shows the pressure versus burning time curve in a rocket motor with a propellant of $n = 0.5$ and $\sigma_p = 0.0030\ \mathrm{K}^{-1}$. When the initial propellant temperature T_0 is 233 K, the chamber pressure is low, about 9.5 MPa. However, the chamber pressure increases to 16 MPa when T_0 is increased to 333 K. Instead, the burning time is reduced from 20 s to 13 s. The increase of the pressure in the rocket motor is relevant as n becomes large and/or σ_p becomes large. Because of this change of pressure and burning time, the thrust generated by the rocket motor is also changed by the relationship of Eq. (1.67).

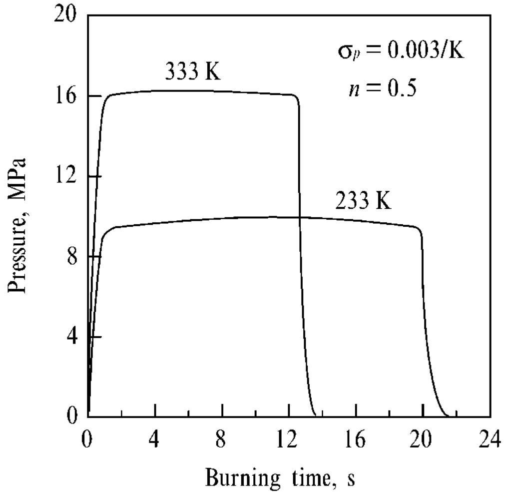

Figure 9-6. Temperature sensitivity of a rocket motor.

9.2 Ignition Transient

9.2.1 Convective Ignition

When a high-temperature gas flow is provided along the surface of a propellant, a convective heat transfer occurs and the temperature at the surface increases. When the temperature reaches the decomposition temperature of the propellant, a gasification reaction occurs endothermically or exothermically. The heat is transferred toward the inside of the propellant and the temperature beneath the surface increases simultaneously. The decomposed gas on and above the surface reacts to produce heat, and then part of the heat is transferred back to the decomposing surface. When this heat is enough to produce self-decomposition at the surface, ignition of the propellant is established. The process of temperature increase in the condensed phase is illustrated in Fig. 9-7.

Since the initiation of decomposition is dependent on the heat flux given from the high-temperature gas flow, the ignition process is dependent on the various gas flow parameters such as temperature, flow velocity, pressure, and the physicochemical properties of the gas.

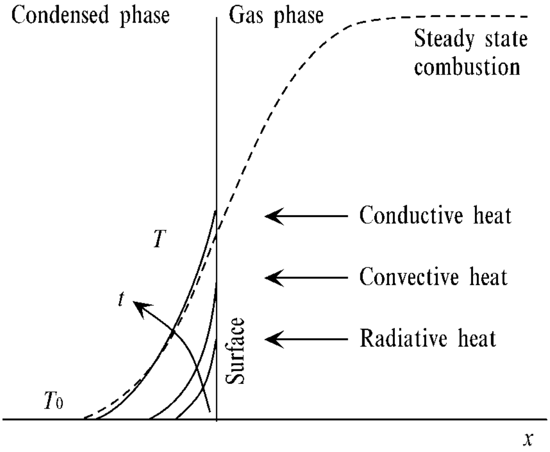

Figure 9-7. Ignition transient process by conductive, convective, and radiative heat.

9.2.2
Radiative Ignition

When high-intensity radiative energy strikes the surface of a propellant, the surface absorbs the heat and the temperature increases. If the propellant is optically translucent, part of the radiation energy penetrates into the propellant by in-depth absorption. When the temperature of the propellant surface reaches the decomposition temperature, the subsequent ignition process is the same as convective ignition.

Figure 9-8 shows the ignition boundaries of double-base propellants on radiative heating. As the incident radiant flux intensity I_f increases, the time of radiant heating for the ignition completion τ_{ig} becomes shorter. As the propellant becomes opaque by the addition of carbon black, τ_{ig} becomes shorter at constant I_f or I_f becomes smaller at constant τ_{ig}. The in-depth absorption is reduced and most of the radiative energy is absorbed at the ignition surface of the propellant.

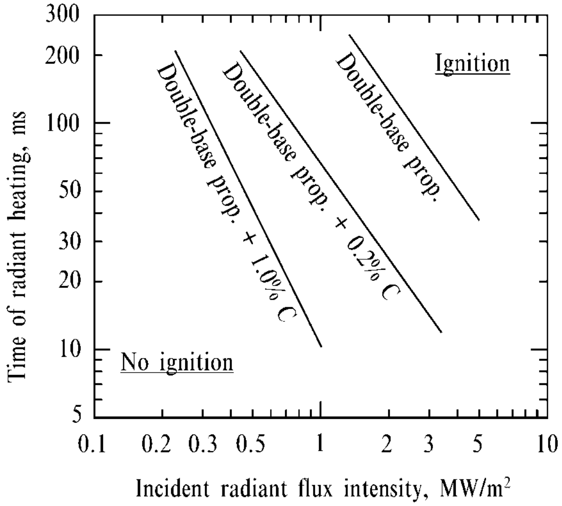

Figure 9-8. Radiative ignition criteria of double-base propellants with and without carbon black.

In simplified analysis based on conductive heating beneath the burning surface, the time of ignition is represented by[4]

$$\tau_{ig} = \frac{\pi}{4}\alpha_p\left[\frac{\rho_p c_p(T_g - T_0)}{I_f}\right]^2 \tag{9.15}$$

The total incident radiant intensity E_f is given by

$$E_f = I_f\tau_{ig} = \frac{\pi}{4}\frac{\lambda_p\rho_p c_p(T_g - T_0)^2}{I_f} \tag{9.16}$$

The linear relationship of ln $\tau_{ig} \sim -2$ ln I_f and thus $\tau_{ig} \sim I_f^{-2}$ is shown for double-base propellants in Fig. 9-8.

9.2.3
Ignition Transient in Rocket Motor

The ignition of a propellant grain in a rocket motor is caused by the heat provided by conductive, convective, and/or radiative energy produced by an igniter attached on the rocket motor. The conductive heat is transferred to the propellant surface by hot metal particles dispersed on the propellant surface. An igniter made of boron particles and potassium nitrate generates a large number of boron oxide particles whose temperature is > 3000 K. Conductive heat transfer to the propellant surface occurs and the temperature of the material surrounding each particle increases to decompose the propellant. The decomposed gas reacts exothermically and increases the rocket motor pressure.

Convective heating by an igniter is done by the combustion of black powder and/or double-base propellant grains, both of which generate high-temperature gaseous products and fewer solid particles. The heat transfer is caused by the flow of the gaseous products. When an aluminized AP composite propellant is used as an igniter, high-temperature aluminum oxide particles produced as combustion products are dispersed on the surface of the propellant grain. Ignition of the propellant occurs from the hot spots of the particles by conductive heat transfer. Ignition delay is caused not only by the process of heat transfer and chemical reaction but also by the process of pressure build-up in the motor. The time of pressure build-up from p_i to p_{eq} is given by Eq. (9.6).

9.3
Erosive Burning

9.3.1
Erosive Burning in a Rocket Motor

The combustion of a propellant grain in internal burning occurs under the combustion gas flow along the burning surface as shown in Fig. 9-1. Since the burning surface regresses perpendicularly to the burning surface, the flow velocity in the port of the propellant grain increases the heat flux transferred to the burning surface, and the burning rate then increases, so-called erosive burning. When the ratio of the length L and the diameter D of the propellant grain, L/D, defined in Fig. 9-9, is

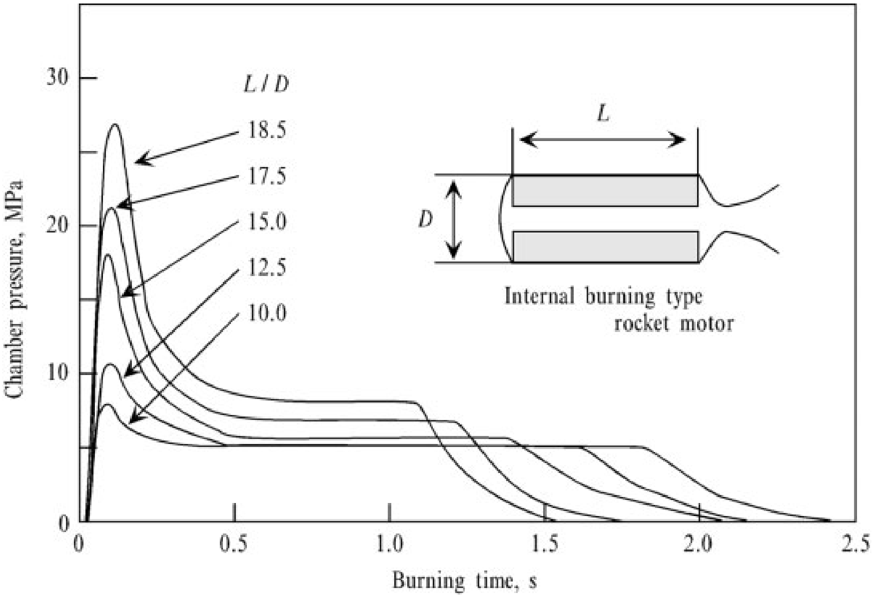

Figure 9-9. Effect of L/D of a rocket motor on erosive burning.

increased where $K_n = A_b/A_t$ = constant, the chamber pressure just after the ignition stage is increased drastically. Though the designed pressure p_{eq} is 5 MPa, the peak pressure is increased more than 5 times at $L/D = 18.5$.

Since the initial port area of the propellant grain is small, the flow velocity becomes large because the velocity at the nozzle throat is always the sonic velocity. Furthermore, K_n is kept constant, and then both A_b and A_t increase simultaneously as L/D increases. Since the port area of the propellant grain is kept constant, the flow velocity increases as A_t increases, in accordance with the mass conservation low given by Eq. (1.49). Therefore, the heat flux transferred from the gas flow increases and the erosive burning ratio increases. However, as the port area increases, the flow velocity decreases and the erosive burning then diminishes.

9.3.2
Erosive Burning Mechanism

When double-base propellants composed of different energy densities are burned under cross-flow conditions, erosive burning occurs. Figure 9-10 is the burning rate with no cross flow, r_0, for High-, Ref.-, and Low-energy propellants[5]. The chemical compositions of the propellants are shown in Table 9-1. The erosive ratio defined as $\varepsilon = r/r_0$ increases as the cross flow velocity increases for the three types of propellants. There exists a threshold velocity for each propellant, approximately 70 m/s for Low-, 100 m/s for Ref.-, and 200 m/s for High-energy propellants. The erosive ratio is about 2.4 for a Low-energy propellant at 300 m/s, approximately Mach 0.3.

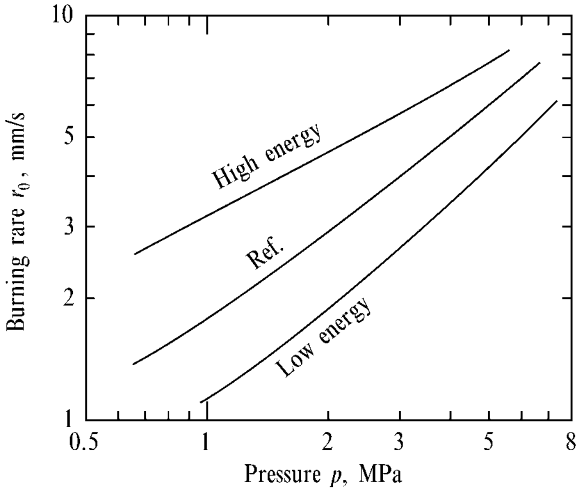

Figure 9-10. Burning rate of high-energy, reference, and low-energy double-base propellants.

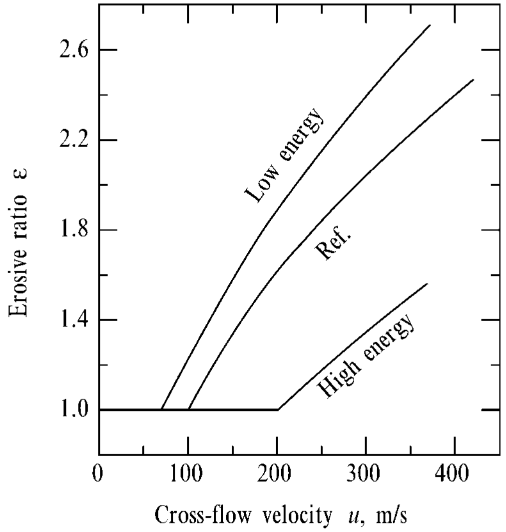

Figure 9-11. Erosive ratio and threshold velocity of erosive burning of high-energy, reference, and low-energy double-base propellants showing that low-energy propellant is sensitive to the heat flux from the convective heat flux.

Table 9-1. Chemical compositions of High-, Ref.-, and Low-energy Propellants (wt %).

Propellant	***NC***	***NG***	***DEP***	***T_g (K)***
High-energy	55.6	40.4	4.0	2720
Ref.-energy	50.4	36.6	13.0	2110
Low-energy	47.5	34.5	18.0	1780

The flow field of a double-base propellant during erosive burning is shown schematically in Fig. 9-12. The flow in internal burning is turbulent and the turbulent boundary layer is established. The luminous flame of the high temperature zone is distended from the burning surface, and the fizz zone, which is the important zone for the determination of the burning rate, is just above the burning surface. When the velocity is low, the fizz zone is inside the viscous sublayer where the velocity is very low. Thus, the fizz zone is not affected by the crossflow, and then the burning rate remains unchanged even under the crossflow. However, when the crossflow velocity is increased, the luminous flame zone approaches the burning surface and the dark zone diminishes because of the increased turbulent intensity. Then the heat flux increases and the burning rate increases.

The burned gas velocity from the burning surface is high for a high-energy propellant because the burning rate is higher than that of a low-energy propellant at constant pressure. In addition, the temperature gradient in the fizz zone is steep and the thickness of the fizz zone is small. Thus, the burning rate is less sensitive to the crossflow for the high-energy propellant[5]. This aerochemical process determines the observed threshold velocity shown in Fig. 9-11.

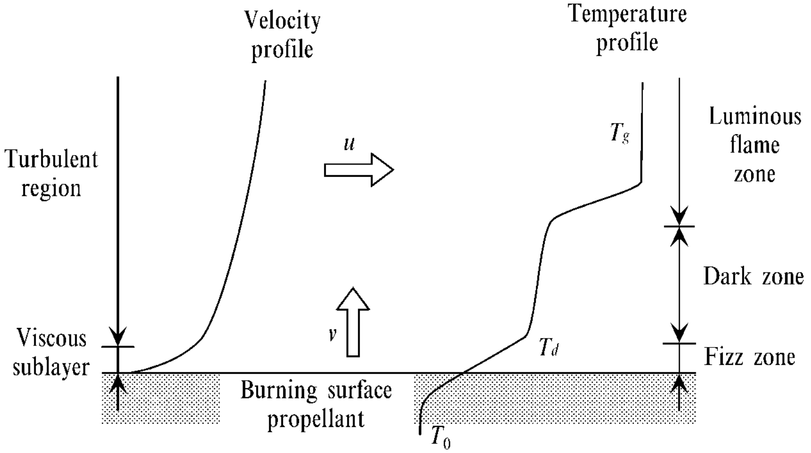

Figure 9-12. Erosive burning effect on the flame structure of double-base propellant.

9.4
Wired-Propellant Burning

The heat flux transferred back from the gas phase to the condensed phase is a dominant role in determining the burning rate of propellants. The burning rate increases with increasing pressure because of the increased reaction rate in the gas phase, and the increased heat flux is then transferred to the propellant. When a metal fine wire is embedded within a propellant along the burning direction, the heat is transferred back to the condensed phase through the wire by heat conduction. Since the heat conductivity and thermal diffusivity of metals are much greater than those of gases, the rate of heat transfer through metal wires is much greater than that through gases. Therefore, the heat flux transferred back by the protruded metal wire from the burning surface to the gas phase is greater than the heat flux transferred back by the combustion gas. The temperature of the propellant surrounding the wire is increased because of the heating by the wire and a portion of the propellant is ignited. Thus, the apparent burning rate of the propellant surrounding the wire is faster than the burning rate of the propellant[6,7].

Figure 9-13 shows the burning surface of a propellant strand with embedded silver wire[7]. The burning surface makes a cone shape, rather than a usual flat burning surface, around the silver wire, and combustion progresses rapidly along the wire. For observation of the burning surface structure, the propellant strand is made of NC-NG double-base propellant which is relatively transparent. Since the burning surface area is increased because of the embedded silver wire, the burning surface area of the propellant grain becomes an intermediate type of burning between end burning and internal burning as shown in Fig. 9-1. The "not possible zone" shown in Fig. 9-2 becomes a "possible zone" by the use of wired propellant grains.

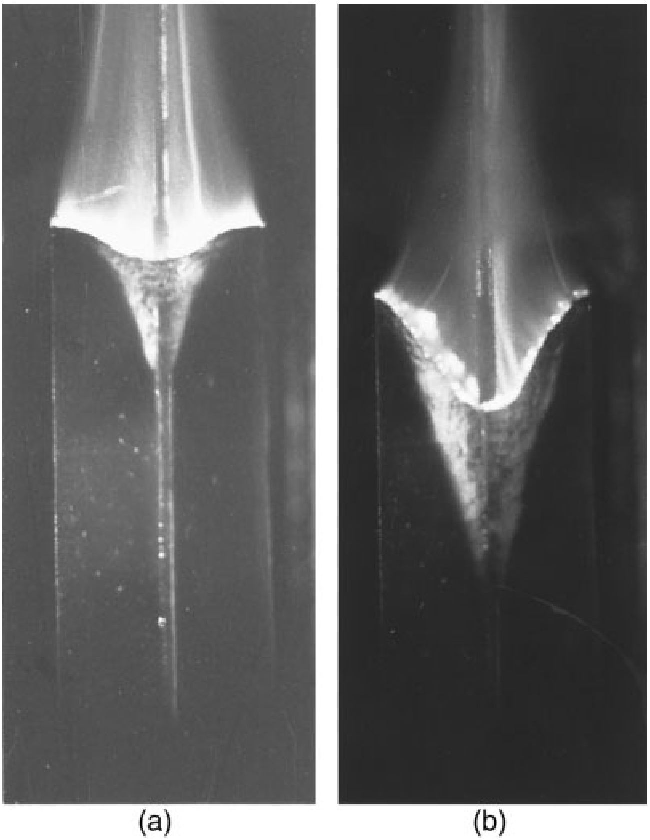
(a) (b)

Figure 9-13. Combustion photographs of a wired propellant: cone-shaped burning surface is formed around a silver wire (0.8 mm in diameter) (a) 0.8 s after ignition and (b) 1.2 s after ignition.

Figure 9-14 shows the burning rate of the propellants with three types of wires embedded; silver (Ag), tungsten (W), and nickel (Ni) wires[7]. The burning rate of nonwired propellant, r_0, increased approximately 4 times by the Ag wire, 2.5 times by the W wire, and 1.5 times by the Ni wire at 1 MPa. The pressure exponent is 0.60 for the nonwired, 0.51 for the Ag wired, 0.55 for the W wired, and 0.51 for the Ni wired propellants. No significant effect of wire on the pressure exponent is seen. The larger the thermal diffusivity of the metal wire, the higher the burning rate along the wire, r_w [7].

The heat flux transferred by metal wires is also dependent on the size of the wires. The rate of heat gain from the high temperature gas to the protruding wire from the burning surface is determined by the size of the wire. When the wire size is small, the rate of heat gain is fast because the heat capacity of the wire is small. However, the rate of heat loss from the heated wire to the propellant beneath the

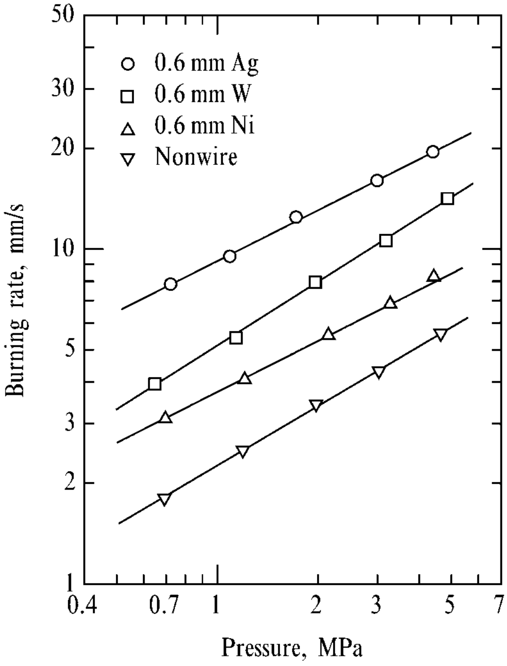

Figure 9-14. Effect of metal wire on burning rate along the wire.

burning surface is small. Figure 9-15 shows variation of the r_w/r_0 due to variation of wire size at 4 MPa. As the wire size decreases, the r_w/r_0 increases when the wire size is larger than d_c However, the r_w/r_0 becomes a maximum when the wire size is d_c. When silver wire is very thin, 5μm or 50μm in diameter, no cone-shaped burning surface along the silver wire is seen.

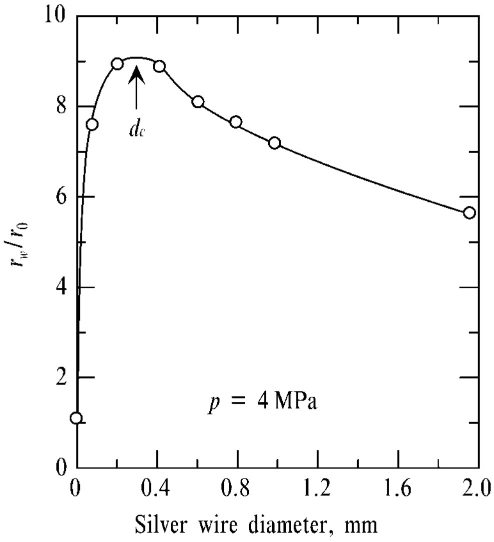

Figure 9-15. Effect of silver wire diameter on burning rate along the wire showing that the maximum burning rate is obtained at about 0.3 mm in diameter.

In order to obtain higher burning rate, various sizes and lengths of wire are added to make propellant grains. Chopped fine wires or very fine metal sheets are useful materials cast within propellant grains.

9.5
Combustion Instability

9.5.1
T^* Combustion Instability

If the combustion products of propellants reach their thermal equilibrium conditions, the combustion temperature is determined theoretically as described in Chapter 2. However, combustion in a rocket motor includes incomplete combustion and the flame temperature falls below the adiabatic flame temperature[8]. If one assumes that the flame temperature T^* varies with pressure p_c in a rocket motor, T^* is expressed by

$$T^* = b{p_c}^{2m} \tag{9.17}$$

where m is the pressure exponent of flame temperature and b is constant over a certain pressure range. The mass balance for rocket motor operation at steady state is given by the use of Eq. (9.7) as

$$\rho_p r A_b = \frac{\zeta A_t p_c}{\sqrt{T^*}} \tag{9.18}$$

where ζ is a parameter of combustion gas given by

$$\zeta = \sqrt{\frac{M_g}{R}}\sqrt{\gamma}\left(\frac{2}{\gamma+1}\right)^{\frac{\gamma+1}{2(\gamma-1)}} \tag{9.19}$$

Substituting the burning rate of a propellant given by Eqs. (3.68) and (9.18) into the stable burning criterion of Eq. (9.9), one gets

$$n + m < 1 \tag{9.20}$$

This criterion is the so-called T^* combustion instability. The stable criterion expressed by Eq. (9.10) is not enough to obtain stable combustion when the flame temperature is dependent on pressure.

In general, m is approximately zero in the high pressure region for most propellants. However, T^* of nitropolymer propellants such as single-base and double-base propellants decreases as pressure decreases below about 5 MPa. Since the direct determination of m is difficult, the heat of explosion H_{exp} is evaluated as a function of pressure. The flame temperature termed T^* is determined by assuming an average specific heat of the combustion products, c_p, as

$$T^* = H_{exp} / c_p + T_0 \tag{9.21}$$

where T_0 is the initial propellant temperature.

The combustion tests done using a rocket motor demonstrate a typical T^* combustion instability. Double-base propellants composed of NC-NG propellants with and without catalyst (1 % nickel powder) are burned. The detailed chemical compositions of both propellants are described in Section 6.4.4 of Chapter 6. The burning rate characteristics are shown in Fig. 6-28. No effect of the nickel addition on burning rate is seen and the pressure exponent is $n = 0.70$ for both propellants.

The heat of explosion of the NC-NG propellant without catalyst decreases rapidly when the pressure is decreased rapidly below about 4 MPa as shown in Fig. 9-16. However, the heat of explosion of the catalyzed NC-NG propellant remains relatively unchanged even below 2 MPa.

Substituting the data of the measured H_{exp} into Eqs. (9.21) and (9.17), one gets an experimentally determined m as a function of pressure. The results indicate that m of the NC-NG propellant without catalyst is approximately 0.35 at 0.6 MPa and decreases gradually as pressure increases, becoming zero at and above 5 MPa, and m of the catalyzed NC-NG propellant is approximately zero in the same pressure range tested. Substituting the results for m and n into Eq. (9.20), one gets

$m + n > 1$ at $p < 1.2$ MPa

$m + n < 1$ at $p > 1.2$ MPa

for the noncatalyzed NC-NG propellant, and

$m + n < 1$ throughout the pressure range tested

for the catalyzed NC-NG propellant.

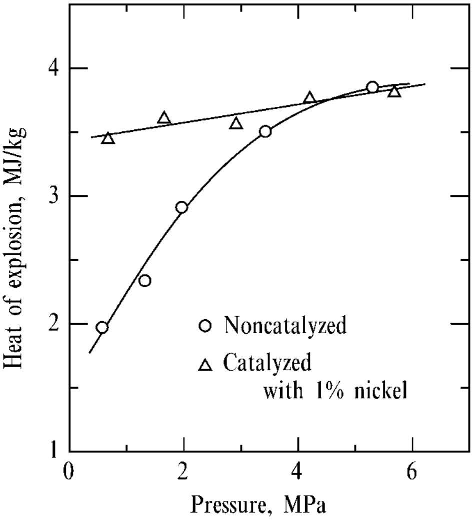

Figure 9-16. Effect of nickel powder addition on heat of explosion of a double-base propellant.

The combustion tests conducted using a rocket motor show that the combustion becomes unstable below 1.7 MPa and the burning becomes a chuffing mode for the noncatalyzed propellant. However, the combustion is stable, as expected, even below 0.5 MPa for the nickel-catalyzed NC-NG propellant. The propellants for which the flame temperature decreases with decreasing pressure tend to give T^* combustion instability.

9.5.2
L^* Combustion Instability

Low frequency oscillation in a rocket motor is associated with the pressure exponent of the propellant burning rate and the dimensions of the free volume of the chamber[9]. When a double-base propellant composed of 51.0 % NC, 35.5 % NG, 12.0 % DEP, and 1.5 % PbSa as a platonized catalyst burns in a strand burner, the burning rate characteristics are divided into four zones shown in Fig. 9-17. The pressure exponent varies according to the pressure zone: $n = 0.44$ in zone I above 3.7 MPa, $n = 1.1$ in zone II between 3.7 MPa and 2.1 MPa, $n = 0.77$ in zone III between 2.1 MPa and 1.1 MPa, and $n = 1.4$ in zone IV below 1.1 MPa.

When the propellant grain burns in an end-burning type of rocket motor in which L^* changes from 4 m to 20 m during burning, typical pressure-time records are as shown in Fig. 9-18. In zone I, pressures above 3.7 MPa, the burning is very stable as expected. In zone II, where the pressure exponent is approximately unity, a

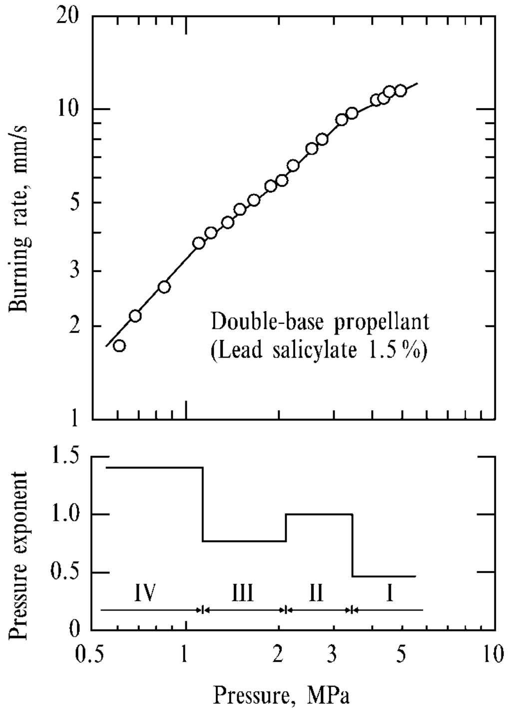

Figure 9-17. Burning rate and pressure exponent of a lead catalyzed double-base propellant.

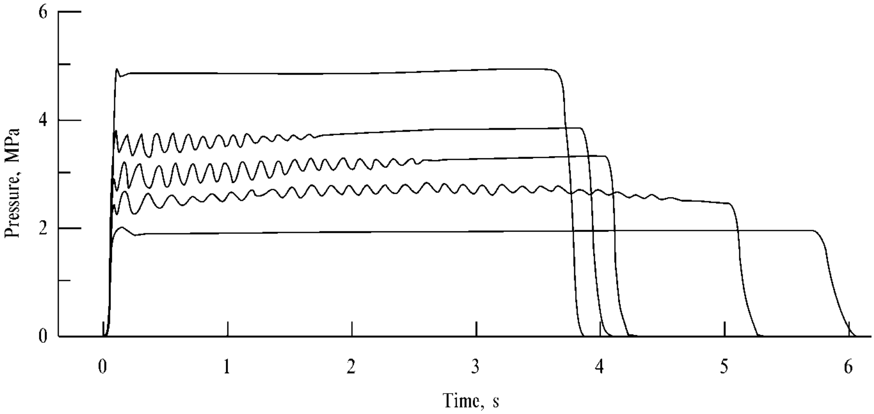

Figure 9-18. Pressure versus time curve of a lead catalyzed propellant in a rocket motor.

sinusoidal oscillatory burning ranging between 6 Hz and 8 Hz occurs when L^* is short[9]. The highest amplitude of oscillation is about 20% of the time-averaged pressure, and the oscillatory burning diminishes as L^* increases. In zone III, between 2.1 MPa and 1.1 MPa, where the pressure exponent is 0.77, the burning is stable without pressure oscillation. In zone IV, where the pressure exponent is 1.4, stable burning is not possible because the mass discharge rate from the nozzle is always higher than the mass generation rate in the chamber. The domains of stable burning, oscillatory burning, and unstable burning are shown in Fig. 9-19. A simplified analysis indicates that the frequency ω in zone II is correlated with n and τ_{ch} represented by the relationship of $\omega = (n^2 - 1)^{1/2}\tau_{ch}$ where τ_{ch} is the chamber time constant given by $\tau_{ch} = L^*/c_D\, RT_f$.

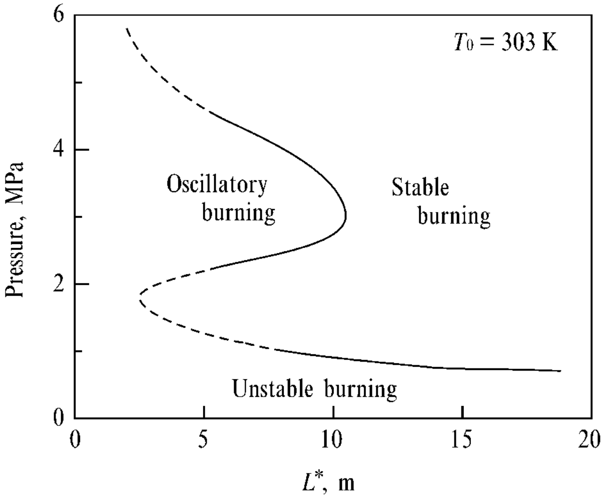

Figure 9-19. Stable, oscillatory, and unstable burning zones of a lead catalyzed double-base propellant.

9.5.3
Acoustic Combustion Instability

Combustion of propellant in a rocket motor accompanied by high-frequency pressure oscillation is one of the most harmful phenomena in rocket motor operation. There have been numerous theoretical and experimental studies on the acoustic mode of oscillation, medium frequency (100 Hz – 1 kHz) and high frequency (1–30 kHz). The nature of oscillatory combustion instability is dependent on various physicochemical parameters such as the burning rate characteristics, mechanical properties, and energy density of the propellants, and the physical shape and dimensions of the propellant grains[10,11].

In general, when the length of an internal burning grain is relatively great, more than 2 meters, a longitudinal mode across the fore head end to the nozzle occurs. When the port of an internal burning grain is small (< 0.2 m), a tangential mode or a radial mode across the interior surface of the port occurs. In order to evaluate the sensitivity of burning rate to pressure oscillation for various types of propellants, response function, i.e., burning rate sensitivity to burning pressure, is determined for each propellant grain experimentally. Figure 9-20 shows a structure and principle of a T burner that is used to measure the response function of propellants. Two propellant samples are set, one at each end of the T burner. The burner is pressurized by nitrogen gas to the test pressure level. The acoustic mode of the burner established in the burner is uniquely determined by the speed of sound in the burner and the distance between the burning surfaces of the two samples. When the propellant samples are ignited, pressure waves travel from one burning surface to the other. When a resonance pressure exists at a certain length of

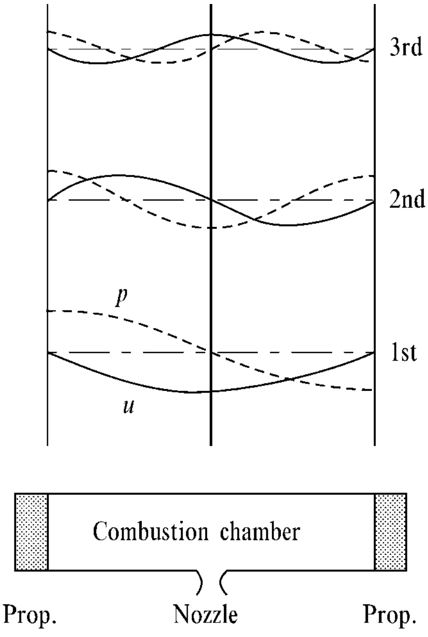

Figure 9-20. Combustion mode in T burner.

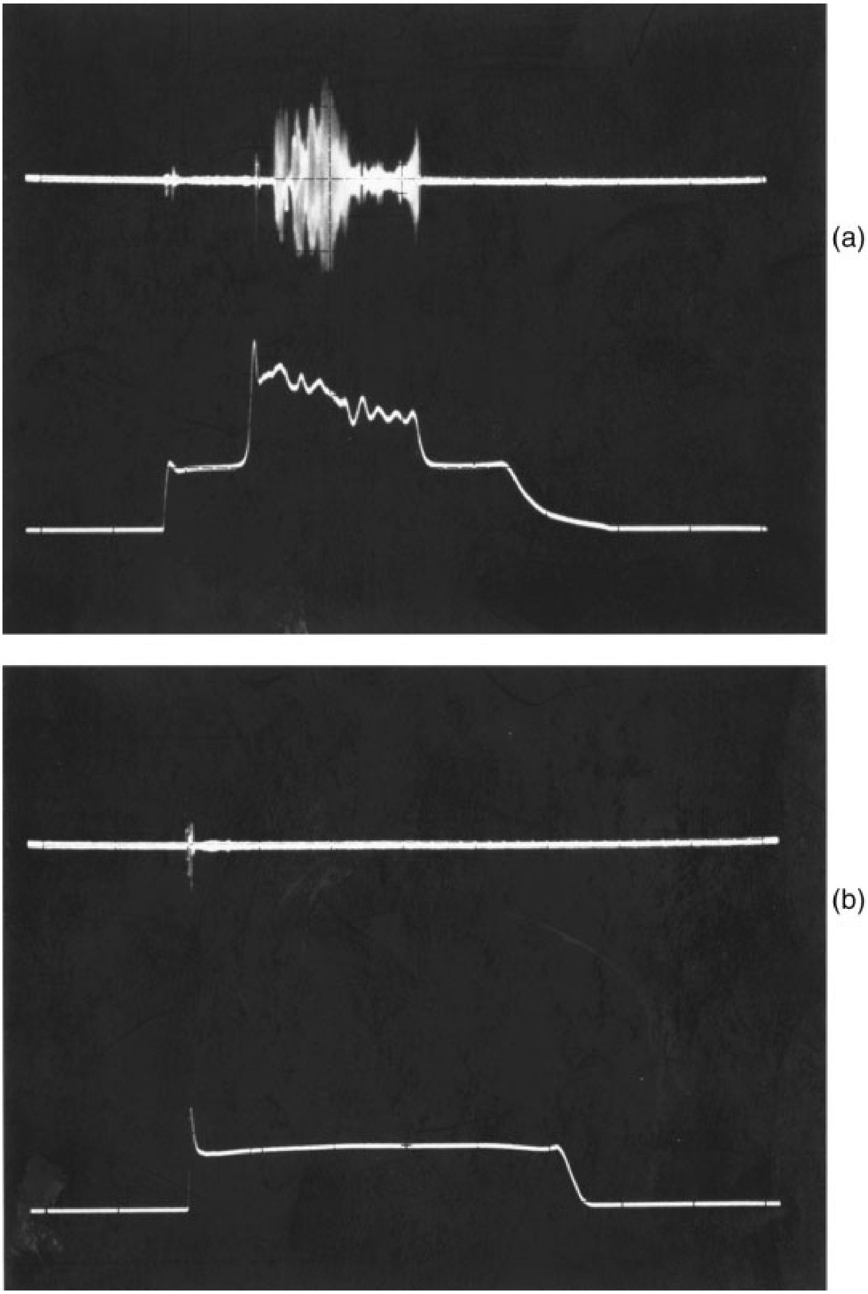

Figure 9-21. A set of pressure versus time curve of RDX/AP-HTPB composite propellants burning in a rocket motor: (a) high frequency combustion oscillation occurs (30 kHz with 4 MPa amplitude maximum and the pressure in stable burning region 4.5 MPa) and (b) the combustion oscillation is eliminated completely by the addition of 0.5 % aluminum particles (5 μm in diameter).

the T burner, the propellant is sensitive to the frequency. The response function is determined by the degree of amplification of the pressure level.

Figure 9-21 shows a typical set of time-pressure curves of stable and unstable combustion in a rocket motor. The propellant grain is an internal-burning star-shaped RDX/AP composite propellant, 43 % RDX (120 μm in diameter), and 43 % AP (20 μm in diameter) and 14 % HTPB with 0.40 % Al (5 μm in diameter). The pressure exponent of the burning rate is $n = 0.46$. The interior grain geometry is a cylindrical grain that burns from the internal cylindrical surface and also from both ends of the grain in order to maintain a flat time versus pressure curve. As shown in Fig. 9-21(a), the propellant burns normally after ignition and the burning time versus pressure curve appears as expected. However, the chamber pressure (shown below) increases abnormally and irregularly accompanied by high frequency oscillation (shown above). The abnormal-burning pressure returns to the normal-burning pressure at a certain time and continues up to the end of the burning. The frequency analysis of the pressure curve indicates the first tangential mode across the interior port whose frequency ranges between 10 kHz and 20 kHz[10].

When 0.5 % Al (5 μm in diameter) is added within the RDX/AP propellant grain, the observed high-frequency oscillatory burning is eliminated completely throughout the burning time, as shown in Fig. 9-21(b). The burning rate and the pressure exponent of the burning rate of the propellant grain remains unchanged by the addition of the Al particles[9]. It has been well established that the solid particles in the combustion chamber absorb the kinetic energy of the oscillatory motion of the combustion gas and then suppress this motion.

9.6
Ducted Rocket Engine

9.6.1
Propulsion of a Ducted Rocket

A ducted rocket is intermediate between a solid rocket and a liquid ramjet in its propulsive characteristics[12,13]. The specific impulse of a ducted rocket is increased significantly by combustion with the air induced from the atmosphere. The combustion efficiency is highly dependent on the physicochemical properties of the fuel-rich gas-generating propellants. The mixture ratio of the fuel-rich gas and the air induced from the atmosphere is an important parameter determining the thrust and the specific impulse. Furthermore, as shown in Fig. 1-3, the thrust of a ducted rocket engine is determined by the momentum difference between the exit and the entrance. The momentum of the incoming air from the entrance is converted to pressure through an aerodynamic process, and the heat energy released by the combustion of fuel-rich gas in the engine is used to increase the temperature. The increased pressure and temperature of the combustion gas in the combustion chamber is converted to the aerodynamic momentum through an exhaust nozzle at the exit. The thrust generated through the momentum change is represented by Eq. (1.62).

The high efficiency operation of a ducted rocket engine is obtained in supersonic flight in the range Mach 2–4 based on aerothermodynamics. The pressure and temperature of the supersonic air flow are changed through the shock wave and the air flow becomes subsonic as described in Section 1.2.1 of Chapter 1. Then the fuel-rich gas generated by the combustion of the propellant (gas-generating propellant) mixes with the air and reacts to produce high temperature combustion gas. Thus, the chemical properties of the gas-generating propellant are different from those of the propellants used for rocket propulsion[12,13].

9.6.2
Principle of the Variable Flow Ducted Rocket

9.6.2.1 Optimization of Energy Conversion

Figure 9-22 shows a schematic drawing of a flight projectile assisted by a ducted rocket engine. The supersonic air induced to the air intakes is converted to a pressurized subsonic air flow through the shock waves in the air intakes. The fuel-rich gas produced in the gas generator pressurizes the primary combustion chamber and flows into the secondary combustion chamber through the gas flow control system. The pressurized air and the fuel-rich gas produce premixed and/or diffusion flames in the secondary combustion chamber. The high temperature combustion gas flows out through the convergent-divergent nozzle and is accelerated to supersonic flow.

Since the mass flow rate of the supersonic air induced from the air intakes is dependent on the flight speed and altitude of the projectile, the mixture ratio of the air and the fuel-rich gas changes. In some cases, the mixture is too air-rich or too fuel-rich to burn in the secondary combustion chamber, i.e., the mixed gas no longer within the flammability limits (see Section 3.4.3 in Chapter 3) and no ignition occurs (see Section 3.4.1 in Chapter 3). In order to optimize the combustion in the secondary combustion chamber under various flight conditions, a variable flow rate system is attached to the gas flow control system.

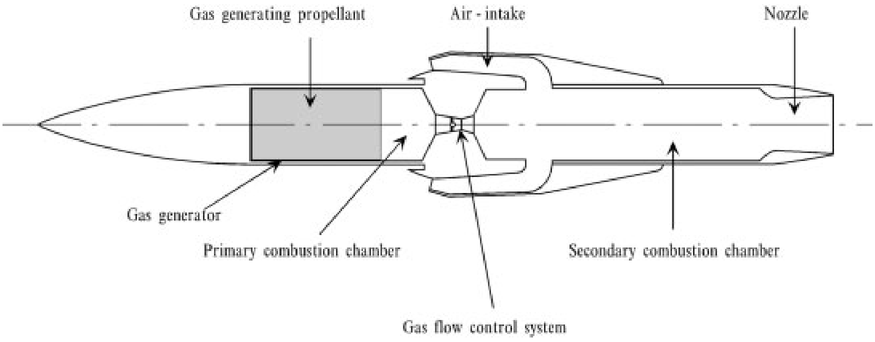

Figure 9-22. Variable flow ducted rocket

9.6.2.2 **Control of Fuel Flow Rate**

The mass generation rate in the primary combustion chamber is controlled by the variable flow system, and the mixture ratio of fuel-rich gas and air in the secondary combustion chamber is optimized. In general, the burning rate of propellants for rockets and guns is given by Eq. (3.68). As in the case of propellants, the burning rate of the gas-generating propellants used as gas generators in a ducted rocket is given by the same relationship between pressure and burning rate. Since the pressure exponent n is given by $0 < n < 1$, the burning rate is changed by the change of burning pressure.

The mass generation rate from the propellant $\dot{m}_g$ and the mass discharge rate from the nozzle $\dot{m}_d$ are given by Eqs. (9.1) and (9.2), respectively. If the pressure change in the primary combustion chamber with respect to time is negligibly small, the rate of mass accumulation in the chamber $\dot{m}_c$ given by Eq. (9.3) is $\dot{m}_c = 0$. The mass balance in the chamber is given by Eq. (9.7). If the nozzle throat area of the primary combustion chamber A_t is changed, the pressure represented by Eq. (9.8) is changed and the burning rate given by Eq. (3.68) is also changed. Accordingly, $\dot{m}_c$ and $\dot{m}_d$ are changed. The fundamental principle of the variable-flow ducted rocket is the change in nozzle area according to the required mass flow rate of the fuel-rich gas.

9.6.3
Energetics of Gas-Generating Propellants

The chemical compositions of the gas-generating propellants for ducted rocket engines are different from those of the propellants used for rocket motors. The physicochemical properties of the gas-generating propellants used for variable flow systems are[12,13]

(1) Self-sustaining decomposition or combustion characteristics with higher fuel concentrations and lower oxidizer concentrations,
(2) High pressure exponent of burning rate: n is approximately equal to 0.7,
(3) High burning rate for end-burning propellant grain: 5 mm/s in the low-pressure region and 30 mm/s in the high-pressure region, and
(4) Low enough combustion temperature to protect the flow rate control valve from heat and high enough to ignite the fuel-rich gas when air is mixed in the secondary combustion chamber : the ideal combustion temperature in the primary combustion chamber is approximately 1400 K.

The gas-generating propellants are (1) ammonium perchlorate-polybutadiene (AP-PB) composite propellants, (2) nitrocellulose-nitroglycerin (NC-NG) double-base propellants, and (3) glycidyl azide polymer (GAP) propellants.

Typical gas-generating propellants are (1) AP-PB composite propellant composed of 50 % AP and 50 % HTPB that is cured with isophorone diisocyanate (IPDI), (2) NC-NG double-base propellant composed of 70 % NC and 30 % NG that is plasticized with diethyl phthalate (DEP), and (3) GAP propellant composed of GAP copolymer that is cured with 12.0 % hexamethylene diisocyanate (HMDI) and cross-linked with 3.2 % trimethylolpropane (TMP).

The AP-HTPB propellant produces relatively high concentrations of solid carbon and hydrogen chloride (HCl). Though the mass fraction of the fuel components increases as the mass fraction of HTPB increases, the self-sustaining burning of AP-HTPB propellant becomes impossible because of the heat of decomposition becomes too low to maintain its thermal decomposition. On the other hand, the NC-NG propellant burns to generate fuel-rich products even when the mass fraction of NC increases. However, the mechanical properties of NC-NG propellant become poor. Furthermore, the burning rate of AP-HTPB and NC-NG propellants becomes low and the pressure exponent also becomes too low for their use as ducted rocket propellants.

Figure 9-23 shows the burning rate characteristics of AP-HTPB composite, NC-NG double-base, and GAP propellants in the primary combustion chamber. The burning rate of GAP propellant is much higher than that of composite and double-base propellants. When the pressure is increased from 2.5 MPa to 10 MPa, the burning rate of GAP propellant increases from 10 mm/s to 25 mm/s. The pressure exponent, *n*, of composite or double-base propellant is too low for their use as gas generators of variable-flow ducted rockets. The pressure exponent of GAP propellant is relatively high and is about 0.7 in the pressure range between 1.0 MPa and 12 MPa.

As described in Section 4.2.2.3 of Chapter 4 and section 5.2.2 of Chapter 5, GAP is a unique energetic material which burns very rapidly without any oxidation reaction. When N_3 groups are decomposed to produce nitrogen gas, a significant amount of heat is released by the thermal decomposition. The heat of formation is positive, 0.957 MJ/kg at 293 K. The GAP prepolymer is polymerized to form GAP copolymer with HMDI and

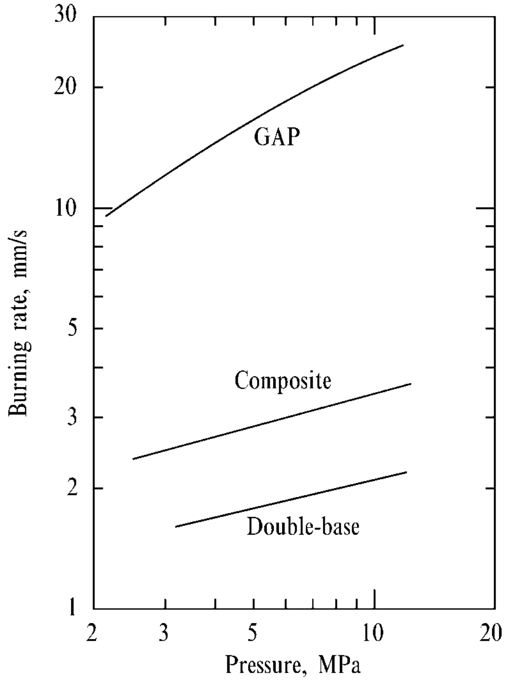

Figure 9-23. Burning rate characteristics of gas-generating propellants.

is crosslinked with TMP. The GAP prepolymer is used as GAP gas-generating propellant whose adiabatic flame temperature is 1370 K at 5 MPa. The major combustion products are H_2 (0.315), C(s) (0.298), and CO (0.139) by mole fraction. These products are combustible fuel fragments with air in the secondary combustor. The remaining products are N_2 (0.190) and minor products are CO_2 and H_2O.

Figure 9-24 shows a typical set of burning rate characteristics of GAP propellants with and without burning rate modifier (graphite: $0.03 \mu m$ in diameter)[12,13]. Considerable modification of burning rate and pressure exponent are possible by the addition of different mass fractions $\xi(C)$ of the modifier. For example, the pressure exponent is increased from 0.3 to 1.5 at a fixed pressure by $\xi(0.10)$ addition of the modifier. The graphite used as the burning rate modifier also acts as a fuel component of GAP propellants.

Metal particles are also used as energetic fuel components. The metal particles mixed with polymeric propellants increase the flame temperature when the particles are mixed with air in the secondary combustion chamber. Typical metal particles are aluminum (Al), magnesium (Mg), titanium (Ti), or zirconium (Zr). Though boron (B) is not metal, the heat generated by boron oxidation is much higher than the heat generated by any metals[14–17].

Figure 9-25 shows the adiabatic flame temperature T_f of GAP propellants containing boron particles as a function of ε, where ε is the air to fuel ratio in the secondary combustion chamber. As ε increases, T_f increases rapidly in the region $\varepsilon < 5$. However, T_f decreases with increasing ε in the region $\varepsilon > 5$. The maximum temperature is 2550 K at $\varepsilon = 5$ for the propellants without boron and is 2650 K for $\xi(0.1)$ and 2730 K for $\xi(0.1)$ and $\xi(0.2)$, respectively, where $\xi(B)$ is the mass fraction of boron.

The specific impulse of a ducted rocket $I_{sp,d}$ is defined by

$$I_{sp,d} = I_{sp} - \varepsilon u_{air} / g \tag{9.22}$$

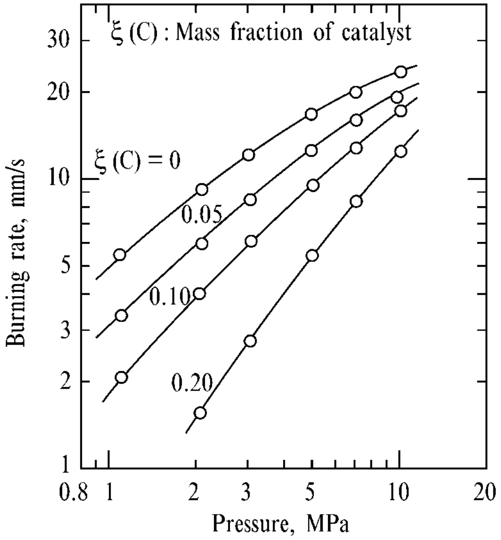

Figure 9-24. Burning rate of GAP copolymer with and without catalyst (graphite) showing that the pressure exponent increases with increasing amount of catalyst.

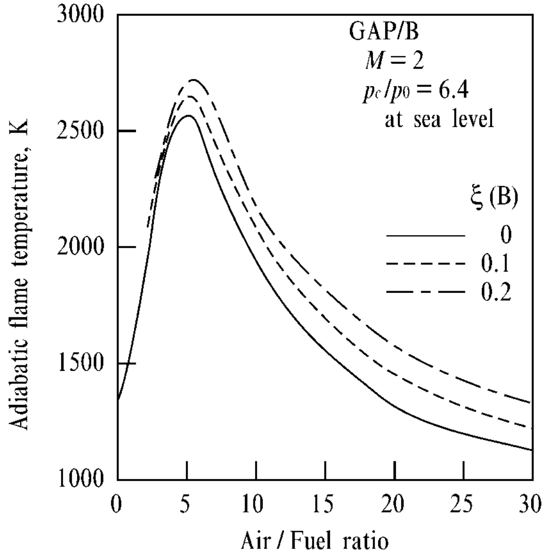

Figure 9-25. Adiabatic flame temperature of GAP/B gas-generating propellant as a function of air to fuel ratio.

where u_{air} is the flight velocity, g is the gravitational acceleration, and I_{sp} is the specific impulse of the gas-generating propellant.

$$I_{sp} = \frac{F}{\dot{m}_g g} \tag{9.23}$$

where F is the thrust of the ducted rocket. The momentum coming in the air intakes is not included in the I_{sp} value that is used to evaluate the thermochemical potential

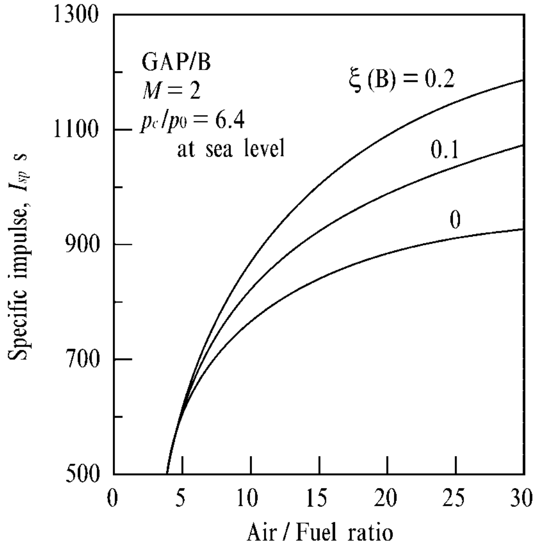

Figure 9-26. Specific impulse of GAP/B gas generating propellant as a function of air to fuel ratio.

of gas-generating propellants. Figure 9-26 shows the I_{sp} of GAP propellants containing boron at the flight speed Mach 2 where the pressure ratio of the pressure in the secondary combustion chamber p_c to atmospheric pressure p_0 is 6.4. The I_{sp} increases as ε increases at fixed $\xi(B)$, and also increases as $\xi(B)$ increases at fixed ε.

References

1 Kubota, N., Survey of Rocket Propellants and their Combustion Characteristics, Fundamentals of Solid-Propellant Combustion, edited by Kuo, K. K. and Summerfield, M., Progress in Astronautics and Aeronautics, Vol. 90, Chapter 1, AIAA, New York (1984).

2 Glassman, I. and Sawyer, F., The Performance of Chemical Propellants, Circa Publications, New York (1970).

3 Sutton, G. P., Rocket Propulsion Elements, 6th edition, John Wiley & Sons, Inc., New York (1992), Chapter 11.

4 Kubota, N., Rocket Combustion, Nikkan Kogyo Press, Tokyo (1995).

5 Ishihara, A. and Kubota, N., Erosive Burning Mechanism of Double-Base Propellants, Twenty-first Symposium (International) on Combustion, The Combustion Institute, Pittsburgh, PA (1986), pp. 1975–1981.

6 Caveny, L. H. and Glick, R. L., The Influence of Embedded Metal Fibers on Solid Propellant Burning Rate, Journal of Spacecraft and Rockets, Vol. 4, No. 1, 1967, pp. 79–85.

7 Kubota, N., Ichida, M. and Fujisawa, T., Combustion Processes of Propellants with Embedded Metal Wires, AIAA Journal, Vol. 20, No. 1, 1982, pp. 116–121.

8 Kubota, N., Role of Additives in Combustion Waves and Effect on Stable Combustion Limit of Double-Base Propellants, Propellants and Explosives, Vol. 3, 1978, pp. 163–168.

9 Kubota, N. and Kimura, J., Oscillatory Burning of High-Pressure Exponent Double-Base Propellants, AIAA Journal, Vol. 15, No. 1, 1977, pp. 126–127.

10 Kubota, N., Kuwahara, T., Yano, Y., Takizuka, M. and Fukuda, T., Unstable Combustion of Nitramine/Ammonium Perchlorate Composite Propellants, AIAA-81–1523, AIAA, New York (1981).

11 Kubota, N., Yano, Y. and Kuwahara, T., Particulate Damping of Acoustic Instability in RDX/AP Composite Propellant Combustion, AIAA-82–1223, AIAA, New York (1982).

12 Kubota, N., Air-Augmented Rocket Propellants, Solid Rocket Technical Committee Lecture Series, AIAA Aerospace Sciences Meeting, Reno, Nevada (1994).

13 Kubota, N., Yano, Y., Miyata, K., Kuwahara, T., Mitsuno, M. and Nakagawa, I., Energetic Solid Fuels for Ducted Rockets (II), Propellants, Explosives, Pyrotechnics, Vol. 16, 1991, pp. 287–292.

14 Schadow, K., Boron Combustion Characteristics in Ducted Rockets, Combustion Science and Technology, Vol. 5, 1972, pp. 107–117.

15 Zhongqin, Z. Zhenpeng, Z. Jinfu, T., and Wenlan, F., Experimental Investigation of Combustion Efficiency of Air-Augmented Rockets, Journal of Propulsion and Power, Vol. 2, 1986, pp. 305–310.

16 Kubota, N., Miyata, K., Kuwahara, T., Mitsuno, M. and Nakagawa, I., Energetic Solid Fuels for Ducted Rockets (III), Propellants, Explosives, Pyrotechnics, Vol. 17, 1992, pp. 303–306.

17 Kubota, N. and Kuwahara, T., Ramjet Propulsion, Nikkan Kogyo Press, Tokyo (1996).

Propellants and Explosives: Thermochemical Aspects of Combustion. Naminosuke Kubota
Copyright © 2002 Wiley-VCH Verlag GmbH & Co. KGaA
ISBNs: 3-527-30210-7 (Hardback); 3-527-60050-7 (Electronic)

Appendix A

List of abbreviations of energetic materials

ADN	ammonium dinitramide
AMMO	3-azidomethyl-3-methyloxetane
AN	ammonium nitrate
AP	ammonium perchlorate
BAMO	bis-azide methyloxetane
BCMO	3,3-bis(chloromethyl)oxetane
CL-20	hexanitrohexaazatetracyclododecane
CTPB	carboxy-terminated polybutadiene
CuSa	copper salicylate
CuSt	copper stearate
DATB	diaminotrinitrobenzene
DBP	dibutylphthalate
DDNP	diazodinitrophenol
DEGDN	diethyleneglycol dinitrate
DEP	diethylphthalate
DNT	dinitrotoluene
DOA	dioctyl adipate
DOP	dioctyl phthalate
DPA	diphenylamine
EC	ethyl centralite
GAP	glycidyl azide polymer
HMDI	hexamethylene diisocyanate
HMX	cyclotetramethylene tetranitramine
HNB	hexanitrobenzene
HNF	hydrazinium nitroformate
HNS	hexanitrostilbene
HTPA	hydroxy-terminated polyacetylene
HTPB	hydroxy-terminated polybutadiene
HTPE	hydroxy-terminated polyether
HTPS	hydoxy-terminated polyester

IDP	isodecyl pelargonate
IPDI	isophorone diisocyanate
MAPO	tris(1-(2-methyl)aziridinyl) phosphine oxide
MT-4	adduct of 2.0 moles MAPO, 0.7 mole adipic acid, and 0.3 mole tartaric acid
nBF	*n*-butyl ferrocene
NC	nitrocellulose
NG	nitroglycerin
NIBGTN	nitroisobutylglycerol trinitrate
NM	nitromethane
NP	nitronium perchlorate
NQ	nitroguanidine
2NDPA	2-nitrodiphenylamine
OXM	oxamide
PB	polybutadiene
PBAN	polybutadiene acrylonitrile
PbSa	lead salicylate
PbSt	lead stearate
Pb2EH	lead 2-ethylhexoate
PE	polyether
PETN	pentaerythritol tetranitrate
Picric Acid	2,4,6-trinitrophenol
PQD	paraquinone dioxime
PS	polyester
PS	polysulfide
PU	polyurethane
PVC	polyvinyl chloride
RDX	cyclotrimethylene trinitramine
SN	sodium nitrate
SOA	sucrose octacetate
TA	triacetin
TAGN	triaminoguanidine nitrate
TATB	triaminonitrobenzene
TDI	toluene-2,4-diisocyanate
TEA	triethanolamine
TEGDN	triethyleneglycol dinitrate
Tetryl	trinitro-2,4,6-phenylmethylnitramine
TMETN	trimethylolethane trinitrate
TMP	trimethylolpropane
TNB	trinitrobenzene
TNChloroB	trinitrochlorobenzene
TNT	trinitrotoluene
Trinanisol	trinitroanisol
Viton	vinylidene fluoride hexafluoropropene polymer

Propellants and Explosives: Thermochemical Aspects of Combustion. Naminosuke Kubota
Copyright © 2002 Wiley-VCH Verlag GmbH & Co. KGaA
ISBNs: 3-527-30210-7 (Hardback); 3-527-60050-7 (Electronic)

Appendix B

Measurements of Burning Rate and Combustion Wave Structure

The burning rate of propellants is one of the important parameters for the design of rocket motors. The burning rate is obtained as a function of pressure and initial temperature, and the pressure exponent of the burning rate and the temperature sensitivity of the burning rate are deduced.

The combustion chamber used for the measurements of burning rate is called a "strand burner". Figure B-1 shows a drawing of a strand burner pressurized to the desired pressure with nitrogen gas. Nitrogen gas is purged from the side of the strand burner at the lower end and exhausted from the center of the top of the burner through a choked orifice. The nitrogen gas flows around the propellant strand and then the burned gas flows together with the nitrogen gas toward the choked orifice. The nitrogen gas purge rate is fixed so as to eliminate the shear flow between the burned gas and the nitrogen gas above the burning strand, thus keeping the

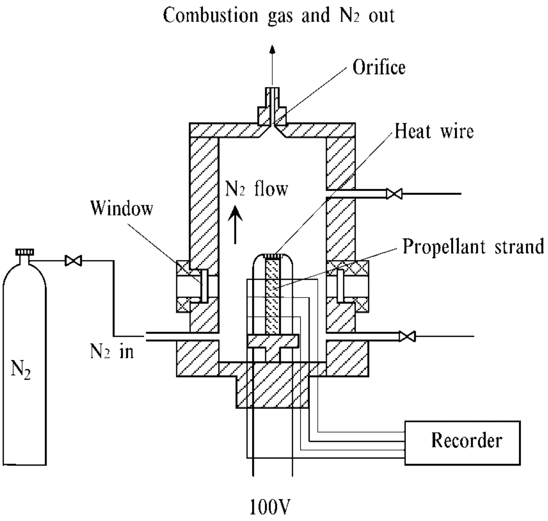

Figure B-1. Chimney-type strand burner with observation windows.

combustion flame stable and the burning surface flat during burning. The strand burner with the gas flow system is called a "chimney-type strand burner".

When a propellant strand is ignited under nitrogen gas purge conditions, the pressure in the strand burner increases because of the addition of the propellant burned gas. However, the pressure valve attached to the nitrogen gas supplier is regulated automatically to reduce the nitrogen gas flow rate in order to maintain the pressure constant. Thus, the pressure in the burner is maintained at the desired pressure.

The propellant used for the measurements of burning rate is in the shape of a strand, 7 × 7 mm in cross-section and 10 mm in length as a standard dimension. The strand is positioned vertically in the center of the burner. A metal fine wire (0.1 mm in diameter) is threaded through the top of the strand. Burning rate is measured by determining the instant of melting of each of 5 low-melting-point fuse wires of lead metal, 0.25 mm in diameter, threaded through the strand at accurately known separation distances (15 mm). These 5 fuse wires, each in series with a resistor, form 5 parallel arms of an electrical circuit, whose output voltage changes discontinuously as soon as a fuse wire melts. The temperature of the strand is measured by a calibrated copper-constantan thermocouple threaded through the strand and the bead of the thermocouple is placed in the center of the strand.

The burning rates at different temperatures are measured by the strand burner, which is kept in a temperature conditioner. The nitrogen gas purged to the strand burner is also cooled or heated to the desired temperature through a heat exchanger that is also kept in the same temperature conditioner. Thus, the temperatures of the strand burner, propellant strand, and nitrogen gas are all kept at the same desired temperature. The high temperature gas generated by the strand burning does not affect the temperature of the strand because the burned gas flows in an upward direction. More than 5 min are needed to establish the temperature of the strand under nitrogen flow conditions.

The chimney-type strand burner for gas phase and burning surface observations consists of a chamber with four quartz windows mounted on the side of the chamber wall. A small cylinder 20 mm in diameter is mounted vertically inside and connected to the base of the chamber. Four transparent glass plates are mounted on the side of the cylinder. The cylinder is used to maintain a flow of nitrogen gas around the burning strand for the purpose of keeping the glass plates free of smoke deposits. The nitrogen gas is supplied through the base of the chamber and the flow rate is adjusted by changing the size of the orifice mounted on the top of the burner.

Photographs of the combustion wave structure in the gas phase are obtained using a high-speed video-camera. The propellant strand is illuminated from the outside of the strand burner by a tungsten lamp or a xenon lamp in order to observe the burning surface. Micro-photographs of the burning surface are obtained using micro-telescope equipment mounted on a high-speed video-camera.

Index